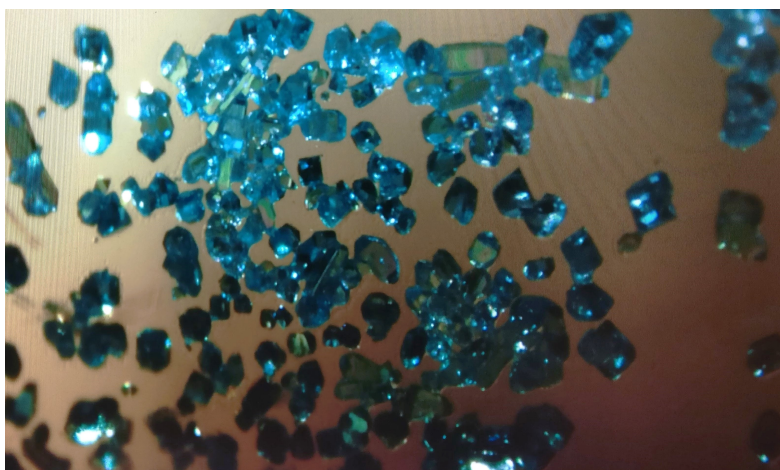


Investigations of Magnetic and Structural Order in Molecular-based Inorganic Framework Materials

Madeleine Geers



A thesis submitted to the University of Nottingham for the degree of DOCTOR OF
PHILOSOPHY



**University of
Nottingham**
UK | CHINA | MALAYSIA

School of Chemistry, University of Nottingham, UK
November 2023

Abstract

This thesis explores the role composition plays on the crystallographic structures of molecular-based frameworks and how, in turn, this influences their magnetic character. Whilst it is understood that the combination of atomic anions and cations selected to build inorganic compounds impacts the connectivity and physical properties of materials, anticipating the relationship for molecular-based frameworks is less reliable. A method to probe both the crystallographic and magnetic structure of compounds simultaneously is by neutron diffraction experiments, which is a technique of particular focus in this work.

In the first chapter, a broad discussion is presented on inorganic framework materials, exploring how the selection of components dictates topologically diverse frameworks. In addition, there is an overview of the experimental techniques employed throughout the thesis.

Chapter 2 describes a method to grow and store single crystals of the deliquescent framework $[\text{Na}(\text{OH}_2)_3]\text{Mn}(\text{NCS})_3$ through controlling the local humidity of the samples. As a result, single crystals of suitable dimensions for neutron diffraction experiments were obtained, showing that the compound magnetically orders as an antiferromagnet. In addition, the neutron measurements revealed the tight-knit hydrogen bonding network between the $[\text{Na}(\text{OH}_2)_3]^+$ cations and the framework.

Chapter 3 presents two unreported post-perovskite thiocyanate frameworks, $\text{CsM}(\text{NCS})_3$, $\text{M} = \text{Mn}, \text{Co}$, and the magnetic properties of $\text{CsMn}(\text{NCS})_3$, $\text{CsCo}(\text{NCS})_3$ and $\text{CsNi}(\text{NCS})_3$. The Co and Ni analogues magnetically order as weak ferromagnets. In comparison, the Mn compound orders as a non-collinear antiferromagnet. The magnetic structures for $\text{M} = \text{Ni}$ and Mn were resolved using low temperature neutron diffraction measurements.

Chapter 4 explains how the pressure-activated structural distortions of $\text{Ni}(\text{NCS})_2$ promote a higher magnetic ordering temperature. Using magnetometry and low temperature neutron diffraction data, the ordering temperature was shown to increase by +19 % when compressed up to 8.4 kbar (+2.3 % kbar^{-1}). Neutron and X-ray diffraction measurements reveal that this increase is a direct result of the compressible framework, with a comparatively low bulk modulus compared to atomic-based two-dimensional materials.

Chapter 5 explores the structural evolution and magnetic character of the solid solutions $[\text{CH}_3\text{NH}_3]\text{Co}_x\text{Ni}_{1-x}(\text{HCOO})_3$, $x = 0.25, 0.50, 0.75$. Magnetometry measurements demonstrate that the solid solutions show a linear continuum of their magnetic ordering temperature between the Co and Ni parent compounds. A combination of Laue and monochromatic neutron diffraction revealed the crystals are modulated and the incommensurate wavevectors and modulated structures for $[\text{CH}_3\text{NH}_3]\text{Co}_{0.5}\text{Ni}_{0.5}(\text{HCOO})_3$ were identified.

Chapter 6 explores the diversity of uncommon and unconventional site orderings and octahedral tilt sequences in four double perovskites, nominally $[\square\text{A}]\text{Mn}\{\text{Bi}(\text{SCN})_6\}$, $\square =$ vacancy; $\text{A} = \text{Cs}^+, \text{K}^+, \text{NH}_4^+$ and $\text{C}(\text{NH}_2)_3^+$. Two previously unreported tilt patterns have been identified *via* X-ray and neutron diffraction, as well as unusual A-site orderings.

Finally, in Chapter 7, the summarising conclusions and outlooks are presented, regarding both the results presented in this thesis and how the interplay between the structure and magnetic properties of molecular-based frameworks can be progressed in the future.

Acknowledgements

Firstly, I would like to thank my supervisors Dr Matthew Cliffe and Dr Laura Cañadillas Delgado for the guidance and support over the last few years. Laura, quería darte las gracias por echarme una mano cuando llegué a Grenoble, sobre todo con la mudanza en unas circunstancias tan complicadas.¹ Matt, thank you for your endless patience and attentiveness, you did not feel a full country away.

In addition, the thesis would not have come together without the support of other scientists and collaborators I have worked with along the way. En particular, a Dr Oscar Fabelo (Institut Laue Langevin, ILL), quien me ha guiado durante mi estancia en el ILL, no solo estuvo presente en prácticamente todos los experimentos de neutrones, sino que también me ha enseñado todo lo que sé sobre FullProf. Also, Dr Stephen Argent (University of Nottingham) for help with the X-ray diffraction whilst I was at the university and sharing entertaining anecdotes as I solved the structures. As is common, for pandemic and non-pandemic related reasons, there are also many collaborators I have not met in person, yet am very grateful for their contributions, Dr Sanliang Ling (University of Nottingham) for all the DFT calculations, Dr Andrew Burnett (University of Leeds) for optical measurements on a very temperamental crystal, Dr Gregor Kieslich (Technical University of Munich) for kindly sharing his beamtime (I15, Diamond) and Dr Jakub Wojciechowski and Dr Robert Bücke (Rigaku Europe SE) for the electron diffraction measurements. Although it is work that did not make it into the thesis, thank you to Dr Andrew Wildes for our neutron experiment (D7, ILL) and also for the many hours you spent “desk-bombing” and cheerfully distracting the office.

I am fortunate to have met many young scientists as well. To all the members of the Cliffe group, thank you for your good humour and acceptance of my (mostly) 2D appearance in group meetings. Dr Jem Pitcairn has helped carry out several magnetometry measurements, as well as always being ready to share his new favourite paper with me. I would also like to thank all the friends I have gained in Grenoble, especially my officemate and chief interior decorator Jen, as well as everybody who I have ever dragged up (and back down) mountains, been on odd adventures around France and accompanied me for the

¹And thank you to Carmen for the translations, I have not secretly been learning Spanish.

everyday happenings at the ILL.

Finally, I would like to thank my family, immediate and extended, who are always ready to celebrate with me. Thank you.

Table of Contents

Abstract	i
Acknowledgements	iii
1 Introduction	1
1.1 Components of a functional compound	1
1.2 Compound identification	2
1.2.1 Crystal symmetry	2
1.2.2 Diffraction	3
1.2.3 Radiation interaction with matter	5
1.2.4 Diffraction experiments	7
1.2.5 Solving the nuclear structure	9
1.3 Magnetic characterisation	15
1.3.1 Magnetometry measurements	15
1.3.2 Magnetic neutron diffraction experiments	19
1.4 Pressure	23
1.5 Thiocyanate ligand profile	25
1.6 Functional design	27
1.7 Designing magnetic materials	34
1.8 Neutrons for complementary information	38
1.9 Objectives	40
2 Magnetic and low temperature structural properties of $[\text{Na}(\text{OH}_2)_3]\text{Mn}(\text{NCS})_3$	42
2.1 Summary	42
2.2 Introduction	42
2.3 Results	45
2.3.1 Synthesis	45
2.3.2 Recrystallisations	45
2.3.3 Prolonging the longevity of a crystal	47
2.3.4 Magnetometry	48
2.3.5 Single crystal neutron diffraction	50

2.4	Second harmonic generation measurements	54
2.5	Discussion	55
2.6	Conclusions	58
2.7	Experimental	59
2.7.1	Synthesis	59
2.7.2	Magnetic Measurements	59
2.7.3	Single crystal neutron diffraction	60
2.7.4	Second harmonic generation measurements	60
2.8	Appendix	61
3	Non-collinear magnetism in the post-perovskite thiocyanate frame- works CsM(NCS)₃	62
3.1	Summary	62
3.2	Introduction	62
3.3	Results	64
3.3.1	Synthesis	64
3.3.2	Structure	65
3.3.3	Magnetism	68
3.3.4	Neutron diffraction	71
3.4	Discussion	77
3.5	Conclusions	79
3.6	Experimental	80
3.6.1	Synthesis of CsM(NCS) ₃	80
3.6.2	Single Crystal X-ray Diffraction	80
3.6.3	Single Crystal Neutron Diffraction	81
3.6.4	Powder Neutron Diffraction	81
3.6.5	Magnetic Measurements	82
3.6.6	Density Functional Theory Calculations	82
3.7	Appendix	83
4	High pressure behaviour of the magnetic van der Waals molecular framework Ni(NCS)₂	87
4.1	Summary	87
4.2	Introduction	87
4.3	Results	90
4.3.1	Nuclear structure under pressure	90
4.3.2	Variable temperature high pressure	92
4.4	Magnetometry	93
4.5	Magnetic structure under pressure	94

4.6	Discussion	96
4.7	Conclusion	99
4.8	Experimental	100
4.8.1	Synthesis of Ni(NCS) ₂	100
4.8.2	Magnetic Measurements	100
4.8.3	DFT	100
4.8.4	Synchrotron diffraction measurements	101
4.8.5	Neutron Diffraction Measurements	102
4.9	Appendix	103
5	Modulated phase transitions and magnetic properties of the solid solutions [CH₃NH₃]Co_xNi_{1-x}(HCOO)₃	106
5.1	Summary	106
5.2	Introduction	107
5.3	Results	111
5.3.1	Synthesis and ambient structure	111
5.3.2	Magnetometry	113
5.3.3	Temperature dependent structural evolutions	116
5.3.4	Monochromatic neutron diffraction	120
5.4	Discussion	125
5.5	Conclusions	130
5.6	Experimental	131
5.6.1	Synthesis	131
5.6.2	Single crystal X-ray diffraction	131
5.6.3	Magnetic measurements	132
5.6.4	Laue neutron diffraction	132
5.6.5	Ambient temperature single crystal neutron diffraction (D9) . . .	132
5.6.6	Low temperature single crystal neutron diffraction (D19)	133
5.7	Appendix	133
6	A-site ordering and octahedral tilts in [□A]Mn{Bi(SCN)₆}	136
6.1	Summary	136
6.2	Introduction	136
6.3	Results	139
6.3.1	Synthesis	139
6.3.2	Structure	139
6.3.3	Magnetisation	153
6.4	Discussion	155
6.5	Conclusion	158

6.6	Experimental	160
6.6.1	Synthesis	160
6.6.2	Powder X-ray diffraction	160
6.6.3	Single crystal X-ray diffraction	161
6.6.4	Single crystal electron diffraction	162
6.6.5	Single crystal neutron diffraction	162
6.6.6	Magnetometry	163
6.7	Appendix	163
7	Conclusions and Outlook	167
	Bibliography	169
	Appendix A	190
	Appendix B	201

Chapter 1

Introduction

1.1 Components of a functional compound

At the heart of a scientists' ambition to design new materials, is the desire to create compounds tailored to specific functions. Inorganic materials, regularly inspired by natural minerals, have a rich history of being exploited for their physical properties.^{1,2} The game for a synthetic chemist is to select and swap components based on the physical properties they aim for. This has been demonstrated, for example, in pyrites (archetype FeS_2)³ or perovskites (CaTiO_3),⁴ in which families of compounds are synthesised with matching stoichiometry and topology, but not the same chemical composition. Depending on the chemical make-up, the composition and functionality within the compound-family can vary greatly from their original mineral analogues.

Functionality is expressed in the form of one or more desirable physical properties which has a practical use. One example is magnetism. The fundamental requirement for magnetism is unpaired electrons. Electrons possess an intrinsic spin which creates an atomic magnetic moment. It can interact with magnetic moments on close-by atoms, giving rise to different magnetic characteristics depending on the nature of the interactions. Therefore, in the pursuit for magnetic materials, components which have unpaired electrons are a key building block.

In general, throughout this thesis, I will refer to compounds with the general nomenclature AMX_n , where A and M are cations and X is an anion. The $[\text{MX}_n]$ components assemble into a connected framework, whilst the A cations are extra-framework components, positioned in voids.

In framework compounds, extended polymeric structures, the unpaired electrons are typically provided by the M-site species, which interact with neighbouring M ions *via* the

X anion that bridges them. As a result of the components incorporated, the M-site positions and how they are connected has a substantial impact on the type of magnetic behaviour observed. In addition, the A-site species has been shown to have a direct impact on the topology of the $[MX_n]$ framework,^{5,6} and, accordingly, the compounds with the same $[MX_n]$ composition exhibit different magnetic character as a result of the A-site components.^{7,8} Throughout this thesis, the consequences of substituting the A and M components are explored, both from a structural perspective, and the effect it has on the magnetic properties.

1.2 Compound identification

After synthesising new compounds, the first step of the analysis is identifying the structure. The physical properties of compounds are heavily dependent on their chemical composition and atom connectivity, so being able to identify the synthesised material is a necessity.

1.2.1 Crystal symmetry

A common and comprehensive method for identifying the structure of materials is by diffraction. For structure determination, there are benefits to using samples that are crystalline. The concepts of diffraction and crystals are closely related, with the International Union of Crystallography (IUCr) defining a crystalline material as having “an essentially sharp diffraction pattern”.⁹ In general, crystals have a three-dimensional periodic structure, built from a repeating unit, the unit cell, which tessellate with identical orientation. Deviations from this periodicity, such as for aperiodic or modulated crystals result in observable changes to the diffraction patterns.¹⁰ It is the content and layout of the unit cell which describes the structure of the compound.

Within a unit cell, the arrangement of atoms is described by symmetry elements. Symmetry elements fall in to two categories, non-translational and translational symmetry. Non-translational symmetry, also point symmetry, defines symmetry operations which when repeatedly applied to an object will eventually lead to the object arriving in its original position again. It includes rotations, reflections and inversions. In contrast, applying translational symmetry to an object will eventually replicate the object in the neighbouring unit cell, namely glide and screw symmetry operations. The summary of symmetry operations necessary to describe the crystal structure is its space group. The list of space groups and their corresponding symmetry can be found in tables, for example compiled by the IUCr,¹¹ or the Bilbao Crystallographic Server.^{12,13}

The symmetry of a compound will have implications for its physical properties. Compounds lacking inversion symmetry operators, non-centrosymmetric space groups, are sought after for their potential multiferroic properties, combining, for instance ferroelectricity,¹⁴ piezoelectricity¹⁵ or non-linear optical behaviour¹⁶ with other properties. In addition, crystals without improper rotation operations (including inversion and reflection) are chiral, which have been integrated into applications for enantioselective filtering¹⁷ or complex magnetic spin textures.⁷

1.2.2 Diffraction

The process of diffraction explains the bending of radiation waves changing their trajectory in the presence of an obstacle. Obstacles that are arranged with a regular spacing, such as symmetry equivalent atoms in neighbouring unit cells, will scatter the radiation coherently from each point. This can be scattering of radiation from two points along the same plane, or two points on parallel planes. This is the basis of Bragg's Law. The angle of the scattered radiation and the d spacing of the parallel planes are indirectly proportional,

$$n\lambda = 2d\sin\theta, \quad (1.1)$$

where n is an integer, λ is the radiation wavelength (units Å), θ is the angle between the incident radiation and the scattering plane and d is the interplanar spacing between a given set of Bragg planes (units Å). Bragg planes describe a set of reflections which are parallel and evenly spaced. Each set of Bragg planes can be identified by Miller indices, which relate the planes to the unit cell axes. Miller indices (hkl) are determined according to the intersection of the plane with the unit cell (abc) , where $(hkl) = \frac{1}{a}\frac{1}{b}\frac{1}{c}$ and h , k and l are integer numbers.

Although diffraction experiments occur in direct space (interplanar separations in Å), it is often necessary to consider diffraction events in reciprocal space (reflections with spacings in Å⁻¹). These are related by Fourier transform. Equation 1.1 can be rearranged to

$$\sin\theta = \frac{1}{2}n\lambda\left(\frac{1}{d}\right), \quad (1.2)$$

showing the relationship between the direct space diffraction angle and the Bragg planes in reciprocal space, where $1/d = d^*$. Reciprocal lattice vectors of the unit cell, a^* , b^* and c^* , correspond to the cross product of the unit cell in direct space, where

$$\mathbf{c}^* = \frac{(\mathbf{a} \times \mathbf{b})}{V}, \quad (1.3)$$

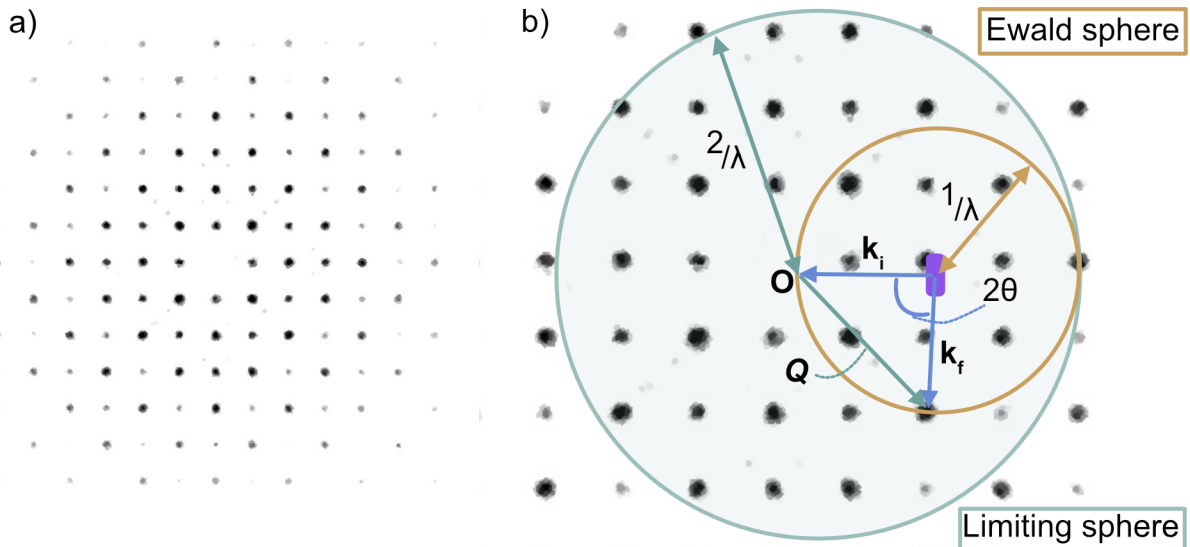


Figure 1.1: a) An example of a diffraction pattern, obtained from X-ray diffraction of $[\text{NH}_4(\text{OH}_2)_x]\text{Mn}\{\text{Bi}(\text{SCN})_6\}$ $x = 2/8 \leq 2.5/8$. The Bragg reflections (intensities shown in black) are generally sharp points and are evenly spaced. b) Illustration of the Ewald construction in two-dimensions. An incident beam of wavelength λ and wavevector \mathbf{k}_i is diffracted from the Bragg planes of the crystal (purple rectangle) with wavevector \mathbf{k}_f . A Bragg reflection is detected at the intersection between \mathbf{k}_f and the Ewald sphere (brown circle). The limiting sphere (teal circle) has its centre (\mathbf{O}) at the origin of the reciprocal lattice with a radius $2/\lambda$.

where V is the unit cell volume. Bragg reflections, the intensities detected during a diffraction experiment, show the reciprocal lattice points—the reciprocal space version of the direct lattice of a crystal (Fig. 1.1a). It is the periodic spacings, and systematic absences, of these Bragg reflections which allow the determination of the symmetry, structure and composition of the crystal.

To visually describe the relationship between the reciprocal lattice and the diffraction angle for a given wavevector, the Ewald representation is used (Fig. 1.1b). For a given crystal orientation, the accessible reflections (i.e. reflections that satisfy Eqn. 1.1) can be determined by identifying the reciprocal lattice points which overlap with the surface of the Ewald sphere, with radius $1/\lambda$. As the crystal is rotated, the reciprocal lattice, with origin (\mathbf{O}) rotates. The lattice points which intersect with the Ewald sphere change, permitting the exploration of reciprocal space. Only reflections which lie within $2/\lambda$ from the origin are accessible. The boundary of accessible reflections is defined as the limiting sphere. Therefore, using a shorter wavelength will increase the range of reciprocal space which can be probed.

Diffraction is an elastic process, therefore the incident and diffracted radiation have identical energies, $E_i = E_f$. The scattering vector, \mathbf{Q} , summarises the relationship of the incident, \mathbf{k}_i , and final, \mathbf{k}_f , wavevectors of the radiation, $\mathbf{Q} = \mathbf{k}_f - \mathbf{k}_i$. Diffraction data may be displayed as a function of Q , the magnitude of the scattering vector ($Q = |\mathbf{Q}|$). Datasets obtained from probes of different wavelengths can be directly compared since

Q removes the wavelength dependence of θ ,

$$Q = \frac{4\pi\sin(\theta)}{\lambda} = \frac{2\pi}{d} \quad (1.4)$$

Laue diffraction

Although many diffraction experiments occur using a single wavelength, monochromatic diffraction, a facile approach to produce a diffraction pattern is by using a continuous spectrum of wavelengths, Laue diffraction. The incident radiation now has a wavelength range between λ_{\min} and λ_{\max} and the Ewald representation corresponds to the volume between $1/\lambda_{\min}$ and $1/\lambda_{\max}$. Each Bragg reflection may arise from the diffraction of one or more discrete wavelengths, and the detected intensity is the summation of all diffracted wavevectors at a given point. As a consequence, due to the overlaying of multiple reflections, structural solution from Laue diffraction is challenging and not routinely attempted.

However, Laue diffraction is very useful for probing a large range of reciprocal space simultaneously. It can be used to explore phase transitions in the crystal,¹⁸ and measurements are commonly taken without the need to rotate the sample or diffractometer once the crystal has been centred within the instrument. Laue diffraction is also often used to determine the orientation of a mounted crystal. This is necessary in the preparation of diffraction measurements which use punctual detectors where intensity is measured at a given angular position, such as the D9 and D10 diffractometers (Institut Laue Langevin), in which the symmetry, unit cell and orientation of the crystal should be known before initiating a measurement.

In this thesis, Laue neutron diffraction has been used to follow temperature dependent phase transitions, for which the results have been reported in Chapter 5. In addition, it has been used to test the quality of crystals, to identify if the crystals have multiple domains, before performing neutron diffraction experiments.

1.2.3 Radiation interaction with matter

Diffraction experiments take advantage of several types of radiation, X-rays, neutrons and electrons. The radiation choice will depend on the information that is desired from the experiment. This will be directed by the elemental composition and, consequently, how the radiation interacts with the sample.

X-rays

X-ray diffraction is the most commonly performed type of diffraction experiment to determine crystal structures.^{19,20} X-rays interact with the sample through electromagnetic interactions between the X-rays and the core orbital electrons of the atom. This is defined as the atomic form factor, $F(Q)$. For a given atom, the magnitude of the signal detected is proportional to the atomic number, Z . X-rays are, therefore, ideal for compounds with heavier elements, such as transition metals, however, the results will be challenging to identify lighter mass atoms such as N, O or H. The intensity for a given reflection hkl is described by a structure factor $F(hkl)$, the superposition of all the X-ray amplitudes scattered along a given hkl direction.

As the X-rays are scattering from essentially a diffuse cloud of electrons which are of a similar size to the wavelength of the X-rays (order of magnitude 10^{-10} m), $F(Q)$ has a strong angular dependence. The scattering power of the X-rays decreases as a function of increasing Q . X-ray radiation is ideal for measurements at a lower Q (smaller θ angles), but the intensity of measured reflections will decrease as Q is increased.

Neutrons (nuclear)

Neutron diffraction arising from the nuclear (crystallographic) structure is mediated by the strong nuclear force, with atoms scattering the neutrons according to their nuclear scattering lengths, b (units fm). b is hypothesised to arise from the interactions between intrinsic spin orientations of both the nucleus and the incident neutrons.²¹ As a result, b is both element and isotope specific. Neutron radiation is an ideal choice for determining atom positions of light elements, including hydrogen atoms to study hydrogen bond interactions, as well as distinguishing between atoms with similar Z , such as Co and Ni.

For most isotopes, b has a positive value, however, there are some outliers, notably ^1H and Mn, which exhibit negative scattering lengths. In these cases, there is an absence of a phase shift between the incident and diffracted wave. This results in the waves being out of phase (by 180°) compared to the isotopes with a positive scattering length. Therefore, scattering density maps of neutron data hold valuable information about the atom position and atom type from both the positive and negative scattering densities.

Since scattering occurs from the nucleus (order of magnitude 10^{-15} m), the neutron (wavelength order of magnitude 10^{-10} m) can be considered to diffract essentially from a single point. As a result, nuclear neutron diffraction, unlike X-rays, has no form factor dependence, and the scattered intensity remains constant to large scattering angles.

Electrons

Using electrons as the radiation source to acquire diffraction data for structural solutions has long been considered a less viable method and, consequently, few structures have been solved from electron diffraction.^{22,23} The electron wavelength is significantly shorter than X-rays or neutrons (approximately $10^{-12} - 10^{-13}$ m). Electrons interact with the sample through the Coulomb interaction. This is a comparatively strong interaction and results in electrons having scattering cross-sections around 1,000 times and up to 1,000,000 times larger than those of X-rays.²⁴ The large scattering-cross section and short wavelength means that single crystal samples can be measured with dimensions several orders of magnitude less than for X-rays. It also, in theory, permits a good signal-to-noise ratio and allows easier identification of lighter (hydrogen, or lithium) atoms.

Unfortunately, the large scattering cross-section also results in strong multiple scattering events (dynamical effects). This will reduce or increase the intensities of the detected reflections, and since the structure determination is reliant on knowing the relative intensities of reflections, this is currently a hindrance to using electron radiation. Advances in experimental set-up have been improving such that structural solutions are possible. However, when reporting or reading about structures obtained from electron diffraction data, it is recommended not to hold the structural models to comparable statistical assessments that X-ray and neutron structures are scrutinised by, largely due to inaccuracies of calculating the expected structure factors accounting for dynamical effects.²⁵ It can be more practical to consider the residual scattering density maps which show comparable values to X-rays if there are inaccuracies in atom position or assignments.²³

1.2.4 Diffraction experiments

Diffraction experiments can be carried out on both single crystal and polycrystalline powder samples. In Chapters 2, 3, 5 and 6, single crystal diffraction is used to determine structures of new compounds. In Chapter 4, the unit cell parameters were followed using powder diffraction data. When carrying out the experiments, there are certain considerations and parameters that should be considered.

Single crystal

In practice, to carry out a single crystal diffraction experiment, a single crystal of suitable quality is a necessity. Identifying crystals suitable for diffraction experiments is typically carried out visually with the aid of a microscope. The crystal selected should have

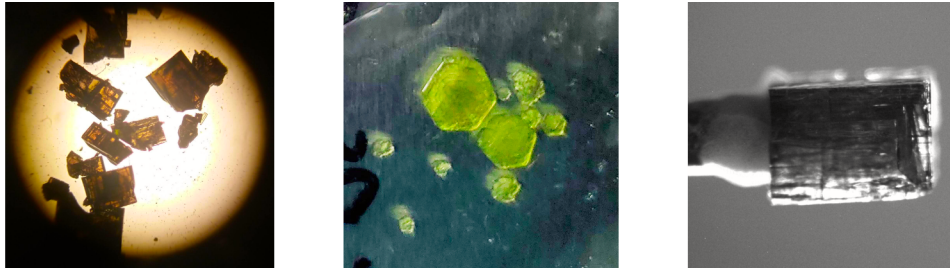


Figure 1.2: Examples of crystals. The samples with flat faces and straight edges are preferred for diffraction experiments.

well-defined faces and edges, has a regular geometry (typically crystals have a cuboid or hexagonal shape) and are a single colour. For a microscope with polarised light, a crystal should extinguish the light once every 90° as the polarisation direction is rotated. This behaviour always occurs for triclinic, monoclinic and orthorhombic crystals, and will be observed for trigonal and tetragonal crystals when viewed along one of the common axes (not the unique axis). The dimension requirements of the crystal will depend on the type of radiation being used, generally lengths of $1\text{--}5\ \mu\text{m}$ for electrons, $50\text{--}200\ \mu\text{m}$ for X-rays and $2\text{--}5\ \text{mm}$ dimensions for neutrons.

The selected crystal is mounted, ensuring it does not unexpectedly move or shift during the experiment. This is typically carried out using glues or inert oils which vitrify, depending on the composition of the crystal and the radiation source. Most diffractometers comprise of several motors, which allow access to a wide range of reciprocal space of the crystal. In many diffractometers there are three or four programmable angles, with the instruments referred to as three- or four-circle diffractometers. A notable distinction is made for Laue diffractometers, where typically only one motor is used, but the quantity of data collected is partly compensated by the use of a continuous spectrum of wavelengths. The centre of gravity of the mounted crystal is positioned at the centre with respect to the motors.

Before a measurement using a monochromatic source, a suitable wavelength is selected. Since the scattering angle is inversely proportional to the wavelength (Eqn. 1.4), the shorter the wavelength, the greater the extent of direct-space that is probed.

When initiating a measurement, considerations are made for the counting time per diffractogram and the scan angles. By optimising the exposure time of the crystal, the expectation is to increase the resolution limit of the data (defined by $\sin(\theta_{\text{max}}/\lambda)$). Longer counting times generally increase the resolution, up to a practical limit, since the diffraction angle is limited by additional factors such as the size of the crystal and the instrument set-up. The scan angles are necessary details to decide the fraction of the limiting sphere that is detected. In theory, a higher symmetry crystal system requires a smaller fraction of reciprocal space to be measured as there are fewer unique reflections. It is recommended

to measure equivalent reflections more than once, hopefully, at least five to seven times. This measure is known as the redundancy of the data. Obtaining a high redundancy allows for spurious measurements to be identified and rejected, as well as aid in corrections related to crystal absorption. In reality, the balance of the parameters is made so that the highest quality dataset is obtained within the available time.

Powder

Powder diffraction essentially measures many crystals at a single time. It requires a sample of homogenous crystallites which are placed in a holder such that all the crystallites have random, and non-equivalent, orientations.

Care should be taken to ensure that the area of the incident radiation beam is not larger than the exposed sample area at the lowest measured Q to avoid additional contributions to the background. This can be controlled through implementing of different mask and slit widths for the incident and diffracted beam. The smaller area beams ensure only the sample is irradiated, however, the intensity of the reflections will suffer proportionally. The signal-to-noise ratio can also be improved by filters such as Soller slits, which reduce the divergence of the incident and diffracted beams.

As a result of the random orientation of crystallites, during a powder diffraction experiment, it is assumed that every possible orientation for a crystal is present. Now, instead of a given d -spacing diffracting to a specific point on the detector, many reflections are detected as concentric rings, known as Debye-Scherrer rings.

In theory, powder diffraction data holds the same potential information as single crystal diffraction. However, whereas single crystal diffractometers record information about the position of a reflection in three-dimensions, in powder diffraction the information is reduced to one-dimension (intensity and scattering angle). There is a high likelihood, particularly for lower symmetry crystals, that the position of non-equivalent reflection will overlap. Consequently, the integrated intensity is sometimes the sum of several reflections, not the intensity for an individual reflection.

1.2.5 Solving the nuclear structure

Single crystal refinements

Having collected the measurements, regardless of the diffraction source, there are a series of steps that should be taken in order to elucidate the structure:

- Reduce the data: Data reduction describes the process in which the raw data from the detectors is converted to a list of integrated intensities. For non-punctual diffractometers (one- or two-dimensional detectors), the unit cell parameters and symmetry of the crystal are determined at this stage. An orientation matrix is calculated, which assigns the Bragg reflections detected at certain positions on the detector to Miller indices (hkl). In addition, the intensities of the reflections are integrated, taking into account corrections for chemical composition (absorption corrections), crystal shape and background. At the end of this process, an *.hkl file is obtained which comprises of a list of intensities, their errors and their assigned Miller indices.
- Solve the structure: After obtaining a list of integrated intensities, the aim is to determine a model for the crystal. There are several mathematical approaches that programs employ to do this. Direct methods is commonly employed, used in programs such as SHELXS²⁶ for X-rays, and is generally successful since there is a direct relationship between the electron density in the unit cell and the intensities of the diffracted beam. If this does not yield a viable model, the structure can be solved using dual space iterative methods, such as the charge flipping algorithm. Programs such as SHELXT²⁷ and *SUPERFLIP*²⁸ rely on defining constraints in both direct and reciprocal space and iteratively modifying the model to achieve a solution. These can be used for both X-ray and neutron data.

For a complex structure, possibly with disorder present, or low quality data, it is not always possible to solve the structure in the space group the data were integrated with. In this case it can be necessary to lower the symmetry of the solution, i.e. remove symmetry elements, potentially working in a triclinic $P\bar{1}$ or $P1$ space group. Once the atoms have been located, the structural model can be implemented into the higher symmetry refinement and symmetry equivalent atoms should be removed.

- Refine the structure: Refinement describes the method of continually altering the structural model to improve its match with the diffraction data. The first steps are to check that the model makes chemical sense and that all the expected atoms have been identified. The fractional atom coordinates for each atom can then be refined to best match the electron density map. Atomic displacement parameters describe the averaged displacement of an atom from its atomic coordinates. During the refinement, atoms will initially be modelled isotropically, meaning the atoms are assumed to be ideally spherical. These can be switched to anisotropic models where the atoms are described by ellipsoids, accounting for thermal motions or

vibrations, static or dynamic disorder and electronic interactions. At this point, care should be taken not to over-parameterise the model. The number of unique reflections should always be larger than the number of parameters being refined, a recommended data-to-parameter ratio is at least eight to ten.²⁹

If the structure is more complex, partial occupancy of the atomic sites can also be considered. This is particularly necessary for moieties with static disorder where the fractional atomic coordinates vary between unit cells. Partial occupancies should be applied whilst ensuring the neutrality of the overall compound is maintained.

- Constraints and restraints: Constraints and restraints can be used to help stabilise a model or include additional information. A constraint implies two parameters a and b are directly related, e.g. $a = b$, so the overall number of parameters is reduced. It can be particularly useful for solid solutions, where two atoms share the same fractional atomic coordinates, which can be constrained to have equivalent values. Restraints imply a relationship, and introduces a statistical penalty, for example, to ensure chemical bond lengths of the same type are similar throughout the molecule. Constraints and restraints are ideal to reduce the number of freely refined parameters, however, this should be carried out cautiously so that the model is improved without misrepresenting the data.

To assess the results of a refinement, there are several values that are commonly quoted in crystallographic tables, and several more which are helpful indicators of the credibility of the model.

The most common values are the crystallographic R -factors. R_{int} is a measure of how similar the symmetry equivalent reflections are. The lower the number, the more closely the integrated data match the symmetry requirements of the crystal system and space group selected. R_1 indicates the measure of agreement between the structure factor of the data, F_{obs} , and the structure factor of the model, F_{calc} . This is commonly presented graphically, plotting F_{calc} against F_{obs} , where an ideally fitted model has a 1 : 1 relationship with the observed data. wR_2 is the weighted R -factor, it is a similar measure to R_1 , however, it uses the square of the structure factors, F^2 , and, therefore, is always larger than R_1 . The “goodness of fit”, GooF (or S , or χ^2), is the ratio between the calculated and weighted-observed structure factors. Ideally the value will converge towards 1.0. Above 1.0 and there is possibly residual scattering density that is not accounted for in the model, and below 1.0 may indicate an overestimation of the errors of the data.

In addition, the quality of the data will be influenced by the redundancy and data completeness. Redundancy is an indicator of the number of times an equivalent reflection

is measured during an experiment. It will ultimately aid in lowering the errors of the intensities by identifying outliers and is used for intensity corrections caused by crystal absorption or beam inhomogeneity corrections. Data completeness refers to the percentage of experimentally collected Bragg reflections compared to the theoretically possible number of reflections considering the crystal symmetry. The more complete the data coverage is, the higher the number of independent reflections are measured. Although these are both measures that cannot be altered once the data have been collected, when regarding published structures they are useful statistics to consider.

Powder diffraction refinements

Sometimes it is not possible to grow single crystals of suitable dimensions or quality to carry out single crystal diffraction. However, with a polycrystalline sample—many small, individual crystallites—powder diffraction can be performed.

The most significant difference to single crystal experiments is the loss of reciprocal lattice information as the data is reduced to one-dimension. This can result in overlapping reflections with only the sum of the integrated intensities. As a result, the structural information that can be obtained from powder diffraction is more limited than for single crystal experiments, usually restricted to phase identification, refinements of known structural models and microstructural analysis of peak shapes. Without prior knowledge of the expected structure, single crystal experiments are generally necessary to determine a structure. In this thesis, I use powder diffraction for structural analyses of $\text{Ni}(\text{NCS})_2$ in Chapter 4. For $\text{Ni}(\text{NCS})_2$ the structural model is already known,³⁰ so the information obtained was related to changes in the unit cell dimensions. I will highlight the details important for this analysis.

The most valuable information obtained is the unit cell and crystal symmetry of the compound. This is obtained from the position of the reflections, collected as a function of Q . Generally the fractional atomic coordinates and atomic displacement parameters are not refined, due to the loss of information in the data. It can be possible to refine these parameters from high quality synchrotron or neutron data where a low number of parameters are refined, however, this was not applicable in this thesis.

Refinements are typically carried out using Rietveld methods,³¹ a least-squares minimisation process. These take into account the crystal symmetry and unit cell, which define where as a function of Q the reflections are expected and which reflections are observed or systematically absent. The calculated intensities of the model take into account the atom type and positions. Refinements can also be carried out using Pawley or Le Bail methods.^{32,33} These assume an atom-free unit cell and, therefore, only take into account

the unit cell and space group. In these fits, the calculated intensities are not meaningful for explicit structural analysis, so the most valuable information to be taken from these refinements is that the assignment of the symmetry and cell dimensions is correct, as well as the peak shape.

Typically, the reported value for fitted powder diffraction models is the weighted powder R -factor, R_{wp} . This considers the total expected intensity at each angle, rather than the calculated intensity for each non-equivalent reflection. Similar to the single crystal R -factor metrics, the lower the value, the closer the model adheres to the observed data.

Powder diffraction can be useful to verify the purity of a powder. Additional peaks that cannot be modelled by the structure may suggest one or more extra phases are present in the powder. For measurements that are particularly sensitive to impurities, such as magnetometry measurements, it is essential to verify phase-pure samples before the measurements.

Modulated crystal structures

Crystals are defined by their symmetry, and their three-dimensional periodicity, dictated by the translational symmetry elements which project the contents of a unit cell into the adjacent one. A subclass of crystals, modulated structures, lack translational symmetry in at least one axis, whilst still maintaining an average periodic structure. Essentially, the translational symmetry in the parent structure is broken by a second periodic modulation.

The identifying feature of modulated compounds is the appearance of satellite reflections in the diffraction pattern (Fig. 1.3a). Whilst the main Bragg reflection retains the information about the average structure, satellite reflections appear surrounding the main reflection at regular intervals, usually at a lower intensity than the main reflection. The position of the satellite peaks holds information about the modulations. The modulations can occur along one-, two-, or three-crystal axes, and the periodicity is described by the modulation wavevector, \mathbf{q} . \mathbf{q} is calculated from the distance between the main and satellite reflections in reciprocal space, which appear at equal distances $\pm\mathbf{q}$. Where \mathbf{q} uses rational reciprocal lattice vector coefficients, the structure is commensurately modulated. For example, $\mathbf{q} = 1/3$ implies a tripling of the unit cell along the given axis. Irrational coefficients indicate an incommensurately modulated structure, i.e. an increase of the periodicity that is not commensurate with the average unit cell. The modulation can arise, for example, as displacements from the average atom position, or atomic site occupancies.^{18,34}

Modulated structures are assigned superspace symmetry in $(3+n)$ dimensions, where

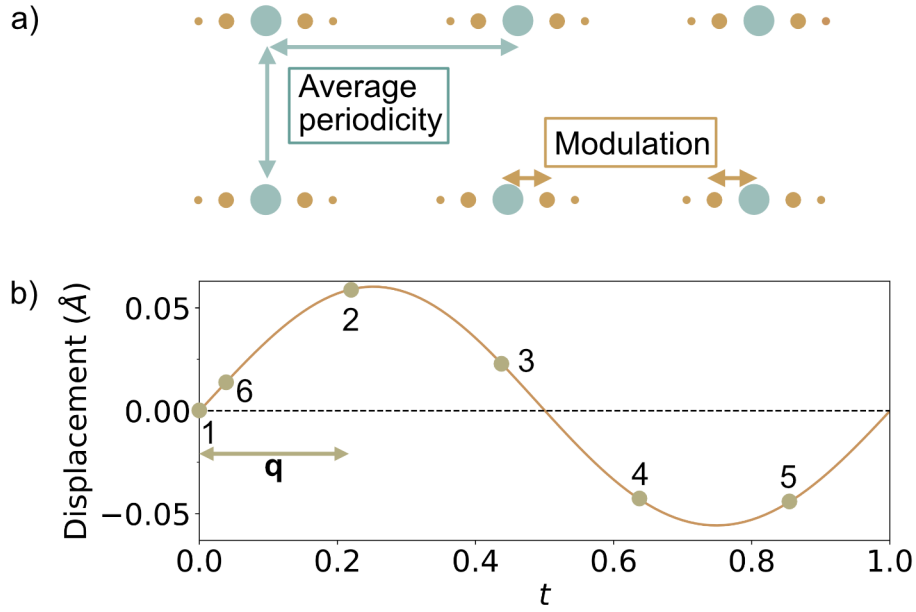


Figure 1.3: a) A diffraction pattern of a modulated crystal. The main Bragg reflections (green circles) arise from the average structure. The satellite reflections (brown circles), observable to the second order satellites, hold information about the modulation. b) The displacement of an atom against the modulation parameter, t . An example of the position of the atom in six adjacent average unit cells are shown at the six t -sections (yellow circles) identified, for a given modulation vector, $q \approx 0.21$.

n is the dimensionality of the modulation. The categorisation consists of the average structure symmetry, the wavevector of the modulation and intrinsic translation along the n^{th} dimension:³⁵ “Average-space-group(modulation-vector)internal-intrinsic-shift”. α , β and γ denote incommensurate components of the modulation vector and the intrinsic translation uses symbols s , t , q and h to denote shifts of $1/2$, $1/3$, $1/4$ and $1/6$. For example, the superspace group $Pnma(00\gamma)0s0$ describes a compound with orthorhombic $Pnma$ symmetry in the average structure, an irrational modulation γ along c^* , and a translation of $1/2$ for the symmetry operators along b^* .

The periodicity of the superstructure is dictated by the modulation parameter, t . The atom displacements can be graphically plotted as a function of t , where one period of the modulation is between $t = 0$ and $t = 1.0$. All sections of t give equivalent, but not identical, representations of the three-dimensional structure. It should be noted that sequential positions along the graph (t -sections) are not adjacent average unit cells. Adjacent unit cells are distributed at sequential intervals of q (Fig. 1.3b).

To solve and refine an incommensurately modulated structure, software which can process superspace groups are used such as Jana2006³⁶ or FullProf.³⁷ A modified hkl file is used, with the data integrated using $3+n$ dimensions, e.g. $hklm$ reflections, where m holds information about the satellite order. $m = 0$ denotes the main Bragg reflection, and $m \neq 0$ for the ordinal of each integrated satellite reflection associated with the main reflection. Chapter 5 presents diffraction data and structural solutions of three modulated

structures.

1.3 Magnetic characterisation

The magnetic moment of an electron arises from its intrinsic property of spin (spin angular momentum) in combination with its movement within an orbital (orbital angular momentum). By incorporating paramagnetic ions, the metal species possess magnetic moments, and the overall behaviour of the material is dictated by how the moments interact with each other. The moment interactions can range from being randomly orientated, to following long-range ordered arrangements. The relative orientations of the moments dictate if the ordering is ferromagnetic, antiferromagnetic, or something more complex.

In this thesis, the temperature-dependence of the magnetic behaviour is explored, as well as magnetic changes with pressure for Chapter 4, however, it is possible to induce changes to the interaction of the moments through other probes, such as applying external magnetic and electric fields.^{38,39} Measurements can be carried out to determine the bulk behaviour of the sample (magnetometry measurements) and the ordering pattern of the moments (magnetic neutron diffraction).

1.3.1 Magnetometry measurements

Generally, the first method employed to explore the magnetism of a sample is by measuring the magnetic susceptibility. Magnetic susceptibility (χ) is a bulk measurement that describes the degree of magnetisation (M) of a sample in an applied magnetic field (H), related by the equation

$$\chi = \frac{M}{H}, \quad (1.5)$$

assuming the small field approximation, where $\chi \ll 1$, so that the magnetic flux density, $B \approx \mu_0 H$, where μ_0 is the permeability of free space.⁴⁰

Magnetic susceptibility is generally measured by a SQUID (Superconducting QUantum Interference Device). It consists of two superconductors, separated by an insulating layer. A fixed magnetic field is applied and the sample is moved through superconducting coils, perturbing the magnetic flux. The change in the flux is proportional to the magnetic moment and is detected as voltage as a function of sample position.

There are several contributions to the overall magnetism to consider, the effect of which is dictated by the arrangement of the electrons in the orbitals. All materials exhibit a

diamagnetic response (χ_0), induced by the repulsion of electron pairs in a magnetic field, which results in a small negative susceptibility. This value is compound specific and is accounted for using species-dependent values.⁴¹

Materials are categorised based on their relative orientations of their moments. Although at suitably high temperatures moments do not exhibit long-range correlations with their neighbours (paramagnetic), below a critical temperature, T_C , the moments spontaneously organise themselves. The moments can align exactly parallel to each other, behaving as a ferromagnet. Conversely, an antiparallel arrangement alignment describes an antiferromagnet (Fig. 1.4). There are also more complex scenarios in which the orientation of the moments are not collinear. From bulk magnetometry measurements these can still be categorised as ferromagnets or antiferromagnets, where long-range correlations persist.

To determine T_C , the magnetisation of the sample is measured as a function of temperature. T_C is marked by the sharp change in the derivative of the susceptibility, $d\chi/dT$. For ferromagnetic compounds, the ordering temperature is termed the Curie temperature, T_C , below which temperature the magnetisation increases rapidly. Antiferromagnets order at the Néel temperature, T_N , below this temperature the susceptibility decreases due to the compensation of the antiparallel moments. In comparison, for a paramagnet with no long-range ordering, the magnetic susceptibility increases exponentially with decreasing temperatures (Fig. 1.4a).

To relate the magnetic susceptibility of a material to a given temperature, a Curie constant (C , units emu K mol⁻¹) can be calculated. The Curie constant is compound specific and indicates the size of the magnetic moment. Assuming only the spin of the moment contribute to the Curie constant, $C_{\text{spin only}}$, can be calculated

$$C_{\text{spin only}} = 0.500 \times S(S + 1), \quad (1.6)$$

where S is the total spin per atom. Experimentally, this value can be extracted by plotting the product of χT against T and obtaining the value C in the paramagnetic temperature range, where $T \gg T_C$ (Fig. 1.4b).

To explore the strength of the magnetic interactions, the magnetometry data is plotted as χ^{-1} against temperature. In the paramagnetic temperature range, the susceptibility of the material should adhere to the Curie-Weiss Law,

$$\chi = \frac{C}{T - \theta_{\text{CW}}} \quad (1.7)$$

or for the inverse susceptibility,

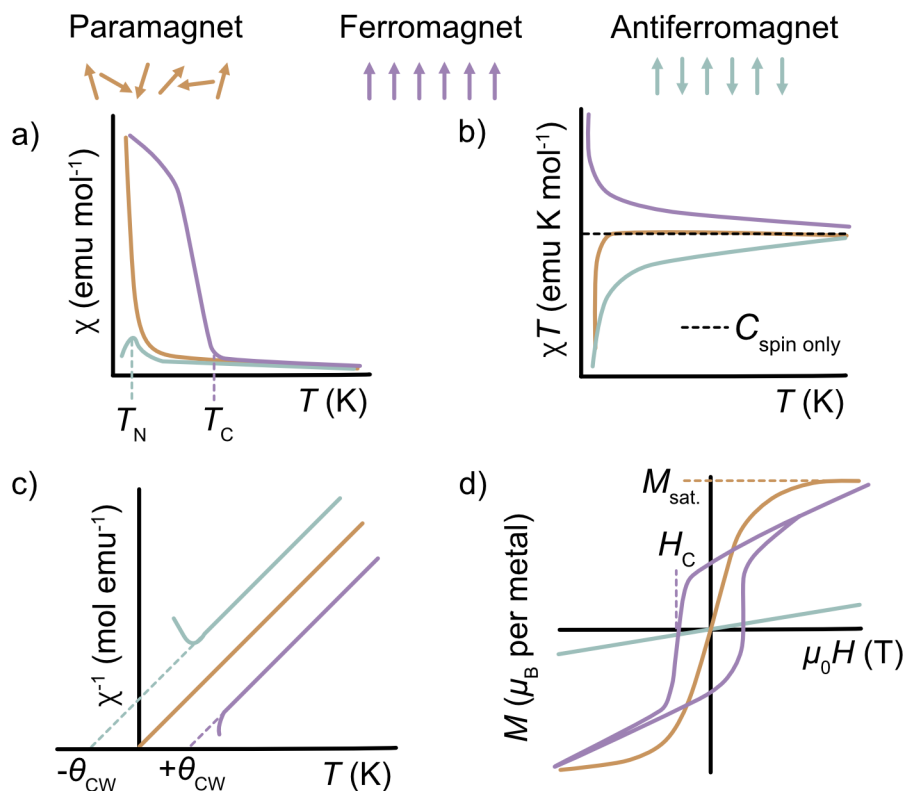


Figure 1.4: The magnetic behaviour of a paramagnet (brown arrows and lines), ferromagnet (purple arrows and lines) and antiferromagnet (teal arrows and lines). The magnetic moment ordering shown with arrows. a) The magnetic susceptibility (χ), with the magnetic ordering temperatures for a ferromagnet (T_C) and an antiferromagnet (T_N) identified. b) The χT product. The Curie constant ($C_{\text{spin only}}$) is shown as a black dotted line. c) The inverse of the magnetic susceptibility. Dotted lines represent fitting of the linear (high temperature) region of the data to the Curie-Weiss Law (Eqn. 1.8), and Curie-Weiss temperatures (θ_{CW}) is extracted from the intercept with the x axis. d) Isothermal magnetisation measurements. Saturation ($M_{\text{sat.}}$) is reached for the paramagnet and ferromagnet. The ferromagnet shows hysteretic behaviour with a coercive field H_C .

$$\chi^{-1} = \frac{T - \theta_{\text{CW}}}{C} \quad (1.8)$$

where θ_{CW} is the Curie-Weiss temperature. There is a linear response between the magnetic susceptibility and temperature, with the gradient $1/C$. θ_{CW} describes the summation (average strength) of the magnetic exchange interactions, the stronger the interactions the larger the value of $|\theta_{\text{CW}}|$. The sign of θ_{CW} is additionally informative, as positive values indicate dominating ferromagnetic interactions, whereas a negative θ_{CW} value suggests predominately antiferromagnetic interactions. For paramagnetic materials $\theta_{\text{CW}} = 0$ K (Fig. 1.4c). To obtain this value, a suitable temperature range must be chosen to apply the equation. Equation 1.8 is only valid in the paramagnetic region, where no long-range or short-range magnetic correlations are occurring. Therefore it is necessary to measure to temperatures significantly higher than T_C .⁴²

When quoting θ_{CW} values for a compound, it is important to be aware of other contri-

butions to the magnetic susceptibility, which will occur within the paramagnetic region and are temperature dependent, but do not follow the Curie-Weiss Law. Sometimes it is necessary to add a diamagnetic correction term, χ_0 , arising from the inherent presence of repulsive electron pairs. A second effect which can vary the value of θ_{CW} is spin-orbit coupling. This occurs where the spin angular momentum of an electron couples to the moment generated by its movement. There must be vacancies in the orbitals within the same subshell as the unpaired electron to permit its movement. This is important in transition metals such as high-spin Co^{2+} , where the effective (measured) magnetic moment, $\mu_{\text{eff.}}$, is larger than the calculated magnetic moment accounting for only the number of unpaired electrons in the atom, $\mu_{\text{spin only}}$. $\mu_{\text{spin only}}$ is calculated by

$$\mu_{\text{spin only}} = g\sqrt{S(S+1)} \quad (1.9)$$

where g is the electron gyromagnetic ratio (or electron g -factor). It is a constant with a value of 2.0 for a free electron. However, g shows the proportionality between the spin and orbital angular momentum, so for ions which have larger spin-orbit interactions, the value of g will be larger than 2.0.⁴³ As a result in these materials, $\mu_{\text{eff.}}$ deviates from the expected $\mu_{\text{spin only}}$ value. This can be observed in the graphs of χT against T where the value of χT at high temperatures, i.e. in the paramagnetic temperature range, is larger than $C_{\text{spin only}}$. $\mu_{\text{eff.}}$ is related to C by $\mu_{\text{eff.}} \approx \sqrt{8C}$ (units cgs), so can be estimated from the susceptibility data as well.

A second measurement which can be carried out using magnetometry are magnetisation measurements. These are isothermal measurements, carried out below T_C , measuring the magnetisation at different field strengths. In an appropriately strong applied magnetic field, the moments will eventually align with the field direction, reaching the saturation magnetisation, M_{sat} ($M_{\text{sat}} = gS$). In antiferromagnets, as 50 % of the moments are aligned antiparallel, a transition can occur to switch the orientation of the moments to be fully parallel, which is observed by a change in gradient, observable in $dM/d\mu_0 H$.

Unlike a paramagnet or antiferromagnet, ferromagnets will exhibit hysteretic behaviour as the magnetic field is removed and reversed. After reaching M_{sat} , as the field is removed, the lag between the change in the field and the change in the magnetisation is known as the remnant magnetisation, M_{rem} . It is identified as the magnetisation at 0 T. As the field is subsequently reversed, there is a delay in the response of the material to align the moments to the reversed field. Materials that require large magnetic fields in order to reverse the magnetisation are described as hard magnets, whereas soft magnets require only a small applied magnetic field. The field at which the magnetisation has been removed, $M = 0 \mu_B$ per atom, is defined as the coercive field, H_C (Fig. 1.4d).

1.3.2 Magnetic neutron diffraction experiments

Neutrons interaction with matter (magnetic)

As well as through the strong nuclear force, neutron radiation also interacts with a sample through dipole-dipole interactions due to the non-zero spin associated with both neutrons and electrons. Similar to X-rays, magnetic neutron scattering has a form factor dependence, $f_M(Q)$. The decline in intensity is more marked than for X-rays, as the diffraction generally occurs from the valence electrons. $f_M(Q)$ is ion specific as electrons can have different sub-shell arrangements.⁴⁴ Consequently, magnetic neutron diffraction experiments are usually focussed on the low Q region.

The observed intensities have additional important dependencies. The intensity depends on the magnetic ion, since it scales proportionally with the square of the number of unpaired electrons. Moreover, the intensity depends on the angle of \mathbf{Q} with reference to the orientation of the magnetic moment. A maximum intensity is measured when \mathbf{Q} is perpendicular to the vector of the magnetic moment, and zero intensity is detected when the two vectors are parallel.⁴⁵

Magnetic structures

Similar to the nuclear (crystallographic) structure, magnetically ordered phases are described by a magnetic unit cell, defining the symmetry operators and repeating unit of the magnetic moment positions and orientations. Although the magnetic ions have a positional order arising from the nuclear structure, the periodicity may be equal to or larger than the nuclear unit cell as a result of the moment orientations and magnitudes. A propagation vector, \mathbf{k} , is used to relate the magnetic unit cell to its nuclear unit cell in reciprocal space. For $\mathbf{k} = (0, 0, 0)$ the magnetic unit cell has equivalent lattice spacings between Bragg reflections, and the dimensions of the unit cell are equivalent to the nuclear one. For $\mathbf{k} = (0, 0, \frac{1}{2})$, magnetic Bragg reflections additionally occur at the mid-points between the nuclear Bragg reflections in reciprocal space, indicating a doubling of the unit cell along the c axis.

Whether the magnetic periodicity is the same or larger than the nuclear unit cell, the orientation of the moments can lead to a structure with lowered symmetry. The symmetry elements for magnetic space groups follow the same convention as for the nuclear counterparts, with the exception of time reversal. The time reversal operation, t , when activated, flips the sign of the moment. To denote this in magnetic space groups, a prime is added to the operation, for example, m' .⁴⁶ The final magnetic structure is assigned a

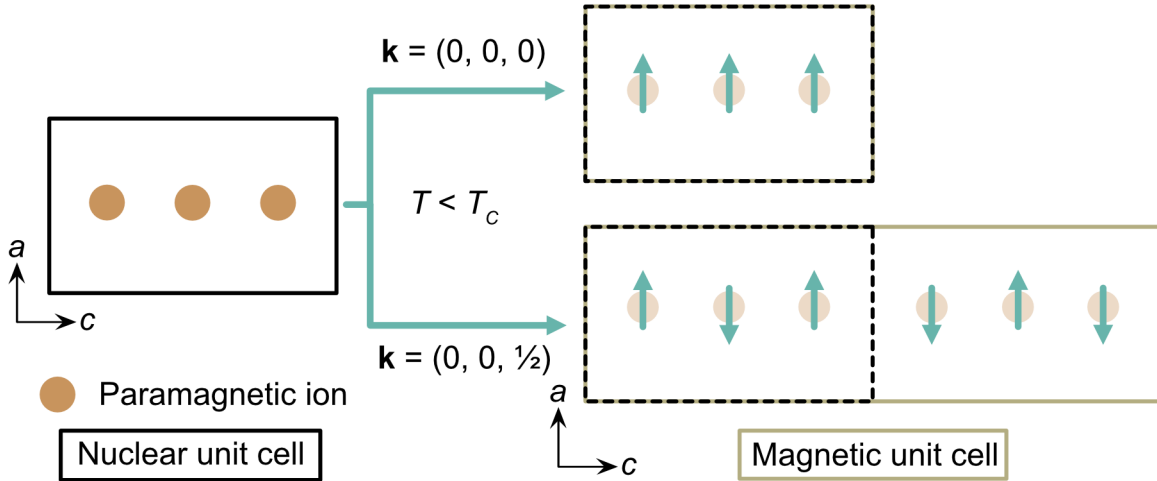


Figure 1.5: Relating a magnetic unit cell (yellow) to its nuclear unit cell (black) for two ordering patterns. For $\mathbf{k} = (0, 0, 0)$, the nuclear and magnetic unit cells are identical. For $\mathbf{k} = (0, 0, \frac{1}{2})$, the magnetic unit cell is doubled along c .

magnetic space group that is equivalent or lower symmetry to that of its nuclear structure. There are several notations available for magnetic space groups, in this thesis I have used the Belov, Neronova and Smirnova (BNS) notation,⁴⁷ although another commonly used notation is Opechowski and Guccione (OG),⁴⁸ and the recently introduced unified magnetic space group symbols (UNI).⁴⁹

Magnetic neutron diffraction

Since neutron measurements for magnetic analysis follow the same underlying principles of diffraction, the set-up for a magnetic diffraction experiment is very similar to that for determining nuclear structures. There are, however, additional considerations to review beforehand. As the magnetic scattering has a form factor dependence, it is necessary to concentrate the data collection to the low Q region where the magnetic scattering intensities will be largest. The intensity of magnetic scattering is weak compared to scattering from the nuclear structure, so selecting a diffractometer and wavelength that permits a higher flux is beneficial. Complex magnetic structures can result in large unit cells, so using a diffractometer with a long wavelength will reduce the overlap of magnetic reflections.

Measurements should be taken, at minimum, at two temperature points, above and below the magnetic ordering temperature. Without the use of polarised neutrons, it is not possible to detect separately the scattering arising from the nuclear and magnetic structures.⁵⁰ The intensities are, therefore, collected simultaneously, and it is necessary to know which reflections are arising from magnetic scattering to extract information about the magnetic structure. Consequently, it is important to collect information about

the nuclear structure in the paramagnetic state as well as in the magnetically ordered phase. Data are typically collected in the paramagnetic region, close to T_C , and below it, typically at 2 K if a helium cryostat is cooling the sample. The paramagnetic dataset is then used to determine a model of the nuclear structure. From this, the reflections arising from the magnetic structure can be more obviously identified.

After making the measurements, there are several steps that should be undertaken to determine the propagation vector and magnetic space group. For single crystal diffraction data, then general method is outlined:

- Determine the propagation vector: Having modelled the nuclear structure, the magnetic reflections are indexed with respect to the nuclear unit cell. If the magnetic reflections occur in reciprocal space with the same periodicity as the nuclear reflections, $\mathbf{k} = 0$, and if superlattice reflections are present $\mathbf{k} \neq 0$.

Note, this step is only necessary for diffractometers with non-punctual detectors. In this thesis, single crystal magnetic structure determination was always carried out using a two-dimensional detector, however, it is more common practice to use a punctual detector. In these cases, the propagation vector is determined from previous measurements, for example, from powder neutron diffraction data, or is determined at the beginning stages of the experiment. If data are collected using a punctual detector, this step is surpassed and the analysis will start at the following stage.

- Identify the possible magnetic space groups: From the nuclear symmetry and \mathbf{k} , the crystallographically-attainable magnetic space groups can be identified. Programs including MAXMAGN,⁵¹ ISODISTORT^{52,53} and Jana2006³⁶ are useful for obtaining these lists.
- Test the models against the data: Each magnetic space group is refined against the data to see if a reasonable model can be obtained. It is worthwhile beginning the search with the highest symmetry space groups, the maximal magnetic space groups, before considering models with lowered symmetry. It is good practice to use the additional information about the magnetic behaviour obtained from magnetometry, or other measurements, to guide and minimise the number of models tested. Some space groups limit the accessible moment arrangements through symmetry restrictions, for example, the moment orientation, which restricts the direction of the uncompensated moment.

- Refine the model: Within a model there can be one or more symmetry-independent magnetic ions. For each magnetic ion, the magnitude of the moment and its orientation are considered during refinements. For insulating materials with 3d valence electrons, to ensure a physically sensible model, the magnitude of the moment should not be larger than S for the ion. Similarly to nuclear refinements, if it is necessary, additional restraints and constraints may be applied to help stabilise the model.

The principles are the same to solve a structure from magnetic powder diffraction, firstly, the additional intensities arising from magnetic neutron scattering are indexed, followed by identifying suitable models. It can be convenient to perform a subtraction of the high temperature (paramagnetic) from the low temperature (magnetically ordered) diffraction pattern. The remaining intensities are assumed to arise from the magnetic reflections. This “difference” diffraction pattern can be used during the indexing and refinement steps whereby a model is defined with only the magnetic parameters and positions of the magnetic ions within the unit cell. Particularly during the refinements, refining a magnetic model against the difference diffraction pattern can remove the prospect of the magnetic parameters compensating for insufficiencies arising from the nuclear model.

In this thesis, I present magnetic structures obtained from neutron diffraction experiments, performed at the Institut Laue Langevin. Single crystal samples have been measured using the D19 diffractometer in Chapters 2, 3 and 5. Powder neutron diffraction experiments were carried out on the D1b diffractometer for data in Chapters 3 and 4.

Magnetic dimensionality

Magnetic materials can be broadly categorised by their dimensionality. In principle, the magnetic interactions, J , may exist in only one or two directions, leading to the terms one- and two-dimensional magnetic orderings. However, in practise, although in magnetically ordered compounds some interactions may be negligibly small, they are rarely zero,⁵⁴ so these compounds can be more appropriately termed quasi-low-dimensional materials. In this case, the magnetic dimensionality is an indication of the comparative strength of the magnetic interactions, J , in each spatial direction. Where J in one or two of the directions is significantly stronger than the third, the magnetic ordering can be considered as low-dimensional.⁵⁵

To probe the strength of J experimentally, inelastic neutron diffraction experiments are performed. However, approximations of the relative interactions can be determined through the temperature-dependent magnetisation behaviour close to T_C . With neu-

tron diffraction measurements, data can be collected in incremental temperature steps around the ordering temperature. For magnetically ordered compounds, as the ordering temperature is reached (on heating), the magnitude of the magnetic moment decreases to $M = 0 \mu_B$ at T_C . Close to T_C , the magnetic moment can be fitted by a power law

$$M = A(T_C - T)^\beta, \quad T < T_C \quad (1.10)$$

where A is a proportionality constant, β is a critical exponent and A , β and T_C are all variables to be fitted. The value of β varies, depending on the ideal model considered. $\beta = 0.125$ for a two-dimensional Ising model and $\beta = 0.367$ for a Heisenberg magnet.⁵⁶ Most compounds exhibit a β within this range, with the more anisotropic arrangements of J values resulting in lower β .⁵⁷ Care should be taken over the fitting range as there is no consistent advice to guide, only that β is valid “near the phase transition temperature (T_C)”,⁵⁶ broadly fitting the temperature regime which is linear in a log plot. Therefore, these values are useful indicators of the magnetic ordering behaviour, however, they should be regarded as just this, rather than precise measures of magnetic dimensionality.

1.4 Pressure

Temperature is the dominant probe used to explore structural and physical properties within this thesis. However, a particular focus on the response to applied pressure is explored in Chapter 4 where both X-ray and neutron diffraction, as well as magnetometry measurements, are performed under pressure.

To apply pressure to a sample a pressure cell is chosen, generally selected by the pressure range that is being measured. For lower pressure experiments, up to 6–7 kbar, gas pressure cells are used, such as for the neutron diffraction measurements, or using hydraulic gauge pumps, as for the X-ray data.⁵⁸ To achieve higher pressures, a variety of diamond anvil cells are commonly used.⁵⁹ To aid in equally dispersing the pressure, pressure transmitting media are added to the cells. Inert gases, oils or alcohol mixtures are commonly used, and are selected based on their ideal pressure and temperature working ranges, as well as the stability of the sample in their presence.⁶⁰ The pressure exerted by the cell is not necessarily equivalent to the pressure experienced by the sample, so, often, a standard is used to measure the internal pressure. Common standards include silicon or lead, which have well established pressure-dependent structural strain or superconducting transitions.^{61,62}

Considering diffraction experiments at pressure, due to the additional scattering arising from the pressure cell, pressure transmitting medium and the standard, the results from

pressure data tend to be of a lower quality than their ambient pressure data.⁶³ In powder data, the full-width half maximum of the peaks generally become broader, due to strain, as the atom positions vary between unit cells. This is part inherent to the compound, but is additionally amplified by inevitable non-uniform distribution of the applied pressure.

From the structural refinements of variable-pressure diffraction data information can be obtained about the strain experienced by the sample. For a given pressure, the change in an axis length, a , is calculated by $\Delta a/a_{\text{initial}}$. However, these values can be distorted for unit cells with at least one angle that is not restricted by symmetry (monoclinic and triclinic symmetry). To make the results more comparable between compounds of different crystal systems, a set of arbitrary orthogonal axes are assigned, principal axes, and the changes in dimension are calculated relative to these. For the pressure analysis in Chapter 4, I have used the software PASCAL,⁶⁴ which assigns principal axes and calculates the metrics listed subsequently.

The linear compressibility, K (units TPa^{-1}), is a measure of the relative change of a parameter in response to a pressure change, where for a given principal axis i , $K_i = -1/\varepsilon_i \frac{d\varepsilon_i}{dP}$ where ε_i is the strain and P is the pressure. ε_i is calculated from an empirical formula $\varepsilon_i(P) = \varepsilon_0 + \lambda(P - P_C)^\nu$, since strain is not typically linear with pressure.⁶⁵ When comparing to published data, it is useful to verify the pressure ranges used to calculate the compressibilities, since, by definition, this values will change with the pressure applied.

A related value commonly reported is the bulk modulus, B_0 (units GPa). This is a measure of how resistant the compound is to pressure. B_0 shows the amount of applied pressure that is needed to reduce the compound to zero volume. A common fitting method uses the Birch-Murnaghan equation of state⁶⁶

$$P(V) = \frac{3}{2}B_0 \left[\left(\frac{V_0}{V}\right)^{\frac{7}{3}} - \left(\frac{V_0}{V}\right)^{\frac{5}{3}} \right] \left\{ 1 + \frac{3}{4}(B'_0 - 4) \left[\left(\frac{V_0}{V}\right)^{\frac{2}{3}} - 1 \right] \right\} \quad (1.11)$$

where V is the unit cell volume, B'_0 is the derivative of the bulk modulus and variables with subscript 0 denote ambient pressure. Note that in some texts, the bulk modulus can also be referred to as K , however, the notation using B_0 is used throughout here. A second order fitting of Birch-Murnaghan equation of state assumes $B'_0 = 4$, negating the second bracket. A lower B_0 suggests the compound is soft and more easily compressed, with values ranging several orders of magnitude.^{67,68}

1.5 Thiocyanate ligand profile

The majority of structures reported and characterised in this thesis use the thiocyanate anion, NCS^- , as the common building block. Before discussing the properties of thiocyanate-based frameworks, it is worth regarding the character of the thiocyanate anion as a ligand from a structural and magnetic perspective.

Thiocyanate as a bridging ligand

NCS^- is a linear, ambidentate ligand, coordinating through either the N or S atom as a result of its resonance forms. In addition, NCS^- will simultaneously coordinate through both atoms, with a variety of coordination modes including $\mu_{1,3}$, $\mu_{1,1,3}$ and $\mu_{1,3,3}-\text{NCS}^-$ ⁶⁹ (Fig. 1.6a). The benefit of two coordinating atoms is that NCS^- can be incorporated into framework compounds as a bridging ligand. Thiocyanate frameworks bridging metal centres have been explored, in particular, for their magnetic⁷⁰ and optical⁷¹ properties.

Unlike many frameworks with molecular ligands, such as HCOO^- , N_3^- , $\text{N}(\text{CN})_2^-$, the coordinating atoms of the thiocyanate are asymmetric, which brings about both synthetic challenges, but, also, structural diversity. The coordination character of the thiocyanate anion can be evaluated by the soft and hard acid/base classification.⁷² By comparison of the extent of polarisability of the terminal atoms, N is considered ‘hard’, typically coordinating to harder metals, such as first row transition metals, as observed in $\text{Mn}(\text{NCS})_6^{4-}$ or $\text{Ni}(\text{NCS})_6^{4-}$ complexes.^{73,74} With an additional electron shell occupied, sulfur has a more diffuse spread of electron density, and shows a preference coordinating to ‘softer’ metals, such as $\text{Pt}(\text{SCN})_6^{4-}$ or $\text{Bi}(\text{SCN})_6^{3-}$.^{75,76}

In addition, the metal–ligand bond angles have pronounced differences, especially in the $\mu_{1,3}$ coordination mode. The $\angle\text{M}-\text{N}-\text{C}$ is close to 180° and $\angle\text{M}-\text{S}-\text{C}$ is towards 100° .⁷⁷ The combination of the more diffuse M–S bonds and narrower $\angle\text{M}-\text{S}-\text{C}$ bond angles in particular, can lead to flexibility in the frameworks and obtain alternative structures to other frameworks with molecular ligands, or compounds with atomic anions.^{78,79} A particular focus on the flexibility and structural diversity of thiocyanate frameworks is explored in Chapters 4 and 6, and the utility of molecular anions over atomic ones for synthetic simplicity and for magnetic behaviour in Chapters 3 and 4.

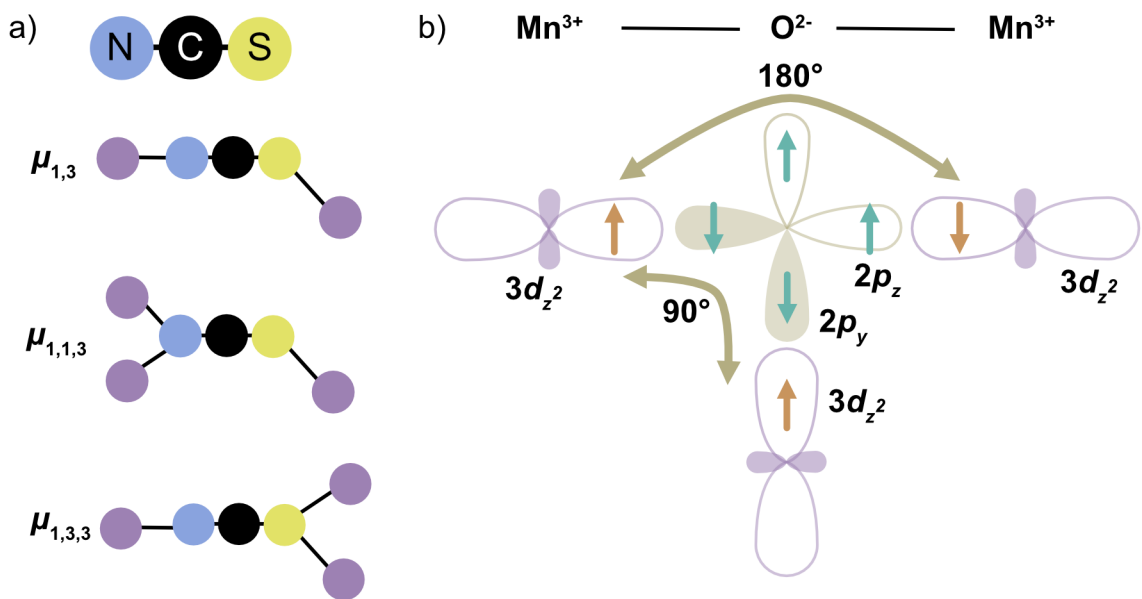


Figure 1.6: a) Three coordination arrangements of bridging thiocyanate anions (NCS^-). N = blue, C = black, S = yellow, paramagnetic metal = purple. b) The superexchange pathway through Mn–O–Mn. The alignment of the unpaired Mn magnetic moments (brown arrows) are antiferromagnetic with a bond angle of 180° and ferromagnetic with a bond angle of 90° .

Thiocyanate for magnetic superexchange

When coordinating to paramagnetic ions, the thiocyanate anion has been used to construct frameworks with long-range magnetic order. Typically, in a framework with $\mu_{1,3}$ –NCS coordination mode, the metal ions are separated by approximately 6 Å, depending on the nature of the metal.^{80,81} This distance is large for the metal ions to directly interact, therefore, the thiocyanate anion acts as a bridge to sustain the magnetic interactions. The interaction route, the superexchange pathway, occurs as the overlapping orbitals of the metal and a non-magnetic ligand promote the exchange interactions.⁸²

For simple, one atom, superexchange pathways, the representative exemplar being Mn–O–Mn, the type of magnetic exchange interactions experienced can be qualitatively predicted by the Mn–O–Mn bond angle.⁸³ As the angle approaches 90° , a ferromagnetic moment arrangement of the two Mn^{2+} ions is experienced. Whereas, for 180° pathways, antiferromagnetic interactions are expected. This is rationalised by the variation of filled and vacant p- and d-orbital overlap⁸⁴ (Fig. 1.6b).

This can be a helpful guide, however, it is not as straightforward when extending this principle to a multi-atom superexchange pathway. There are examples of isomorphous thiocyanate frameworks with varying magnetic properties, by only altering the metal ion, without large alterations to the superexchange angle. This is demonstrated in Chapter 3 for the isomorphous $\text{CsM}(\text{NCS})_3$, M = Mn, Co, Ni, which have varied magnetic properties.

In general, the strength of the magnetic interaction decreases with the superexchange

distance, which grows with the number of atoms in the superexchange anion.⁸⁵ This is notable in dicyanamide ($\text{N}(\text{CN})_2^-$, dca) anions, where the $\mu_{1,3}$ -dca (three-atom) superexchange pathway permits long-range magnetic ordering, but $\mu_{1,5}$ -dca (five-atom pathway) compounds do not.^{86,87}

The thiocyanate anion is proving to be a versatile superexchange ligand, with ferromagnetic,⁸⁰ antiferromagnetic ($[\text{Na}(\text{OH}_2)_3]\text{Mn}(\text{NCS})_3$, Chapter 2) and non-collinear magnetic orderings ($\text{CsM}(\text{NCS})_3$, Chapter 3).

From both a crystallographic and a magnetic point of view, the thiocyanate anion has the potential to exhibit a variety of structures and more unusual magnetic orderings.

1.6 Functional design

With different components to add or combine as well as ligands with multiple coordination modes, a whole host of structures are possible for inorganic framework materials. Therefore, from a design point of view, there are several considerations that can be taken into account to encourage certain structural or physical properties. This can include the steric bulk of the components, dimensionality of the framework and the crystal symmetry.

A-site cation size

Although usually interacting with the framework through non-covalent interactions, the A-site cations, where present, play an important role in dictating the connectivity of the framework components.

The ratio of the steric bulk of the A- and M-site species is known to drive certain structure types.^{5,88} The relationship is defined by the Goldschmidt tolerance factor (t), in the simplest terms,

$$t = \frac{r_{\text{A}} + r_{\text{X}}}{\sqrt{2}(r_{\text{M}} + r_{\text{X}})}, \quad (1.12)$$

where the radii of the A, M and X sites are defined by r_{A} , r_{M} and r_{X} .⁵ This follows for perovskite materials, with corner-sharing MX_6 octahedra in three-dimensions. An ideal, undistorted perovskite has a t broadly between 0.9 and 1.0, CsPbCl_3 ($t = 0.87$)⁸⁹ but by adopting tilted octahedra a ratio between 0.75 and 0.9 is observed, such as for BaCeO_3 ($t = 0.856$).⁹⁰ $t > 1.0$ and < 0.75 will likely result in hexagonal and orthorhombic structure-types, as is reported for $\text{Ba}_2\text{TiMnO}_6$ ($t = 1.08$)⁹¹ More recently, this approach has been adapted by including a term for the oxidation states,⁹² or by accounting for

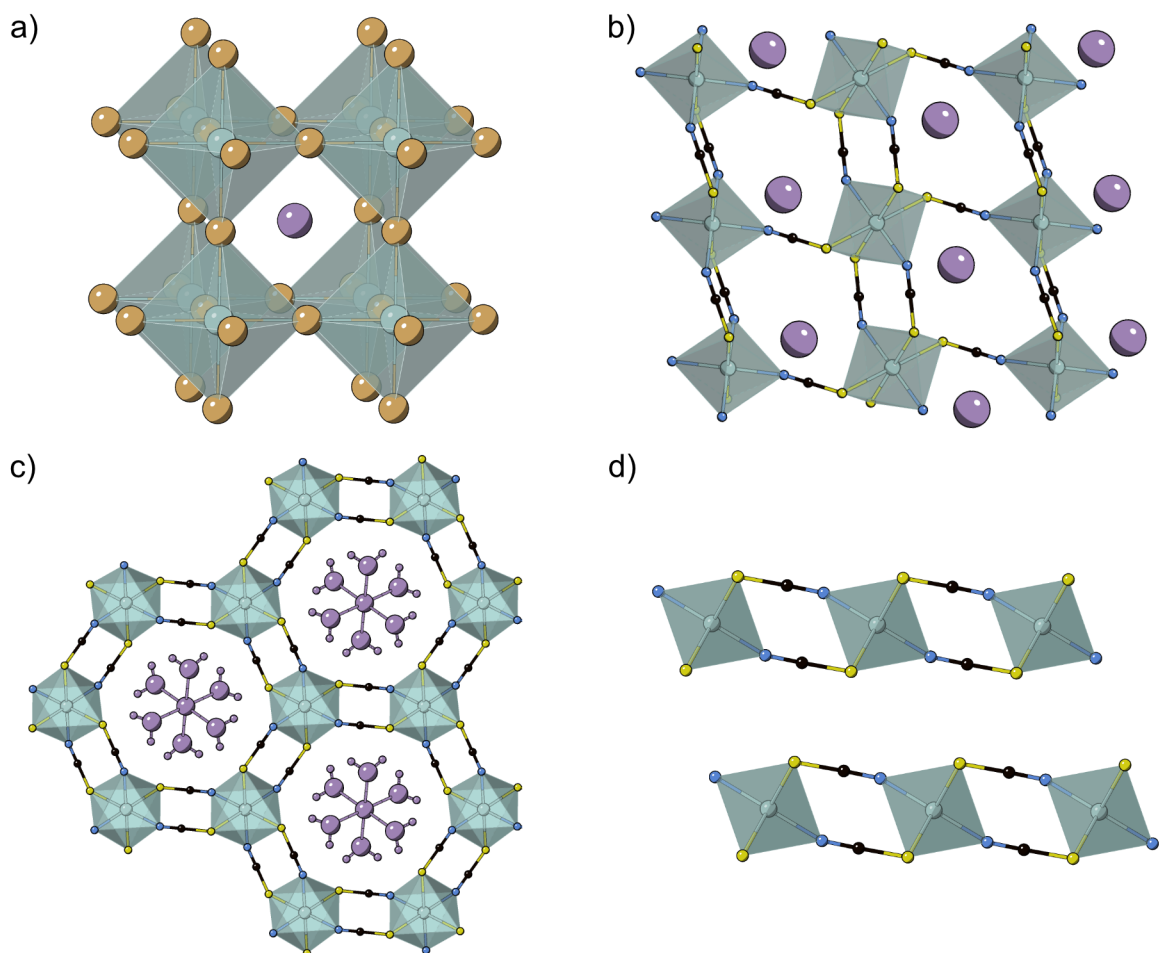


Figure 1.7: Different M–X connectivity by changing the size of the A-site species. a) An ideal perovskite with a tolerance factor close to 1. b), c) and d) show three thiocyanate-based frameworks, b) with a monoatomic A-site species, $\text{CsM}(\text{NCS})_3$, c) a multi-atom species, $[\text{Na}(\text{OH}_2)_3]\text{Mn}(\text{NCS})_3$ and d) with no A-site component, $\text{M}(\text{NCS})_2$. A = purple, M = teal, X = brown, N = blue, C = black, S = yellow.

molecular, non-spherical A and X species.^{6,93}

Using the tolerance factor has proved reliable for compounds with only atomic components, yet, AMX_3 compounds with at least one molecular component exhibit a range of structures, which are not predictable by radius ratios alone. For thiocyanate based compounds, the $\text{AM}(\text{NCS})_3$ family are less numerous, including $\text{CsNi}(\text{NCS})_3$,⁷⁸ $[\text{Na}(\text{OH}_2)_3]\text{Mn}(\text{NCS})_3$,⁸¹ $[1,3\text{-Im}]\text{Mn}(\text{NCS})_3$ (1,3-Im = 1-ethyl-3-methyl imidazolium),⁹⁴ $\text{RbHg}(\text{NCS})_3$,⁹⁵ $\text{CsCd}(\text{NCS})_3$ ⁹⁶ and $\text{RbCd}(\text{NCS})_3$.⁹⁶ Of these, only $\text{CsCd}(\text{NCS})_3$ adopts the perovskite structure. The other compounds adopt one-dimensional ($\text{RbHg}(\text{NCS})_3$) or two-dimensional frameworks. $\text{CsNi}(\text{NCS})_3$ and $\text{RbCd}(\text{NCS})_3$ have post-perovskite connectivity. Post-perovskite structures are closely related to perovskite structure-type, with a combination of edge-sharing and corner-sharing octahedra (Fig. 1.7b). $\text{CsNi}(\text{NCS})_3$ has paramagnetic Ni ions, however, previously no magnetic data had been reported for the compound. The post-perovskite structure-type and magnetic structures are discussed in more detail in Chapter 3. Both $[\text{Na}(\text{OH}_2)_3]\text{Mn}(\text{NCS})_3$ and

[1,3-Im]Mn(NCS)₃ adopt edge-sharing, honeycomb frameworks (Fig. 1.7c). The A-site cations are positioned within the hexagonal voids, and it is likely that the frameworks are templated by the larger A-site cation, compared to Cs⁺ or Rb⁺. The influence of the Na(OH₂)₃⁺ cations on the structure and magnetic properties of [Na(OH₂)₃]Mn(NCS)₃ are discussed in Chapter 2. Several thiocyanate double perovskites exist which do adopt the perovskite structure-type, [NH₄]NiCd(SCN)₆,⁹⁷ ANiBi(SCN)₆ A = K⁺, NH₄⁺, CH₃NH₃⁺, C(NH₂)₃⁺⁹⁸ and MPt(SCN)₆ M = Mn, Fe, Co, Ni, Cu⁹⁹ where the A-site is not occupied.

In protonated amine formate (HCOO⁻) frameworks, the size of the cation has a direct effect on the topology of the framework. Where the counteranion is CH₃NH₃⁺,¹⁰⁰ NH₂(CH₃)₂⁺¹⁰¹ and C(NH₂)₃⁺,⁸ the frameworks adopt three-dimensional, perovskite-type frameworks. In comparison, the incorporation of the smaller NH₄⁺ cation results in a three-dimensional hexagonal structure,¹⁰² whilst A-site species larger than C(NH₂)₃⁺, such as [CH₃NH₂(CH₂)₂NH₂CH₃]²⁺,¹⁰³ result in an alternative framework with open, hexagonal channels to accommodate the bulkier cations, which would be too large to be positioned within the perovskite-type cavities.¹⁰⁴

Similarly, in dicyanamide (N(CN)₂⁻, dca) frameworks, a modified tolerance factor has been developed to determine the A-site cation volume limits, for AM(dca)₃ frameworks to adopt perovskite topology.¹⁰⁵ The longer M–X–M distances for dca frameworks, compared to thiocyanate or formate frameworks, means that the A-site cavity is larger ($d_{\text{M-dca-M}} \approx 10.6 \text{ \AA}$, $d_{\text{M-NCS-M}} \approx 6.1 \text{ \AA}$ and $d_{\text{M-HCOO-M}} \approx 5.9 \text{ \AA}$)^{106,107} and cations with a larger volume, like [CH₃(CH₂)₃]₃BnN⁺ Bn = C₆H₅CH₂, can be incorporated into a dca-perovskite framework, before reaching the upper boundary.¹⁰⁵ Ph₄As⁺, depending on the calculation method, has an equivalent or slightly larger cation radius than [CH₃(CH₂)₃]₃BnN⁺.¹⁰⁵ Instead of a perovskite structure, [Ph₄As]M(dca)₃ M = Co, Ni, Ph₄ = tetraphenyl,¹⁰⁸ adopt post-perovskite topology, isostructural to CsNi(NCS)₃.⁷⁸

Vacant A-sites

Compounds without A-site cations do not necessarily form perovskite structures with empty A-site positions, there is a variety of other structure-types these compounds have been reported to adopt.¹⁰⁹ Halide compounds with MX₂ and MX₃ stoichiometry, adopt two-dimensional layers, grouped under the van der Waals family. The thiocyanate anion is regarded as a pseudohalide, highlighting its similarity in reactivity and ligand topology to that of its halide counterparts. This is particularly evident in the binary thiocyanates M(NCS)₂ M = Mn, Co, Fe, Ni, Hg,^{30,70,80,110} which are isostructural to their analogous metal halide MX₂ (Fig. 1.7d). The compounds consist of edge-sharing octahedra, with

$\mu_{1,3,3}$ -NCS connectivity. Although the $M \cdots M$ separation is elongated within the plane, the interlayer $M \cdots M$ separation is comparable, NiCl_2 $d_{\text{interlayer}} = 6.14 \text{ \AA}^{111}$ compared to Ni(NCS)_2 $d_{\text{interlayer}} = 6.16 \text{ \AA}^{80}$. The symmetry, however, is not the same, with the incorporation of a linear, non-symmetric thiocyanate. It lowers the symmetry to a monoclinic space group, compared to the spherical halide anions which crystallise with hexagonal symmetry.

Denser frameworks are observed for binary dca frameworks, M(dca)_2 $M = \text{Cr, Mn, Fe, Co, Ni, Cu}$,^{112,113} which crystallise with a three-dimensional network through $\mu_{1,3,5}$ -dca coordination. This is in contrast to the binary thiocyanates or halide, as a result of the additional coordination site at the central N atom.

Combining functionality

The expression of some physical properties are inherently dependent on the crystal symmetry. This is particularly evident in physical properties that demand polarity. Compounds which adopt non-centrosymmetric space groups hold potential for exhibiting ferroelectric behaviour.^{16,114} Electrical conducting materials are sought after for their more robust memory storage as a result of their hysteretic behaviour,¹¹⁵ whilst piezoelectrics and opto-electrics are components of sensors, for example, for wearable devices.¹¹⁶ There are several routes that can be employed to favour a polar space group, with methods including phase transitions and structural distortions.

At ambient temperature, components have sufficient energy to exhibit dynamic disorder. This is particularly observed in both A-site cations and X-site anions. As the compound is cooled, these compounds undergo temperature-induced phase transitions as the disordered components settle into a fixed orientation. In the formate frameworks $[\text{MHy}]\text{M}(\text{HCOO})_3$, $\text{MHy} = \text{methyl hydrazinium } (\text{CH}_3\text{NH}_2\text{NH}_2^+)$, $M = \text{Mn, Mg, Fe, Zn}$,¹⁰⁴ the high temperature phase has the $R\bar{3}c$ space group, with the MHy cations rotating around a two-fold axis. As the compounds are cooled, these rotations are thermally inhibited, leading to a phase transition to the polar $R3c$ space group. Similar behaviour has been observed for formate frameworks with imidazolium ($\text{C}_3\text{H}_5\text{N}_2^+$),¹¹⁷ formamidinium ($\text{NH}_2\text{CHNH}_2^+$),¹¹⁸ ethyl ammonium ($\text{EMA, CH}_3\text{CH}_2\text{NH}_3^+$)¹¹⁹ and dimethyl ammonium ($\text{DMA, (CH}_3)_2\text{NH}_2^+$).^{120,121} The essential requirement is using an A-site cation without $\bar{1}$ point group symmetry, so that static disorder gives rise to non-equivalent cation orientations. Conversely, $[\text{DMA}]\text{M}(\text{HCOO})_3$, $M = \text{Na}_{0.5}\text{Fe}_{0.5}$ ¹²² and $[\text{NH}_2\text{NH}_3]\text{M}(\text{HCOO})_3$, $M = \text{Mn, Zn}$,¹²³ have polar structures at room temperature, and undergo a phase transition to a non-polar structure when heated.

With longer, flexible ligands, such as dca, the order-disorder phase transition can arise

from ligand positional order as well. $[\text{C}_5\text{H}_{13}\text{NX}]\text{M}(\text{dca})_3$ $X = \text{Cl}, \text{Br}$; $\text{M} = \text{Mn}, \text{Cd}$,^{124,125} exhibit both A-site and X-site positional ordering with lowered temperatures. Where $X = \text{Br}$, this results in polar symmetry, for $X = \text{Cl}$, the cations and dca order so that the centre of inversion is retained.

Structural distortions

It is a common pursuit to obtain compounds with more than one desirable physical property. Termed multiferroic compounds, a polar property such as ferroelectricity is combined with magnetic or elastic behaviour. These are advantageous as the material has more than one ferroic order parameter, and so, for example the magnetic behaviour can be controlled by electric fields. Most compounds exhibit type-I multiferroic behaviour, where, for example, the magnetic and electric transitions occur at different temperatures. This results in the behaviour of the two properties being weakly coupled. The majority of molecular ferroelectrics have been reported for formate frameworks, triggered by magnetostriction and ferroelastic distortions, such as in $[\text{DMA}]\text{M}(\text{HCOO})_3$, $\text{M} = \text{Mn}, \text{Ni}$.^{126,127} Type-II multiferroics exhibit a phase transition to a long-range magnetically ordered and electrically ordered state simultaneously, overcoming the weak cooperative nature of Type-I multiferroics. Magnetic ordering with complex helical or non-collinear moment arrangements can break the inversion centres, therefore ordering in a polar space group. These are significantly sparsely reported, mainly due to the complex magnetic structures required. Reports of Type-II multiferroics have been limited, almost exclusively, to compounds with triangular lattices which induce geometrically frustrated magnetic layers.^{128,129}

Structural and chemical distortions can also be considered in terms of chemical and positional orderings. The mechanisms explored in this thesis are octahedral tilts, A-site and M-site orderings. Although these distortions can occur in any crystalline compound with M–X octahedra, they are usually explained using the aristotypic cubic perovskite. Starting from an ideal perovskite with $Pm\bar{3}m$ symmetry,¹³⁰ a double perovskite can be formed by incorporating two cations on the same site, $\text{AA}'\text{M}_2\text{X}_6$ or $\text{A}_2\text{MM}'\text{X}_6$. Cations on the same site may distribute themselves randomly, forming a solid solution, or they can exhibit an ordered arrangement within the structure. The most common ordering patterns are rocksalt, layered and columnar ordering (Fig. 1.8a). The types and combination of the cation orderings systematically reduce the symmetry of the structure.

Ordering of the M-site cations is observed for both atomic and molecular perovskites. For the majority of compounds with only atomic components, rocksalt ordering is observed. This ordering is favoured as it favours separating ions with large charge differ-

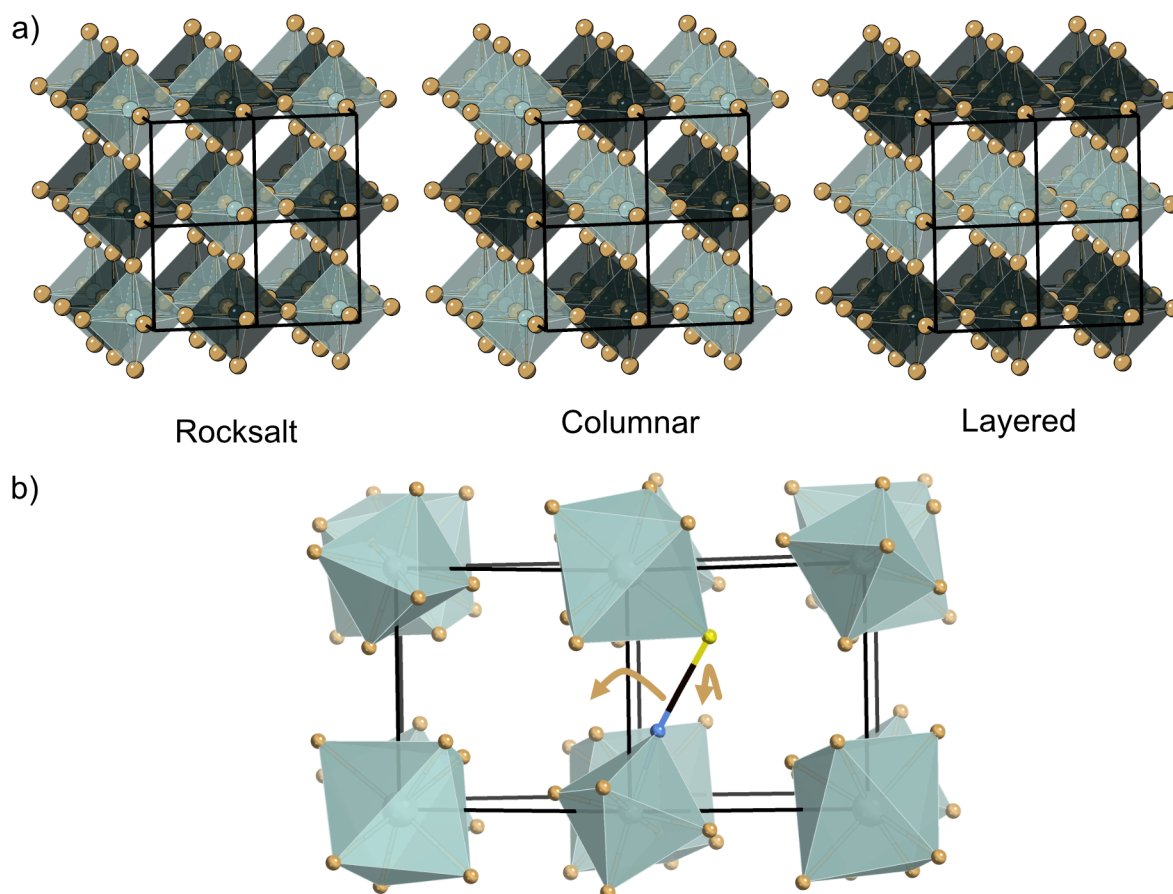


Figure 1.8: a) The three common site orderings: rocksalt (left), columnar (middle) and layered (right), shown for M-site ordering in $A_2MM'X_6$ double perovskite. The A-site cations have been removed for clarity. Black lines represent the M_8X_{12} metal cages, which are not equivalent to the unit cell. b) How the rotation of the octahedra will change the position of the thiocyanate ligand relative to the pseudocubic cages (black lines). The ligand can be in the left or right cage (left arrow) or in one of the cages in the row in front (right arrow) depending on the tilt of the octahedra. M = teal octahedra, M' = black octahedra, X = brown, N = blue, C = black, S = yellow.

ences and reduces strain where ionic radii vary,¹³¹ as observed for Sr_2MMoO_6 , M = Mg, Mn, Fe, Co, Ni.¹³² In thiocyanate frameworks, all M-site double perovskites show rocksalt ordering: $[NH_4]_2Ni\{Cd(SCN)_6\}$,⁹⁷ $M\{Pt(SCN)_6\}$, M = Mn, Fe, Co, Ni, Cu⁹⁹ and $[\square]Ni\{Bi(SCN)_6\}$, \square = vacancy; A = K^+ , NH_4^+ , $CH_3NH_3^+$, $C(NH_2)_3^+$.⁹⁸ This ordering may be further influenced by the alternate coordination preferences of the thiocyanate termini, which acts as a template. All the compounds have $[NiN_6]$ and $[MS_6]$ M = Cd, Pt, Bi, coordination spheres, based on the likelihood of coordination to the N and S atoms. In comparison, of the dicyanamide or formate perovskite-type compounds, randomly arranged solid solutions of the M-site are generally reported.^{133,134}

A-site cation ordering is significantly less commonly reported. Without a large electrostatic or steric persuasion, the cations will likely be distributed randomly. A-site vacancy oxide perovskites have been reported to adopt layered A-site order, in $[\square_{\frac{2}{3}}La_{\frac{1}{3}}]MO_3$ M = Nb, Ta,¹³⁵ $[\square_{\frac{2}{3}}Ln_{\frac{1}{3}}]MO_3$ Ln = lanthanide; M = Ta, Nb,^{136,137} whereas, long-range rocksalt

ordering has been observed in $[\text{NaBa}]\text{LiNiF}_6$ ¹³⁸ and $\text{Na}_2\text{BaFe}_4\text{F}_{12}$.¹³⁹ Despite the distortions through A-site ordering, these compounds remain in centrosymmetric space groups, with the exception of $[\square_{\frac{2}{3}}\text{Dy}_{\frac{1}{3}}]\text{MO}_3$.

It is difficult to separate the A-site ordering from the octahedral tilt sequences observed, as the rotation of the octahedra are closely linked to the size of the A-site cation. Tilt sequences are usually activated when there is a size mismatch between the void within the $[\text{M}_8\text{X}_{12}]$ cage and the A-site cations.¹⁴⁰ To describe the tilt sequences, Glazer notation can be employed.¹⁴¹ Here, superscript “+” denotes in-phase tilts (rotations of all the octahedra along a given axis occur in the same sense), and superscript “−” describes out-of-phase tilts (octahedra alternate between clockwise and anticlockwise rotations). For completeness, “0” identifies an axis where the octahedra are not rotated relative to the axis. Arbitrary letters are assigned to the axes (a , b and c) defining a comparative magnitude of the rotation. For example, the most common tilt pattern reported for perovskites is $a^-a^-c^+$, describing out-of-phase tilts along the a and b directions of equal magnitudes, and in-phase rotations along c , of a different magnitude.

In perovskites with atomic components, the combination of tilt sequences, defined as conventional tilts, are restricted since the octahedra are directly joined through the X anions. However, by introducing molecular X species, the octahedra are connected, but no longer share the same atom, so that the octahedra have additional freedom to adopt tilt sequences that are not observed in atomic perovskites, known as unconventional tilts.¹⁴² Thiocyanate frameworks have octahedra that are inherently tilted due to the bond angles of the N ($\approx 180^\circ$) and S ($\approx 100^\circ$) atoms. In the doubly ordered perovskites $[\square\text{A}]\text{Ni}\{\text{Bi}(\text{SCN})_6\}$, where $\text{A} = \text{CH}_3\text{NH}_3^+$ and $\text{C}(\text{NH}_2)_3^+$ uncommon or complex tilt sequences are reported.⁹⁸ It has been noted for $\text{A} = \text{CH}_3\text{NH}_3^+$, that the unconventional tilt pattern arises in conjunction with complex orderings of the A-site species. Due to the bent nature of the M–S–C bond angle, the thiocyanate ligands are not positioned parallel to the $[\text{M}_8(\text{NCS})_{12}]$ cage edges, they point within a cage (Fig. 1.8b). In addition to the octahedral tilting which inherently changes the volume of the A-sites, the presence of thiocyanate anions within the cage will further reduce the volume. Consequently, the more ligands that are positioned within a cage, the more likely that the A-site within the cage will be vacant, due to steric bulk. The complexity in the orderings do not intrinsically result in a polar space group, with $[\square(\text{CH}_3\text{NH}_3)]\text{Ni}\{\text{Bi}(\text{SCN})_6\}$ adopting $P2/n$ symmetry.

Complex ordering have also been observed in hypophosphites and azides, for example $[\text{NH}_2(\text{CH}_3)_2]\text{MnX}_3$, $\text{X} = (\text{H}_2\text{POO})$ ¹⁴³ and N_3 .¹⁴⁴ Nevertheless, a molecular anion is not the only requirement to achieve unconventional tilts and orderings. Formate frameworks generally adopt structures with conventional tilt sequences, which has been attributed to

the rigidity of the M–O–C bond angles.¹⁴² A variability in the M–X bond angle is also necessary.

1.7 Designing magnetic materials

Although paramagnetic ions are integral components of magnetic materials, there are several factors which will influence their behaviour by considering the nature of the non-magnetic components. Magnetic properties have been altered through the dimensionality of the framework, the superexchange species or the connectivity of the lattice.

Two-dimensional magnets: atomic superexchange species

Low-dimensional frameworks have a connectivity in only one or two directions, forming chains or layers. Although low-dimensional frameworks do not inherently engender low-dimensional magnetism, the spatial separation of metal ions can encourage magnetic interactions of differing strengths. Magnetic low-dimensionality, where the magnetic interactions are primarily limited to one or two directions, is particularly enticing from a magnetic design approach. Magnetically ordered phases in two-dimensions were originally thought to not exist, yet there are now several experimentally realised examples.^{145,146} With the progression of spintronics technologies, where the spin is utilised for information storage or transport, the push for smaller and more compact devices has driven scientists to search for low dimensional designs.^{54,147}

A commonly explored family of compounds are the van der Waals materials. These are layered compounds, so-called for their weak interlayer interactions. In MX_2 and MX_3 halides, helimagnetic ground states are observed in NiBr_2 below $T_C = 23 \text{ K}$ ¹⁴⁸ and MnI_2 $T_C = 3.4 \text{ K}$.¹⁴⁹ These, like several halides, including MI_2 $\text{M} = \text{Co}, \text{Ni}$ ¹⁵⁰ and FeCl_3 ,¹⁵¹ adopt non-collinear, and sometimes incommensurate, magnetic structures. MX_2 compounds crystallise with either trigonal CdI_2 -type structures or rhombohedral CdCl_2 -type structures, the difference being the off-set of the stacked layers. In both structures, the compounds have triangular lattices with metal vertices, bridged by two $\mu_{1,1}\text{-X}$ anions. In comparison, MX_3 halides adopt rhombohedral BiI_3 -type structures or monoclinic AlCl_3 structure-types, again dependent on stacking arrangements. In this case, the magnetic ions are connected in hexagons. For both MX_2 and MX_3 compounds with helimagnetic structures, the complex orderings have been attributed to the metal lattice arrangement creating competing interactions.^{152,153}

In particular, layered materials are attractive for the low energy barrier to cleave layers,¹⁵⁴

which has motivated investigations into exfoliating van der Waals materials to few-layer or monolayer limits.¹⁵⁵ Recently, monolayer magnetism has been experimentally reported in CrI_3 ,¹⁵⁶ the chalcogenides FePS_3 ¹⁵⁷ MnSe_2 ¹⁵⁸ and the tellurides Fe_3GeTe_2 ^{159,160} and CrGeTe_3 .¹⁶¹ Notably, except FePS_3 , at the single-layer extreme, the compounds order as ferromagnets. As the demand for larger storage capacity continues, the need for more compact methods to hold information follows accordingly, and incorporating magnetic thin films into devices as materials with higher density data storage is one method to meet technological needs.¹⁶²

Frameworks with molecular ligands

Although it is expected that the magnetic interactions are weakened by a longer, molecular superexchange pathway, this has not deterred scientists from exploring this territory. Exploring magnetism in frameworks with molecular ligands can lead to an array of magnetic behaviour, including weak ferromagnetism and non-collinear magnetic structures.

Frameworks with weak ferromagnetism are commonly attributed to arising from anti-symmetric exchange (Dzyaloshinskii-Moriya) interactions. This is commonly explored in formate-based frameworks with protonated amine cations which show non-collinear orderings. $\text{NH}_4\text{M}(\text{HCOO})_3$ $\text{M} = \text{Co}, \text{Ni}$ adopt weak ferromagnetic structures¹⁰² as well as $[\text{CH}_3\text{NH}_3]\text{M}(\text{HCOO})_3$ ¹⁶³ and $[\text{C}(\text{NH}_3)_2]\text{M}(\text{HCOO})_3$ ⁸ $\text{M} = \text{Mn}, \text{Fe}, \text{Co}, \text{Ni}$. These arrangements are generally attributed to having competing interactions and antisymmetric exchange interactions mediated by the non-centrosymmetric formate anion, which favour canted spin arrangements.¹⁶⁴

The binary thiocyanates $\text{M}(\text{NCS})_2$ $\text{M} = \text{Mn}, \text{Fe}, \text{Co}, \text{Ni}$ ^{30,80,165} adopt structures that are isostructural to that of the MX_2 halides, with the inclusion of the thiocyanate lowering the structure to a monoclinic symmetry. They all magnetically order between $T_N = 20-78$ K,^{30,80} yet, despite the ligands and framework topology being the same, the ground state magnetic structures are not all equivalent. The Mn, Fe and Co analogues order with in-plane antiferromagnetic stripes, which are ferromagnetically coupled between the layers. In contrast, $\text{Ni}(\text{NCS})_2$ orders with ferromagnetic layers coupled antiferromagnetically,¹⁶⁶ similar to MCl_2 , $\text{M} = \text{Co}, \text{Fe}, \text{Ni}$.^{167,168} The switch in magnetic ordering is believed to arise from the d -subshell occupancies and arrangement for the transition metal (e_g^x and t_{2g}^y), in combination with the orbital overlap with the thiocyanate.⁸⁰ This rationale has been observed experimentally for halide-based and molecular-based superexchange pathways as well.^{169,170}

The binary dicyanamides, $\text{M}(\text{dca})_2$, despite matching stoichiometry to the thiocyanates, have a three-dimensional connectivity through $\mu_{1,3,5}$ -dca coordinations. Unlike

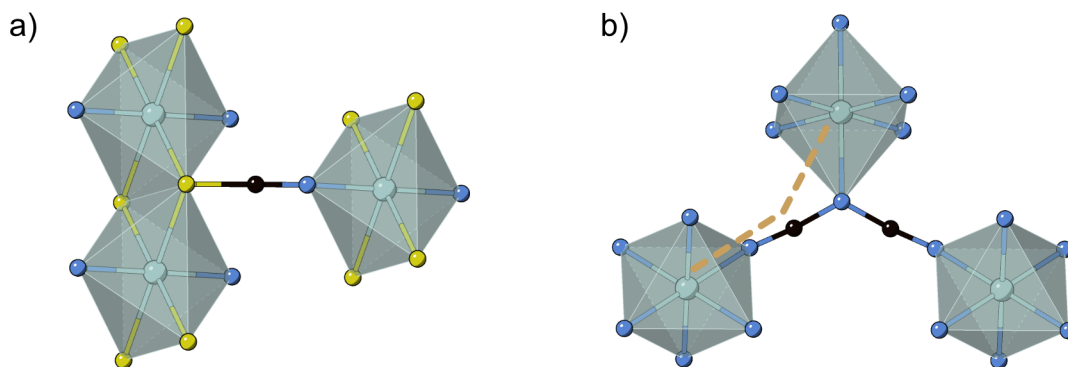


Figure 1.9: The ligand coordination for the binary compounds, a) $M(\text{NCS})_2$ and b) $M(\text{dca})_2$ $\text{dca} = \text{N}(\text{CN})_2$. The brown line indicates the $M \cdots C \cdots M$ angle. $M = \text{teal}$, $\text{N} = \text{blue}$, $\text{C} = \text{black}$, $\text{S} = \text{yellow}$.

$M(\text{NCS})_2$, $M(\text{dca})_2$, $M = \text{Co}, \text{Ni}$,¹¹² order as collinear ferromagnets, whereas $M = \text{Cr}, \text{Mn}$ and Fe ^{171,172} order as weak ferromagnets. The changes in orbital electron occupancy cannot be applied to rationalise the trend in magnetic behaviour alone. Both the ordering temperatures and Curie-Weiss values are lower than that of their comparative $M(\text{NCS})_2$ members, which are tentatively attributed to a competing number of simultaneous ferromagnetic and antiferromagnetic interactions, arising from the three coordination sites of the dca anion.¹⁷²

The principle of predicting exchange interactions from the superexchange angle have proved a useful explanation for the magnetic behaviour in atomic-based compounds. This has been particularly apparent for compounds under applied pressure. It has been noted for several metal halides, MX_2 , MX_3 and chalcogenides MPS_3 , that as the $M-X-M$ bond deviates further from 90° under compression, the ferromagnetic character is less dominant,^{173,174} to the extent that the magnetic ordering temperature decreases for CrGeTe_3 despite the shortening $\text{Cr} \cdots \text{Cr}$ distances.¹⁷⁴ For molecular-based frameworks, the adherence to the angle dependence for predicting magnetic interactions is not straightforward. $M(\text{dca})_2$ was hypothesised to have a critical $M \cdots C \cdots M$ angle above which the magnetic ordering switches from weak ferromagnet to collinear ferromagnet.¹⁷⁵ However, this was disproved by the characterisation of $[\text{Fe}_{0.5}\text{Ni}_{0.5}](\text{dca})_2$, which has a $M \cdots C \cdots M$ angle of 141.7° , but does not magnetically order with an analogous structure to either the ferromagnets or weak ferromagnets.⁸⁶ This superexchange angle has also been explored for azide frameworks, regarding the $\text{Ni}-\text{N}-\text{N}$ bond angle. As the angle widens (approximately 122° to 151°) the strength of the antiferromagnetic interactions generally decreased.¹⁷⁶

The spatial relationship of the magnetic ions, closely related to ligand connectivity and superexchange angles, is a common design consideration to tune the magnetic properties. It is well known for frustrated magnets, which do not exhibit long-range magnetic ordering, that by choosing a triangular lattice, the likelihood of a frustrated system is in-

creased (geometrical frustration).¹⁷⁷ The arrangement of magnetic ions has been explored in azide-coordinated frameworks, where by keeping the superexchange pathway the same, $\mu_{1,3}-\text{N}_3$, but altering the topology of the framework, different magnetic characteristics could be obtained. The distorted honeycomb framework, $\text{trans}-\text{Mn}(\text{N}_3)_2(4-\text{Mpy})_2$ Mpy = 4-methylpyridine, orders as an antiferromagnet,¹⁷⁸ whereas the $[\text{M}_4(\text{N}_3)_4]$ square topology, including $\text{NiN}_3(2-\text{apy})_2(\text{ClO}_4) \cdot n\text{H}_2\text{O}$ 2-apy = 2-amino-ethyl pyridine¹⁷⁶ and $\text{Mn}(4-\text{PMK})(\text{N}_3)_2$ 4-pyridylmethylketazine,¹⁷⁹ order as weak ferromagnets. The azide framework with a Kagomé lattice, $\text{Co}(\text{N}_3)_2(\text{bpg}) \cdot \text{DMF}_{4/3}$ bpg = meso- α,β -bi(4-pyridyl) glycol, potentially shows ferrimagnetic ordering.^{180,181}

The effect of the paramagnetic ion arrangement has also been explored in thiocyanate frameworks. One-dimensional $\text{M}-(\text{NCS})_2-\text{M}$ chains of doubly bridged cations is a common motif.¹⁸² By changing the arrangement of the Co cations in $\text{Co}(\text{NCS})_2(4-\text{cp})_2$ 4-cp = 4-chloropyridine, from a linear chain to a corrugated chain, the anisotropy could be switched, resulting in a change from an antiferromagnetic to weak ferromagnetic behaviour. Here, the single-ion anisotropies could be tuned based on the *cis* or *trans* arrangements of the thiocyanate ligands.¹⁸²

Heteroleptic frameworks

Ligand choice is undoubtedly important for magnetic materials, having an impact through their bonding angles, connectivity and lattice arrangements. To further tune the magnetic properties, compounds have been synthesised with more than one type of bridging ligand within the framework, a heteroleptic framework. By mixing bridging motifs, such as azides and carboxylates in $\text{Mn}_2\text{L}_2(\text{N}_3)_3$ L = isonicotinate,¹⁸³ the ligands can bring about conflicting interactions.¹⁸⁴ It has been reported that the competing interactions brought about by the azides and carboxylates leads to frustrated magnetic behaviour,^{183,185} identified by a θ_{CW} over 10 times larger than T_C .

In addition, ligands can be explored where the strength of the magnetic interaction is altered between different superexchange pathways, for example, $\text{ML}_2(\text{NCS})_2$ M = Co, Ni, L = pyrimidine or pyrazine.¹⁸⁶⁻¹⁸⁸ The addition of the longer ligands tends to decrease the overall strength of the magnetic interactions and lower the ordering temperature, for example, $\text{Co}(\text{pym})(\text{NCS})_2$ has $T_N = 7.1 \text{ K}$ ¹⁸⁸ compared to $\text{Co}(\text{NCS})_2$ $T_N = 20 \text{ K}$.⁸⁰

A similar trend in ordering temperature is observed for terminally coordinating, ancillary, ligands as well. A variety of ligands have been included for thiocyanate frameworks, including $\text{ML}_x(\text{NCS})_2$ M = Co, Ni, L = ethyl isonicotinate, $x = 4$;⁷⁹ M = Co, Ni, Fe, L = 4-acetylpyridine, $x = 2$.^{189,190} In these examples, the ordering temperatures are consistently lower than their $\text{M}(\text{NCS})_2$ members, likely influenced by the less effi-

cient superexchange paths. It is sometimes synthetically unavoidable to create mixed ligand thiocyanate frameworks, which are probably influenced by the preferential coordination of the first row transition metals to the N over the S atom. It is common for transition metal thiocyanate compounds to coordinate to solvent molecules as well, including $\text{Mn}(\text{NCS})_2 \cdot 2\text{H}_2\text{O}$,¹⁹¹ $\text{M}(\text{NCS})_2(\text{THF})_2$ $\text{THF} = (\text{CH}_2)_4\text{O}$,¹⁹² $\text{M}(\text{NCS})_2(\text{NCMe})_2$, $\text{Me} = \text{CH}_3$ ¹⁹² and $\text{Mn}(\text{NCS})_2(\text{EtOH})$, $\text{EtOH} = \text{C}_2\text{H}_5\text{OH}$.¹⁹³ These ligands are typically terminal, although the small steric bulk of OH_2 and NCMe permit two-dimensionally bridged thiocyanate frameworks, with a Curie-Weiss temperature an order of magnitude larger than, for example, the THF or EtOH compounds which adopt one-dimensional $\text{M}-(\mu_{1,3}\text{NCS})_2-\text{M}$ chains.^{192,193}

Compounds with bridging molecular ligands exhibit a variety of magnetic orderings, influenced by several factors, including spin anisotropy, orbital occupancy, the superexchange angle and the framework topology. These factors are not distinct, and cannot necessarily be separated as many of these mechanisms overlap or co-exist depending on the structure and composition of the compound.

1.8 Neutrons for complementary information

This thesis has a focus on using neutron diffraction to gain information about the materials studied. Sometimes, neutron diffraction measurements reveal information that might be obscured or undetectable through other techniques alone. Two examples are outlined below, highlighting how neutron experiments can complement other analyses and further probe the structural and magnetic properties of materials.

Modulated structures and hydrogen bonds

Although the phenomenon of modulated structures is not uniquely accessible by neutron diffraction, there are instances where synchrotron radiation may be used, in certain scenarios, neutron diffraction proves to be a powerful tool. Neutrons may be chosen as the preferred radiation source for a compound with long-range magnetic ordering, so that the nuclear and magnetic structure are probed simultaneously. In addition, if the quantity of powder or dimensions of the single crystal are large enough, neutrons have the benefit of no form factor dependence, permitting data collection to large Q ranges, ideal for structural analysis.

Neutron diffraction was proved a beneficial technique for the formate frameworks $[\text{CH}_3\text{NH}_3]\text{M}(\text{HCOO})_3$ $\text{M} = \text{Co}, \text{Ni}$, which undergo several temperature-dependent phase

transitions to incommensurately modulated structure.^{18,194} Neutron diffraction experiments were employed to follow these transitions and determine the structural evolutions in each phase. Below its magnetic ordering temperature, $[\text{CH}_3\text{NH}_3]\text{Ni}(\text{HCOO})_3$ orders with concomitant nuclear and magnetic modulated structures, which is only evident through the neutron studies. The phase transitions are activated by changes, and competition, of hydrogen bonds between CH_3NH_3^+ and the ligands. Since the coherent scattering of neutrons from hydrogen atoms is detectable, determining the position of hydrogen atoms and defining hydrogen bond lengths is possible. For these compounds, both the structure and the trigger for the modulated phases were determined from the neutron data. The use of neutron diffraction for modulated structures are reported in Chapter 5. In addition, hydrogen atom positions and hydrogen bond interactions are reported, in particular, for $[\text{Na}(\text{OH}_2)_3]\text{Mn}(\text{NCS})_3$ in Chapter 2 and $[\text{CH}_3\text{NH}_3]\text{M}(\text{HCOO})_3$, $\text{M} = [\text{Co}_x\text{Ni}_{1-x}]$ in Chapter 5.

Non-collinear magnetism

There has been a heightened interest towards identifying materials with non-collinear magnetic structures, which are believed to be useful for spin-based memory storage, where the orientation of the moment holds information.¹⁹⁵ Weak ferromagnetic structures are evident from magnetometry measurements alone: their signature traits exhibiting dominating antiferromagnetic behaviour in the susceptibility, and likely a negative θ_{CW} , combined with hysteretic behaviour in magnetisation measurements and a magnetisation moment well below the expected M_{sat} .

However, compounds have also been shown to order with non-collinear antiferromagnetic orderings. In these examples, such as $\text{Pr}_2\text{PdAl}_7\text{Ge}_4$,¹⁹⁶ there is more than one crystallographically independent moment which align antiparallel to themselves, but are not collinear with each other distinct moment. Other ordering exhibit complex helical and/or incommensurate orderings, such as the extensively studied multiferroic BiFeO_3 .¹⁹⁷ Since magnetometry measurements detect the average of all the moments, and all the moments are compensated, the intricacy of these structures is not perceptible from magnetometry data. The magnetic structure of the non-collinear antiferromagnet $\text{CsMn}(\text{NCS})_3$ is determined from neutron diffraction data in Chapter 3, which is otherwise hidden in the magnetometry data.

1.9 Objectives

The principle aim of this thesis is to explore the crystallographic properties of molecular-bridged frameworks and the interplay with their magnetic behaviour. Especially, there is an emphasis on expanding and exploring the family of thiocyanate-based framework compounds. This will be achieved through the synthesis of reported and new frameworks, and identifying techniques for crystal growth. This is followed by analysis of their structural and magnetic characteristics. A particular focus will be given to using neutron diffraction data to obtain information on their nuclear or magnetic structures.

In Chapter 2, a method is developed to grow and store single crystals of the deliquescent $[\text{Na}(\text{OH}_2)_3]\text{Mn}(\text{NCS})_3$ through controlling the local humidity of the samples. A combination of magnetometry and low temperature neutron diffraction experiments are undertaken to determine the magnetic behaviour. In addition, second harmonic generation measurements are carried out to confirm the centro-symmetric nature of the magnetic structure.

In Chapter 3, I present two new post-perovskite thiocyanate frameworks, $\text{CsM}(\text{NCS})_3$ $M = \text{Mn}, \text{Co}$, and report the magnetic properties of $\text{CsMn}(\text{NCS})_3$, $\text{CsCo}(\text{NCS})_3$ and $\text{CsNi}(\text{NCS})_3$. This work highlights the role of neutron diffraction experiments in determining non-collinear magnetic structures and the extent of canting which cannot be inferred from magnetometry measurements.

Chapter 4, explains how the pressure-activated structural distortions of $\text{Ni}(\text{NCS})_2$ promote higher magnetic ordering temperatures. Here, the evolution of the lattice parameters, determined through synchrotron X-ray and neutron diffraction experiments, demonstrates the compressible nature of the material, whilst magnetometry and low temperature neutron diffraction data show the magnetic response to pressure.

Chapter 5 explores the structural evolution and magnetic character of the solid solutions $[\text{CH}_3\text{NH}_3]\text{Co}_x\text{Ni}_{1-x}(\text{HCOO})_3$ $x = 0.25, 0.50, 0.75$. Neutron diffraction is valuable for calculating the Co and Ni contents in the crystals, and to solve the modulated phases and magnetic structure of $[\text{CH}_3\text{NH}_3]\text{Co}_{0.5}\text{Ni}_{0.5}(\text{HCOO})_3$.

Finally, Chapter 6 explores the diversity of uncommon and unconventional site ordering and octahedral tilt sequences in four double perovskites, nominally $[\square\text{A}]\text{Mn}\{\text{Bi}(\text{SCN})_6\}$ $\square = \text{vacancy}; \text{A} = \text{Cs}^+, \text{K}^+, \text{NH}_4^+$ and $\text{C}(\text{NH}_2)_3^+$. This chapter highlights the complementary nature of diffraction from different radiation sources, with analysis from combinations of X-ray, neutron and electron powder and single crystal diffraction to determine the crystal structures.

The thesis is concluded by an overall summary and outlook for future ventures exploring

the composition-structure-magnetic characteristics of molecular-based frameworks.

Publications arising from the thesis

The published articles from this thesis are detailed below, along with their location in the thesis. The articles have been appended in Appendix A and B:

- Chapter 3: Non-collinear magnetism in the post-perovskite thiocyanate frameworks $\text{CsM}(\text{NCS})_3$. M. Geers, J.Y. Lee, S. Ling, O. Fabelo, L. Cañadillas Delgado, M.J. Cliffe, *Chemical Science*, **14**, 3531 (2023).
- Chapter 4: High-pressure behaviour of the magnetic van der Waals molecular framework $\text{Ni}(\text{NCS})_2$, M. Geers, D.M. Jarvis, C. Liu, S.S. Saxena, J. Pitcairn, E. Myatt, S.A. Hallweger, S.M. Kronawitter, G. Kieslich, S. Ling, A.B. Cairns, D. Daisenberger, O. Fabelo, L. Cañadillas Delgado, M.J. Cliffe, *Physical Review B*, **108**, 144439 (2023).

Chapter 2

Magnetic and low temperature structural properties of $[\text{Na}(\text{OH}_2)_3]\text{Mn}(\text{NCS})_3$

2.1 Summary

- A method to grow and store single crystals of the deliquescent $[\text{Na}(\text{OH}_2)_3]\text{Mn}(\text{NCS})_3$ has been developed using a controlled humidity environment.
- Magnetometry measurements show the compound magnetically orders with antiferromagnetic correlations below $T_N = 18.1(6)$ K.
- A combination of low temperature neutron diffraction data and low temperature optical measurements revealed the compound maintains its trigonal symmetry, ordering in the $P\bar{3}'$ magnetic space group.

2.2 Introduction

Honeycomb lattices, compounds with paramagnetic ions arranged in hexagon motifs, promise attractive magnetic and mechanical properties. Atomic halides, such as RuCl_3 order as zig-zag antiferromagnets,¹⁹⁸ or with more complex spiral spin states, for example FeCl_3 .¹⁹⁹ However, there are also MX_3 halides which present more simple ordering patterns, either as ferromagnets, for example CrBr_3 ²⁰⁰ and CrI_3 ²⁰¹ or as antiferromagnets with in-layer ferromagnetism, including CrCl_3 ,²⁰² FeBr_3 ²⁰³ and NaMnCl_3 .²⁰⁴ These two-dimensional compounds have low cleavage energies,²⁰⁵ providing a facile route to exfoliate to few-layer and monolayer samples, which are sought after to act as spintronic

and semiconducting components integrate into atomically thin devices.^{206,207}

Honeycomb frameworks built from molecular ligands are suitable for host-guest chemistry such as selective gas separation which are welcomed by the larger hexagonal voids created by longer, flexible ligands.^{208,209} Shorter, three atom, ligands which adopt this motif include an azide (N_3^-) framework with alternating $\mu_{1,3}\text{N}_3^-$ and $\mu_{1,1}\text{N}_3^-$ bridged metals, $\text{Co}(\text{N}_3)_2(\text{bpg}) \cdot \text{DMSO}$ ($\text{bpg} = 1,2\text{-dipyridin-4-ethane-1,2-diol}$, $\text{DMSO} = \text{SO}(\text{CH}_3)_2$),¹⁸⁰ however, the honeycomb lattice is more commonly observed in thiocyanates. Cadmium thiocyanates, $[\text{DAIm}]_2\text{Cd}_2(\text{NCS})_6$, ($\text{DAIm} = \text{N,N-dialkyl imidazolium}$)²¹⁰ and $[\text{NBpy}]\text{Cd}_2(\text{NCS})_6$ ²¹¹ ($\text{NBpy} = \text{bis}[4\text{-}(\text{N-benzyl pyridinium})]$ piperazine) have honeycomb frameworks consisting of Cd^{2+} ions bridged by two $\mu_{1,3}\text{NCS}$ ligands. Unfortunately, Cd^{2+} is diamagnetic (d^{10} electron configuration), and are therefore not suitable for magnetic studies. There are also two Mn^{2+} (high-spin d^5 electron configuration) compounds, $[\text{Na}(\text{OH}_2)_3]\text{Mn}(\text{NCS})_3$ ⁸¹ and $[1,3\text{-Im}]\text{Mn}(\text{NCS})_3$ ($1,3\text{-Im} = 1\text{-ethyl-3-methyl imidazolium}$),⁹⁴ however, there are no magnetic studies of these materials.

The ambient temperature structure of $[\text{Na}(\text{OH}_2)_3]\text{Mn}(\text{NCS})_3$ adopts the trigonal space group $P\bar{3}$, determined from single crystal X-ray data.⁸¹ The $[\text{Mn}(\text{NCS})_3]^-$ framework forms two-dimensional layers, with the edge-sharing Mn^{2+} octahedra connected to the three adjacent Mn^{2+} *via* two $\mu_{1,3}\text{NCS}$ ligands (Fig. 2.1a). The layers lie in the ab plane and are stacked along the c axis. The Mn^{2+} ions have the special position $(\frac{2}{3}, \frac{1}{3}, z)$, (Wyckoff site $2d$) and are located on three-fold rotation symmetry operators. Within the voids of the honeycomb network are the $[\text{Na}(\text{OH}_2)_3]^+$ cations. These stack in the c direction with alternating between a Na^+ cation and water molecules which coordinate to the Na^+ above and below them (Fig. 2.1b).

Although the structure of this compound is known, there are no reports on its physical properties. It has been noted that the compound is hygroscopic,⁸¹ which makes this compound more challenging to handle.

In this chapter, I report the synthesis of $[\text{Na}(\text{OH}_2)_3]\text{Mn}(\text{NCS})_3$ single crystals, which were of suitable size and quality for neutron diffraction measurements. In addition, a method was established to store the crystals without degradation. The bulk magnetic properties and magnetic structure have been explored through a combination of magnetometry, low temperature neutron diffraction and second harmonic generation measurements.

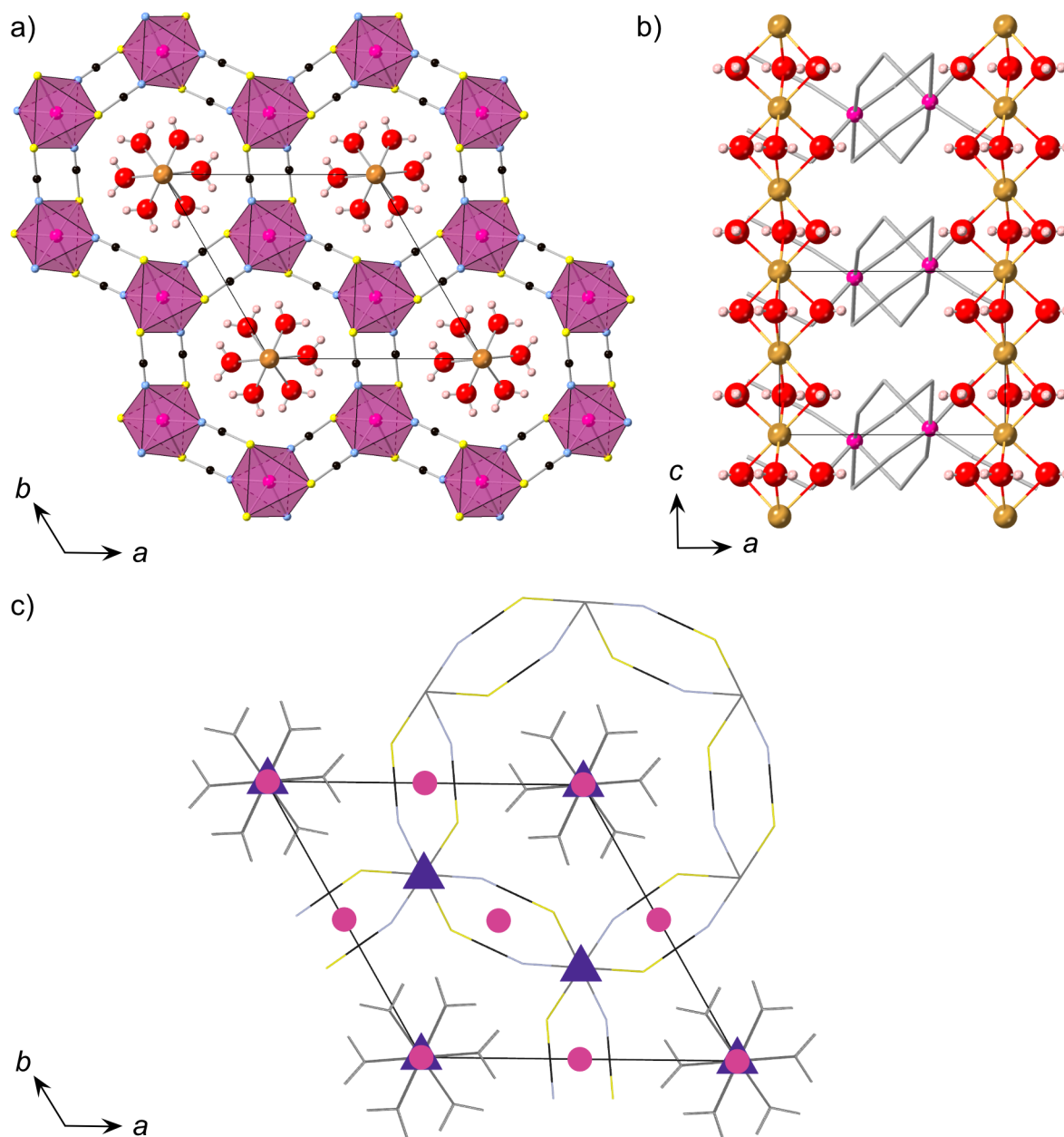


Figure 2.1: The structure of $[\text{Na}(\text{OH}_2)_3]\text{Mn}(\text{NCS})_3$ from data collected with the D19 diffractometer (ILL). a) The structure viewed along the c axis. b) View of the $[\text{Na}(\text{OH}_2)_3]^+$ cation chains. The $[\text{Mn}(\text{NCS})_3]^-$ framework has been shown as a wireframe for clarity. c) Space group diagram for the $P\bar{3}$ symmetry operators, with the structure shown as a wireframe. The symmetry elements are identified as centre of inversions (pink circles) and proper three-fold rotations (purple triangles). Mn = pink octahedra, N = blue, C = black, S = yellow, Na = orange, O = red, H = pale pink.

2.3 Results

2.3.1 Synthesis

I synthesised $[\text{Na}(\text{OH}_2)_3]\text{Mn}(\text{NCS})_3$ from salt metathesis of manganese(II) sulfate and sodium thiocyanate with barium thiocyanate in aqueous solution in a 1 : 1 : 1 ratio. On removing the solvent, a pale green-yellow powder was obtained. It is deliquescent in ambient conditions, however, it was found that a hydrated sample can be recreated once it has dissolved by heating at no more than 60°C . At the other end of the spectrum, it is also sensitive to dry environments, particularly where moisture is being actively removed (such as vacuum desiccators filled with silica gel) and will decompose, likely forming $\text{Mn}(\text{NCS})_2$ and NaNCS , although the lack of crystallinity in the resulting powders prevented confirmation of this.

2.3.2 Recrystallisations

As $[\text{Na}(\text{OH}_2)_3]\text{Mn}(\text{NCS})_3$ is sensitive to ambient humidity, deliquescent and decomposes at temperatures above 80°C , some planning was necessary to identify a route to obtain crystal of the compound.

Initially, slow evaporation recrystallisation from an aqueous solution was attempted. As the solution was concentrated *in vacuo*, a colour change was observed from transparent, to pale pink, pale green and eventually to aqua blue (Fig. 2.2).

Concentrating the solution to a pale green colour and leaving the water to slowly evaporate was not successful. Due to the hygroscopic nature of the compound, it would absorb water faster than water would evaporate from the solution, meaning that over time the solution became less concentrated. This method never produced single crystals.



Figure 2.2: Variations in colour of aqueous $[\text{Na}(\text{OH}_2)_3]\text{Mn}(\text{NCS})_3$ at varied concentrations. Comparative concentrations of a) too dilute, b) ideal concentration, and c) too concentrated solutions.

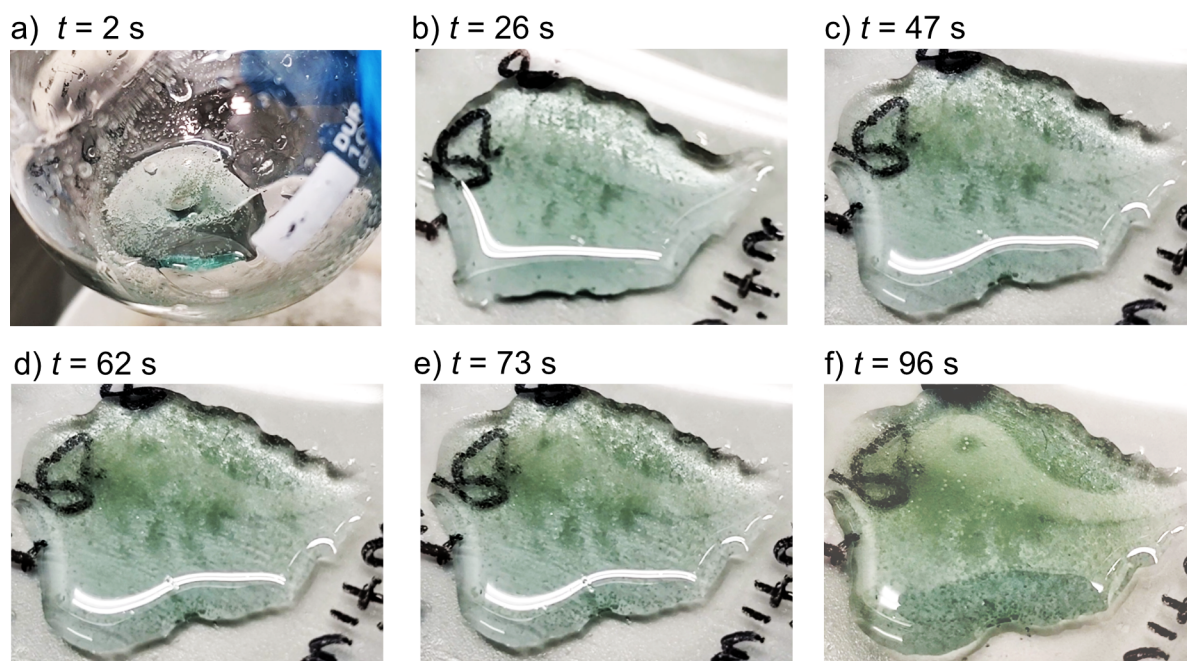


Figure 2.3: Following an over-concentrated aqueous solution of $[\text{Na}(\text{OH}_2)_3]\text{Mn}(\text{NCS})_3$ with time. The solution becoming more cloudy or opaque is an indication of where the crystals are growing. Images taken at t seconds after removing the vacuum.

Due to the high solubility of the compound, it was generally not possible to completely remove the solvent *in vacuo*. However, it was possible to ‘over-concentrate’ the solution, in which case well defined single crystals were not obtained. This stage could be identified if the solution was an intense aqua blue colour (Fig. 2.2c). In this scenario, once the solution was removed from the rotary evaporator, crystals would grow to approximately $100\ \mu\text{m}$, nucleating on the surface of the bulk solution. This growth would occur over 1 to 2 min and could be followed by eye (Fig. 2.3). Although it is appealing to be able to watch crystals grow on such a short time scale, these did not produce large enough crystals, or crystals of good quality to use for neutron experiments.

In the ‘over-concentrated’ stage, it was observed that the compound had a great predisposition to nucleating on any surface it was presented with. More specifically, it would nucleate from vibrations if the solution was moved, on dust and also on glass pipettes—meaning a small trail of crystals could be made by slowly moving a pipette through an over-concentrated solution. The solution also had a propensity to nucleating on other crystals. This led to the next method for recrystallisation: serial seeding.



Figure 2.4: Stages of serial seeding recrystallisation for aqueous solutions of $[\text{Na}(\text{OH}_2)_3]\text{Mn}(\text{NCS})_3$. Crystals are shown after a) 2 days, b) 5 days and c) 9 days. d) A crystal with a 5 mm scale bar for reference.

In this method, the approach was to take advantage of the ease of nucleating, whilst monitoring the concentration of the solution. The solution was concentrated *in vacuo* until the pale green colour was at its most intense, but had not turned blue yet (Fig. 2.2b). This occurred at approximately the same pressure of the rotary evaporator, 16 – 20 mbar depending on quantity of liquid and volume of the glassware used, however, this will probably vary between instruments. The resulting solution was covered and cooled at 7°C for 24 h. Despite the recrystallisations being covered, the solutions absorbed ambient moisture at a faster rate than water evaporated from the recrystallisations, meaning the solution became less concentrated over time. After 24 h, the largest, regular-hexagonal crystals were set aside, whilst the rest of the solution was re-concentrated under reduced pressure. Once the solution was pale green in colour again, the newly obtained crystals were placed in the solution before once again cooling the crystal for 24 h. This process was repeated daily for 9 days at which point pale green, hexagonal crystals of $[\text{Na}(\text{OH}_2)_3]\text{Mn}(\text{NCS})_3$ were collected, suitable for neutron diffraction experiments ($4 \times 3 \times 1 \text{ mm}^3$, Fig. 2.4d).

2.3.3 Prolonging the longevity of a crystal

Since crystals of $[\text{Na}(\text{OH}_2)_3]\text{Mn}(\text{NCS})_3$ had been obtained, it was necessary to find a method to store the crystals without them degrading. In ambient conditions the air contained too much water vapour, however, in a desiccator, the environment was too dry and the sample would become too dry and crumble. In order to safely store the crystals, an environment of intermediate humidity was needed.

To control the humidity of the environment, saturated aqueous solutions of varying salts were explored. This method exploits the differences in solubilities of varying salts to control the water vapour in equilibrium with the saturated solution in a closed environment. The humidities of the closed environment is quoted as a percentage relative to ambient humidity (100 %). To identify the optimal conditions for storing, several environments were set up at relative humidities of 54 % ($\text{Mg}(\text{NO}_3)_2(\text{aq.})$), 39 % ($\text{NaI}(\text{aq.})$), 32

% ($\text{CaCl}_{2(\text{aq.})}$) and 23 % ($\text{KCH}_3\text{COO}_{(\text{aq.})}$).^{212,213}

At relative humidities of 39 % and above, the concentrated solution of $[\text{Na}(\text{OH}_2)_3]\text{Mn}(\text{NCS})_3$ lost its pale green colour and the volume of the liquid increased. At the other extreme, using a relative humidity of 23 %, the $[\text{Na}(\text{OH}_2)_3]\text{Mn}(\text{NCS})_3$ solution was dried completely over a period of three weeks. This atmosphere was too arid.

A relative humidity of 32 % was within the Goldilocks zone for the compound. In this environment, an aqueous solution remained the same colour, therefore suggesting the concentration had not increased or decreased. In addition, crystals stored at this humidity did not visibly degrade, based on their shape and colour. Up to the time of writing this paragraph, the crystals have been successfully stored in this environment for 15 months, in comparison to 1 week, where the crystal was stored in an Eppendorf tube with a small amount of the mother liquor.

This method should also, in theory, be possible to control the rate of water loss for a slow evaporation recrystallisation of $[\text{Na}(\text{OH}_2)_3]\text{Mn}(\text{NCS})_3$. Unfortunately, despite several attempts, I did not find an optimal relative humidity for this to work. If this did work, it would be significantly less labour intensive to grow crystals of the sample, which would be advantageous.

2.3.4 Magnetometry

To see if $[\text{Na}(\text{OH}_2)_3]\text{Mn}(\text{NCS})_3$ magnetically orders and its magnetic behaviour, susceptibility measurements were carried out in an applied field of 0.01 T, as well as isothermal magnetisation measurements at 2 K over the range $-5.00(1)$ to $+5.00(1)$ T.

The susceptibility increases on cooling the sample until a broad maximum is reached around 25 K. Below this temperature, the susceptibility decreases until a sharp drop at the ordering temperature, $T_N = 18.1(6)$ K (Fig. 2.5a, b). The increase in the susceptibility below the T_N either arises from a small ferromagnetic component of the magnetic structure, or is as a result of hydrated impurities in the sample. The Curie-Weiss law was fitted to the high temperature region of the data ($200 < T < 300$ K), giving a Curie-Weiss temperature $\theta_{\text{CW}} = -27(1)$ K. The Curie constant, C , is $3.88(3)$ emu K mol⁻¹, which is lower than the spin only value, $C_{\text{spin only}} = 4.375$ emu K mol⁻¹ (Fig. 2.5d). This gives an effective moment of $\mu_{\text{eff.}} = 5.6 \mu_{\text{B}}$, lower than the spin only moment $\mu_{\text{spin only}} = 5.92 \mu_{\text{B}}$, expected for high spin Mn^{2+} .

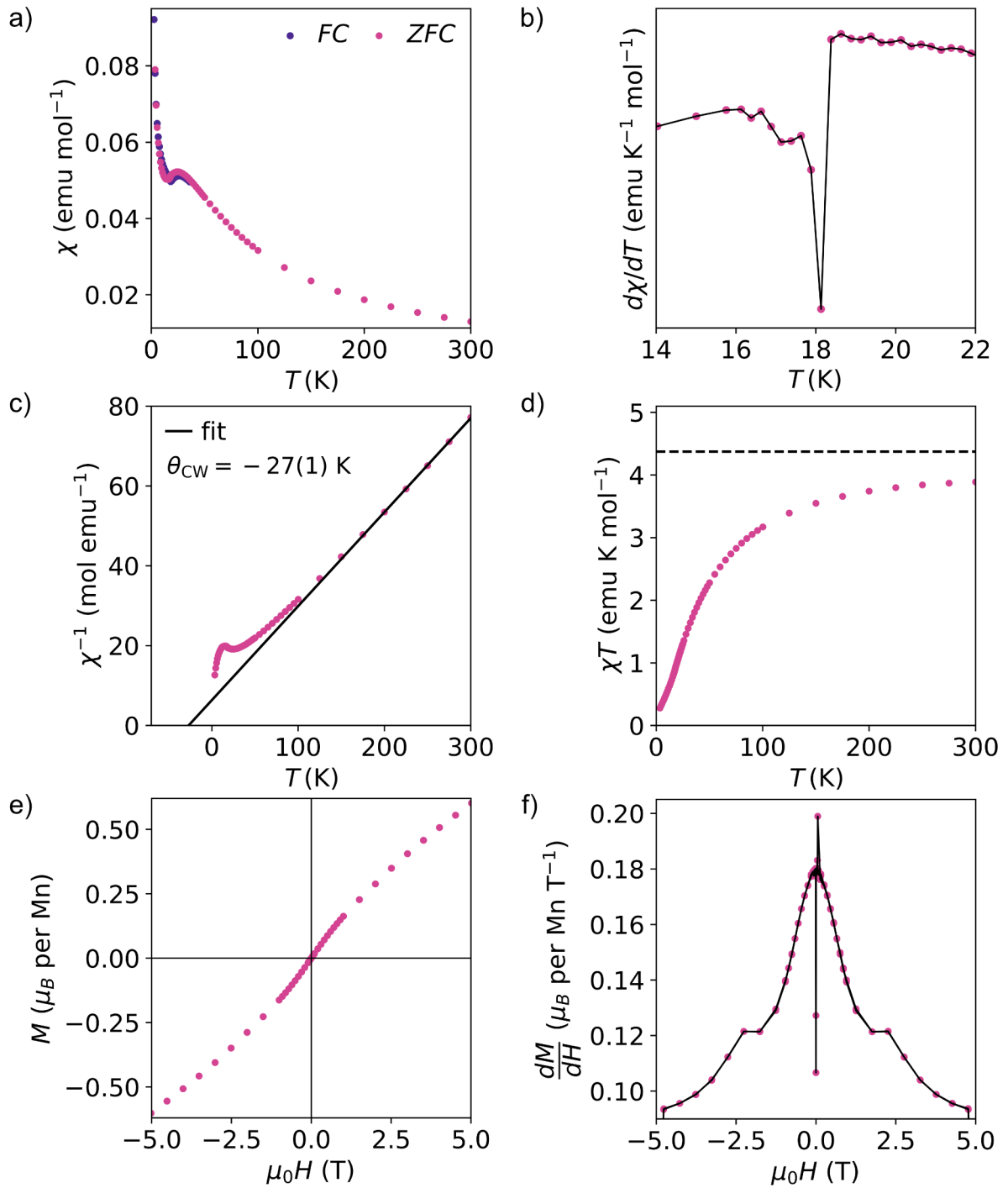


Figure 2.5: Magnetisation data for $[\text{Na}(\text{OH}_2)_3]\text{Mn}(\text{NCS})_3$. a) The field-cooled (*FC*, purple circles) and zero-field cooled (*ZFC*, pink circles) susceptibilities. b) The derivative of the susceptibility. c) The inverse magnetic susceptibility, with a Curie-Weiss fit (black line) where $200 < T < 300$ K. d) Variable temperature magnetic susceptibility product. The high temperature spin only Curie constant $C_{\text{spin only}} = 4.375$ emu K mol $^{-1}$ is shown with a dashed line. e) Isothermal magnetisation data, measured between $+5.00(1)$ and $-5.00(1)$ T at 2 K. f) The derivative of the isothermal magnetisation.

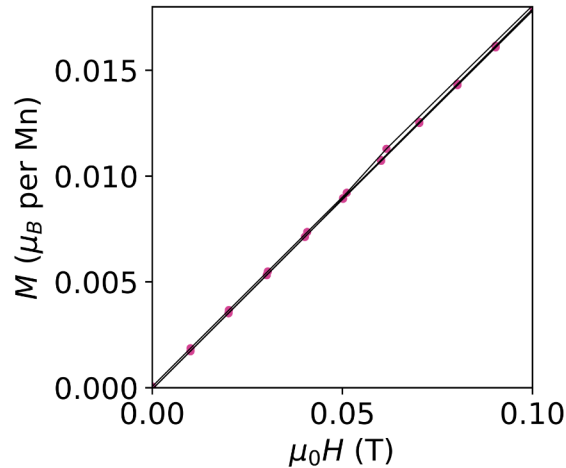


Figure 2.6: Isothermal magnetisation data shown between 0.00 and 0.01 T for $[\text{Na}(\text{OH}_2)_3]\text{Mn}(\text{NCS})_3$. The black line joins the data points and acts as a guide, showing a lack of conclusive hysteresis.

The isothermal data show an increase in the magnetisation up to $0.60(1) \mu_B$ per Mn at $5.00(1)$ T (Fig. 2.5e). There is no observable hysteresis within the error limits of the measurements (Fig. 2.6). A change in the gradient at $2.0(3)$ T suggests that above this applied magnetic field $[\text{Na}(\text{OH}_2)_3]\text{Mn}(\text{NCS})_3$ adopts a second magnetic structure.

The combination of the negative θ_{CW} and lack of hysteresis in the isothermal magnetisation data, suggests that $[\text{Na}(\text{OH}_2)_3]\text{Mn}(\text{NCS})_3$ magnetically orders as an antiferromagnet. If there is a ferromagnetic component, suggested by the up-turn in the low temperature susceptibility data, the compound is ordering as a weak ferromagnet (canted antiferromagnet), with a very small ferromagnetic component.

2.3.5 Single crystal neutron diffraction

To determine the low temperature nuclear and magnetic structure of $[\text{Na}(\text{OH}_2)_3]\text{Mn}(\text{NCS})_3$, single crystal neutron diffraction measurements were performed (D19, ILL, crystal dimensions: $4 \times 3 \times 1$ mm³). Data were collected above (25 K) and below (2 K) the ordering temperature of $T_N = 18.1(6)$ K.

The data at 25 K ($\lambda = 1.45$ Å, 631 independent reflections) could be integrated with the same space group as the reported structure at ambient temperature, $P\bar{3}$. The atom positions and anisotropic displacement parameters were refined freely, with a final $\chi^2 = 23.20$. From each OH_2 molecule one hydrogen is directed towards a nitrogen, whilst the other is positioned towards a sulfur atom with $\angle \text{O}-\text{H}\cdots\text{N} = 153.291(2)^\circ$ and $\angle \text{O}-\text{H}\cdots\text{S} = 164.258(2)^\circ$. The distances of the hydrogens to the acceptor atoms are $d_{\text{H1}\cdots\text{N}} = 2.355(5)$ Å and $d_{\text{H2}\cdots\text{S}} = 2.326(7)$ Å.

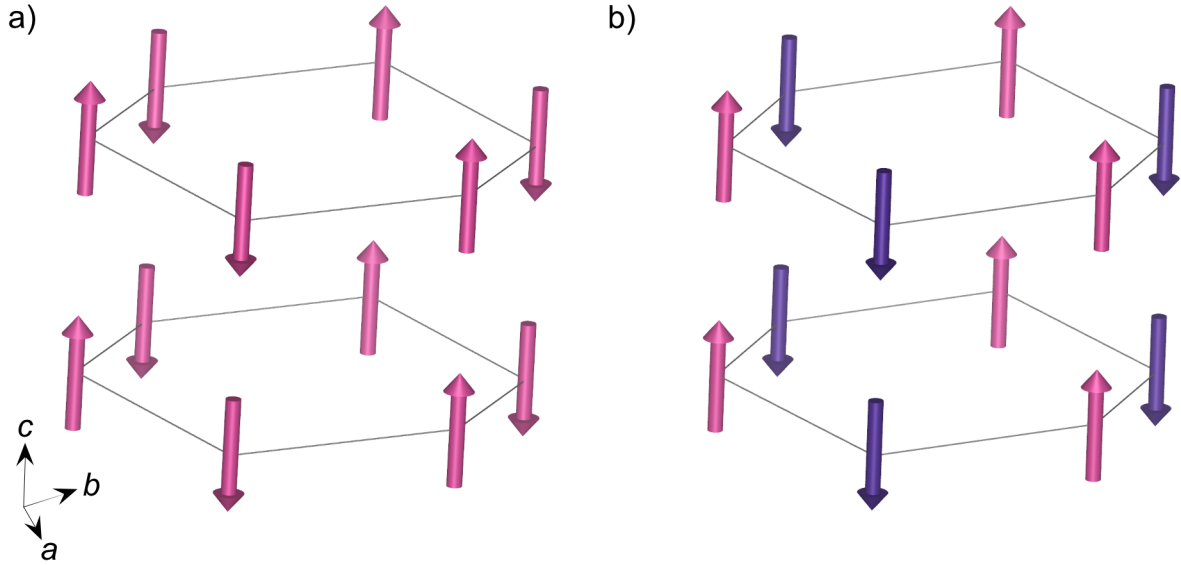


Figure 2.7: The arrangement of the magnetic moments in the a) $P\bar{3}'$ magnetic space group with one symmetry distinct moment (pink), and b) $P3$ magnetic space group with two symmetry distinct Mn sites (pink and purple), with moment sizes of $-4.0(2)$ and $3.9(2) \mu_B$.

From the low temperature data collection at 2 K, all the Bragg reflections (651 unique reflections) could be indexed by the nuclear space group $P\bar{3}$, so that the propagation vector was determined to be $\mathbf{k} = (0, 0, 0)$. The potential magnetic space groups with this propagation vector were identified using the Bilbao Crystallographic Server.^{12,51,214} These were determined to be $P\bar{3}'$, $P\bar{3}$, $P3$, $P\bar{1}'$, $P\bar{1}$ and $P1$ in BNS notation,²¹⁴ in descending order of symmetry.

Initially the three maximal symmetry magnetic space groups were considered: $P\bar{3}'$, $P\bar{3}$ and $P3$. Of these, the $P\bar{3}$ magnetic space group only allows for a collinear ferromagnetic order. This does not match the magnetometry results of antiferromagnetic or weak ferromagnetic orderings, so $P\bar{3}$ could be discarded as an unsuitable model. $P\bar{3}'$ permits only collinear antiferromagnetic order, whereas $P3$ can allow for antiferromagnetic orderings, although it is also possible for a ferromagnetic or ferrimagnetic arrangement of the moments.

Refinements were carried out with both the $P\bar{3}'$ and $P3$ space groups. The results of the refinements provided comparable models with similar refinement statistics, $\chi^2 = 9.49$ ($P\bar{3}'$) and $\chi^2 = 9.8$ ($P3$). The significant difference between these models is the loss of the inversion centres in the $P3$ space group. This results in two unique Mn sites, compared to one unique site in $P\bar{3}'$ (Fig. 2.7). The Mn atoms are positioned on a 3-fold rotation axis and, therefore, to retain the trigonal symmetry, the moments only have a collinear contribution along the c axis, not along the a or b axes. As a result, the $P\bar{3}'$ magnetic space group only permits antiferromagnetic ordering, with a refined moment size of $4.9(2) \mu_B$ per Mn (Fig. 2.8). In the $P3$ model, the magnitude of the two moments

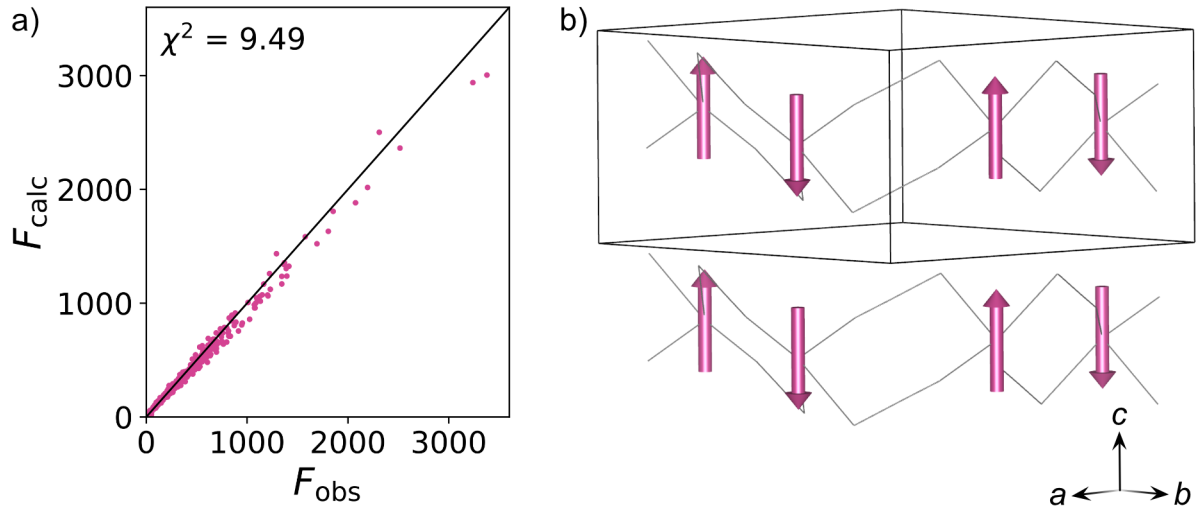


Figure 2.8: Results of the refinement in the $P\bar{3}'$ magnetic space group at 2 K (D19, ILL). a) F_{obs} against F_{calc} plot. b) The magnetic structure, showing the antiferromagnetic arrangement of moments (pink arrows). The $[\text{Mn}(\text{NCS})_3]^-$ framework is shown as a wireframe and $[\text{Na}(\text{OH}_2)_3]^+$ ions have been removed for clarity.

Table 2.1: Comparison of integration and refinement parameters for $[\text{Na}(\text{OH}_2)_3]\text{Mn}(\text{NCS})_3$ using the $P\bar{3}'$ and $P\bar{1}'$ models at 2 K. θ and ϕ are the angles in spherical coordinates (radians), where θ describes the inclination with respect to the c axis and ϕ describes the rotation around c . In the $P\bar{3}'$ space group, θ and ϕ are restricted by symmetry.

	$P\bar{3}'$	$P\bar{1}'$
a (Å)	10.0806(3)	10.084(3)
b (Å)	10.0806(3)	10.083(3)
c (Å)	6.2581(2)	6.258(2)
α (°)	90	89.97(2)
β (°)	90	90.03(2)
γ (°)	120	120.04(4)
χ^2	11.83	51.3
Moment (μ_{B})	4.9(2)	4.0(2)
θ (rad)	0	4(5)
ϕ (rad)	0	-40(70)
No. of independent reflections	651	873
No. of parameters	20	57
(Reflections)/(Parameters)	32.6	15.3

are $-3.4(3)$ and $5.4(2) \mu_B$. These moments were closely correlated, and were only stable during the refinements when the moments were constrained to refine between -5.0 and $5.0 \mu_B$. This resulted in moments of $-4.0(2)$ and $3.9(2) \mu_B$. Within error these moments have the same magnitude, although any uncompensated moment would result in a net magnetisation along the c axis.

It is possible that the compound experiences structural distortions along with the magnetic ordering, or that the moments are canted. In this case, the symmetry could be lowered from a trigonal space group to a triclinic one. Both magnetic space groups $P\bar{1}'$ and $P1$ permit antiferromagnetic correlations. To test this, the data were integrated with triclinic symmetry and the $P\bar{1}'$ model was refined against the data. The integrated data had a unit cell that was, within error, equivalent to the trigonal unit cell (Table 2.1). In this model, there is one symmetry distinct Mn site, with a moment magnitude of $4.1(2) \mu_B$. The moments point predominately along the c axis with the ferromagnetic canting occurring in the ab plane, however, the significantly large errors mean the direction cannot be precisely defined. For the refinement, $\chi^2 = 51.3$, which is larger than for either model with trigonal symmetry. Despite the lowering of symmetry, the refinement did not improve, potentially as a result of increasing the number of atoms in the unit cell (9 atoms in $P\bar{3}'$ to 21 atoms in $P\bar{1}'$), whilst the number of independent reflections did not increase proportionally. This resulted in a lower, although still reasonable, ratio of independent reflections to the number of refined parameters, where atom positions and magnetic sizes and angles were refined freely (where permitted by symmetry). The refinement in the $P\bar{1}'$ magnetic space group provided no indication that the structure distorts from its trigonal symmetry, through either the integrated lattice parameters or by the orientation of the moment. Therefore, magnetic ordering in a trigonal space group models the data more appropriately, so the triclinic magnetic space groups were discarded as possible solutions.

To follow the temperature dependence of selected Bragg reflections, data were collected between 2 and 25 K with 0.25 K steps. For the 100 Bragg reflection, the greatest intensity is at 2 K, decreasing until a constant intensity is reached at $18.3(3)$ K (Fig. 2.9a). This decrease in intensity on heating is characteristic of a magnetic Bragg reflection. Above $18.3(3)$ K, the outstanding intensity arises from diffraction from the nuclear structure. The intensity below the ordering temperature was fitted to the power law

$$M = A(T_N - T)^\beta, \quad (2.1)$$

where A is a proportionality constant, T_N is the ordering temperature and β is a critical exponent. For the 100 reflection, chosen as a reflection with one of the highest intensities at 2 K and significant decrease at 25 K, the fitted values were $\beta = 0.31(3)$ and $T_N =$

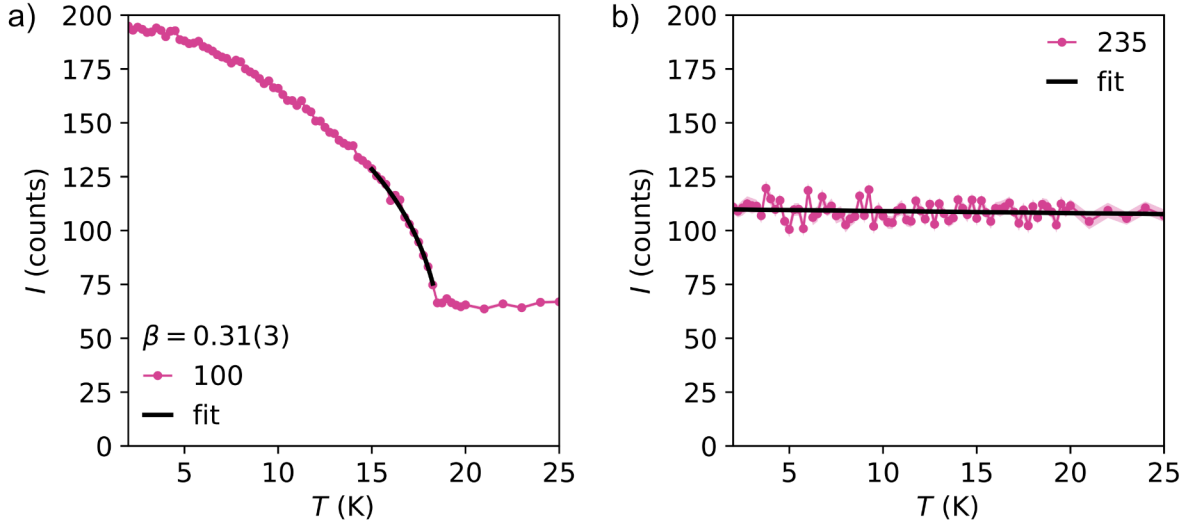


Figure 2.9: The temperature dependence of selected Bragg reflections for $[\text{Na}(\text{OH}_2)_3]\text{Mn}(\text{NCS})_3$ measured between 2 and 25 K (D19, Institut Laue Langevin). a) The 100 Bragg reflection which shows additional intensity from diffraction from the magnetic structure, fitted to a power law (black line), $\beta = 0.31(3)$. b) The 235 Bragg reflection fitted with a linear equation (black line) $I = 0(1)T + 109.9(3)$, showing, within error, no temperature dependence above and below the magnetic ordering temperature, $T_N = 18.1(6)$ K. The shaded regions denotes the errors.

18.94(7). This is between the expected values for a two-dimensional Ising antiferromagnet ($\beta = 0.125$) and a three-dimensional Heisenberg antiferromagnet ($\beta = 0.367$).²¹⁵ Other Bragg reflections, for example the 235 reflection, shows almost no change in intensity with temperature, suggesting there is no magnetic contribution to the intensity of this reflection (Fig. 2.9b).

At 2 K, the in-plane Mn \cdots Mn distance $d_{\text{Mn-Mn}} = 5.820(4)$ Å and the interlayer distance $d_{\text{Mn layer}} = 6.2581(2)$ Å. The Mn–N bond length is 2.146(2) Å and the Mn–S bond length is 2.693(2) Å. Similar to the 25 K measurements, at 2 K the position of the hydrogen atoms were located. The hydrogen bond network is not altered, with one hydrogen from each OH_2 interacting with a nitrogen acceptor, and the second hydrogen interacting with a sulfur of a different ligand (Fig. 2.10). The hydrogen bond distances are $d_{\text{H1}\cdots\text{N}} = 2.344(5)$ Å and $d_{\text{H2}\cdots\text{S}} = 2.332(4)$ Å. $\angle \text{O-H}\cdots\text{N} = 153.088(2)^\circ$ and $\angle \text{O-H}\cdots\text{S} = 163.607(2)^\circ$.

2.4 Second harmonic generation measurements

To determine if $[\text{Na}(\text{OH}_2)_3]\text{Mn}(\text{NCS})_3$ has inversion centres in its low temperature ($T < 18.1(6)$ K) structure, second harmonic generation (SHG) measurements were explored. SHG is a non-linear optical process where the incident light frequency is doubled as a result of combining two photons of the same incident energy. A requirement for this phenomenon is that the sample does not have inversion symmetry. Therefore, obtain-

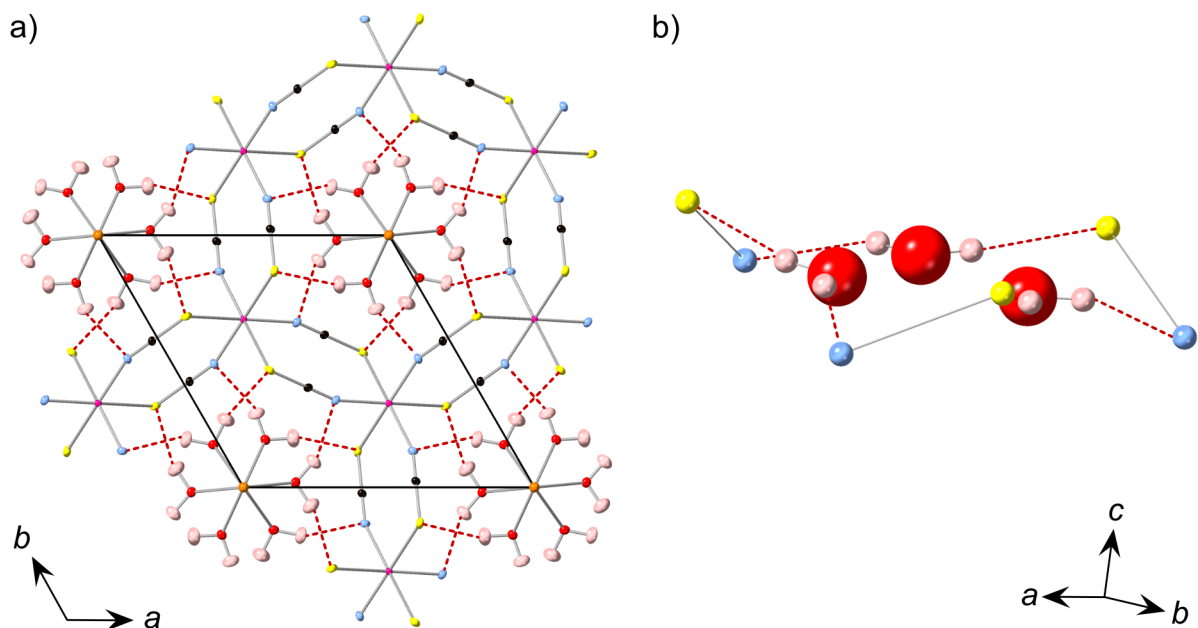


Figure 2.10: The 2 K nuclear structure of $[\text{Na}(\text{OH}_2)_3]\text{Mn}(\text{NCS})_3$ (D19, Institut Laue Langevin). The hydrogen bonding network (dashed red lines) is identified for $\text{H1} \cdots \text{N}$ and $\text{H2} \cdots \text{S}$. a) Viewed along the c axis. Ellipsoids are shown with 50 % probability. b) The hydrogen bond interactions between three OH_2 molecules and the surrounding thiocyanate ligands. The carbon atoms have been removed for clarity. Mn = pink, N = blue, C = black, S = yellow, O = red, H = pale pink.

ing a signal from the SHG measurements would support a magnetic model with weak ferromagnet ordering and $P3$ magnetic space group, whilst no signal would suggest an antiferromagnet structure with the centrosymmetric $P\bar{3}'$ magnetic space group.

Low temperature SHG measurements are challenging to carry out, Dr Andrew Burnett (University of Leeds) agreed to perform these experiments for $[\text{Na}(\text{OH}_2)_3]\text{Mn}(\text{NCS})_3$. Low temperature (4 K) SHG data were collected with incident wavelengths of 800 and 400 nm. From the initial measurements, there was no evidence of signal generation of 400 or 200 nm light, suggesting the compound is centrosymmetric. To further probe the sample, it is, in theory, possible to move to lower energies to directly measure signal from the magnetic excitations. However, it is likely that the magnetic signal is weaker than the expected signal from probing the nuclear structure, so it is not an assured method to improve detection.

The results suggest that $[\text{Na}(\text{OH}_2)_3]\text{Mn}(\text{NCS})_3$ retains its inversion centre, therefore ordering in the $P\bar{3}'$ magnetic space group.

2.5 Discussion

The $[\text{Mn}(\text{NCS})_3]^-$ layers of $[\text{Na}(\text{OH}_2)_3]\text{Mn}(\text{NCS})_3$ stack uniformly along the c axis such that for a given atom, adjacent layers have the same absolute positions for the atom

on each layer. This is in contrast to its closest non-molecular compound, NaMnCl_3 .²¹⁶ Despite having comparable in-plane connectivity, edge-sharing Mn octahedra bridged by two anions, the layers in NaMnCl_3 are shifted by $\frac{1}{3}a + \frac{2}{3}b$ in adjacent layers. This leads to ABC type stacking (Fig. 2.11) with the Na^+ cations intercalated between the layers. The hydrated sodium cations in $[\text{Na}(\text{OH}_2)_3]\text{Mn}(\text{NCS})_3$ are coordinated not as individual $[\text{Na}(\text{OH}_2)_3]^+$ entities, but as chains which propagate perpendicular to the layers (Fig. 2.10b). The steric bulk arising from this arrangement likely acts as a template for the $[\text{Mn}(\text{NCS})_3]^-$ framework to build around the cations. The $[\text{Na}(\text{OH}_2)_3]^+$ cations are an optimal size to be positioned within the hexagonal voids, whilst forcing successive layers to stack directly in line with each other. The hydrogen bond network anchors the countercation to the framework, with the interactions switching between nitrogen and sulfur acceptor atoms on alternating layers. A similar stacking arrangement can be observed in $[1,3\text{-Im}]\text{Mn}(\text{NCS})_3$ (1,3-Im = 1-ethyl-3-methyl imidazolium),⁹⁴ with the structure adopting two-dimensional honeycomb layers of $[\text{Mn}(\text{NCS})_3]^-$ and the 1,3-Im cations positioned within the centre of the hexagonal voids. There are no available hydrogen bond donors from the 1,3-Im cations, and the larger steric bulk of the cations distorts the framework so that the honeycomb network forms irregular hexagons. Including a cation which penetrates the framework layers may also reduce sliding of layers, which is commonly observed in the two dimensional halide materials, identified by diffuse scattering which was not observed in these diffraction experiments.²¹⁷

The propagating chain arrangement of $[\text{Na}(\text{OH}_2)_x]^+$ countercations is not unique to $[\text{Na}(\text{OH}_2)_3]\text{Mn}(\text{NCS})_3$, and similar connectivity has been observed in halide compounds, such as $[\text{Na}_2(\text{OH}_2)_6]\text{ReCl}_6$ ²¹⁸ and $[\text{Na}(\text{OH}_2)_2]\text{AuCl}_4$.²¹⁹ In both these compounds the Cl^- act as hydrogen bond acceptors for the H_2O molecules, but also electrostatically interact with the Na^+ cation, potentially taking the position of a coordinating H_2O . For example, in $[\text{Na}_2(\text{OH}_2)_6]\text{ReCl}_6$ each Na^+ is coordinated to five OH_2 and one Cl^- . Perhaps the sterically bulkier NCS^- ligands are prevented from interacting with the Na^+ ions directly, permitting the six H_2O molecules to coordinate with a Na^+ cation.

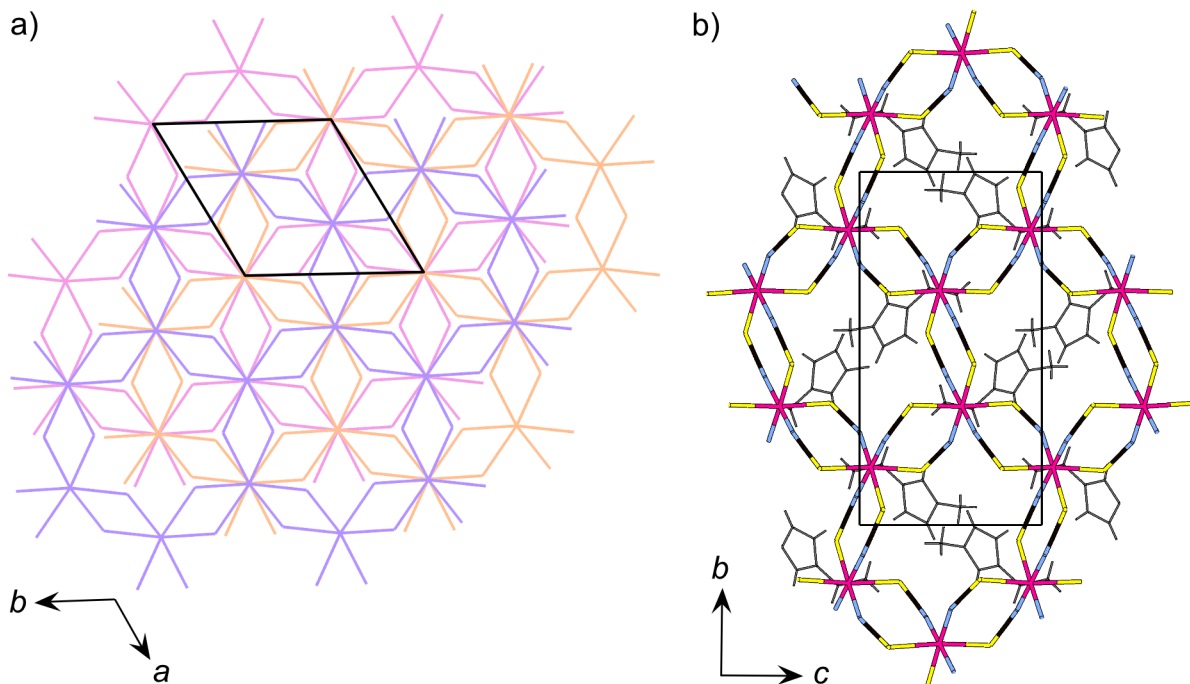


Figure 2.11: a) Wireframe representation of the $[\text{MnCl}_3]^-$ framework stacking in NaMnCl_3 .²¹⁶ The three layers (pink, purple and orange) show the three positions of the ABC stacking within the unit cell (black lines). The Na^+ cations have been removed for clarity, which are positioned above Cl^- anions. b) Structure of $[\text{1,3-Im}]\text{Mn}(\text{NCS})_3$.⁹⁴ The irregular hexagonal framework is shown as a wireframe and the counteranions are shown as grey wireframes for clarity. Colour for framework atoms, Mn = pink, N = blue, C = black, S = yellow.

The closest halide counterpart to $[\text{Na}(\text{OH}_2)_3]\text{Mn}(\text{NCS})_3$, NaMnCl_3 , orders at $T_N = 6.5$ K with ferromagnetic layers which are coupled antiferromagnetically.²⁰⁴ $[\text{Na}(\text{OH}_2)_3]\text{Mn}(\text{NCS})_3$ has an ordering temperature almost three times as high as NaMnCl_3 ($T_N = 18.1(6)$ K). In addition, the magnetic correlations in this compound, $|\theta_{\text{CW}}| = 27(1)$ K, are stronger than those indicated in NaMnCl_3 , $|\theta_{\text{CW}}| = 4.2$ K. Despite NaMnCl_3 having the shorter in-plane superexchange pathway (Mn–Cl–Mn compared to Mn–NCS–Mn), the magnetic pathways are weaker. This could be related to d-orbital occupancy (t_{2g} vs e_g), which can induce competition between ferromagnetic and antiferromagnetic exchange depending on the extent of the orbital overlap and angle of the metal–ligand orbitals in both halide^{169,220} and thiocyanate frameworks.⁸⁰

Fitting an exponential to the intensities of the temperature dependent Bragg reflections gives $\beta = 0.31(3)$. This value is lower than an ideal three-dimensional Heisenberg magnet ($\beta = 0.367$),²¹⁵ but is similar to layered halide materials such as FeBr_3 ($\beta = 0.324$),²⁰³ NiCl_2 ($\beta = 0.27$)²²¹ and FeCl_2 ($\beta = 0.29$).²²² Since $[\text{Na}(\text{OH}_2)_3]\text{Mn}(\text{NCS})_3$ does not show evidence of magnetic frustration, the lowered value of β may arise due to the larger Mn···Mn interlayer separation, $d_{\text{Mn-Mn}} = 6.2581(2)$ Å (2 K). The steric bulk of the $[\text{Na}(\text{OH}_2)_3]^+$ cations may act to prevent shorter interlayer Mn···Mn distances, preventing stronger interlayer correlations. This could be further investigated through

computational calculations or experimental inelastic neutron diffraction data to explore the interlayer interactions of the compound.

It is worth noting the implications if $[\text{Na}(\text{OH}_2)_3]\text{Mn}(\text{NCS})_3$ adopts $P3$ magnetic symmetry (2 uncompensated moments, Fig. 2.7b) rather than the $P\bar{3}'$ space group. In the $P3$ symmetry, the inversion centre has been lost, resulting in a polar space group. This would permit $[\text{Na}(\text{OH}_2)_3]\text{Mn}(\text{NCS})_3$ to be categorised as a Type II multiferroic. Multiferroics exhibit the coexistence of long-range magnetic and electric orderings. Type II multiferroics undergo the loss of inversion centres through the onset of magnetic ordering, therefore breaking the symmetry of the centrosymmetric structure observed in the paramagnetic state.²²³ This consequently induces ferroelectricity which is strongly coupled with the magnetism. Generally, type II multiferroics adopt complex magnetic orderings, for example helical incommensurate states,¹²⁸ or with structural triangular lattice arrangements which introduce frustration. The latter is particularly prevalent in low dimensional magnetic structures, such as $\text{Sr}_3\text{NiTa}_2\text{O}_9$ ¹²⁹ and $\text{Ba}_3\text{MnNb}_2\text{O}_9$.²²⁴ It would be unusual for a collinear magnetic ordering to induce this behaviour, and even more so for a molecular framework.

To induce the switching between a centrosymmetric and non-centrosymmetric space group, there should be a driving force inducing the change. In the nuclear structure of $[\text{Na}(\text{OH}_2)_3]\text{Mn}(\text{NCS})_3$ there is one Mn environment. Therefore in the magnetic structure, without further distortions or changes to the nuclear structure, there is little basis to account for the Mn environments adopting two symmetry distinct environments or having moments which are not of equal magnitude. In addition, the negative result from the SHG measurements further supports the centrosymmetric $P\bar{3}'$ model.

2.6 Conclusions

Low temperature structural and magnetic properties have been reported for $[\text{Na}(\text{OH}_2)_3]\text{Mn}(\text{NCS})_3$. A single crystal suitable for neutron diffraction was grown and a method was developed to store the sample to avoid degradation through the use of humidity controlled environments. Neutron diffraction data permitted the hydrogen atoms to be located, which showed that hydrogen bonding network influences the position of the countercations and the connectivity of the framework. The compound magnetically orders in the $P\bar{3}'$ magnetic space group. Despite potential ambiguity arising from likely a hydrated paramagnetic impurity in the magnetometry data, the neutron diffraction data could be complemented by second harmonic generation measurements to directly probe the centrosymmetric nature of the compound in its magnetically ordered state.

This work has looked at the magnetic ordering of a hexagonal thiocyanate framework. To further probe these materials, investigations into honeycomb frameworks incorporating metal ions which exhibit magnetic anisotropy may lead to more complicated or non-collinear magnetic orderings. A transition metal, such as Ni^{2+} , which generally forms thiocyanate frameworks which are not sensitive to ambient humidity, may also lead to more straightforward methods to grow and store crystals in future studies as well.

2.7 Experimental

2.7.1 Synthesis

$\text{Ba}(\text{NCS})_2 \cdot 3\text{H}_2\text{O}$ was heated at 50°C until a constant mass of $\text{Ba}(\text{NCS})_2$ was obtained (approx. 48 hrs). Aqueous solutions of $\text{Ba}(\text{NCS})_2$ (4.87 g, 19.2 mmol, approx. 50 mL) and $\text{MnSO}_4 \cdot \text{H}_2\text{O}$ (3.25 g, 19.2 mmol, approx. 15 mL) were combined and stirred. A white precipitate was filtered from a pale pink solution. The solution was heated just below boiling and a dry beige powder of $\text{Mn}(\text{NCS})_2$ was collected (2.24 g, 13.1 mmol, 68 %). The $\text{Mn}(\text{NCS})_2$ was dissolved in distilled H_2O (approx. 15 mL) and NaSCN (1.06 g, 13.1 mmol) was added and dissolved in the solution and stirred overnight. The solution was concentrated *in vacuo*, until a pale green-yellow powder of $[\text{Na}(\text{OH}_2)_3]\text{Mn}(\text{NCS})_3$ was obtained.

To obtain single crystals, the method of ‘serial recrystallisation’ was used. Aqueous solutions of $[\text{Na}(\text{OH}_2)_3]\text{Mn}(\text{NCS})_3$ were concentrated *in vacuo* until the solution was pale green. The solution was covered and cooled at 7°C for 24 h, with care not to create vibrations or knock the sample. From the crystals obtained, the largest crystal was removed, whilst the rest of the mixture was redissolved in distilled H_2O . The solution was concentrated *in vacuo* until the solution was a pale green colour. The selected crystal was placed in the solution and the mixture was covered and cooled at 7°C for 24 h. This process was repeated daily for 9 days at which point a green, hexagonal plate-shaped crystal of $[\text{Na}(\text{OH}_2)_3]\text{Mn}(\text{NCS})_3$ was collected ($4 \times 3 \times 1 \text{ mm}^3$).

2.7.2 Magnetic Measurements

Measurements of the magnetic susceptibility were carried out by Dr Matthew Cliffe (University of Nottingham) and myself on $[\text{Na}(\text{OH}_2)_3]\text{Mn}(\text{NCS})_3$ (9.29 mg) using a Quantum Design Magnetic Property Measurements System (MPMS) 3 Superconducting Quantum Interference Device (SQUID) magnetometer. The zero-field-cooled and field-cooled sus-

ceptibility was measured in an applied field of 0.01 T over the temperature range 2 – 300 K. As $M(H)$ is linear in this field, the small-field approximation for the susceptibility, $\chi(T) \simeq \frac{M}{H}$, where M is the magnetisation and H is the magnetic field intensity, was taken to be valid.

Isothermal magnetisation measurements were carried out at 2 K over the field range -5 to $+5$ T. Data were corrected for diamagnetism of the sample using Pascal’s constants.⁴¹

2.7.3 Single crystal neutron diffraction

Monochromatic single crystal neutron diffraction data were collected on the four-circle D19 diffractometer at the Institut Laue Langevin (ILL) Grenoble, France, by Dr Laura Cañadillas Delgado (ILL), Dr Oscar Fabelo (ILL), Dr Matthew Cliffe and myself. Neutrons with a wavelength of 1.456 Å were provided by a flat Cu monochromator using the 220 reflection at $2\theta_M = 69.91^\circ$ take-off angle. The sample was placed in a closed-circuit displax cooling device, which was operated following a ramp of 2 K min⁻¹. Measurements were taken at 2 and 25 K. In addition, measurements were taken between 2 and 20 K in 0.25 K steps, and between 20 and 25 K in 1 K steps, following selected reflections. The sample was wrapped in aluminium foil with a small amount of grease before being mounted to avoid direct contact with the glue which can degrade the sample.

NOMAD software from the ILL was used for data collection.²²⁵ Unit cell determinations were performed using PFIND and DIRAX programs, and processing of the raw data was applied using RETREAT, RAFD19 and Int3D programs.^{226–229} The data were corrected for the absorption of the low-temperature device using the D19ABS program²³⁰ and for the size and composition of the crystal. Refinements of the nuclear and magnetic model were completed using the FullProf program.³⁷

2.7.4 Second harmonic generation measurements

Second harmonic generation measurements were performed by Dr Andrew Burnett (University of Leeds). The crystal was mounted between two Cu plates, which was clamped onto a Cu cold finger. It was placed in an Oxford instrument microstat-He and cooled to 4 K. An incident laser of $\lambda = 800$ nm (40 fs pulses, 1 KHz rep. rate) was generated by a Spectra-Physics Spitfire system. A Thorlabs band pass filter was used, blocking light above 450 nm. Additional measurements were carried out at 400 nm, generated by a Beta barium borate (BBO) crystal.

2.8 Appendix

Table 2.2: Single crystal experimental details for $[\text{Na}(\text{OH}_2)_3]\text{Mn}(\text{NCS})_3$ determined from neutron diffraction at 25 K (D19, Institut Laue Langevin)

Crystal data	$[\text{Na}(\text{OH}_2)_3]\text{Mn}(\text{NCS})_3$
Chemical formula	$\text{C}_3\text{MnN}_3\text{S}_3\text{H}_6\text{NaO}_3$
M_r	306.22
Temperature (K)	25
λ (Å)	1.456
Radiation type	Neutron
Crystal system	Trigonal
Space group	$P\bar{3}$
a (Å)	10.0384(3)
b (Å)	10.0384(3)
c (Å)	6.2313(2)
V (Å ³)	543.79(8)
Z	2
μ (mm ⁻¹)	0.029
Crystal size (mm)	$4 \times 3 \times 1$
Data collection	
Diffractometer	D19
No. of measured reflections	1942
No. of independent reflections	632
No. of observed reflections [$I > 2\sigma(I)$]	628
R_{int}	0.0534
$(\sin \theta / \lambda)_{\text{max}}$ (Å ⁻¹)	0.5992
Data completeness	0.959
Refinement	
$R[F^2 > 2\sigma(F^2)], \omega R(F^2)$	0.090, 0.094
No. of reflections	1942
No. of parameters	65

Chapter 3

Non-collinear magnetism in the post-perovskite thiocyanate frameworks $\text{CsM}(\text{NCS})_3$

3.1 Summary

- Post-perovskites, related to the perovskite family, are AMX_3 materials with frameworks built from two-dimensional layers from corner- and edge-sharing octahedra.
- $\text{CsM}(\text{NCS})_3$ $M = \text{Mn}, \text{Co}, \text{Ni}$ have been synthesised and characterised with single crystal diffraction (X-rays and neutrons) and bulk magnetisation measurements.
- $\text{CsNi}(\text{NCS})_3$ and $\text{CsCo}(\text{NCS})_3$ order as weak ferromagnets with magnetometry data suggesting canting angles of 6.7° and 15.3° . This was confirmed for $\text{CsNi}(\text{NCS})_3$ by single crystal and powder neutron diffraction measurements.
- $\text{CsMn}(\text{NCS})_3$ magnetically orders as an antiferromagnet with four independent sublattices.

3.2 Introduction

A unifying goal in solid-state science is control over the physical properties of materials, and the tunability of perovskites is perhaps the most striking example.^{231–234} Traditionally these compounds are three-dimensional frameworks with a general chemical formula AMX_3 built from $[\text{MX}_6]$ corner-sharing octahedra. The perovskite structure is, however, only one of a wide-range of AMX_3 structure-types, with one of the most closely related being the post-perovskite structure. In contrast to perovskites, post-perovskites are built

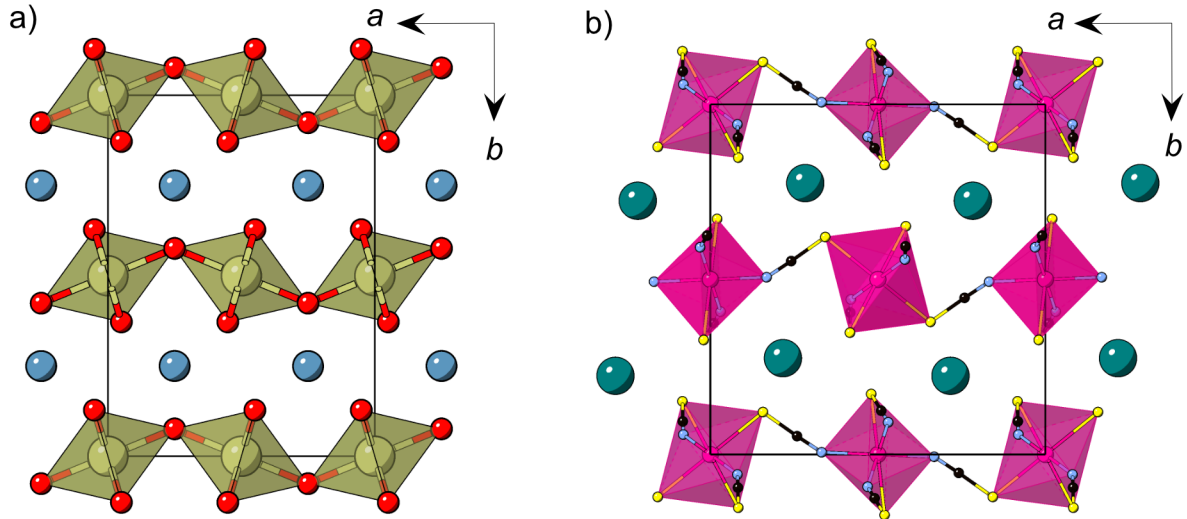


Figure 3.1: a) The structure of the post-perovskite CaIrO_3 , with iridium polyhedra connected *via* corner-sharing (a axis) and edge-sharing (c axis) $[\text{IrO}_6]$ octahedra, Ca = blue, Ir = brown, O = red. b) Crystal structure of the thiocyanate post-perovskite $\text{CsMn}(\text{NCS})_3$, showing an analogous structure and framework connectivity to CaIrO_3 .

from $[\text{MX}_6]$ octahedra that both edge- and corner-share, resulting in two-dimensional anionic $[\text{MX}_3]^-$ layers, rather than a three dimensional framework. These layers are stacked with interstitial A cations positioned between them.

Post-perovskites are amongst the most abundant terrestrial minerals, as the MgSiO_3 perovskite that makes up much of the Earth's lower mantle undergoes a critical high-pressure and temperature phase transition ($P_{\text{critical}} \approx 125$ GPa, $T_{\text{critical}} \approx 1250$ K) to the post-perovskite structure-type near the mantle-core boundary.^{235,236} Due to the difficulty of reaching these extreme pressures, post-perovskites which form at more accessible pressures and can be recovered on quenching have proved useful analogues. These include the second- and third-row transition metal oxides AMO_3 , A = Na, Ca, and M = Pt, Rh, Ir ($P_{\text{synthesis}} \approx 5$ GPa);²³⁷⁻²⁴⁰ and first-row fluorides NaMF_3 , M = Mg, Ni, Co, Fe, Zn.²⁴¹⁻²⁴⁵ A handful of post-perovskite compounds can even be obtained at ambient conditions: notably CaIrO_3 (Fig. 3.1),²⁴⁶ the post-actinide chalcogenides AMnSe_3 (A = Th, U)²⁴⁷ and UFeS_3 ,²⁴⁸ and TlPbI_3 .²⁴⁹ As a result of this synthetic challenge, systematic tuning of the properties of post-perovskites is much less well explored than for perovskites.

In particular, there are limits on our current understanding of the magnetic properties of post-perovskites, in part because neutron diffraction studies require large sample sizes. This is despite the fact that post-perovskites, unlike perovskites, tend to have non-collinear magnetic structures.^{242,245,246,250} As a result, both the exploration of fundamental properties of post-perovskites and the potential utility of their non-trivial spin textures for spintronic devices^{251,252} or quantum memory storage²⁵³ remains limited.

In contrast to the relative scarcity of atomic post-perovskites, molecular post-perovskites,

where X is a molecular anion, are a growing class of materials.^{78,87,124,254,255} Unlike their atomic analogues, the majority of molecular post-perovskites are stable and synthesisable at ambient pressure.

Metal dicyanamides, $AM(dca)_3$ $dca = N(CN)_2^-$, are the best established family of molecular post-perovskites.^{125,256,257} The metal ions are separated by five atom bridges ($\mu_{1,5}-dca$) and tend to be magnetically isolated, with no conclusive evidence of long-range magnetic ordering.^{87,108,254} To explore collective magnetic behaviour in molecular post-perovskite analogues it is worthwhile, therefore, to focus on ligands capable of propagating stronger superexchange interactions. In addition to the dicyanamides, there are two reported thiocyanate frameworks with the post-perovskite structure: $RbCd(NCS)_3$ ⁹⁶ and $CsNi(NCS)_3$.⁷⁸ These both have reported structures, but there are currently no studies on their physical properties.

In this work, I present $CsM(NCS)_3$, $M = Ni, Mn$ and Co . The synthesis of $CsMn(NCS)_3$ and $CsCo(NCS)_3$ are described and their structures determined, by single crystal X-ray diffraction, to be post-perovskites isomorphic with $CsNi(NCS)_3$. Bulk magnetometry is used to show that all three magnetically order. $CsNi(NCS)_3$ and $CsCo(NCS)_3$ order as weak ferromagnets, whereas $CsMn(NCS)_3$ orders as an antiferromagnet. Neutron diffraction measurements have been carried out with single crystal and powder samples. These found $CsNi(NCS)_3$ to be a canted ferromagnet, $\mathbf{k} = (0, 0, 0)$, and $CsMn(NCS)_3$ to be a non-collinear antiferromagnet which orders with $\mathbf{k} = (0, \frac{1}{2}, \frac{1}{2})$. Additionally, density functional theory (DFT) calculations were undertaken, which confirm the intralayer interactions are at least an order of magnitude stronger than the interlayer interactions in these compounds.

3.3 Results

3.3.1 Synthesis

$CsM(NCS)_3$ $M = Ni, Mn, Co$, were synthesised by salt metathesis of the metal sulfate and caesium sulfate with barium thiocyanate in aqueous solution in stoichiometric ratios (1 : 1 : 3). $CsNi(NCS)_3$ is a reported structure⁷⁸ which is stable in ambient conditions. In comparison, $CsMn(NCS)_3$ and $CsCo(NCS)_3$ are both sensitive to humidity, $CsMn(NCS)_3$ is deliquescent and becomes a liquid if left at ambient humidity for too long. A powder of $CsMn(NCS)_3$ can be recovered by heating gently in an oven (approx. 70 °C). The correct phase of $CsCo(NCS)_3$ yields a purple powder, however, a teal-green powder consisting of a mixture of phases was regularly obtained.

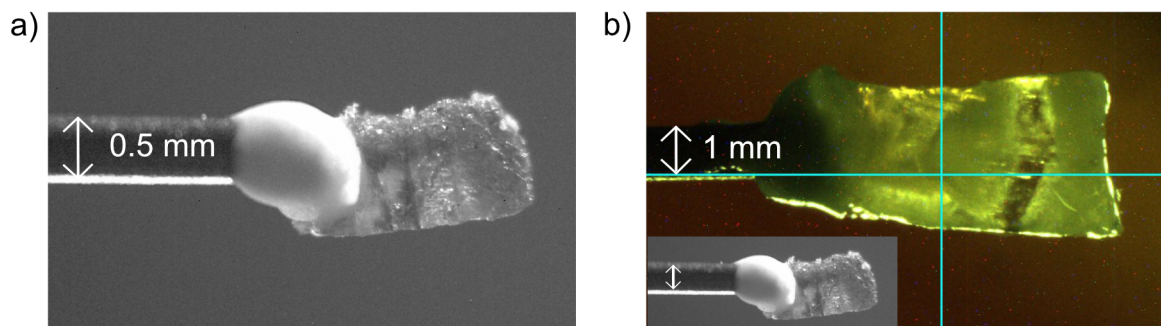


Figure 3.2: Images of the crystals selected for the single crystal neutron diffraction experiments (D19, Institut Laue Langevin) grown from slow evaporation recrystallisations, a) CsNi(NCS)_3 and b) CsMn(NCS)_3 . The inset shows the CsNi(NCS)_3 crystal on the same scale as CsMn(NCS)_3 .

CsNi(NCS)_3 crystals were obtained by seeding from smaller single crystals in a concentrated aqueous solution ($1.8 \times 0.9 \times 0.3 \text{ mm}^3$, Fig. 3.2a). Crystals of CsMn(NCS)_3 were grown by concentrating an aqueous solution *in vacuo* until the solution became incredibly concentrated and viscous. The solution was cooled in an ice bath for several hours, yielding small pale green crystals. Leaving it undisturbed in the sealed flask for three days produced a large pale green single crystal of CsMn(NCS)_3 ($6.3 \times 2.5 \times 1.1 \text{ mm}^3$, Fig. 3.2b). Unlike the nickel and manganese analogues, the recrystallisation of CsCo(NCS)_3 appeared to occur with a two-step mechanism: firstly, deep blue crystals of a phase believed to be $\text{Cs}_2\text{Co(NCS)}_4$ were obtained. If left undisturbed in the mother liquor in ambient conditions for several weeks, the crystals eventually recrystallised into smaller, deep purple crystals of CsCo(NCS)_3 . From this method it was possible to obtain smaller single crystals ($0.13 \times 0.041 \times 0.016 \text{ mm}^3$) and powder samples for single crystal X-ray diffraction and magnetisation measurements. However, it was not possible to yield either a pure-phase powder or large enough single crystals suitable to perform neutron studies on CsCo(NCS)_3 .

3.3.2 Structure

The structures of CsM(NCS)_3 $M = \text{Mn, Co}$, were determined through single crystal X-ray diffraction measurements. I found that the Mn and Co analogues are isomorphous to that of the Ni compound. They all crystallise in the monoclinic space group $P2_1/n$ and adopt the post-perovskite structure. The structure consists of anionic $[\text{M(NCS)}_3]^-$ layers in the ac plane (Fig. 3.3). The transition metal M^{2+} ions are connected through $\mu_{1,3}\text{NCS}$ ligands. Between the layers, which are stacked along the b axis, lie the charge balancing caesium counterions. The M^{2+} ions are octahedrally coordinated and there are two crystallographically and chemically distinct metal sites. One transition metal ion (M1, Wyckoff site $2c$) is coordinated by four nitrogen atoms and two sulfur atoms, whilst the second transition metal ion (M2, Wyckoff site $2b$) is bonded to four sulfur and

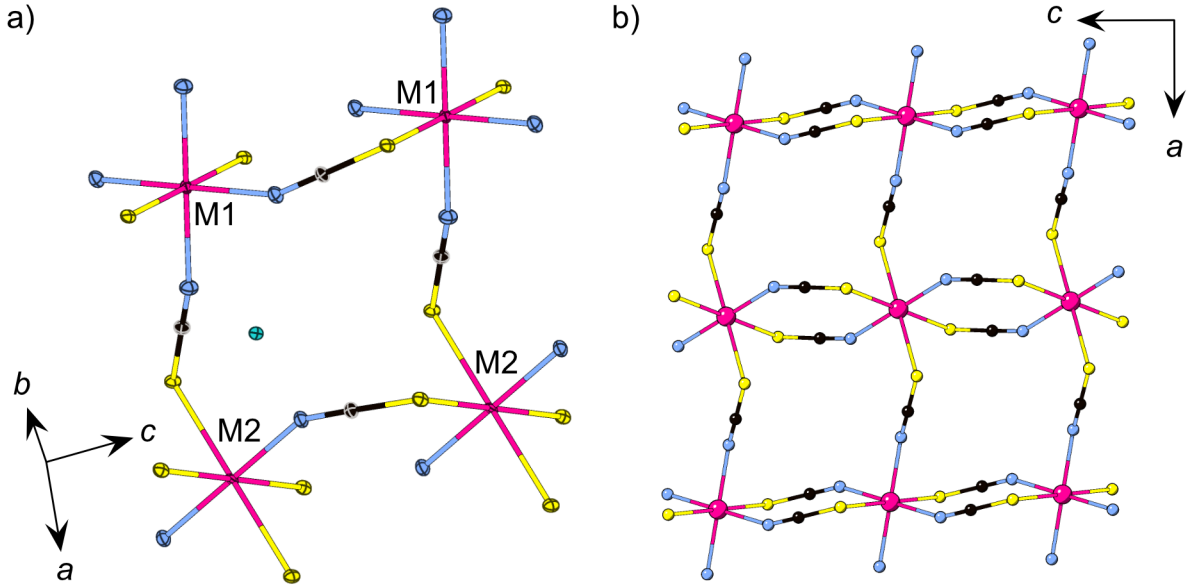


Figure 3.3: The crystal structure of $\text{CsMn}(\text{NCS})_3$ at 20 K obtained from single crystal neutron diffraction. a) View of the metal coordinations highlighting the two chemically independent metal ions (M1, M2). Ellipsoids are shown with 50 % probability. b) A single $[\text{Mn}(\text{NCS})_3]^-$ layer. Cs = green, Mn = pink, N = blue, C = black, S = yellow.

two nitrogen atoms. The metal octahedra corner-share along the *a* axis and alternate between M1 and M2. Along the *c* axis, the metal octahedra edgeshare, and all the metal sites within an edge-sharing chain are the same.

Moving along the period from manganese to nickel, the average M–N and M–S bond lengths, $d_{\text{M-N}}$ and $d_{\text{M-S}}$, decrease (for a tabulated summary see Table 3.1): $d_{\text{Mn-N}}(13 \text{ K}) = 2.1607(14) \text{ \AA}$, $d_{\text{Co-N}}(120 \text{ K}) = 2.072(3) \text{ \AA}$, $d_{\text{Ni-N}}(15 \text{ K}) = 2.035(5) \text{ \AA}$ and $d_{\text{Mn-S}} = 2.674(3) \text{ \AA}$, $d_{\text{Co-S}} = 2.5652(10) \text{ \AA}$, $d_{\text{Ni-S}} = 2.350(20) \text{ \AA}$.

There are two intralayer $\text{M} \cdots \text{M}$ distances, between the edge-sharing octahedra ($d_{\text{M1-M1}} = d_{\text{M2-M2}} = c$) and the corner-sharing octahedra ($d_{\text{M1-M2}} = a$). Again, following the trend from Mn^{2+} to Ni^{2+} , the distance decreases, with $d_{\text{Mn1-Mn1}} = 5.6540(4) \text{ \AA}$ compared to $d_{\text{Co1-Co1}} = 5.57860(11) \text{ \AA}$ and $d_{\text{Ni1-Ni1}} = 5.5409(6) \text{ \AA}$; and $d_{\text{Mn1-Mn2}} = 6.37315(5) \text{ \AA}$, $d_{\text{Co1-Co2}} = 6.30515(5) \text{ \AA}$ and $d_{\text{Ni1-Ni2}} = 6.2631(6) \text{ \AA}$. The interlayer spacing (*b* axis) also decreases, with the shortest $\text{M} \cdots \text{M}$ distances, $d_{\text{M layer}}$, decreasing from $d_{\text{Mn layer}} = 7.20052(15) \text{ \AA}$, through $d_{\text{Co layer}} = 7.18340(10) \text{ \AA}$ to $d_{\text{Ni layer}} = 7.1050(8) \text{ \AA}$.

In addition to this post-perovskite structure, there are two different perovskite structure-types with the composition $\text{AM}(\text{NCS})_3$, $\text{CsCd}(\text{NCS})_3$ ⁹⁶ and $(\text{NH}_4)_2\text{NiCd}(\text{NCS})_6$ ⁹⁷ (Fig. 3.4). To understand the relative stability of the post-perovskite structure compared to the perovskite-type structures, density functional theory (DFT) calculations were performed. Hypothetical perovskite structures were generated through atom-swaps, replacing the M-site for Mn, Co and Ni and the A-site with Cs. The geometry optimised

Table 3.1: Average bond lengths and distances for selected atoms in $\text{CsM}(\text{NCS})_3$ $M = \text{Ni}, \text{Mn}, \text{Co}$. Distances for $\text{CsNi}(\text{NCS})_3$ are obtained from neutron data at 15 K, $\text{CsMn}(\text{NCS})_3$ from neutron data at 13 K and $\text{CsCo}(\text{NCS})_3$ X-ray data at 120 K.

Atoms	Distance (Å)	Atoms	Distance (Å)
Mn–N	2.1607(14)	Mn–S	2.674(3)
Co–N	2.072(3)	Co–S	2.5652(10)
Ni–N	2.035(5)	Ni–S	2.350(20)
Mn1–Mn1	5.6540(4)	Mn1–Mn2	6.37315(5)
Co1–Co1	5.57860(11)	Co1–Co2	6.30515(5)
Ni1–Ni1	5.5409(6)	Ni1–Ni2	6.2631(6)
Mn layer	7.20052(15)		
Co layer	7.18340(10)		
Ni layer	7.1050(8)		

Table 3.2: DFT calculated relative energies between the experimental post-perovskite phase ($\text{CsM}(\text{NCS})_3 = \text{pPv}$) and the two known $\text{AM}(\text{NCS})_3$ perovskite structure types: $\text{CsCd}(\text{NCS})_3 = \text{Cs}[\text{Cd}]$; $(\text{NH}_4)_2\text{NiCd}(\text{NCS})_6 = \text{NH}_4[\text{NiCd}]$. The perovskite structures were generated by swapping the A-site cation for Cs^+ and the M-site cation(s) by the appropriate transition metal, M^{2+} .

M^{2+}	$E / \text{meV per formula unit}$		
	$E(\text{pPv})$	$E(\text{Cs}[\text{Cd}])$	$E(\text{NH}_4[\text{NiCd}])$
Ni	0.0	+90.8	+177.3
Mn	0.0	+84.8	+137.0
Co	0.0	+286.7	+114.5

relaxation of these structures was calculated relative to the experimentally observed post-perovskite structure (Table 3.2). For simplicity, only the spin-ferromagnetic solution of the three structure-types were focused on for the comparison.

The post-perovskite structure-type was found to be more stable than the perovskite structures by around 10 kJ mol^{-1} (0.1 eV per formula unit). This energy discrepancy is consistent with the observed formation of the post-perovskite structure, rather than the other frameworks. However, it does elude to the possibility that with the use of non-standard experimental conditions, these other perovskite phases may be obtainable for $\text{CsM}(\text{NCS})_3$.

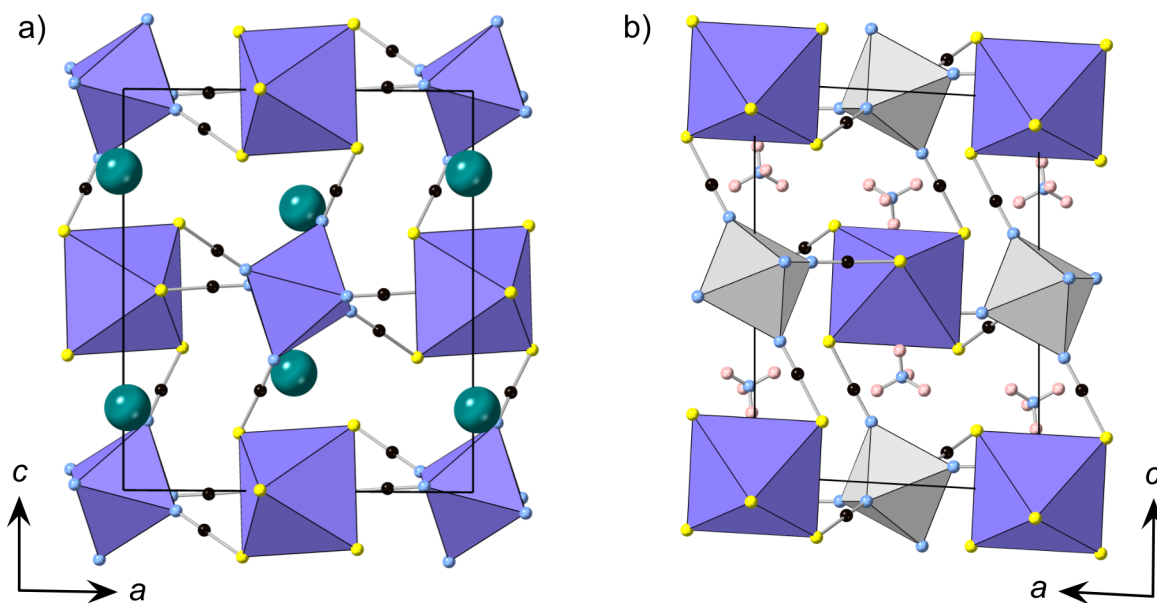


Figure 3.4: Other $AM(NCS)_3$ structures with perovskite-analogue structure types: a) $CsCd(NCS)_3$ ⁹⁶ and b) $[NH_4]_2NiCd(NCS)_6$.⁹⁷ Cs = green, Cd = purple, Ni = grey, N = blue, C = black, S = yellow, H = pale pink.

3.3.3 Magnetism

Having synthesised an isostructural series of thiocyanate post-perovskites containing paramagnetic ions, the following step was to understand their magnetic behaviour. The bulk magnetic susceptibility of each compound was measured. To determine the magnetic ordering temperatures and average interaction strength, susceptibility measurements were carried out in an applied field of 0.01 T. Isothermal magnetisation measurements at 2 K over the range -7 to $+7$ T (or -6 to $+6$ for $M = Ni$) were used to assess the degree of magnetic hysteresis.

The zero-field-cooled and field-cooled susceptibility of $CsNi(NCS)_3$ diverge below the ordering temperature $T_C = 8.5(1)$ K (Fig. 3.5a). The Curie-Weiss law was fitted to the high temperature region of the data. When starting the fit above 180 K, the Curie-Weiss temperature, θ_{CW} , is $-8.6(8)$ K. However, this value is particularly sensitive to the fitting temperature range: $\theta_{CW} = +1.5(4)$ K when $100 < T < 300$ K, whereas $\theta_{CW} = -12.7(8)$ K for a fit $200 < T < 300$ K. This variation is likely due to the presence of significant single-ion anisotropy, which is typical of Ni^{2+} .^{258,259} The Curie constant, C , is $0.85(2)$ emu K mol⁻¹, which is lower than the spin only value, $C_{spin\ only} = 1.00$ emu K mol⁻¹ (Fig. 3.5g). This lower than expected Curie constant is likely due to a sample mass error.

The isothermal magnetisation of $CsNi(NCS)_3$ at 2 K shows hysteresis with a coercive field of $H_C = 0.331(2)$ T and a remnant magnetisation $M_{rem} = 0.106(1)$ μ_B per Ni

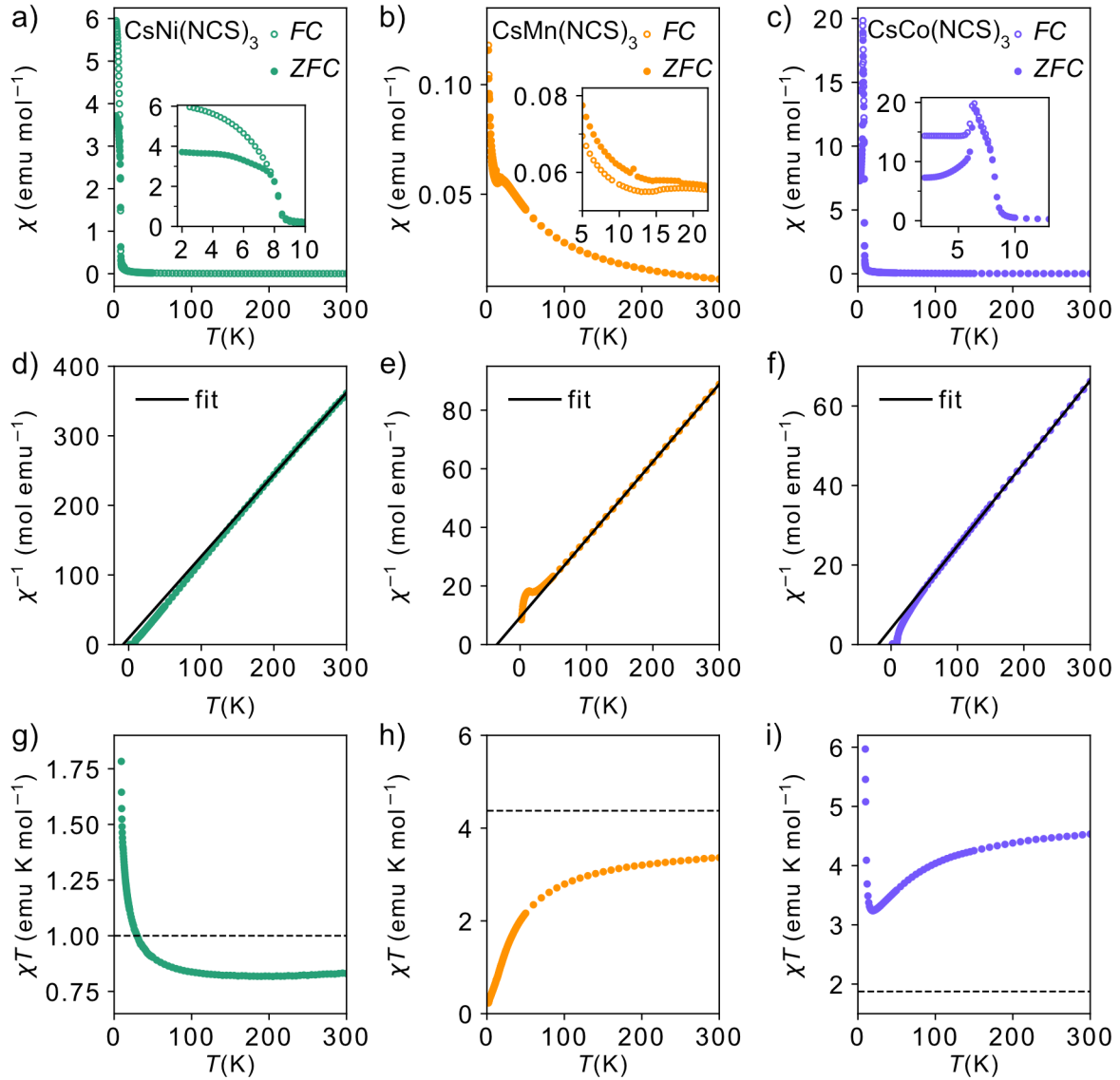


Figure 3.5: Magnetic susceptibility data with an applied field of 0.01 T for a) CsNi(NCS)_3 , b) CsMn(NCS)_3 , c) CsCo(NCS)_3 . d), e) and f) show the inverse susceptibility fitted by the Curie-Weiss law over the temperature ranges d) $180 < T < 300$ K, e) and f) $100 < T < 300$ K. g), h) and i) show the variable temperature magnetic susceptibility product. The high temperature spin only Curie constant, $C_{\text{spin only}}$, is indicated with a dashed line for g) CsNi(NCS)_3 ($C_{\text{spin only}} = 1.000 \text{ emu K mol}^{-1}$), h) CsMn(NCS)_3 ($C_{\text{spin only}} = 4.375 \text{ emu K mol}^{-1}$) and i) CsCo(NCS)_3 ($C_{\text{spin only}} = 1.875 \text{ emu K mol}^{-1}$).

(Fig. 3.6a). This would imply a canting angle of 6.1° if there are only two distinct spin orientations. Beyond $1.19(1)$ T, the hysteresis loop closes and there is a magnetic phase transition to a second magnetic phase, reaching a magnetisation of $1.54(1) \mu_B$ per Ni at $6.00(1)$ T.

The magnetic susceptibility of CsMn(NCS)_3 has a cusp at $16.8(8)$ K indicating the onset of antiferromagnetic order (Fig. 3.5b). An increase in susceptibility at low temperature is likely due to a small fraction of a hydrated impurity, difficult to avoid due to the hygroscopic nature of the compound. Fitting the Curie-Weiss law to the inverse susceptibility between $100 < T < 300$ K gives $\theta_{\text{CW}} = -33.6(2)$ K, and $C = 3.75(2)$ emu

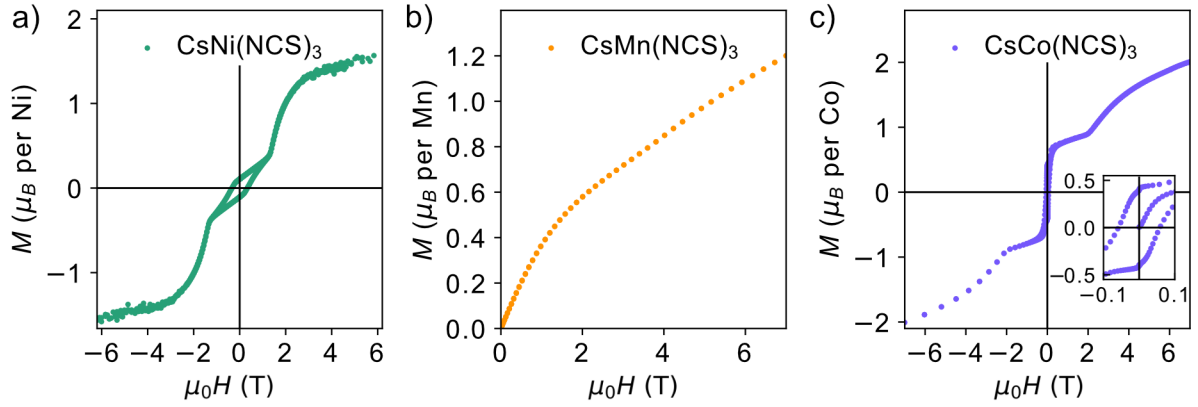


Figure 3.6: Isothermal magnetisation measurements at 2 K for a) CsNi(NCS)_3 (field -6 to $+6$ T); b) CsMn(NCS)_3 (field 0 to $+7$ T); and c) CsCo(NCS)_3 (field -7 to $+7$ T).

K mol^{-1} (Fig. 3.5e, h), which is lower than the high-spin spin only expected value of $C_{\text{spin only}} = 4.375 \text{ emu K mol}^{-1}$ for Mn^{2+} .

There is no observable evidence of hysteresis in the isothermal magnetisation data, consistent with antiferromagnetic order (Fig. 3.6b). The magnetisation reaches $1.20(6) \mu_{\text{B}}$ per Mn at the largest field measured $7.00(1) \text{ T}$, which is well below the spin only saturation magnetisation, $M_{\text{sat.}} = 5 \mu_{\text{B}}$ per Mn. This is indicative of the presence of significant antiferromagnetic interactions. The ratio of the Curie-Weiss temperature to the ordering temperature is $f = |\theta_{\text{CW}}/T_{\text{N}}| = 2.1$, suggestive of slight frustration or low-dimensionality.

Curie-Weiss fitting of the magnetic susceptibility of CsCo(NCS)_3 between $100 < T < 300 \text{ K}$ implying predominately antiferromagnetic interactions, $\theta_{\text{CW}} = -19.7(2) \text{ K}$ (Fig. 3.5f). The large Curie constant, $C = 4.8(2) \text{ emu K mol}^{-1}$, compared to the high-spin spin only value $C_{\text{spin only}} = 1.875 \text{ emu K mol}^{-1}$, indicates that the unquenched orbital moment remains significant in this compound. The determined θ_{CW} therefore likely also includes the effects of the first order spin-orbit coupling. $d\chi/dT$ shows two sharp minima, suggesting that there are potentially two ordering temperatures for the compound at $6.7(1)$ and $8.4(1) \text{ K}$.

The isothermal magnetisation data measured at 2 K show a hysteresis with $H_{\text{C}} = 0.052(2) \text{ T}$ and a remnant magnetisation $M_{\text{rem}} = 0.400(1) \mu_{\text{B}}$ per Co, suggesting a canting angle of 15.3° (Fig. 3.6c). The hysteresis disappears at $1.86(1) \text{ T}$, when $M = 0.88(4) \mu_{\text{B}}$ per Co. Above this applied magnetic field, the magnetisation steadily increases, reaching $2.00(7) \mu_{\text{B}}$ per Co at $7.00(1) \text{ T}$, although the moment remains unsaturated, due to a combination of single-ion anisotropy and antiferromagnetic interactions.

The bulk magnetic properties measurements suggest that both CsNi(NCS)_3 and CsCo(NCS)_3 are weak ferromagnets (canted antiferromagnets), or more generally

have uncompensated magnetic moments, with appreciable hystereses and field-induced magnetic phase transitions. Comparatively, the absence of hysteresis and a negative θ_{CW} for $\text{CsMn}(\text{NCS})_3$ suggests it is an antiferromagnet.

3.3.4 Neutron diffraction

To explore the magnetic properties of these post-perovskites further, neutron diffraction experiments were therefore carried out, both single crystal and powder, to determine their ground state magnetic structures. It was possible to scale-up the synthesis of $\text{CsNi}(\text{NCS})_3$ and $\text{CsMn}(\text{NCS})_3$ to obtain high quality powder and single crystal samples on a scale suitable for neutron diffraction.

Single crystal neutron diffraction (SCND) measurements of $\text{CsNi}(\text{NCS})_3$ ($1.8 \times 0.9 \times 0.3 \text{ mm}^3$) were carried out using the D19 diffractometer at the Institut Laue Langevin (ILL). A low temperature data collection at 2 K, below the magnetic ordering temperature of 8.5 K, saw the addition of Bragg reflections arising from the magnetic ordering. By indexing the magnetic Bragg reflections, the propagation vector was determined to be $\mathbf{k} = (0, 0, 0)$.

Due to the small size of the crystal, the magnetic Bragg reflections were too weak to definitively determine a magnetic space group from this data alone. Therefore, these single crystal data were combined with powder neutron diffraction (PND) data collected on a polycrystalline sample (1.1 g) using the powder neutron diffractometer D1b, ILL (Fig. 3.7). The magnetic space groups with maximal symmetry which permit magnetic moments to exist on both the Ni^{2+} ions were identified using the Bilbao Crystallographic Server^{12,51,214} to be $P2'_1/c'$ and $P2_1/c$ (BNS notation).²¹⁴ Both of these models have the same unit cell as the nuclear structure.

The models in each space group were refined against the combined PND and SCND data with a multi-pattern refinement. Only $P2_1/c$ was able to model the additional intensity arising from the magnetic reflections. This refined structure shows weak ferromagnetic order with two unique magnetic sites, corresponding to the two crystallographic Ni^{2+} ions (Ni1 and Ni2) in the nuclear structure. The two moments have a magnitude of $2.01(3) \mu_{\text{B}}$ and were constrained to refine to equivalent sizes. The moments are directed predominately along the c axis with the canting only present along the b axis. The Ni1 moments (purple arrows Fig. 3.8) are canted at an angle of 162° along the $-b$ direction (18° away from an antiferromagnetic alignment), whilst the Ni2 moments (green arrows Fig. 3.8) are canted at an angle of 105° in the $+b$ direction (75° away from an antiferromagnetic alignment). The asymmetric canting of the two sublattices results in a net magnetisation of $0.116 \mu_{\text{B}}$ per Ni along the b axis ($+b$ direction). This is equivalent

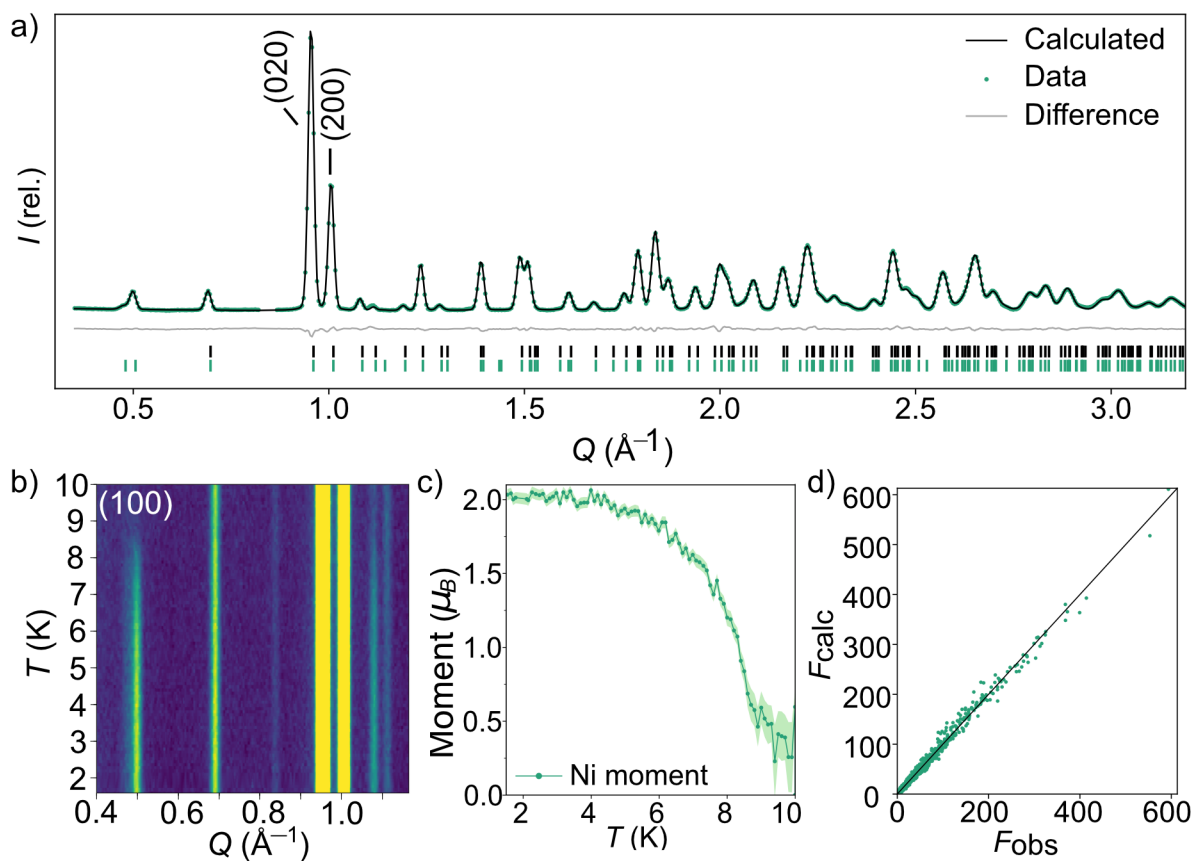


Figure 3.7: Neutron diffraction data for $\text{CsNi}(\text{NCS})_3$. a) Rietveld fit for the multi-pattern refinement (D1b powder and D19 single crystal) of the $P2_1/c$ magnetic model at 1.5 K. The tickmarks show the position of the nuclear reflections (black) and magnetic reflections (green). b) Thermodiffractogram measured between 1.5 and 10 K on the D1b diffractometer (ILL). The most intense magnetic Bragg reflection is indexed as the (100) planes. c) The magnetic moment of the Ni^{2+} ions as a function of temperature obtained by Rietveld refinements of the data collected at each temperature point. d) The F_{obs} against F_{calc} plot obtained from the multi-pattern refinement.

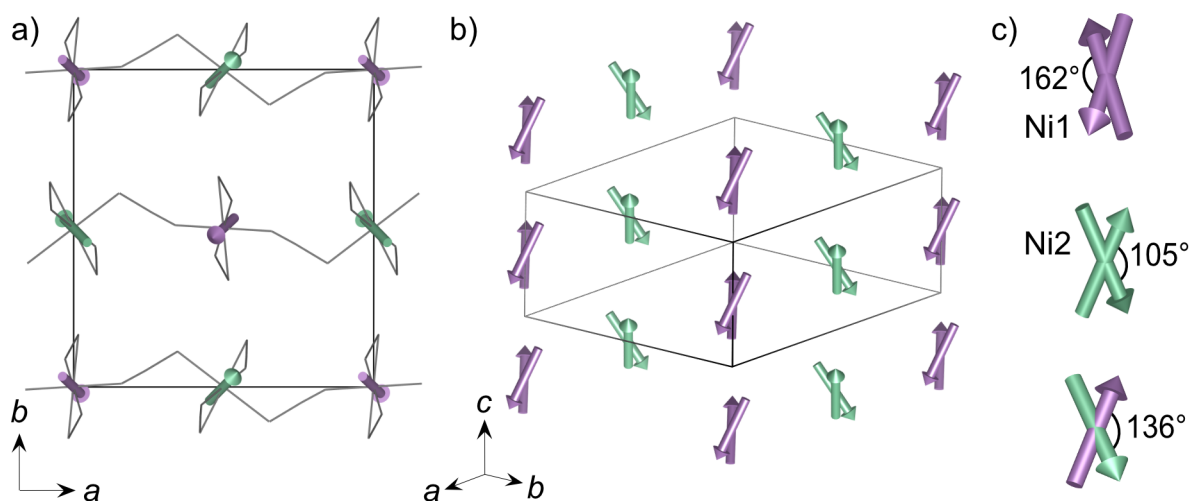


Figure 3.8: The magnetic structure of $\text{CsNi}(\text{NCS})_3$. The two unique magnetic vectors are represented with purple arrows (Ni1) and green arrows (Ni2). The Cs^+ cations have been omitted for clarity and the thiocyanate ligands are represented as a wire frame. a) The structure viewed along the c axis, b) The magnetic structure viewed along the [111] direction. c) Angles describing the canting of the moments.

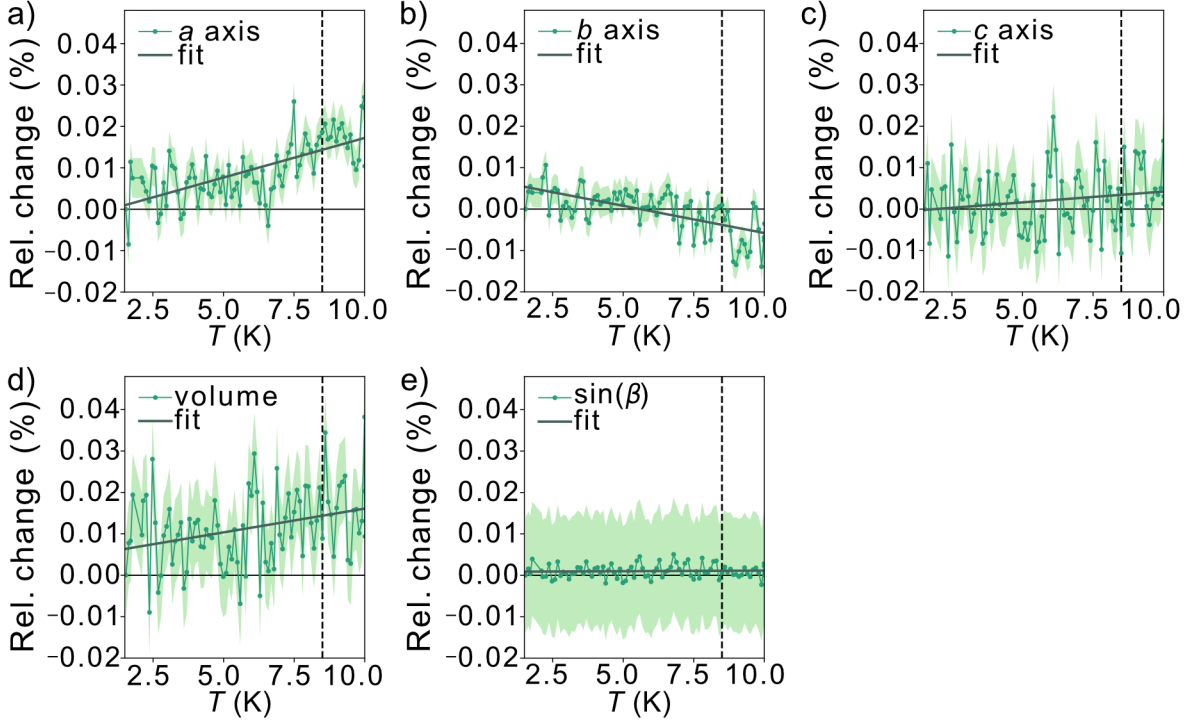


Figure 3.9: CsNi(NCS)_3 lattice parameters between 1.5 and 10 K, obtained from Rietveld refinements of neutron diffraction data measured using the D1b diffractometer (ILL). The vertical dashed black line indicates the magnetic ordering temperature ($T_C = 8.5$ K). A linear fit (dark green line) was used to calculate the coefficient of thermal expansion. a) a axis, b) b axis, c) c axis, d) volume, e) $\sin(\beta)$.

to a single Ni^{2+} canting at an angle of 6.7° , which is in agreement with the magnetometry data. The magnetic moment of Ni1 and Ni2 present a relative tilt of 136° between them.

It was found that when subtracting the 2 K PND data from the 10 K data, there are some nuclear peaks which do not directly overlap at the two temperatures. This is particularly evident in the (020) and (200) reflections, which are the most intense in the diffraction patterns (Fig. 3.7a). The thermal expansion coefficients were estimated by calculating a linear fit for the change in each axis over the temperature range (Fig. 3.9). Since the change in $\sin(\beta)$ is at least one order of magnitude smaller than the variations observed in the a , b and c axes, the thermal expansion tensors will not be significantly rotated over this temperature range. Therefore, the calculated thermal expansion parameters should be a reasonable approximation. For the a axis, $\alpha_a = 19(3) \text{ MK}^{-1}$, the b axis contracts by $\alpha_b = -13(3) \text{ MK}^{-1}$, and for the c axis $\alpha_c = 5(2) \text{ MK}^{-1}$. The angle $\alpha_{\sin(\beta)} = 0.3(1) \text{ MK}^{-1}$ and the volume expands by $\alpha_V = 11(5) \text{ MK}^{-1}$. On heating from 2 to 10 K, the a axis increases by $+0.028\%$, whereas the b axis notably decreases in length by -0.019% . In contrast, the c axis remains almost constant within this temperature range.

A single crystal of CsMn(NCS)_3 ($6.3 \times 2.5 \times 1.1 \text{ mm}^3$) was also measured on D19 (ILL). In the diffraction data collected at 2 K, below $T_N = 16.8$ K, a number of additional Bragg reflections (2938 unique reflections) were identified which were not present in the

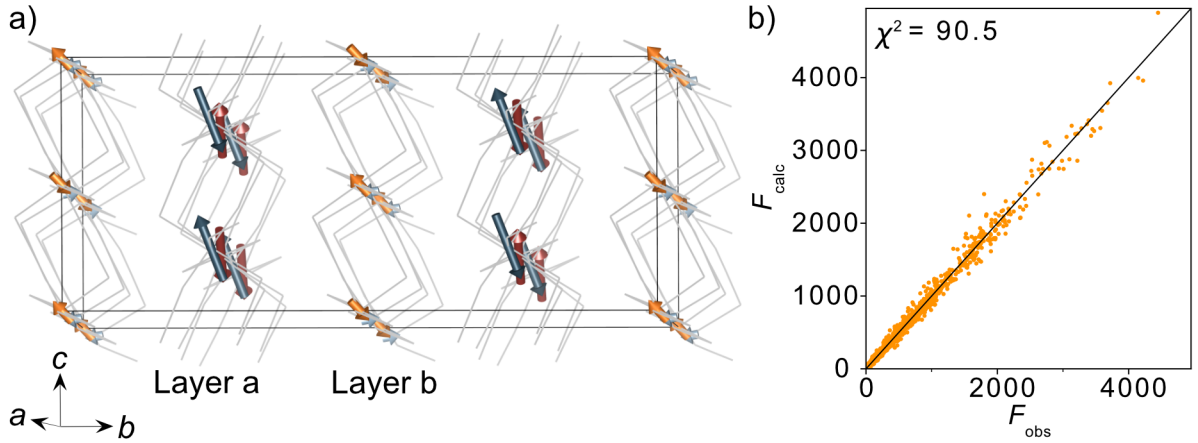


Figure 3.10: Results from the initial magnetic refinement of the single crystal neutron diffraction data of CsMn(NCS)_3 (2 K), allowing all magnetic parameters to refine freely. a) The magnetic structure, with the moments shown with red and orange arrows for Mn1 (red = Mn1a and orange = Mn1b) and blue arrows for Mn2 (dark = Mn2a and light = Mn2b). The Cs^+ cations have been omitted for clarity and the thiocyanate ligands are represented as a wire frame. b) F_{obs} against F_{calc} for the refinement.

data collected at 20 K and could not be indexed to the nuclear structure. These additional magnetic Bragg reflections were indexed with $\mathbf{k} = (0, \frac{1}{2}, \frac{1}{2})$. Using the Bilbao Crystallographic Server the possible magnetic space groups for this propagation vector were determined to be $P_S\bar{1}$ and P_S1 .

I solved the magnetic structures in both magnetic space groups, and found that the $P_S\bar{1}$ better fitted the experimental data. Initially the independent magnetic Mn sites were free to refine independently, both the moment magnitude and angles. The four unique magnetic sites are defined as: Mn1a and Mn1b, which arise from nuclear site Mn1 but are in alternate layers (red and orange arrows Fig. 3.10), and Mn2a and Mn2b from nuclear site Mn2 (light and dark blue arrows Fig. 3.10). Despite giving a statistically “acceptable” fit ($\chi^2 = 90.5$), the model was not satisfactory. Two moments on the same layer (Mn1a and Mn2a, Layer “a”) had large moments of $7.06(\pm 1.07) \mu_B$ and $4.93(\pm 1.39) \mu_B$, whilst the “b” layer moments (from Mn1b and Mn2b) were very small $-0.710(\pm 0.14) \mu_B$ and $-0.65(\pm 0.17) \mu_B$. The angles of the moments were unstable during the refinement, with significantly large errors. Since Mn^{2+} has the valence electron occupation d^5 , the magnitude for any given moment should not be above $5 \mu_B$, so this was not a viable model.

To explore the range of accessible magnetic structure, simulated annealing was carried out. This is a useful method to explore a vast number of structural models, by optimising the agreement between the model and the experimental data. For this, the symmetry of the system was lowered to $P1$, meaning that each Mn ion (16 sites) within the unit cell would refine independently without symmetry constraints. The results were generally in agreement with the previous refinement, specifically, that the moments have similar

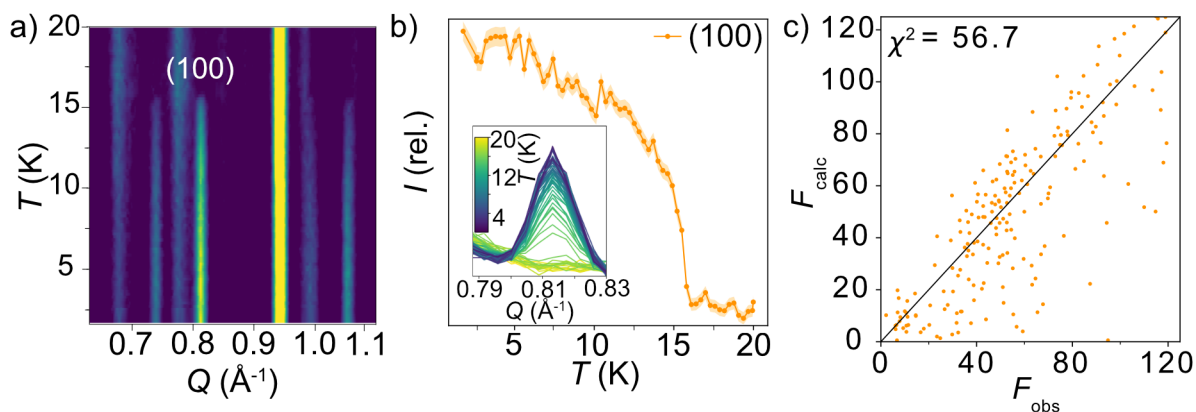


Figure 3.11: Neutron diffraction data used to determine the magnetic structure for $\text{CsMn}(\text{NCS})_3$. a) Thermodiffractogram measured between 1.5 and 20 K on the D1b diffractometer (ILL). The most intense magnetic Bragg reflection is indexed as the (100) planes. b) The integrated intensity of the (100) magnetic reflection at 0.81 \AA^{-1} as a function of temperature. c) F_{obs} against F_{calc} for the final refinement using only magnetic reflections.

behaviours on the alternating layers. Layer a has moments that are close to aligning antiferromagnetically, whilst the Layer b moments are non-collinear with respect to each other and to the moments on Layer a. From inspection of the mcifs generated, it was clear that the $P_5\bar{1}$ magnetic space group possesses the symmetry elements which match the behaviour of the magnetic moments from the data. However, the initial problems regarding unphysical moment sizes and unstable moment angles still persisted.

To verify that the model being used was the most fitting for the data, another avenue was considered. Refinements were attempted with a multi- \mathbf{k} magnetic structure using $\mathbf{k}_1 = (0, \frac{1}{2}, 0)$ and $\mathbf{k}_2 = (0, 0, \frac{1}{2})$. These refinements could not fit the data well and were quickly discarded. This exercise was useful to confirm that the propagation vector was indeed $(0, \frac{1}{2}, \frac{1}{2})$ as initially suggested.

Having verified that the propagation vector and magnetic space group were matching the data, the following task was to modify the refinement conditions, so that a stable solution was reached. Firstly, I started performing the refinements on only the magnetic Bragg reflections. Only reflections with odd k and l values were used in the refinements. In addition, the Q range in which the refinements were performed was limited to the lower Q region where magnetic reflections would be expected to be observed ($Q < 3.7 \text{ \AA}^{-1}$).

It was also necessary to identify ways in which the model could be constrained to aid in stabilising the refinement. It was evident from previous refinements that the moment sizes were closely correlated: within a layer as one moment increased, the second moment decreased proportionally. To avoid this, the size of all four moments were constrained to refine together. I found that within Layer a, Mn1a and Mn2a were orientated such that, within error, they were at an angle of 180° from each other. The angles of these moments were therefore constrained to remain at 180° during the refinements. Additional

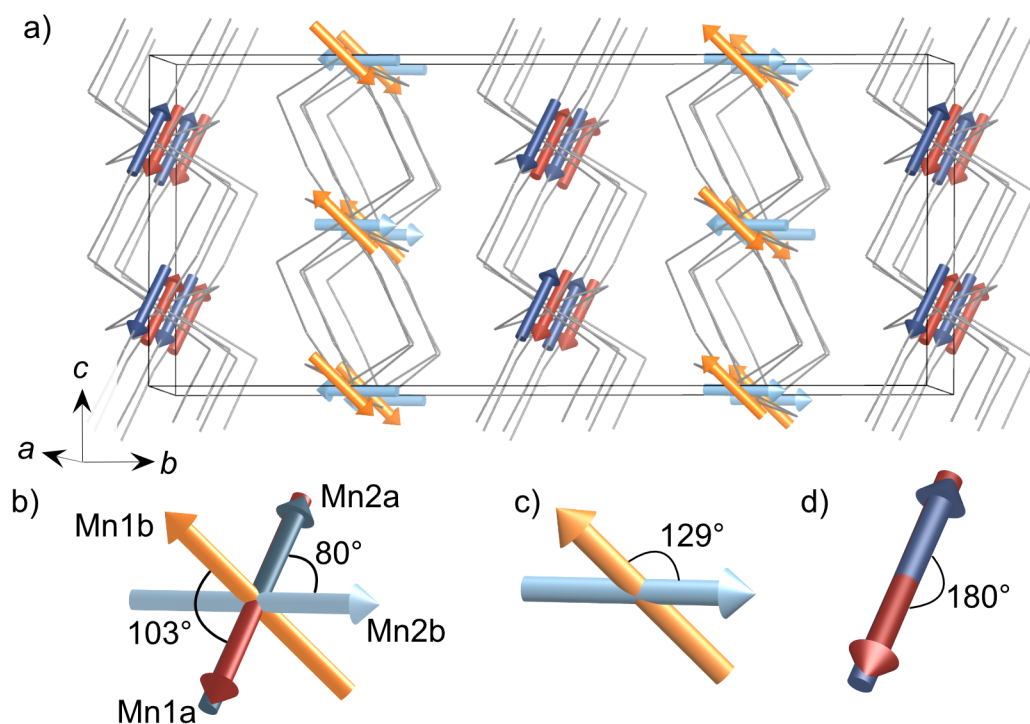


Figure 3.12: The magnetic structure of $\text{CsMn}(\text{NCS})_3$. The magnetic vectors are depicted with red and orange arrows for Mn1 (red = Mn1a and orange = Mn1b) and blue arrows for Mn2 (dark = Mn2a and light = Mn2b). The Cs^+ cations have been omitted for clarity and the thiocyanate ligands are represented as a wire frame. b), c) and d) show the angles between the magnetic vectors.

constraints were also trialed: constraining the moment angles of Mn1b and Mn2b to be collinear (while allowing Mn1a and Mn2a to be non-collinear) gave $\chi^2 = 120.3$, and constraining all four moments to be collinear gave $\chi^2 = 807.6$.

By constraining the angles of Mn1a and Mn2a and allowing a free angle refinement for Mn1b and Mn2b, the final magnetic model was reached ($\chi^2 = 56.7$). The model comprises of four unique magnetic sites, as defined previously (Mn1a = red, Mn1b = orange, Mn2a = dark blue, Mn2b = light blue arrows, Fig. 3.12). The magnetic unit cell dimensions are related to the nuclear cell as follows $a_{\text{mag}} = a_{\text{nuc}}$, $b_{\text{mag}} = 2b_{\text{nuc}}$ and $c_{\text{mag}} = 2c_{\text{nuc}}$. The magnitude of the moments for all Mn sites is $4.63(9) \mu_{\text{B}}$. In the determined model, each of the four magnetic sublattices, derived from a unique Mn^{2+} site, order antiferromagnetically as expected from the bulk antiferromagnetic order observed in the magnetisation data. Mn1a and Mn2a moments are aligned antiparallel within the layer, while Mn1b and Mn2b are at an angle of 103° relative to each other (Fig. 3.12b). Powder neutron diffraction data were collected on the D1b diffractometer, which clearly shows the additional magnetic Bragg reflections. However, the limited data quality possibly prevented quantitative refinement of these data (Fig. 3.11).

3.4 Discussion

The $\text{CsM}(\text{NCS})_3$ compounds all crystallise with the post-perovskite structure. However, unlike most atomic analogues, these thiocyanate compounds adopt the structure at ambient pressure. A common characteristic of atomic post-perovskites is the presence of large octahedral tilt angles in the corresponding perovskite phase, which leaves them more susceptible to undergo the post-perovskite phase transition.²⁴¹ Thiocyanate perovskites are already very tilted, due to the shape of the frontier bonding orbitals, which could explain the ease for formation of this structure type for $\text{CsM}(\text{NCS})_3$.²⁶⁰ Defining the plane as the ac axes, the tilting occurring in these thiocyanate compounds along the edge- and corner-sharing directions can be compared. The corner-sharing octahedra, along the a axis, have smaller deviations away from the ac plane, with angles of $\angle ac - \text{M} - \text{S} = 42(1)^\circ$ and $\angle ac - \text{M} - \text{N} = 9(1)^\circ$ (Fig. 3.13). Along the c axis, the edge-sharing octahedra adopt greater tilting angles as an inherent consequence of having two thiocyanate ligands bridging each pair of metal centres in this direction. The deviation away from the ac plane is $\angle ac - \text{M} - \text{S} = 58(1)^\circ$ and $\angle ac - \text{M} - \text{N} = 36(1)^\circ$. The incorporation of a molecular ligand permits access to this greater degree of tilting without the need for external pressure. This is evident from the DFT calculations which show that for these $\text{CsM}(\text{NCS})_3$ compounds the post-perovskite structure-type is lower energy than other reported thiocyanate perovskite-type structures (Table 3.2).

The magnetometry and neutron diffraction measurements show that the compounds magnetically order between 6 and 16 K, significantly lower than the closest chemical analogues, the binary thiocyanates $\text{M}(\text{NCS})_2$ $\text{M} = \text{Mn}, \text{Fe}, \text{Co}, \text{Ni}, \text{Cu}$,^{80,260} which order at $T_N = 29$ K for $\text{Mn}(\text{NCS})_2$, $T_N = 20$ K for $\text{Co}(\text{NCS})_2$ ^{80,165} and $T_N = 54$ K for $\text{Ni}(\text{NCS})_2$.^{80,261} The atomic post-perovskites have a range in ordering temperatures, with the fluorides ordering at similar temperatures to $\text{CsM}(\text{NCS})_3$, for example post-perovskite NaNiF_3 orders at $T_N = 22$ K (compared to $T_C = 156$ K for the perovskite phase²⁴²). The reported ordering temperatures of the oxide post-perovskites are an order of magnitude larger, for example CaIrO_3 has $T_N = 115$ K,^{238,262,263} likely as the oxides lie closer to the metal-insulator boundary.

One key difference between $\text{CsM}(\text{NCS})_3$ and $\text{M}(\text{NCS})_2$ is that the post-perovskites only have three-atom connections between transition metals ($\mu_{13}\text{NCS}$ coordination mode), whereas $\text{M}(\text{NCS})_2$ have both one-atom and three-atom connections ($\mu_{133}\text{NCS}$). The additional $\text{M}-\text{S}-\text{M}$ superexchange pathway in the binary thiocyanates likely strengthens the magnetic interactions, although DFT calculations of $\text{Cu}(\text{NCS})_2$ suggest that interactions through the $\text{M}-\text{S}-\text{C}-\text{N}-\text{M}$ can be as strong or stronger than through $\text{M}-\text{S}-\text{M}$ bridges.²⁶⁰ The DFT calculations further support this, showing appreciable superexchange through the end-to-end bridging thiocyanates.

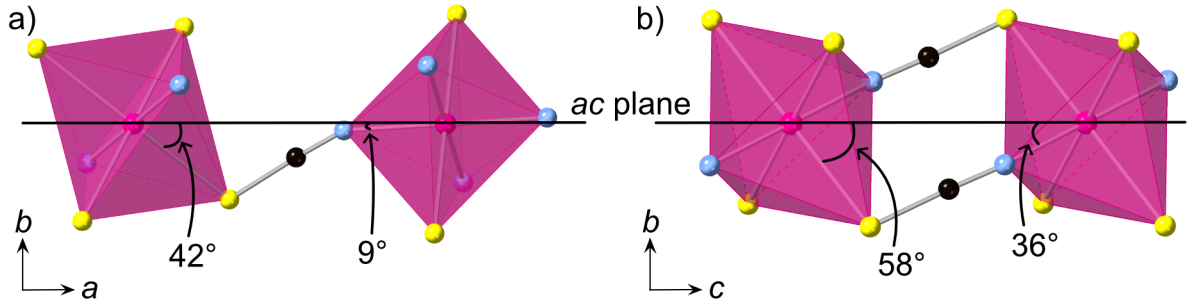


Figure 3.13: The angles between the ac plane (black line) and M–N and M–S bond angles for $\text{CsM}(\text{NCS})_3$ in the direction of a) the corner-sharing octahedra and b) the edge-sharing octahedra. These angles are the same (to the nearest integer) for both M1 and M2. Metal = pink, N = blue, C = black, S = yellow.

In contrast to these compounds, dicyanamide (dca^-) based post-perovskites containing magnetic ions do not appear to order.^{87,108,254} The transition metals in these compounds are separated by six bonds where $d(\text{Mn-NCNCN-Mn}) = 8.9825(4) \text{ \AA}$ ($[\text{Ph}_4\text{P}]\text{Mn}(\text{dca})_3$),⁸⁷ compared to four bonds and $d(\text{Mn-NCS-Mn}) = 6.37315(5) \text{ \AA}$ ($\text{CsMn}(\text{NCS})_3$). This likely reduces the superexchange interactions further. However, $\text{Cr}[\text{Bi}(\text{SCN})_6]$, with even longer superexchange pathways does order at $T_N = 4.0 \text{ K}$,²⁶⁴ indicating that orbital overlap and orbital energy matching are also playing a key role in this.

$\text{CsM}(\text{NCS})_3$, $M = \text{Ni, Mn, Co}$, all adopt non-collinear magnetic structures. Non-collinearity also appears to be typical in the atomic perovskites. The only previous experimentally reported magnetic structure of a post-perovskite is of CaIrO_3 , which used magnetic resonant X-ray scattering to reveal a canted stripe antiferromagnetic ground state.²⁴⁶ Octahedral tilting is predicted to be a key parameter in determining the degree of non-collinearity,²⁶⁵ so it is expected that the post-perovskite structures are sensitive to this factor as well. Analysis of the isothermal magnetisation data for $\text{CsNi}(\text{NCS})_3$ (Fig. 3.6a), assuming that there is only a single magnetic site (i.e. only two distinct spin orientations), gives a canting angle of 6° . However, the magnetic structure has two magnetic sites (i.e. four spin orientations), and so there are in fact three ‘canting angles’, all of which are larger than 6° (18° , 44° , and 75°). The symmetry constraints of the $P2_1/c$ magnetic space group means that for each pair of canted moments (i.e. a single magnetic site), the components of the magnetic moments along the a and c axes will be of equal magnitude and so the uncompensated magnetisation lies only along the b axis. In $\text{CsNi}(\text{NCS})_3$, the uncompensated moments from each magnetic site have opposite signs: $+0.80 \mu_B$ per Ni2 and $-0.57 \mu_B$ per Ni1, with a net moment of $+0.116 \mu_B$. Using bulk measurements for materials with complex magnetic structures can therefore lead to underestimates of the degree of non-collinearity.

The magnetic structure of $\text{CsMn}(\text{NCS})_3$, unlike the nickel and cobalt analogues, orders as an antiferromagnet. The neutron data reveal a $\mathbf{k} = (0, \frac{1}{2}, \frac{1}{2})$ propagation vector, which leads to four unique sublattices. As a result of the anticentering translation in

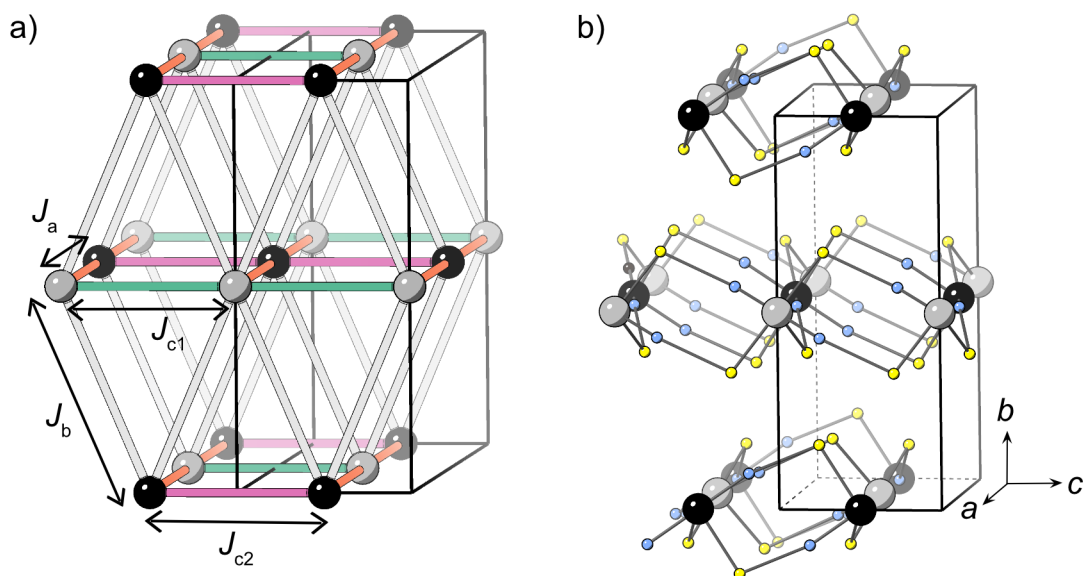


Figure 3.14: The four nearest-neighbour magnetic interactions in $\text{CsM}(\text{NCS})_3$. M1 and M2 are grey and black respectively and the thiocyanate ligands are represented with sulfur (yellow) and nitrogen (blue) atoms only. Caesium cations and carbon atoms have been removed for clarity.

the $P_5\bar{1}$ magnetic space group, each sublattice, and therefore the overall structure, is antiferromagnetic. There are two distinct kinds of layer within the magnetic structure, ‘a’ and ‘b’ (Fig. 3.10a). Layer a, containing Mn1a and Mn2a, is antiferromagnetically correlated; but Mn1b and Mn2b are non-collinear both with respect to each other and also to Mn1a and Mn2a. The complexity of this structure is perhaps surprising, considering the relative simplicity of the nuclear structure and the lack of spin-orbit coupling expected for high spin Mn^{2+} . The layers stack so that each consecutive layer is offset by $c_{\text{nuc}}/2$, resulting in a triangular relationship between the interlayer moments (Fig. 3.14). This layered stacking pattern may generate frustration, which could explain the observed non-collinear structure.

3.5 Conclusions

The synthesis, structure, magnetometry, single crystal and powder neutron diffraction data for three isomorphous post-perovskite thiocyanate frameworks, $\text{CsM}(\text{NCS})_3$ $M = \text{Ni}, \text{Mn}, \text{Co}$ has been reported. The magnetic susceptibility measurements show that all the materials magnetically order, $\text{CsNi}(\text{NCS})_3$ $T_C = 8.5(1)$ K, $\text{CsMn}(\text{NCS})_3$ $T_N = 16.8(8)$ K and $\text{CsCo}(\text{NCS})_3$ $T_C = 6.7(1)$ K. Neutron diffraction experiments on $\text{CsNi}(\text{NCS})_3$ and $\text{CsMn}(\text{NCS})_3$ revealed both compounds have complex non-collinear ordering. $\text{CsNi}(\text{NCS})_3$ orders as a weak ferromagnet with two magnetically distinct nickel moments. $\text{CsMn}(\text{NCS})_3$, on the other hand, orders as an antiferromagnet with a magnetic unit cell which is doubled along the nuclear b and c axes, and has four unique

sublattices.

This study has demonstrated the role neutron diffraction studies have in uncovering unusual magnetic orderings. The neutron diffraction data have shown that despite the relative simplicity of the chemical structures, these thiocyanate post-perovskites are a rich source of surprising magnetic orderings which cannot be recognised through magnetometry data alone.

3.6 Experimental

3.6.1 Synthesis of $\text{CsM}(\text{NCS})_3$

Aqueous solutions of $\text{MnSO}_4 \cdot \text{H}_2\text{O}$ (254 mg, 1.5 mmol, 3 mL) and $\text{Ba}(\text{SCN})_2 \cdot 3 \text{H}_2\text{O}$ (461 mg, 1.5 mmol, 15 mL) were combined and stirred for 24 h. The opaque white solution was filtered, and the white residue of BaSO_4 removed to leave a filtrate of aqueous $\text{Mn}(\text{NCS})_2$. Cs_2SO_4 (272 mg, 0.75 mmol) and $\text{Ba}(\text{SCN})_2 \cdot 3 \text{H}_2\text{O}$ (231 mg, 0.75 mmol) were dissolved in distilled water (10 mL) and added to the $\text{Mn}(\text{NCS})_2$ solution. The mixture was stirred for 24 h, and filtered, removing a white residue of BaSO_4 . The colourless filtrate solution of $\text{CsMn}(\text{NCS})_3$ was concentrated under reduced pressure and left to stand for 48 h yielding pale green single crystals of $\text{CsMn}(\text{NCS})_3$.

$\text{CsCo}(\text{NCS})_3$ and $\text{CsNi}(\text{NCS})_3$ were synthesised in an analogous method from $\text{CoSO}_4 \cdot 7 \text{H}_2\text{O}$ (421 mg, 1.5 mmol) and $\text{NiSO}_4 \cdot 6 \text{H}_2\text{O}$ (394 mg, 1.5 mmol) respectively. This yielded purple, $\text{CsCo}(\text{NCS})_3$, and green, $\text{CsNi}(\text{NCS})_3$, microcrystalline powders. Single crystals of these compounds were obtained by slow evaporation recrystallisations from concentrated aqueous solutions. The synthesis of $\text{CsNi}(\text{NCS})_3$ has been previously reported through the reaction of $\text{NiCl}_2 \cdot 6 \text{H}_2\text{O}$, Cs_2CO_3 and NH_4SCN .⁷⁸

3.6.2 Single Crystal X-ray Diffraction

Single crystal X-ray diffraction measurements were carried out by Dr Matthew Cliffe (University of Nottingham) and myself. Single crystals were selected and mounted using Fomblin® (YR-1800 perfluoropolyether oil) on a polymer-tipped MiTeGen MicroMount™ and cooled rapidly to 120 K in a stream of cold N_2 using an Oxford Cryosystems open flow cryostat.²⁶⁶ Single crystal X-ray diffraction data were collected on an Oxford Diffraction GV1000 (AtlasS2 CCD area detector, mirror-monochromated Cu-K α radiation source; $\lambda = 1.541 \text{ \AA}$; ω scans). Cell parameters were refined from the observed positions of all strong reflections and absorption corrections were applied using a Gaus-

sian numerical method with beam profile correction (CrysAlisPro).²⁶⁷ The structure was solved within Olex2²⁶⁸ by dual space iterative methods (SHELXT),²⁷ least squares refinement of the structural model was carried using (SHELXL).²⁶⁹ Structures were checked with checkCIF (<https://checkcif.iucr.org>).

3.6.3 Single Crystal Neutron Diffraction

Monochromatic single crystal neutron diffraction data for CsMn(NCS)₃ and CsNi(NCS)₃ were collected on the four-circle D19 diffractometer at the Institut Laue Langevin (ILL) Grenoble, France, by Jie Lee (University of Nottingham), Dr Oscar Fabelo (ILL), Dr Laura Cañadillas Delgado (ILL), Dr Matthew Cliffe and myself. Neutrons with a wavelength of 1.455 Å (CsMn(NCS)₃) and 1.457 Å (CsNi(NCS)₃) were provided by a flat Cu monochromator using the 220 reflection at $2\theta_M = 69.91^\circ$ take-off angle. The samples were each placed in a closed-circuit displux cooling device, which was operated following a ramp of 2 K min⁻¹.

NOMAD software from the ILL was used for data collection. Unit cell determinations were performed using PFIND and DIRAX programs, and processing of the raw data was applied using RETREAT, RAFD19 and Int3D programs.²²⁶⁻²²⁹ For CsNi(NCS)₃, the data were corrected for the absorption of the low-temperature device using the D19ABSCAN program²³⁰ and for the size and composition of the crystal. For CsMn(NCS)₃ the data were corrected for the absorption of the low-temperature device using the D19ABSCAN program.

3.6.4 Powder Neutron Diffraction

Constant wavelength powder neutron diffraction data for CsMn(NCS)₃ and CsNi(NCS)₃ were collected on the high-intensity medium resolution D1b diffractometer²⁷⁰ at the ILL by Dr Oscar Fabelo, Dr Laura Cañadillas Delgado, Dr Matthew Cliffe and myself. The incident wavelength was $\lambda = 2.52$ Å and the scattering was measured over an angular range of $2 < 2\theta < 128^\circ$. Thermal diffractograms for CsMn(NCS)₃ were collected between 1.5 K and 20 K heated with a programmed ramp of 0.06 K min⁻¹. Long acquisition measurements were collected at 1.5 K and 20 K. Thermal diffractograms for CsNi(NCS)₃ were collected between 1.5 K and 10 K heated with a programmed ramp of 0.025 K min⁻¹. Long acquisition measurements were collected at 1.5 K and 10 K. NOMAD software from the ILL was used for data collection. Refinements of the magnetic model were completed using the FullProf program.³⁷

3.6.5 Magnetic Measurements

Measurements of the magnetic susceptibility were carried out by Dr Matthew Cliffe and myself on samples of CsNi(NCS)_3 (34.5 mg) and CsCo(NCS)_3 (14.3 mg) using a Quantum Design Magnetic Property Measurements System (MPMS) 3 Superconducting Quantum Interference Device (SQUID) magnetometer, and for CsMn(NCS)_3 (9.6 mg) using an MPMS XL. The zero-field-cooled (ZFC) and field-cooled (FC) susceptibility was measured in an applied field of 0.01 T over the temperature range 2300 K. As $M(H)$ is linear in this field, the small-field approximation for the susceptibility, $\chi(T) \simeq \frac{M}{H}$, where M is the magnetisation and H is the magnetic field intensity, was taken to be valid.

Isothermal magnetisation measurements were carried out at 2 K over the field range -7 to $+7$ T for CsMn(NCS)_3 and CsCo(NCS)_3 , and a range of -6 to $+6$ T for CsNi(NCS)_3 . Data were corrected for diamagnetism of the sample using Pascal’s constants.⁴¹

3.6.6 Density Functional Theory Calculations

Density functional theory (DFT) calculations were performed by Dr Sanliang Ling (University of Nottingham) to probe the structures and energetics of spin order of the compounds considered in this study. The spin-polarised DFT+ U method (with Grimme’s D3 van der Waals correction)²⁷¹ was employed in structural optimisations and energy calculations, using the Vienna Ab initio Simulation Package (VASP 5.4.4).²⁷² In the DFT+ U calculations, U values of 3.6, 5.0 and 5.1 eV were used for d-electrons of Mn^{2+} , Co^{2+} and Ni^{2+} cations,^{273,274} respectively, and a range of ferromagnetic and anti-ferromagnetic spin solutions were considered for divalent magnetic cations (Table 3.3). A plane-wave basis set with a kinetic energy cutoff of 520 eV to expand the wave functions. The Perdew-Burke-Ernzerhof functional²⁷⁵ in combination with the projector augmented wave method^{276,277} were used to solve the Kohn-Sham equations. An energy convergence threshold of 10^{-4} eV was used for all total energy calculations, and the structural optimisations, including cell parameters and atomic positions, were considered converged if all interatomic forces fall below 0.01 eV \AA^{-1} . All DFT calculations have been performed in the $2 \times 1 \times 1$ supercell (8 formula units per cell) using a $6 \times 5 \times 5$ k-grid (which corresponds to a k-points spacing of around 0.1 \AA^{-1}).

3.7 Appendix

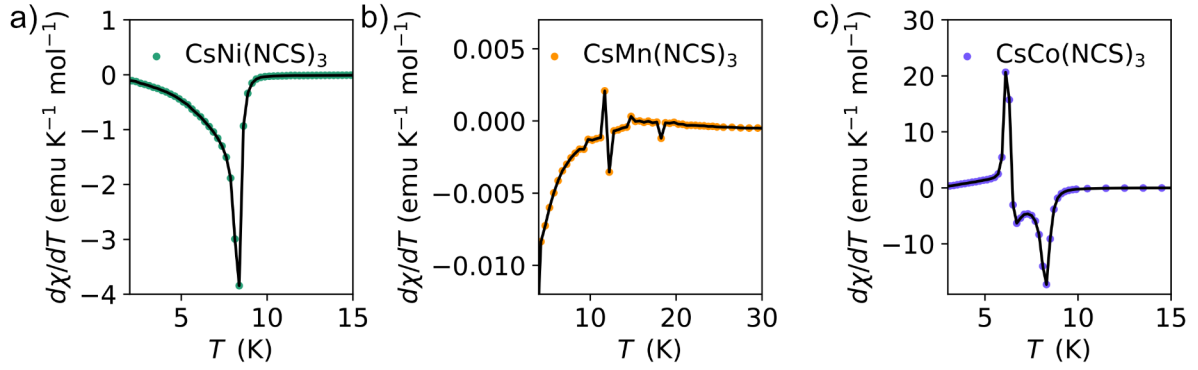


Figure 3.15: The derivative of the susceptibility for a) $\text{CsNi}(\text{NCS})_3$, b) $\text{CsMn}(\text{NCS})_3$ and c) $\text{CsCo}(\text{NCS})_3$.

Table 3.3: The configurations used to calculate the ground state interactions and the relative energy of each configuration for $\text{CsM}(\text{NCS})_3$, $M = \text{Ni}, \text{Mn}$. Each interaction is given as a relative interaction where + is ferromagnetic, - is antiferromagnetic, and 0 where the interactions are compensated.

Structure	J_a	J_b	J_{c1}	J_{c2}	$E(\text{CsNi}(\text{NCS})_3)^*$	$E(\text{CsMn}(\text{NCS})_3)^*$
FM	+	+	+	+	0.000	0.000
AFM1	+	-	+	+	-1.184	-3.349
AFM2	-	+	+	+	-0.212	-0.121
AFM3	0	-	-	-	-0.041	-11.511
AFM4	0	-	-	-	-0.171	-11.587
AFM5	0	+	-	-	0.389	-8.669
AFM6	-	-	+	+	-0.914	-3.330
AFM7	0	0	+	-	-0.238	-6.643
AFM8	0	0	-	+	+0.014	-5.425

* meV per formula unit

Table 3.4: Single crystal experimental details for CsCo(NCS)₃ (X-ray data) and CsNi(NCS)₃ (neutron data), S = "Goodness of fit"

Crystal data	Co 120K X	Ni 15K N
Chemical formula	C ₆ Co ₂ N ₆ S ₆ · 2 (Cs)	C ₆ Ni ₂ N ₆ S ₆ · 2 (Cs)
M_r	732.16	731.69
Temperature (K)	120	15
λ (Å)	1.54184	1.4568
Radiation type	Cu $K\alpha$	Neutron
Crystal system	Monoclinic	Monoclinic
Space group	$P2_1/n$	$P2_1/n$
a (Å)	12.6103 (1)	12.5261 (10)
b (Å)	13.2395 (2)	13.0853 (17)
c (Å)	5.5786 (1)	5.5409 (5)
β (°)	96.445 (1)	96.560 (6)
V (Å ³)	925.48 (2)	902.25 (16)
Z	2	2
μ (mm ⁻¹)	50.61	0.02
Crystal size (mm)	0.13 × 0.04 × 0.02	1.8 × 0.9 × 0.3 (radius= 1)
Data collection		
Diffractometer	GV1000, AtlasS2	D19 (ILL)
Transmission min., max.	0.445, 0.942	—
No. of measured, independent and observed [$I > 2\sigma(I)$] reflections	17041, 1847, 1809	3115, 1304, 876
R_{int}	0.051	0.077
$(\sin \theta/\lambda)_{\text{max}}$ (Å ⁻¹)	0.620	0.598
Data completeness	0.999	0.806
Refinement		
$R[F^2 > 2\sigma(F^2)], \omega$	0.019, 0.048, 1.04	0.114, 0.119, 3.72
$R(F^2), S$		
No. of reflections	1847	1304
No. of parameters	103	99
$\Delta\rho >_{\text{max}}, \Delta\rho >_{\text{min}}$ (e Å ⁻³)	+0.66, -0.87	-

Table 3.5: Single crystal experimental details for CsMn(NCS)₃, 2 – 20 K (neutron data), S = "Goodness of fit"

Crystal data	Mn 2K N	Mn 13K N	Mn 20K N
Chemical formula	C ₆ Mn ₂ N ₆ S ₆ · 2 (Cs)	C ₆ Mn ₂ N ₆ S ₆ · 2 (Cs)	C ₆ Mn ₂ N ₆ S ₆ · 2 (Cs)
M_r	724.18	724.18	724.18
Temperature (K)	2	13	20
λ (Å)	1.4451	1.4451	1.4451
Radiation type	Neutron	Neutron	Neutron
Crystal system	Monoclinic	Monoclinic	Monoclinic
Space group	$P2_1/n$	$P2_1/n$	$P2_1/n$
a (Å)	12.7468 (3)	12.7463 (3)	12.7469 (3)
b (Å)	13.2446 (3)	13.2447 (3)	13.2457 (3)
c (Å)	5.6541 (1)	5.6540 (1)	5.6542 (1)
β (°)	95.8390 (16)	95.8382 (16)	95.8446 (16)
V (Å ³)	949.61 (4)	949.56 (4)	949.70 (4)
Z	2	2	2
μ (mm ⁻¹)	0.02	0.02	0.02
Crystal size (mm)	6.3 × 2.6 × 1.1 (radius= 3)	6.3 × 2.6 × 1.1 (radius= 3)	6.3 × 2.6 × 1.1 (radius= 3)
Data collection			
Diffractometer	D19 (ILL)	D19 (ILL)	D19 (ILL)
Absorption correction	-	-	-
No. of measured, independent and observed [$I > 2\sigma(I)$] reflections	5326, 1659, 1616	5513, 1656, 1649	5516, 1656, 1649
R_{int}	0.030	0.027	0.027
$(\sin \theta/\lambda)_{\text{max}}$ (Å ⁻¹)	0.601	0.599	0.599
Data completeness	0.959	0.968	0.968
Refinement			
$R[F^2 > 2\sigma(F^2)], \omega$	0.033, 0.081, 2.49	0.035, 0.097, 3.60	0.037, 0.108, 2.97
$R(F^2), S$			
No. of reflections	1659	1656	1656
No. of parameters	103	103	103
$\Delta\rho >_{\text{max}}, \Delta\rho >_{\text{min}}$ (e Å ⁻³)	-	-	-

Table 3.6: Single crystal experimental details for CsMn(NCS)₃, 50 – 300 K (50 and 300 K neutron data, 120 K X-ray data), S = "Goodness of fit"

Crystal data	Mn 50K N	Mn 120K X	Mn 300K N
Chemical formula	C ₆ Mn ₂ N ₆ S ₆ · 2 (Cs)	C ₆ Mn ₂ N ₆ S ₆ · 2 (Cs)	C ₆ Mn ₂ N ₆ S ₆ · 2 (Cs)
M_r	724.18	724.18	724.18
Temperature (K)	50	120	300
λ (Å)	1.4451	1.54184	1.4451
Radiation type	Neutron	X-ray	Neutron
Crystal system	Monoclinic	Monoclinic	Monoclinic
Space group	$P2_1/n$	$P2_1/n$	$P2_1/n$
a (Å)	12.7661 (3)	12.8159 (3)	12.8136 (5)
b (Å)	13.2731 (4)	13.3648 (3)	13.4916 (7)
c (Å)	5.6588 (2)	5.6774 (1)	5.6692 (2)
β (°)	95.9037 (17)	95.999 (2)	96.346 (2)
V (Å ³)	953.77 (5)	967.11 (6)	974.06 (13)
Z	2	2	2
μ (mm ⁻¹)	0.02	45.62	0.02
Crystal size (mm)	6.3 × 2.6 × 1.1 (radius= 3)	0.37 × 0.21 × 0.14	6.3 × 2.6 × 1.1 (radius= 3)
Data collection			
Diffractometer	D19 (ILL)	SuperNova, Dual, Cu at home/near, Atlas	D19 (ILL)
Transmission min., max.	-	0.007, 0.181	-
No. of measured, independent and ob- served [$I > 2\sigma(I)$] reflections	3875, 1432, 1401	8091, 1924, 1875	2318, 1158, 1046
R_{int}	0.030	0.093	0.026
$(\sin \theta/\lambda)_{\text{max}}$ (Å ⁻¹)	0.600	0.622	0.599
Data completeness	0.832	0.993	0.664
Refinement			
$R[F^2 > 2\sigma(F^2)], \omega$ $R(F^2), S$	0.035, 0.085, 1.96	0.063, 0.160, 1.05	0.039, 0.076, 1.70
No. of reflections	1432	1924	1158
No. of parameters	103	103	103
$\Delta\rho >_{\text{max}}, \Delta\rho >_{\text{min}}$ (e Å ⁻³)	-	+4.76, -1.57	-

Chapter 4

High pressure behaviour of the magnetic van der Waals molecular framework $\text{Ni}(\text{NCS})_2$

4.1 Summary

- The van der Waals molecular framework $\text{Ni}(\text{NCS})_2$ was compressed up to 8.4 kbar.
- The structural distortions were followed through X-ray and neutron diffraction experiments, and revealed that $\text{Ni}(\text{NCS})_2$ has anisotropic compressibilities, both within the layers and between layers.
- From magnetometry and low temperature neutron diffraction data, it was found that the magnetic ordering temperature increases by +19 % (+2.3 % kbar^{-1}). This occurs as a result of the soft, in-layer compressibility of the framework.

4.2 Introduction

Pressure is a ubiquitous external parameter which can be used to activate alterations to the physical attributes of materials, including charge transfer correlations leading to metallisation,^{278,279} superconductivity,²⁸⁰ magnetic ordering^{281,282} and spin-crossover behaviour.^{283,284} In particular, research has been drawn towards van der Waals materials (vdW), compounds characterised by their two-dimensional layers, which weakly interact through dispersion interactions. This prominent feature in vdW materials has been exploited by exfoliating materials to their few-layer or monolayer extremes,^{285,286} with the aim of employing these compounds as single-layer magnetic materials incorporated into

spintronic devices.⁵⁴

Transition metal halides, MX_2 and MX_3 , M = transition metal, X = halide, are a subset of the vdW category which have been shown to undergo substantial enhancements of their magnetic ordering temperature, T_C . Included is NiI_2 and FeCl_2 which report increases in T_C of +313 % when compressed to 190 K²⁸² and +1091 % at pressures of 420 kbar.²⁸⁷ This results in a responsiveness to pressure of $Q = \frac{dT_C}{T_C} \frac{1}{dP} = +1.6 \text{ \% kbar}^{-1}$ (NiI_2) and $Q = +2.4 \text{ \% kbar}^{-1}$ (FeCl_2). In addition, bilayers of CrI_3 undergo an antiferromagnetic to ferromagnetic transition at 27 kbar.¹⁵⁶

As well as strengthening superexchange pathways to alter T_C , pressure can promote further changes to the electronic structure of a compound.²⁸⁸ Metal-insulator transitions are reported for NiI_2 at a critical pressure of $P_C = 190 \text{ kbar}$,²⁸² FeCl_2 ($P_C = 320 \text{ kbar}$)²⁸⁹ and FePS_3 ($P_C = 140 \text{ kbar}$).²⁷⁸ Moreover, FePSe_3 exhibits superconductivity above 90 kbar as the layer separation reduces.²⁸⁰

Molecular frameworks, made from metals and molecular ligands, are also a rich source for exploring pressure-activated property control. Materials which contain molecular components provide compounds with an inherently higher flexibility than materials comprising of only atomic ions due to the extended length of the ligands.^{290,291} They therefore can be expected to produce larger responses at pressures closer to those realisable in practical devices. For example, the magnetic order temperature of the three-dimensional cyanides, $[\text{Mn}(4\text{-dmap})]_3[\text{Mn}(\text{CN})_6]_2$, 4-dmap = 4-dimethylaminopyridine, which has $Q = +13 \text{ \% kbar}^{-1}$ ²⁹² and $[\text{Ru}_2(\text{O}_2\text{CCH}_3)_4]_3[\text{Cr}(\text{CN})_6]$, where $Q = +6.5 \text{ \% kbar}^{-1}$,²⁹³ rapidly increase with pressure. However, not all molecular frameworks show such large pressure responses, with the binary dicyanamides, $\text{M}(\text{dca})_2$ $\text{M} = \text{Mn, Co, Fe, Ni}$, $\text{dca} = \text{N}(\text{CN})_2^-$, with three-atom superexchange pathways ($\mu_{1,3}\text{-dca}$), demonstrating a pressure sensitivity between $Q = +0.4$ and $+3.9 \text{ \% kbar}^{-1}$.^{281,294} Nevertheless, the understanding of the pressure response of the magnetism of vdW molecular framework magnets is rapidly developing.^{80,295,296}

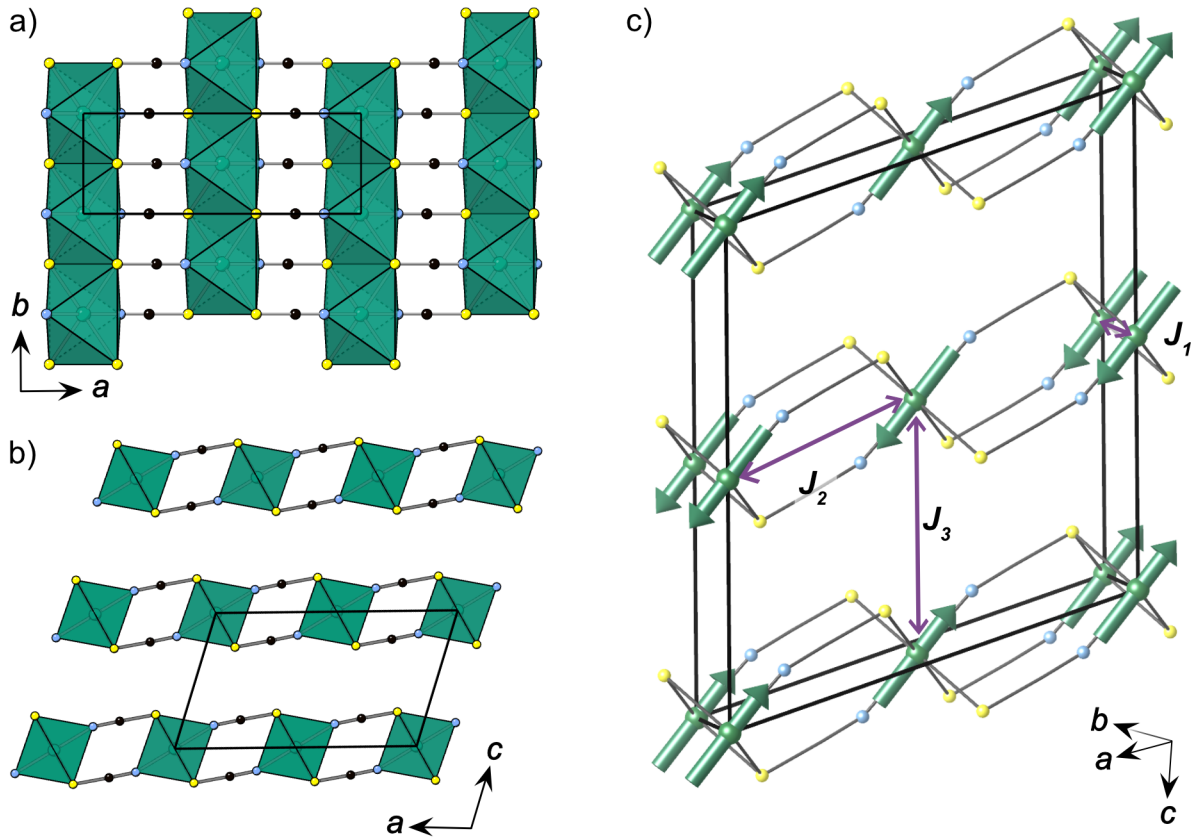


Figure 4.1: Summary of the nuclear and magnetic structure of $\text{Ni}(\text{NCS})_2$ at ambient pressure.⁸⁰ a) The in-plane structure, viewed along the c axis, showing the connectivity of the $[\text{NiS}_4\text{N}_2]$ octahedra. b) Viewed along the b axis, showing the layer stacking. c) The antiferromagnetic ordering (moments as green arrows), with the three nearest neighbour interactions identified (purple arrows). The carbon atoms have been removed for clarity. Ni = green (atoms and octahedra), N = blue, C = black, S = yellow.

Nickel(II) thiocyanate, $\text{Ni}(\text{NCS})_2$, is a member of the binary pseudo-halides $\text{M}(\text{NCS})_2$, $\text{M} = \text{Mn}, \text{Co}, \text{Fe}, \text{Ni}, \text{Cu}$,^{30,80,165,260} which adopt analogous structures to the two-dimensional metal halides MX_2 (Fig. 4.1a, b).²⁹⁷ $\text{Ni}(\text{NCS})_2$ crystallises in the $C2/m$ monoclinic space group, with edge-sharing octahedra which form layers in the ab plane, which stack along the c axis.⁸⁰ It is the only reported member to antiferromagnetically order, $T_N = 54$ K, with ferromagnetic layers (Fig. 4.1c).⁸⁰ The moments correlate ferromagnetically within the ab plane and antiferromagnetically between adjacent planes, ordering with a propagation vector of $\mathbf{k} = (0, 0, \frac{1}{2})$ in the magnetic space group C_c2/c .⁸⁰ The moments are oriented along the N–Ni–N bond direction and are restricted to the ac plane by symmetry. The three nearest neighbour interactions are: J_1 through Ni–S–Ni (b direction), J_2 along Ni–NCS–Ni (a direction) and J_3 occurs between the metals on adjacent layers (c direction, Fig. 4.1d).

Here I report the structural and magnetic changes of $\text{Ni}(\text{NCS})_2$ as it is compressed to pressures up to 8.4 kbar. The evolution of both lattice parameters and the structure under compression have been followed through X-ray and neutron powder diffraction experiments. The combination of magnetometry and low temperature neutron diffraction

measurements show the enhancement of the magnetic ordering temperature with pressure and confirm the magnetic ground state remains throughout compression. Density functional theory (DFT) calculations have been carried out which explain the energetic origins of the observed behaviour.

4.3 Results

4.3.1 Nuclear structure under pressure

To explore the distortions that $\text{Ni}(\text{NCS})_2$ experiences with pressure, ambient temperature powder diffraction measurements were carried out using X-rays (I15, Diamond, UK) and neutrons (D2b, ILL, France).

The variable pressure X-ray data were collected between 0.001 and 4.0 kbar in 0.2 kbar steps, and neutron data were collected at 1.7, 3.4, 5.1 and 6.7 kbar. Rietveld refinements were performed for each dataset, refining the lattice parameters, background and peak shape parameters (Fig. 4.2). The atom positions and anisotropic displacement parameters were fixed to that of the structure at ambient pressure throughout.⁸⁰

From the refinements, the lattice parameters were determined. Both data sets, X-ray and

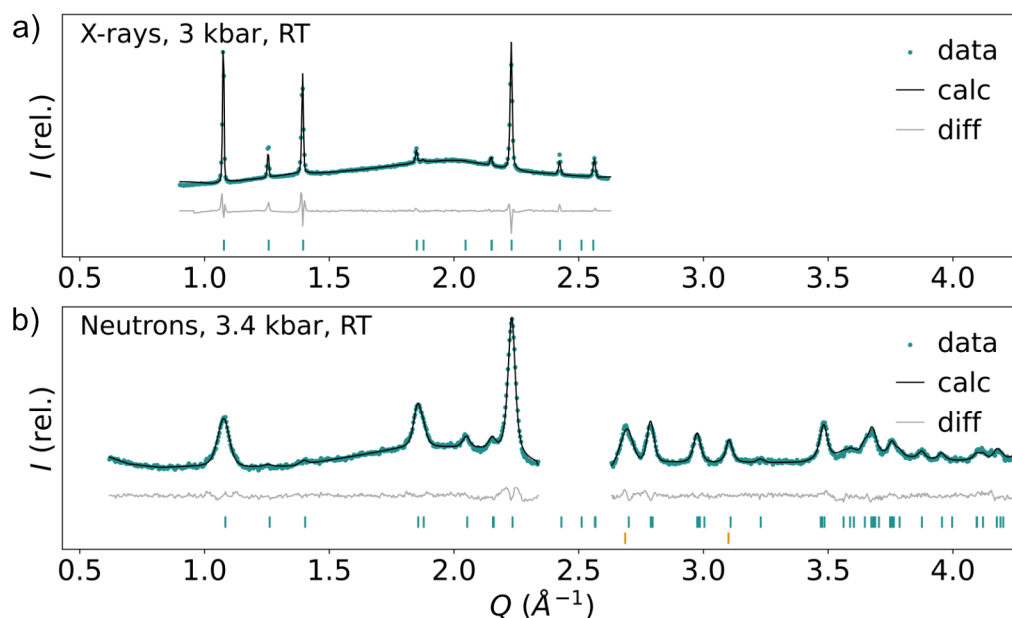


Figure 4.2: Examples of Rietveld refinement results. a) From synchrotron X-ray data (I15, Diamond) measured at 3 kbar and ambient temperature (RT). b) From neutron data (D2b, Institut Laue Langevin, ILL), measured at 3.4 kbar and ambient temperature. Le Bail fits were made to account for reflections arising from the aluminium sample holder. The tickmarks show the position of structural reflections (turquoise) and aluminium (orange).

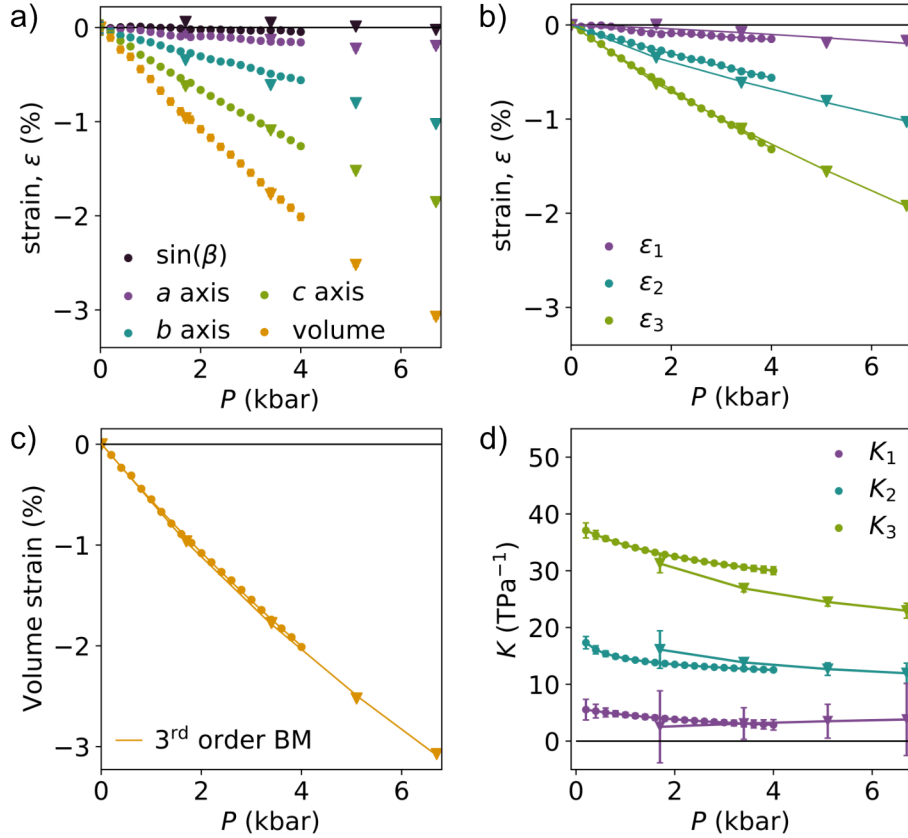


Figure 4.3: Crystallographic parameter variations determined from Rietveld refinements at ambient temperature using X-rays (circles, measured with I15, Diamond, 0.001 to 4 kbar) and neutrons (triangles, measured with D2b, ILL, 0.001 to 6.7 kbar). a) Normalised change of the unit cell parameters. b) Strain (ϵ_i) along the principal axes (X_i) with lines showing the linear compressibilities. c) The volume dependence with pressure, fitted with the third-order Birch-Murnaghan (BM) equation of state with $B_0 = 170(2)$ kbar and $B' = 15(1)$ for X-rays and $B_0 = 156(6)$ kbar and $B' = 22(3)$ for neutrons. d) The compressibility (K) along the principal axes as a function of pressure. Standard errors are shown with vertical lines.

neutron, show that as $\text{Ni}(\text{NCS})_2$ is compressed, all unit cell axes decrease in length while the β angle remains broadly constant (Fig. 4.3a). From refinements of the X-ray data, the volume is reduced from $225.18(6) \text{ \AA}^3$ at 0.001 kbar to $220.65(6) \text{ \AA}^3$ at 4.0 kbar. Fitting the X-ray data to a third-order Birch-Murnaghan equation of state,⁶⁶ gives a bulk modulus $B_0 = 170(2)$ kbar and $B' = 15(1)$ (Fig. 4.3c, circles). Comparable trends are observed for the compressibilities and reduction in axes observed for the neutron (triangles) data up to 6.7 kbar as well ($B_0 = 156(6)$ kbar and $B' = 22(3)$).

To define the strain experienced by the compound, principal axes X_1 , X_2 and X_3 were assigned, where $X_1 \approx a$, along the Ni–NCS–Ni pathway; $X_2 = b$, along the Ni–S–Ni bonds and $X_3 \approx c$, between the layers. The compressibilities $K_i = -1/\epsilon_i \frac{d\epsilon_i}{dP}$ are derived from fitting an empirical equation of state ($\epsilon_i(P) = \epsilon_0 + \lambda(P - P_C)^\nu$). From the pressure dependence of the principal axes, it was found that the compressibilities are very anisotropic. At 4 kbar for the X-ray data, $K_3 = 32.5(3) \text{ TPa}^{-1}$, which is more than double $K_2 = 13.5(1) \text{ TPa}^{-1}$, and $K_1 = 3.8(4) \text{ TPa}^{-1}$ is an order of magnitude smaller. Similar results are obtained for the neutron data up to 6.7 kbar (Table 4.1).

Table 4.1: Compressibilities (K) for the principle axes of $\text{Ni}(\text{NCS})_2$ calculated from synchrotron X-ray data (I15, Diamond) at 4 kbar and from neutron data (D2b, ILL) at 6.7 kbar. The definition of the principal axes (X_i) are given relative to the unit cell (a, b, c) for the structure at 4 kbar

Axes	K (TPa $^{-1}$)		a	b	c
	X-rays	Neutrons			
X_1	3.8(4)	3(2)	0.990	0.0	0.141
X_2	13.5(1)	13.9(8)	0.0	1.0	0.0
X_3	32.5(2)	26.9(6)	0.124	0.0	0.992
V	50.0(5)	48(1)			

To explore the changes in the structure over a broader pressure range, DFT calculations were performed at pressures of 0, 5, 10, 20, 50 and 100 kbar. The calculations, at 0 K, were carried out in the experimentally-derived layered antiferromagnetic ground-state. The bulk modulus, fitted using the third-order Birch-Murnaghan equation of state, is 255.7(2) kbar, with $B' = 6.42(9)$. The compressibilities at 10 kbar are $K_3 = 18.1(5)$ TPa $^{-1}$, $K_2 = 10.1(4)$ TPa $^{-1}$ and $K_1 = 3.0(2)$ TPa $^{-1}$, broadly consistent with the measured compressibilities (Table 4.1). On increasing the pressure to 100 kbar, there is a significant stiffening of all the axes, $K_3 = 5.1(5)$ TPa $^{-1}$, $K_2 = 5.5(8)$ TPa $^{-1}$ $K_1 = 1.9(5)$ TPa $^{-1}$.

4.3.2 Variable temperature high pressure

To investigate the effect of high pressure on the thermal expansion of this material, variable-temperature neutron diffraction data, $T = 20, 40, 180$ and 298 K, were collected at the maximum pressure measured of 6.7 kbar.

$\text{Ni}(\text{NCS})_2$ has normal, positive volumetric thermal expansion, with a coefficient of thermal expansion $\alpha_V = 1/V \frac{dV}{dT} = 42(3)$ MK $^{-1}$. At 6.7 kbar, the thermal expansion is anisotropic with linear thermal expansivities along the principal strain directions of $\alpha_1 = 1/\varepsilon_1 \frac{d\varepsilon_1}{dT} = 26(1)$ MK $^{-1}$, $\alpha_2 = 14(2)$ MK $^{-1}$ and $\alpha_3 = 1.12(5)$ MK $^{-1}$ (Fig. 4.4a). The principal axes definitions are broadly in the same directions as those for the compressibilities.

Within the unit cell, there are also notable structural changes. $\angle\text{Ni-S-Ni}$ (along X_2) expands significantly on cooling, $\Delta\sin(\text{Ni-S-Ni}) = -0.0041(2)$ %, whereas $\angle\text{Ni-N-C}$ and $\angle\text{Ni-S-C}$ (predominantly along X_1) change much less, $\Delta\sin(\text{Ni-N-C}) = -0.00160(6)$ % and $\Delta\sin(\text{Ni-S-C}) = +0.0016(2)$ %. The torsion angle between Ni-S-C-N decreases by $\Delta\sin(\text{Ni-N-C}) = -0.0111(7)$ % (Fig. 4.4b).

At this highest pressure, 6.7 kbar, additional peaks emerged in the neutron datasets at

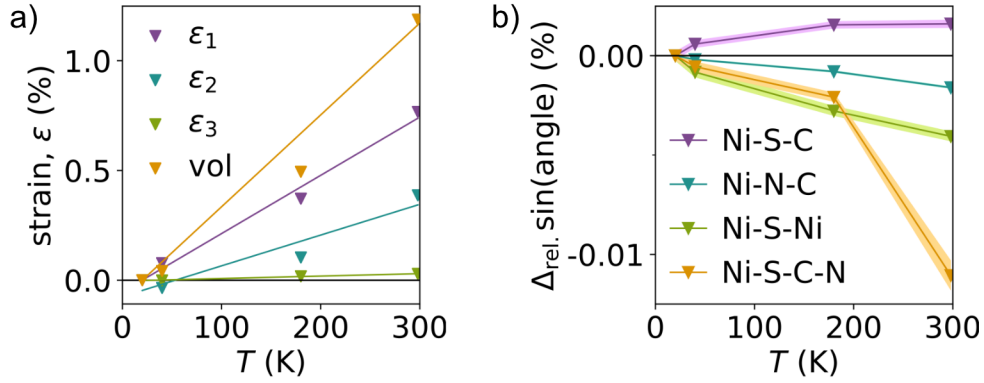


Figure 4.4: Selected results from Rietveld refinements at 6.7 kbar measured at 20, 40, 180 and 298 K using the D2b diffractometer (ILL). a) Relative strain (ϵ_i) in the principle axes and volume, b) relative change in $\sin(\text{angle})$ of Ni–ligand bonds and the dihedral angle Ni–S–C–N. The shaded regions show the calculated errors.

high Q ($\geq 2.7 \text{ \AA}^{-1}$) at temperatures below approximately 55 K. This is well into the magnetic ordered phase, and likely arise from a combination of oxygen and/or nitrogen phases crystallising due to the presence of air in the pressure cell. These were accounted for by including additional Le Bail phases.^{298,299} In addition, no anomalies observed in the magnetometry data corresponding to this transition, further supporting the assumption that this is not sample related.

4.4 Magnetometry

Zero-field-cooled susceptibility measurements were carried out at 1.2(1), 3.8(1), 5.2(1) and 8.4(1) kbar on a pelletised polycrystalline sample. At each pressure, the magnetic susceptibility increases on cooling until a broad maximum is reached at the ordering temperature (Fig. 4.5a). The ordering temperature shifts to higher values as the sample is compressed, and is accompanied by a decrease in the maximum susceptibility. At the highest measured pressure, 8.4(1) kbar, $\text{Ni}(\text{NCS})_2$ orders at $T_N = 64.6(4)$ K, a +19 % increase from ambient pressure. This demonstrates a pressure-sensitivity of $Q = +2.3 \text{ \% kbar}^{-1}$.

Isothermal magnetisation measurements were also carried out at the same pressure points at 10 K between -7 and $+7$ T (Fig. 4.5b). At all pressures, the sample did not show saturation up to 7 T, as expected for a bulk antiferromagnet. The maximum magnetisation measured increases from 1.2(1) to 3.8(1) kbar, before decreasing at higher pressures.

4.5 Magnetic structure under pressure

Since the bulk magnetic measurements showed a significant enhancement in the magnetic ordering temperature, to understand the evolution of the magnetic structure, neutron diffraction measurements were carried out on a powder sample (1.2 g) using the high flux D1b diffractometer (ILL).

Neutron diffraction data were collected below the ordering temperatures at 3, 4.5 and 6.7 kbar at the lowest temperatures for each pressure ($P = 3$ kbar, $T = 34$ K; $P = 4.5$ kbar, $T = 44$ K; $P = 6.7$ kbar, $T = 20$ K). In these low temperature data sets, an additional Bragg reflection appears at 0.54 \AA^{-1} at all pressures (Fig. 4.6a) and no other additional reflections. From the position of the reflection, the propagation vector, \mathbf{k} , was confirmed to be $\mathbf{k} = (0, 0, \frac{1}{2})$, identical to that of the ambient pressure material. This propagation vector corresponds to a doubling of the unit cell along the c axis. From the two maximal magnetic space groups, C_c2/c and C_c2/m , only the ambient pressure magnetic model, C_c2/c , was able to reproduce the observed intensity with a reasonable moment size.

Rietveld refinements were carried out on these datasets in which the magnitude of the nickel moment was fixed to $1.75 \mu_B$, in accordance with the reported size of the moment at 2 K at ambient pressure,⁸⁰ due to the paucity of magnetic Bragg peaks. This then allowed for the angle to be refined as the only free magnetic parameter. At all three pressures, the angle of the moment remains broadly unchanged from the ambient structure model, that is, the moment is oriented along the N–Ni–N bond within the ac plane.

As the moment direction does not change up to 6.7 kbar or on warming at ambient pressure,⁸⁰ for the following magnetic refinements, therefore, the moment orientation was

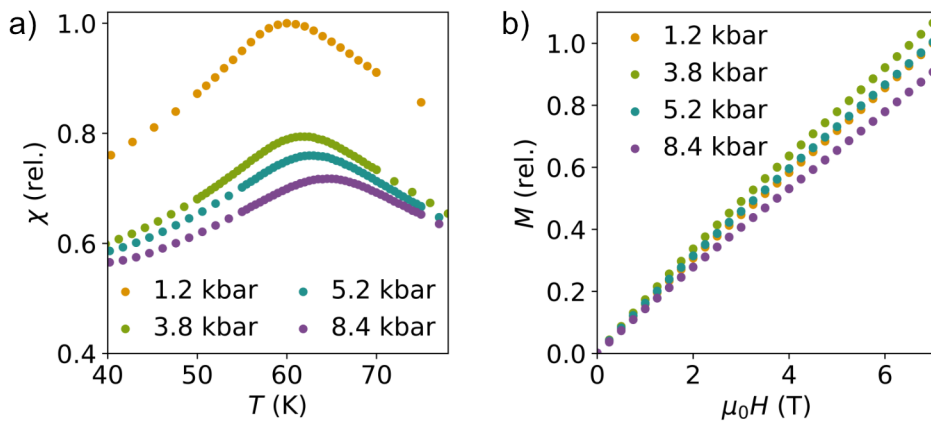


Figure 4.5: a) Magnetic susceptibility measured at 1.2(1), 3.8(1), 5.2(1) and 8.4(1) kbar, the relative susceptibility has been normalised to the maximum susceptibility at 1.2 kbar. b) Isothermal magnetisation measurements carried out at 10 K plotted between 0 to +7 T, showing the relative magnetisation normalised to the maximum magnetisation at 1.2 kbar.

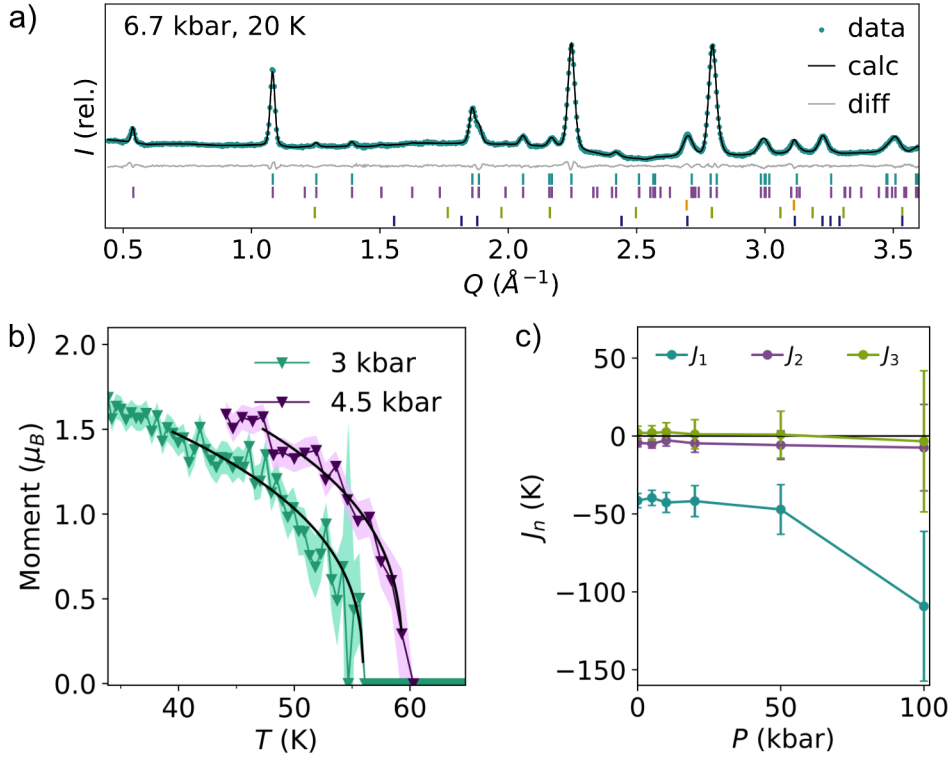


Figure 4.6: Magnetic refinement results from neutron diffraction data (D1b, ILL) a) at 6.7 kbar and 20 K. Le Bail fits were made to account for reflections arising from the aluminium sample holder, oxygen and nitrogen. The tickmarks show the position of structural reflections (turquoise), magnetic reflections (purple), aluminium (orange), oxygen (light green) and nitrogen (dark blue) phases. b) The temperature dependence of the magnetic moment determined from Rietveld refinements of neutron diffraction data at 3 and 4.5 kbar, fitted by a power law Eqn. 4.1 (black line). The shaded regions show the calculated errors of the magnitude of the moment. c) Calculated enthalpies of the three nearest neighbour interactions obtained from DFT calculations at ambient pressure, 5, 10, 20, 50 and 100 kbar, where $J > 0$ describes antiferromagnetic interactions and $J < 0$ for ferromagnetic interactions. The calculated uncertainties associated with fitting to the Heisenberg Hamiltonian are shown with vertical lines.

fixed to point along the N–Ni–N bonds. This allowed the size of the magnetic moment to be refined as the only free magnetic parameter in the final cycles of the refinement.

Having established that the magnetic ground state remains unchanged up to 6.7 kbar, the nature of the magnetic ordering transition was explored. Variable temperature data was collected at 3 kbar ($T = 34$ – 65 K) and 4.5 kbar ($T = 44$ – 60 K). At 3 kbar, the magnetic moment was refined to $1.68(7) \mu_B$ for the lowest temperature point ($T = 34$ K) and the ordering temperature is found at $T_N = 56.1(5)$ K. At 4.5 kbar the refined moment is $1.58(7) \mu_B$ ($T = 44$ K) and decreases with temperature to $0 \mu_B$ at $T_N = 58.0(5)$ K. The refined magnetic moments was fitted to a power law in the vicinity of the transition,

$$M = A(T_N - T)^\beta, \quad (4.1)$$

where A is a proportionality constant, T_N is the ordering temperature and β is a critical exponent (Fig. 4.6b). At 3 kbar, the fitted values were $\beta = 0.36(6)$ and $T_N = 55.9(7)$

K. At 4.5 kbar, $\beta = 0.33(5)$ and $T_N = 59.3(3)$ K. The values of β are in between 0.326 and 0.367 expected for a three-dimensional Ising and Heisenberg antiferromagnet.²¹⁵

In addition, DFT calculations were performed to understand the exchange interactions responsible for the magnetic behaviour observed. Geometry optimisations, including both atomic positions and cell parameters, were carried out to probe the magnetic ground state at pressures of 0, 5, 10, 20, 50 and 100 kbar, for six high symmetry configurations and the resultant energies and enthalpies were calculated using the Hamiltonian $E = \sum_{ij} J_{ij} S_i \cdot S_j + E_0$.

The DFT energies obtained from the calculations were fitted to a Heisenberg collinear spin Hamiltonian to extract three interactions, J_1 along the Ni–S–Ni direction, J_2 along the Ni–S–C–N–Ni direction and J_3 corresponding to the interactions between layers. At ambient pressure, J_1 is large and ferromagnetic $-43(8)$ K, J_2 weaker and also ferromagnetic $-4(4)$ K and J_3 is zero within error, consistent with the expected ground state (Fig. 4.6c). The large values of the errors suggest that the Heisenberg Hamiltonian employed is perhaps not appropriate: either due to large single ion effects or higher order interactions (e.g. biquadratic interactions). It is likely that up to 50 kbar the reported ambient antiferromagnetic structure is the most stable configuration. However, there is not a strong trend in the predicted J values with pressure beyond the error of the calculations. The relative energy differences between selected spin configurations here are less than 1 meV/metal, which are close to the limits of accuracy for these DFT calculations.

4.6 Discussion

From the diffraction data, the bulk modulus of $\text{Ni}(\text{NCS})_2$ is calculated to be $B_0 = 170(2)$ kbar, which shows that $\text{Ni}(\text{NCS})_2$ is one of the softer van der Waals compounds, for instance, CrBr_3 has $B_0 = 230$ kbar³⁰⁰ and FePSe_3 has $B_0 = 828$ kbar.²⁸⁰ High pressure structural phase transitions are common in layered compounds,^{278,301,302} however, the DFT calculations do not provide any evidence of a structural phase transition up to 100 kbar. Ab initio structure searches and larger supercell calculations together with higher pressure calculations would allow further exploration of the potential for new $\text{Ni}(\text{NCS})_2$ phases. These calculations also suggest that any metallisation transition occurs significantly above 100 kbar, compared to NiI_2 $P_c = 190$ kbar,³⁰³ FeCl_2 $P_c = 450$ kbar²⁸⁹ and FePS_3 $P_c \approx 140$ kbar.²⁷⁸

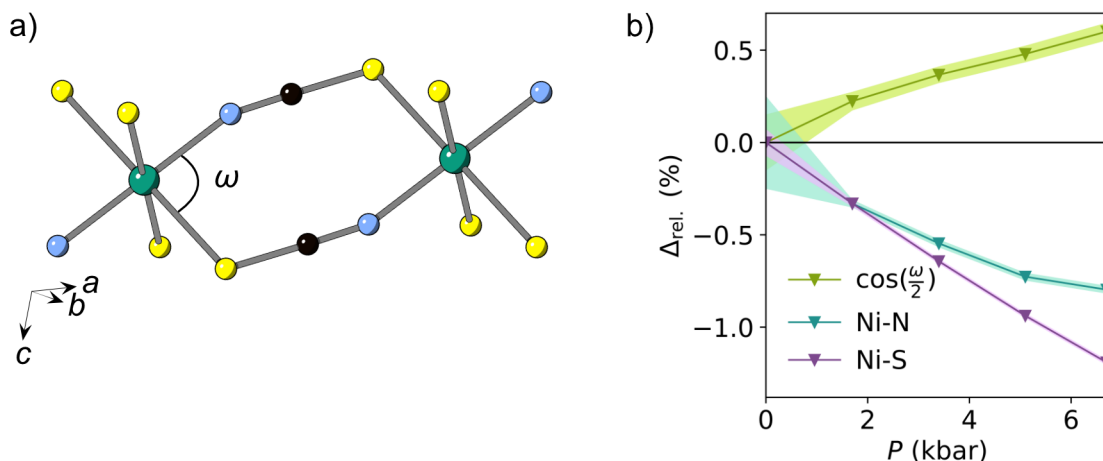


Figure 4.7: a) Nickel ions connected through two NCS⁻ ligands, showing the ‘hinge’ angle, ω . Ni = green, N = blue, C = black, S = yellow. b) Relative change in the bond lengths Ni–N and Ni–S, and the relative change in $\cos(\frac{\omega}{2})$ with pressure. The ambient pressure values were obtained from ref.³⁰ The shaded regions show the errors.

Ni(NCS)₂ can also be compared with other pseudobinary molecular frameworks. Since substituting the metal cation species can influence the flexibility of the structure, the discussion is focussed on Ni²⁺ frameworks.³⁰⁴ The three-dimensional Ni(dca)₂ (dca = N(CN)₂) has a larger bulk modulus, $B_0 = 360$ kbar,³⁰⁵ than Ni(NCS)₂. As the ligand length increases, it would be expected that the structure becomes more flexible,³⁰⁶ and, therefore have a lower B_0 . However, as Ni(dca)₂ is three-dimensionally connected, the resultant bulk modulus is larger than that of layered Ni(NCS)₂. The volumetric compressibility provides only a partial picture, as both compounds are anisotropic. The compressibility of Ni(dca)₂ along the b and c axes is similar to that of Ni(NCS)₂ along the X_2 and X_3 ($K_b = 11.1$ TPa⁻¹ and $K_c = 24.1$ TPa⁻¹ for Ni(dca)₂), but Ni(dca)₂ shows negative linear compressibility (NLC) in the third (a) direction. The materials have similar ligand arrangements along the a axis, where the nickel ions are bridged by two ligands coordinated in an end-to-end arrangement. In both materials, the ‘hinge’ ligand–metal–ligand bond angles, ω ($\omega = \angle\text{N–Ni–S}$ and $\angle\text{N–Ni–N}$, Fig. 4.7a), decrease: $[\Delta \cos(\frac{\omega}{2})]/P = 0.09$ % kbar⁻¹ (NCS), compared to $[\Delta \cos(\frac{\omega}{2})]/P = 0.16$ % kbar⁻¹ (dca). Ni(NCS)₂ has softer Ni–L bonds, meaning that there is still contraction in the bond lengths (Ni–N = -0.12 % kbar⁻¹ and Ni–S = -0.18 % kbar⁻¹, Fig. 4.7b). This competition between the two components is likely the cause of the apparent stiffness of the a axis. In contrast, the square-planar Ni(CN)₂ is significantly stiffer, $B_0 = 1050$ kbar, perhaps due to the planarity of the structure and linearity of Ni–CN–Ni bonds.³⁰⁷

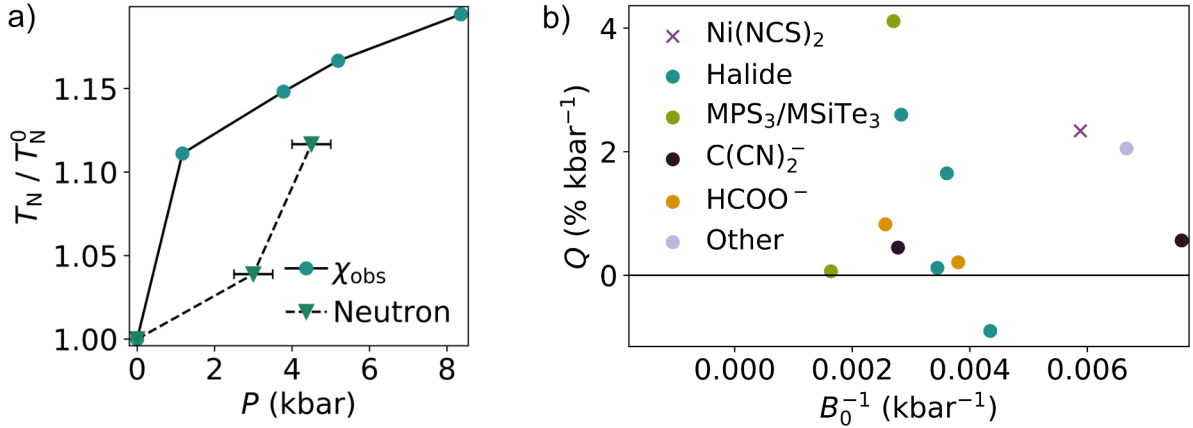


Figure 4.8: Relative change in T_N as a function of pressure, derived from susceptibility (circles) and neutron diffraction data (triangles). Error bars related to pressure determination are shown for the neutron data, the error bars are contained within the symbols for the magnetometry data. The ordering temperatures were normalised to the ambient pressure ordering temperature, $T_N^0 = 54$ K. b) Selected values for the reciprocal bulk moduli (B_0^{-1}) against Q ($\frac{dT_N}{T_N} \frac{1}{dP}$) for reported values and Ni(NCS)₂ (purple cross, from this work). The compounds have been grouped by ligand. Tabulated values can be found in the appendix, Table 4.5.

The high pressure variable temperature data show that, despite being a layered structure, Ni(NCS)₂ has near zero thermal expansion along the X_3 direction. In comparison, there is positive thermal expansion along X_1 and X_2 directions (Fig. 4.4a). Calculating the thermal expansion coefficients from the published ambient pressure data⁸⁰ gives values of $\alpha_1 = 26(2) \text{ MK}^{-1}$, $\alpha_2 = 2.1(9) \text{ MK}^{-1}$ and $\alpha_3 = -5.9(9) \text{ MK}^{-1}$. Here, the principal axes are defined as $X_1 = 0.47a + 0.88c$, $X_2 = b$ and $X_3 = -0.56a + 0.83c$ at 100 K. This is rotated slightly in comparison to the high pressure data (whose definitions are approximately equal to directions given in Table 4.1). X_3 at ambient pressure exhibits negative thermal expansion which is uncommon, however, it can be observed in other anisotropic molecular framework compounds.^{308,309} These values are comparable to those seen at 6.7 kbar, but the within-layer expansion has decreased. This behaviour is not uncommon in layered molecular frameworks and likely reflects the stiffening of the transverse out-of-plane vibrations.³⁰⁸ Since the ambient pressure structure was measured between 1 and 100 K, and the high pressure data were measured between 20 and 298 K, direct comparison of the coefficients should be done cautiously. Future investigations would be needed for detailed quantitative comparisons.

The most significant change observed on compressing Ni(NCS)₂ is the marked increase in magnetic ordering temperature, $Q = +2.3 \text{ \% kbar}^{-1}$. This increase is large compared to other nickel molecular frameworks, such as Ni(dca)₂ ($Q = +0.4 \text{ \% kbar}^{-1}$),²⁹⁴ NH₄Ni(HCOO)₃ ($Q = +0.2 \text{ \% kbar}^{-1}$)³¹⁰ and NiCl₂(pym)₂, pym = pyrimidine, ($Q = +1.3 \text{ \% kbar}^{-1}$).³¹¹ The increase of ordering temperatures in these compounds results from both changes in exchange interactions, including the increase in strength of interactions and reduction of frustrating interactions, and the single-ion anisotropy. The DFT calcula-

tions suggest this compound is not magnetically frustrated, and so the general anticipated enhancement of exchange will be largely reinforcing. The significant uncertainties in the DFT-derived superexchange parameters suggest that higher level calculations, incorporating single-ion anisotropy and higher-order exchange interactions, might be necessary for complete understanding of the underlying magnetic Hamiltonian. The interlayer J_3 pathway, through Ni–S··S–Ni, decreases in distance significantly, and is likely this is the limiting factor in the high pressure ordering temperature.

There is no evidence of changes in spin orientation with pressure in Ni(NCS)₂ up to 6.7 kbar. This is consistent with the behaviour of other vdW metal halides, including NiI₂, CoI₂³⁰³ and FeCl₂.³¹² This is perhaps due to strong easy-axis single-ion anisotropy in this material.^{261,313}

This shift towards a three-dimensional exchange network can be seen in the critical exponent of the temperature dependence of the staggered magnetic moment. A power law fit (Eqn. 4.1) of the Rietveld-refined magnetic moment as a function of temperature at 3 and 4.5 kbar (Fig. 4.6b) gave critical exponents of $\beta = 0.36(6)$ and $0.33(5)$, comparable to the three-dimensional Heisenberg results ($\beta = 0.367$). Whereas, fitting Eqn. 4.1 to the published ambient pressure data⁸⁰ gave $\beta = 0.25(4)$ and $T_N = 60.3(6)$ K. The high pressure values are consistent with those of three-dimensional molecular framework magnets, e.g. Mn(dca)₂(pyz) (pyz = pyrazine) where $\beta = 0.38$,³¹⁴ compared to the ambient pressure exponent which is closer to that of other vdW magnets, such as NiCl₂ where $\beta = 0.27$ ²²¹ and FeCl₂ where $\beta = 0.29$.²²²

4.7 Conclusion

The effect of pressure on the structure and magnetism of the vdW framework Ni(NCS)₂ has been studied. X-ray and neutron powder diffraction data reveal strongly anisotropic strain with the interlayer direction being an order of magnitude more compressible than the a direction. Low temperature neutron diffraction measurements combined with susceptibility data show there is a significant increase in the magnetic ordering temperature with pressure, driven by the reduction of the interlayer separation.

This work has demonstrated the use of a thiocyanate framework as a source of flexibility to enhance the changes in the magnetic properties of a vdW material. It suggests that further molecular framework magnets hold potential to show marked responses to compression. Following this work, it could also be rewarding to explore the response of monolayer Ni(NCS)₂ under pressure to observe if more drastic changes to the magnetic structure can be obtained for a few-layer molecular framework.

4.8 Experimental

4.8.1 Synthesis of Ni(NCS)₂

The synthesis of the powder samples of Ni(NCS)₂ was carried out following the reported synthetic method of Bassey *et al.*⁸⁰ A typical synthesis (quantities as for the neutron sample) is described below.

NiSO₄ · 6 H₂O (16.56 g, 63 mmol) was dissolved in deionised H₂O (50 mL), giving a clear green solution. An aqueous solution of Ba(SCN)₂ · 3 H₂O (19.37 g, 63 mmol, 120 mL) was added, with the rapid formation of a white precipitate and a green solution. The reaction mixture was stirred at room temperature overnight and the precipitate was removed by centrifugation and filtering under reduced pressure. The solution was removed *in vacuo*, giving a green-brown microcrystalline powder of Ni(NCS)₂. The compound is stable to humidity in the investigated conditions.

4.8.2 Magnetic Measurements

Measurements of the magnetic susceptibility were carried out by Dr David Jarvis (University of Cambridge), Dr Cheng Liu (University of Cambridge), Dr Siddharth Saxena (University of Cambridge) and Dr Matthew Cliffe (University of Nottingham) on a pelletised powder sample of Ni(NCS)₂ using a Quantum Design Magnetic Property Measurements System (MPMS) 3 Superconducting Quantum Interference Device (SQUID) magnetometer with moment measurements carried out in direct current (DC) mode. The measured data were collected at pressures of 1.2, 3.8, 5.2, 8.4 kbar. The zero-field-cooled (ZFC) susceptibility was measured in an applied field of 0.01 T over the temperature range 2 to 300 K. The pressure was applied using a BeCu piston cylinder pressure cell from CamCool Research Limited, with a Daphne 7373 oil pressure medium. A small piece of Pb was included in the sample space to act as a pressure gauge.⁶² As $M(H)$ is linear in this field regime, the small-field approximation for the susceptibility, $\chi(T) \simeq \frac{M}{H}$, where M is the magnetisation and H is the magnetic field intensity, was taken to be valid. Isothermal magnetisation measurements were carried out on the same sample at 10 K over the field range -7 to $+7$ T for each pressure point.

4.8.3 DFT

Density functional theory calculations were performed by Dr Sanliang Ling (University of Nottingham) to probe the structures and energetics of spin order of Ni(NCS)₂. Spin-

polarized DFT+ U method (with Grimme’s D3 van der Waals correction²⁷¹) was employed in structural optimisations and energy calculations, using the Vienna Ab initio Simulation Package (VASP)²⁷². In the DFT+ U calculations, a U value of 5.1 eV was used for the d-electrons of Ni²⁺ cations,^{273,274} and a range of ferromagnetic and antiferromagnetic spin solutions were considered for magnetic Ni²⁺ cations (see Table 4.4). A plane-wave basis set was used with a kinetic energy cutoff of 520 eV to expand the wavefunctions. The Perdew-Burke-Ernzerhof functional²⁷⁵ in combination with the projector augmented wave method^{276,277} were used to solve the Kohn-Sham equations. An energy convergence threshold of 10^{-6} eV was used for electronic energy minimisation calculations, and the structural optimisations, including cell parameters and atomic positions, were considered converged if all interatomic forces fall below 0.01 eV/Å. All DFT calculations have been performed in the primitive cell (2 formula units per cell) using a k -grid with a k -points spacing of around 0.1 \AA^{-1} . To improve the accuracy of the three nearest neighbour magnetic interactions determined from DFT calculations at different pressures, single point DFT energy calculations were additionally performed of the various spin configurations at the optimised structures with a higher planewave cutoff energy of 800 eV. It is noted that the relative energy difference between several spin configurations in the DFT calculations can be less than 1 meV/metal (depending on pressure), which is close to the DFT accuracy that can be achieved with the current computational settings.

4.8.4 Synchrotron diffraction measurements

X-ray powder diffraction experiments were performed at beamline I15 at the Diamond Light Source, UK, by Jem Pitcairn (University of Nottingham), Emily Myatt (University of Nottingham), Sebastian Hallweger (Technical University of Munich), Silva Kronawitter (Technical University of Munich), Dr Matthew Cliffe (University of Nottingham) and Dr Gregor Kieslich (Technical University of Munich). A wavelength of $\lambda = 0.4246 \text{ \AA}$ was used, applying a custom-made high pressure powder X-ray diffraction setup suitable for measurements up to 4 kbar.⁵⁸ A powder sample of Ni(NCS)₂ was filled into a soft plastic capillary together with silicone oil AP-100 as non-penetrating pressure transmitting medium to maintain hydrostatic conditions. The capillaries were sealed with Araldyte-2014-1. The capillary was loaded into, and in direct contact with, the sample chamber consisting of a metal block filled with water. The water acts as a pressure transmitting medium, controlled with a hydraulic gauge pump.

Constant wavelength powder X-ray diffraction data were collected at room temperature in the pressure range 0.001 to 4 kbar with a step of 0.2 kbar and an estimated error of ± 0.0030 bar. The data were processed by myself using DAWN³¹⁵ with a LaB₆ calibration. Rietveld refinements of the nuclear model were completed by myself using the FullProf

program³⁷ and strain analysis carried out using PASCAL.⁶⁴

4.8.5 Neutron Diffraction Measurements

4.8.5.1 High resolution measurements (D2b)

Constant wavelength neutron powder diffraction data were collected on the high-resolution D2b diffractometer³¹⁶ at the Institut Laue-Langevin (ILL) by Dr Laura Cañadillas Delgado (ILL), Dr Oscar Fabelo (ILL), Dr Matthew Cliffe, Dr Andrew Cairns (Imperial College London) and myself. The incident wavelength was $\lambda = 1.59 \text{ \AA}$ and the scattering was measured over an angular range of $10 < 2\theta < 160^\circ$. The sample was loaded in an aluminium holder and placed within an aluminium gas pressure cell with helium used as a pressure transmitting medium. Diffraction data were collected at room temperature with applied pressures of 1.7, 3.4, 5.1 and 6.7 kbar, with an estimated error of ± 0.5 kbar. Further diffraction data were collected at a pressure of 6.7 kbar at temperatures of 20, 40 and 180 K. The pressure was set at room temperature, then the system was cooled for the low temperature data. The cell was operated with a gas compressor to regulate the pressure as the temperature was lowered and ensure maintenance of constant pressure. A heater inside the gas capillary ensured the helium was gaseous at low temperatures. NOMAD software²²⁵ from the ILL was used for data collection. Refinements of the nuclear models were completed using the FullProf program.³⁷

4.8.5.2 High intensity measurements (D1b)

Constant wavelength powder neutron diffraction data were collected on the high-intensity medium resolution D1b diffractometer²⁷⁰ at the ILL by Dr Laura Cañadillas Delgado, Dr Oscar Fabelo, Dr Matthew Cliffe, Dr Andrew Cairns and myself. The incident wavelength was $\lambda = 2.52 \text{ \AA}$ and the scattering was measured over an angular range of $2 < 2\theta < 128^\circ$. The sample was loaded in an aluminium holder and placed within an aluminium gas pressure cell with helium used as a pressure transmitting medium. Diffraction data were collected at room temperature with applied pressures of 3, 4.5 and 6.7 kbar, with an estimated error of ± 0.5 kbar. A thermal diffractogram was collected at 3 kbar, heated with a programmed ramp of 0.05 K min^{-1} between 34 and 65 K. A second thermal diffractogram was collected at 4.5 kbar, heated with a programmed ramp of 0.07 K min^{-1} between 44 and 60 K. At a pressure of 6.7 kbar, data were collected at a constant temperature of 20 K. The pressure was set at room temperature, then the system was

cooled for the low temperature data. The cell was operated with a gas compressor to regulate the pressure as the temperature was lowered and ensure maintenance of constant pressure. A heater inside the gas capillary ensured the helium was gaseous at low temperatures. NOMAD software²²⁵ from the ILL was used for data collection. Refinements of the nuclear and magnetic model were completed using the FullProf program.³⁷

4.9 Appendix

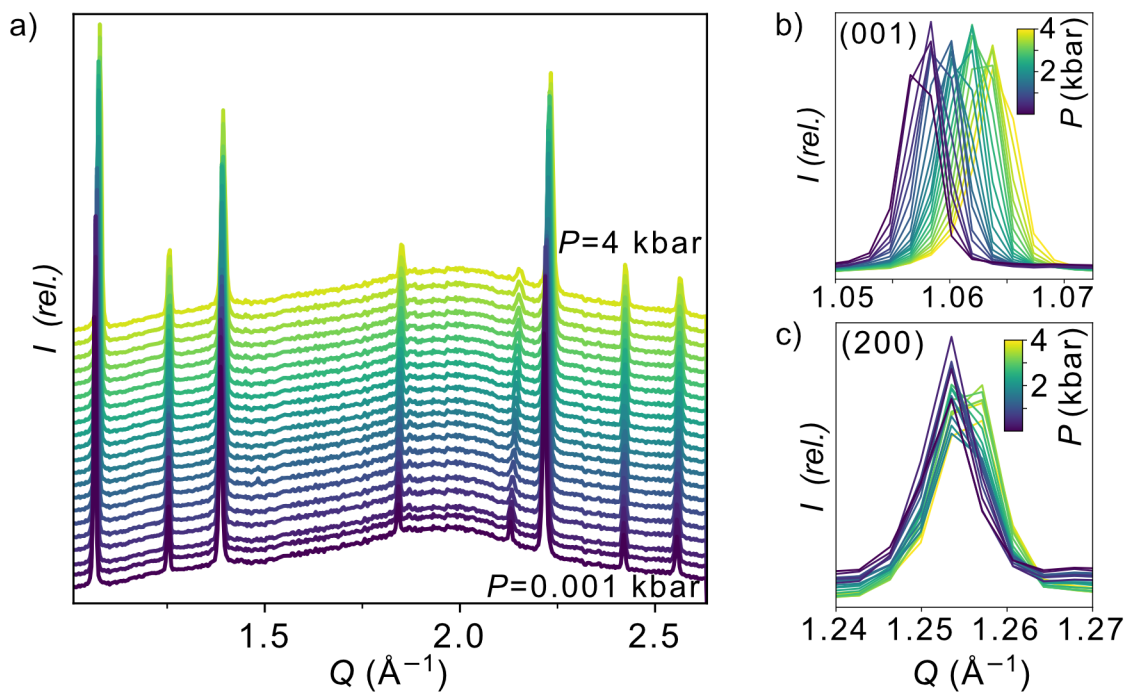


Figure 4.9: X-ray diffraction patterns (I15, Diamond) between 0.001 and 4 kbar with 0.2 kbar intervals. Evolution of the selected Bragg reflection are shown for b) the (001) plane and c) the (002) plane.

Table 4.2: Summary of the pressure dependence of the Néel temperature (T_N) determined from the magnetisation data, the change in T_N relative to the ambient $T_N^0 = 54$ K and the change in the maximum susceptibility relative to 1.2 kbar

P (kbar)	T_N (K)	T_N/T_N^0	$\Delta_{\text{rel.}}\chi$
1.2(1)	60.3(2)	1.11	0.0
3.8(1)	61.9(2)	1.15	-0.21
5.2(1)	62.8(2)	1.17	-0.24
8.4(1)	64.6(4)	1.19	-0.28

Table 4.3: Spin configurations considered for DFT calculations, with antiferromagnetic (−), ferromagnetic (+) interactions, and 0 where the interactions are compensated, for the the three nearest neighbour interactions

Model	J_1	J_2	J_3
FM	+	+	+
AFM1	+	+	−
AFM2	+	−	+
AFM3	+	−	−
AFM4	−	0	−
AFM5	−	0	+

Table 4.4: Relative enthalpies, H of the high pressure structures of $\text{Ni}(\text{NCS})_2$ considering the ferromagnetic and several antiferromagnetic spin state between ambient and 100.0 kbar

Model	ΔH ambient (meV/Ni)	ΔH 5 kbar (meV/Ni)	ΔH 10 kbar (meV/Ni)	ΔH 20 kbar (meV/Ni)	ΔH 50 kbar (meV/Ni)	ΔH 100 kbar (meV/Ni)
FM	0.0	0.0	0.0	0.0	0.0	0.0
AFM1	−1.81	−1.87	−2.35	−3.06	−4.51	+14.36
AFM2	+0.32	+0.37	−0.83	−1.18	−2.46	−16.09
AFM3	+0.86	+1.19	+0.39	+1.35	+1.99	−3.43
AFM4	+7.13	+6.78	+6.57	+6.47	+6.68	−27.34
AFM5	+6.85	+6.76	+6.75	+6.50	+7.08	−27.28

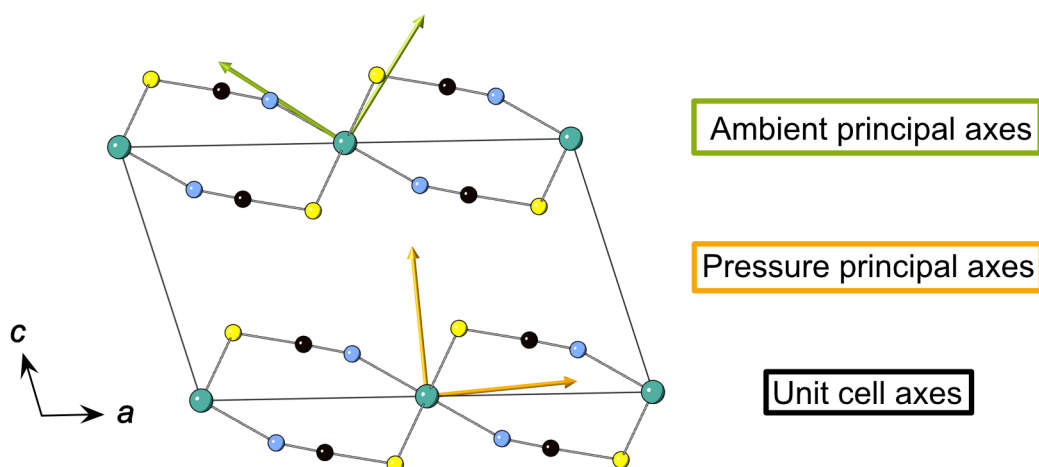


Figure 4.10: Comparison of the principal axes at ambient pressure (green arrows) and at 4 kbar (orange arrows). At ambient pressure and 100 K: $X_1 = 0.47a + 0.88c$, $X_2 = b$ and $X_3 = -0.56a + 0.83c$. At 4 kbar and 298 K: $X_1 = 0.99a + 0.141c$, $X_2 = b$ and $X_3 = 0.124a + 0.992c$.

Table 4.5: Selected values of bulk moduli (B_0) and magnetic pressure responsiveness, $Q = \frac{dT_c}{T_c} \frac{1}{dP}$, with the maximum pressure measured ($P_{\max}(T_c)$) and the value of the ordering temperature at the maximum pressure ($T_{c \max}$) relative to the ambient pressure ordering temperature (T_{c0}). DA = dimethyl ammonium, dca = dicyanamide ($\text{N}(\text{CSN})_2^-$), pym = pyrimidine

Compound	$P_{\max}(T_c)$ (kbar)	T_{c0} (K)	$T_{c \max}$ (K)	B_0 (kbar)	$Q / \%$ kbar $^{-1}$	Ligand
Ni(NCS) $_2$	8.4	54	64.6(4)	170(2)	2.3	NCS
NiI $_2$	190	75	310 ²⁸²	277 ³⁰³	1.6	halide
CrBr $_3$	8.4	33	30.50 ³¹⁷	230 ³¹⁷	-0.9	halide
FeCl $_2$	4	23	23.11 ³¹²	290 ²⁸⁹	0.1	halide
FeCl $_2$	420	23	274 ²⁸⁷	353 ²⁸⁹	2.6	halide
CrSiTe $_3$	78	32.8	138 ³¹⁸	370 ³¹⁹	4.1	SiTe $_3$
FePS $_3$	200	118	133 ²⁷⁸	611 ²⁸⁰	0.1	PS $_3$
Ni(dca) $_2$	17	21	22.6 ²⁹⁴	360 ³⁰⁵	0.4	dca
Co(dca) $_2$	10	8	8.45 ²⁹⁴	131.5 ³²⁰	0.6	dca
NH $_4$ Ni(HCOO) $_3$	10	29.1	29.71 ³¹⁰	263 ³²¹	0.2	formate
DAMn(HCOO) $_3$	10	8.5	9.2 ³¹⁰	390 ³²¹	0.8	formate
Fe(pym)Cl $_2$	7.5	6.5	7.5 ³¹⁰	150 ³²¹	2.1	pym

Chapter 5

Modulated phase transitions and magnetic properties of the solid solutions



5.1 Summary

- Solid solutions of the methylammonium metal formates, $[\text{CH}_3\text{NH}_3]\text{Co}_x\text{Ni}_{1-x}(\text{HCOO})_3$ $x = 0.25, 0.50, 0.75$, have been synthesised, obtaining single crystals suitable for neutron studies.
- Susceptibility measurements showed that all of the compounds magnetically order with ordering temperatures on a linear continuum between the cobalt and nickel end-members.
- Single crystal Laue neutron diffraction measurements show $[\text{CH}_3\text{NH}_3]\text{Co}_{0.75}\text{Ni}_{0.25}(\text{HCOO})_3$ and $[\text{CH}_3\text{NH}_3]\text{Co}_{0.25}\text{Ni}_{0.75}(\text{HCOO})_3$ follow similar phase transitions to their respective parent compounds.
- The series of phase transitions of $[\text{CH}_3\text{NH}_3]\text{Co}_{0.50}\text{Ni}_{0.50}(\text{HCOO})_3$ were followed through monochromatic neutron diffraction experiments. Two modulated phase transitions are observed, before a modulated magnetic phase is obtained below the magnetic ordering temperature.

5.2 Introduction

The fundamental concepts of diffraction rely on the crystal exhibiting a three-dimensional periodicity, driven by translational symmetry. However, this translational symmetry is broken in modulated crystals. A structure is modulated where the average translational symmetry is disrupted by the introduction of an additional periodic function. The modulation can describe the atomic displacements or occupancies (for structural modulations),³²² where the periodicity of the modulations are larger than that of the average structure. If the modulation periodicity can be described by a simple fraction, the structure is categorised as a commensurately modulated compound. If an irrational value is necessary, the compound is said to adopt an incommensurately modulated structure.

The primary indicator of modulated phases are their satellite reflections, reflections that cannot be indexed by a three-dimensional space group and are positioned around the main Bragg reflection at specific d -spacings. From the satellite reflections, the modulation periodicity, described by the wavevector \mathbf{q} , can be calculated. The driving force behind the modulated phases lie in unresolved frustration in the system. Explored examples of mechanisms which have induced modulated compounds include hydrogen bonding,¹⁸ Jahn-Teller distortions³²³ and inter/intra-molecular steric constraints.³²⁴ In each case, the competing interactions result in the loss of translational symmetry between average unit cells.

Reports of molecular frameworks which exhibit incommensurately modulated phases are limited. Two compounds which have reported structures describing phase transitions to incommensurately modulated structures fall under the same family of molecular framework, methylammonium metal formates, $[\text{CH}_3\text{NH}_3]\text{M}(\text{HCOO})_3$, $\text{M} = \text{Co}$ and Ni .^{18,194} Although isomorphous at ambient temperature, the series of temperature-induced phase transitions exhibited by the two compounds are not equivalent (Fig. 5.1).

At ambient temperature $[\text{CH}_3\text{NH}_3]\text{M}(\text{HCOO})_3$, $\text{M} = \text{Co}$ and Ni , crystallise in the orthorhombic space group $Pnma$.³²⁵ On cooling, $[\text{CH}_3\text{NH}_3]\text{Co}(\text{HCOO})_3$ experiences its first phase transition at approximately 128 K to the superspace group $Pnma(00\gamma)0s0$.¹⁸ In this phase, there is a modulated unit cell, with the wavevector $\mathbf{q} = 0.1430(2)\mathbf{c}^*$, describing a modulation length $c/\mathbf{q} = 8.26/0.1430 = 57.76 \text{ \AA}$, 6.99 times that of the average c axis. At 96 K, a second transition is observed where there is a change in the wavevector $\mathbf{q} = 0.1247(2)\mathbf{c}^*$, however the symmetry of the crystal remains the same, $Pnma(00\gamma)0s0$. In this phase, the modulation length is approximately 65.46 Å , 7.92 times larger than the average unit cell. For both the modulated phases, the atom displacement occurs predominately along the b axis, with the amplitude displacements larger for the second modulated phase. Below 78 K a fourth phase is obtained, a twinned, non-modulated

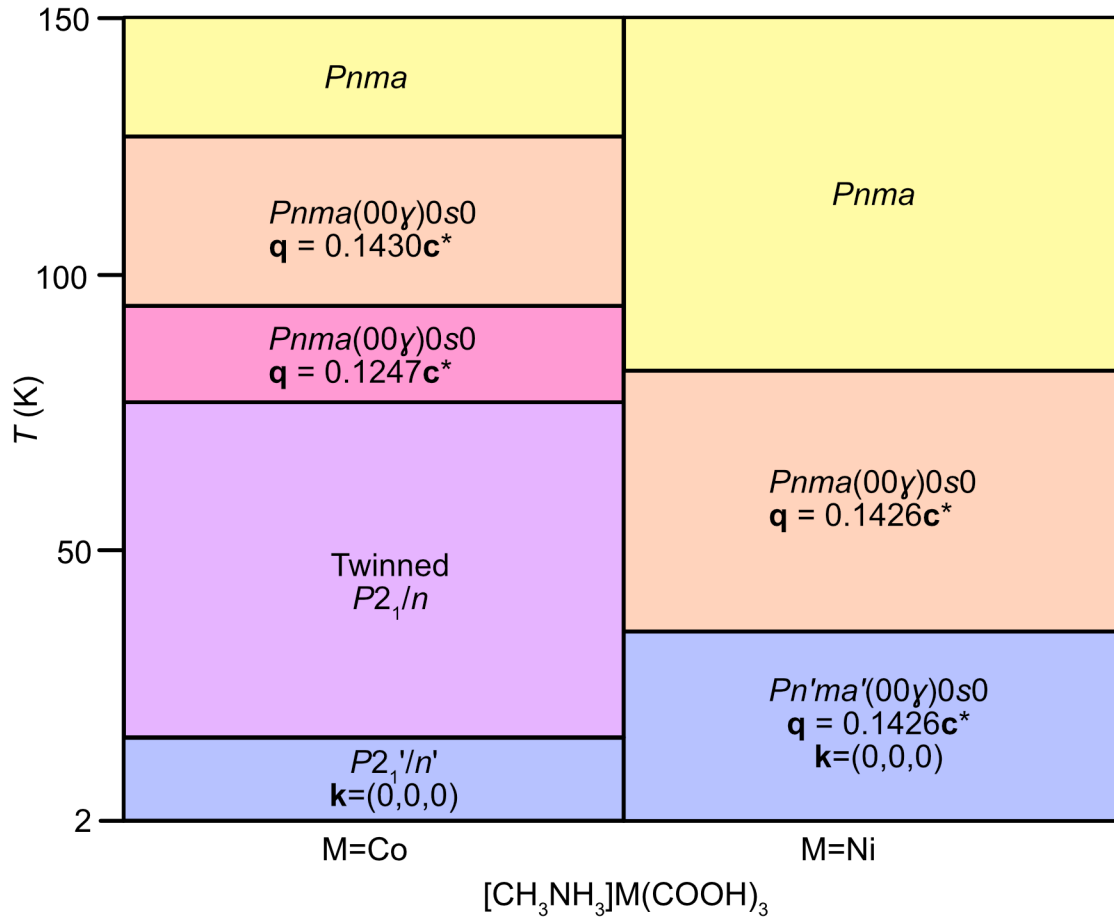


Figure 5.1: The temperature dependent phase evolution for a single crystal of $[\text{CH}_3\text{NH}_3]\text{Co}(\text{HCOO})_3$ and $[\text{CH}_3\text{NH}_3]\text{Ni}(\text{HCOO})_3$ from 2 to 150 K. Above 150 K to ambient temperature, there are no further phase transitions observed. The lowest temperature transitions for each metal (blue) indicate the magnetic phase.

monoclinic structure with $P2_1/n$ symmetry.³²⁶ The onset of long-range magnetic ordering with weak ferromagnetic behaviour is observed at 16 K, with the ferromagnetic component along the c axis (Fig. 5.2).^{163,327,328} In the single crystal study, only the monoclinic $P2_1/n'$ magnetic structure is observed,¹⁸ however, with powder neutron diffraction data a combination of $P2_1/n'$ and $Pn'ma'$ magnetic phases are reported.³²⁶

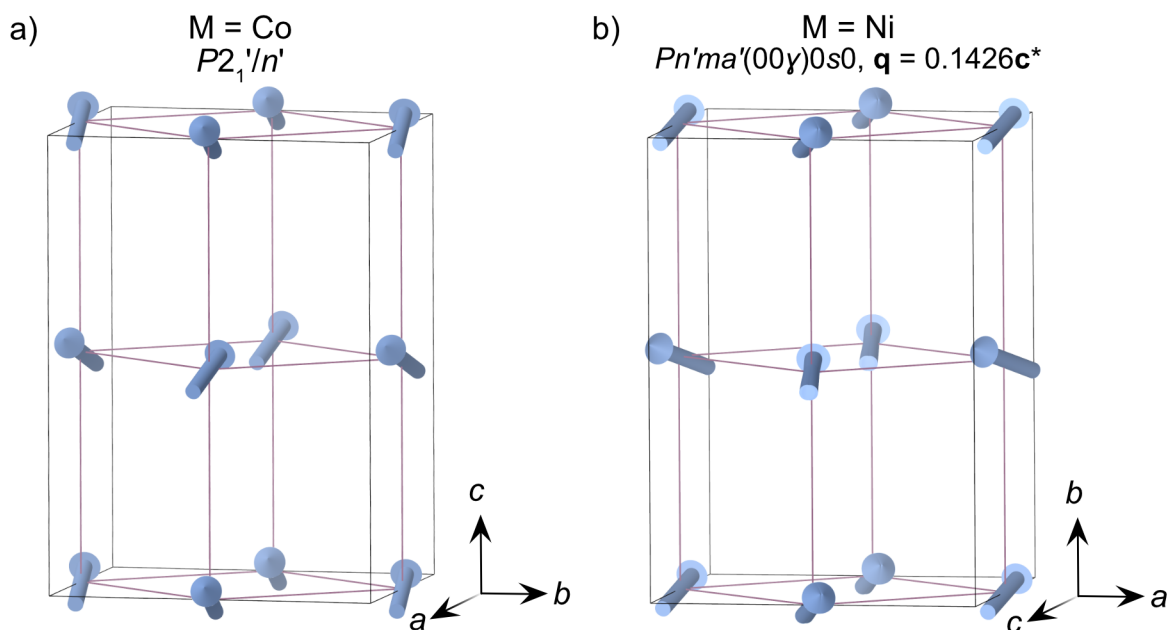


Figure 5.2: The magnetic structures for $[\text{CH}_3\text{NH}_3]\text{M}(\text{HCOO})_3$. Both compounds magnetically order with weak ferromagnetic interactions. The nearest neighbour interactions are shown with purple lines. a) $[\text{CH}_3\text{NH}_3]\text{Co}(\text{HCOO})_3$ in the non-modulated, monoclinic $P2_1'/n'$ magnetic space group, measured at 2 K.³²⁶ b) The average magnetic structure of $[\text{CH}_3\text{NH}_3]\text{Ni}(\text{HCOO})_3$ ordering in the incommensurately modulated $Pn'ma'(00\gamma)0s0$ magnetic superspace group, measured at 5 K.¹⁹⁴ The position of the atoms modulate, displaced predominantly along the b axis, and the direction of the magnetic moments modulate with oscillations in the ac plane.

In comparison, the nickel analogue remains in the non-modulated $Pnma$ space group on cooling until 84 K.¹⁹⁴ Below this temperature, it adopts the superspace group $Pnma(00\gamma)0s0$ with $\mathbf{q} = 0.1426(2)\mathbf{c}^*$. $[\text{CH}_3\text{NH}_3]\text{Ni}(\text{HCOO})_3$ remains in this incommensurately modulated phase until the onset of long-range magnetic ordering at 34 K,¹⁶³ where the compound orders in the magnetic superspace group $Pn'ma'(00\gamma)0s0$. Here, the phase is described as a proper incommensurate magnetic structure, as the magnetic structure contains magnetic modes which modulate the moment. Consequently, in this phase there is the coexistence of an incommensurately modulated nuclear and magnetic structure. The moments are orientated primarily along the c axis, with an uncompensated contribution in the b direction (Fig. 5.2). The modulation of the moments occurs as librations in the ac plane.

The stimulus driving the modulated phase transitions for both the formate compounds is the hydrogen bond network between the NH_3 hydrogens of the methylammonium cations and the oxygens of the formate ligands. In the ambient temperature phase, two of the hydrogens participate in hydrogen bond interactions, whilst the third is too far in proximity to interact with the neighbouring oxygens (Fig. 5.3a). In the low temperature $P2_1/n$ phase, adopted by $[\text{CH}_3\text{NH}_3]\text{Co}(\text{HCOO})_3$, a third permanent hydrogen bond is present (Fig. 5.3b dark blue dotted line). The methylammonium cation, which is positioned along a mirror plane in the orthorhombic phase, rotates in the monoclinic phase

breaking the symmetry element. H1 (atom labels as in Fig. 5.3d), which was originally equidistance to O3a and O3b, is now closer to one of the oxygens, establishing a hydrogen bond interaction. In the modulated phases, H1 is close enough in distance to interact with the oxygens of the formate ligand. However, there are two competing hydrogen bond acceptors (O3a and O3b, Fig. 5.3c light and dark blue dotted lines), equidistance from H1 in the average structure. This frustration distorts the structure and results in the modulated displacement of all the atoms. As a consequence, at a given point in the structure O3a will be closer in distance to H1, yet, in other areas along the modulation the N–H···O3b distance will be shorter.

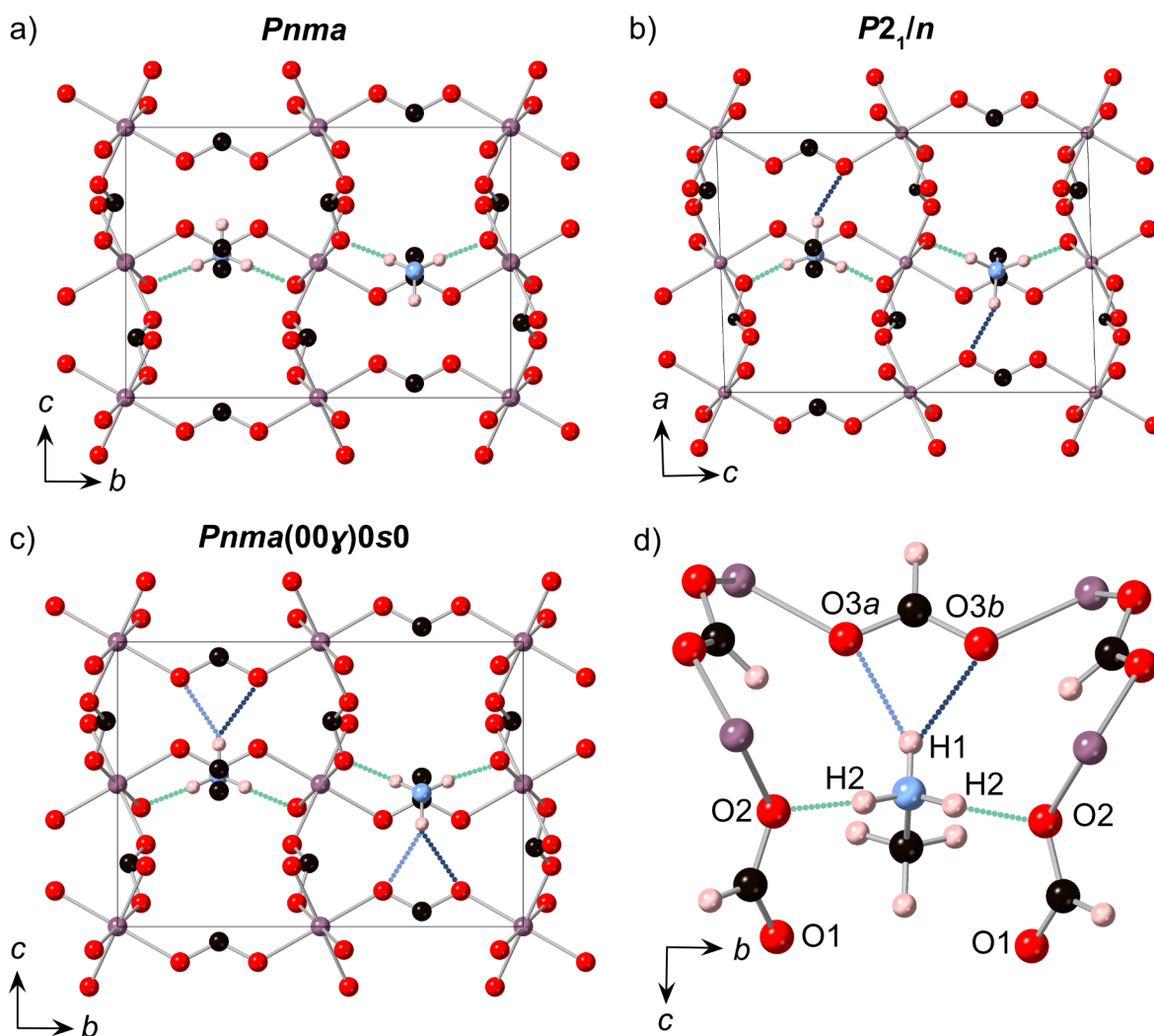


Figure 5.3: Schematic of the possible hydrogen bonds in $[\text{CH}_3\text{NH}_3]\text{M}(\text{HCOO})_3$ M = Co, Ni. a) For the non-modulated $Pnma$ phase at ambient temperature.¹⁹⁴ b) The low temperature, non-modulated $P2_1/n$ phase obtained for M = Co below $T = 78$ K.³²⁶ c) The average structure of the incommensurately modulated phases $Pnma(00\gamma)0s0$. The permanent hydrogen bond interactions are shown with green dotted lines throughout. Blue dotted lines indicate the permanent hydrogen bond interaction in b) and the two possible interactions in c). d) Zoom of the hydrogen bond interactions in the modulated phase, viewed along the a axis, subfigure adapted from ref.¹⁸ Metal = purple, O = red, C = black, N = blue, H = pale pink.

To explore the possibility of tuning the phase transitions and magnetic properties of these formate compounds, solid solutions have been synthesised from the methylammonium metal formates, $[\text{CH}_3\text{NH}_3]\text{Co}_x\text{Ni}_{1-x}(\text{HCOO})_3$, $x = 0.25$ ($\text{Co}_{25}\text{Ni}_{75}$), $x = 0.50$ ($\text{Co}_{50}\text{Ni}_{50}$) and $x = 0.75$ ($\text{Co}_{75}\text{Ni}_{25}$). Their temperature dependent phase transitions have been followed using single crystal Laue and monochromatic neutron diffraction. In addition, their magnetic properties have been characterised with magnetisation data and low temperature neutron diffraction measurements. The low temperature nuclear and magnetic structures for $\text{Co}_{50}\text{Ni}_{50}$ from neutron diffraction data were integrated and solved by Dr Laura Cañadillas Delgado.

5.3 Results

5.3.1 Synthesis and ambient structure

I synthesised the methylammonium formate solid solutions under solvothermal conditions from aqueous solutions of $\text{NiCl}_2 \cdot 6 \text{H}_2\text{O}$, $\text{CoCl}_2 \cdot 6 \text{H}_2\text{O}$, $\text{CH}_3\text{NH}_3\text{Cl}$ and NaHCOO in stoichiometric quantities following the method previously reported.^{101,326} The solutions were heated at 413 K (140 °C) for 72 h before cooling, within the sealed autoclave, to room temperature. This yielded mm^3 sized crystals of $\text{Co}_{75}\text{Ni}_{25}$ (dark red), $\text{Co}_{50}\text{Ni}_{50}$ (dark green) and $\text{Co}_{25}\text{Ni}_{75}$ (dark green).

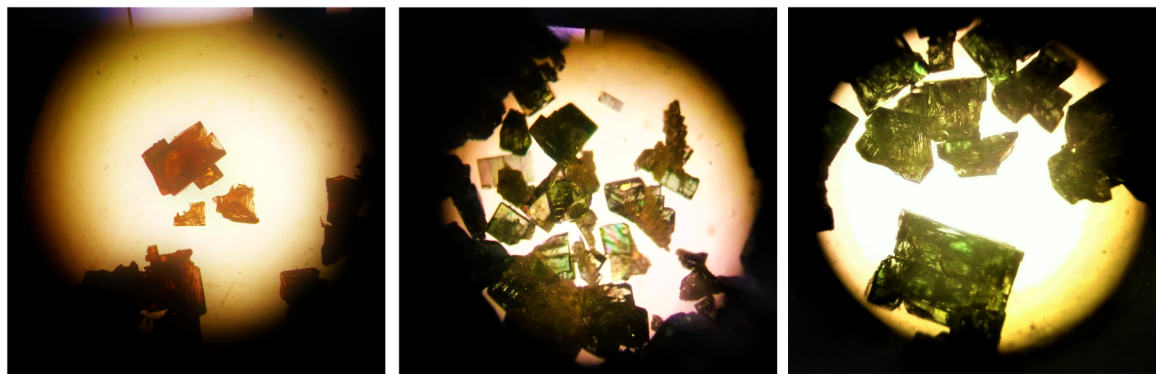


Figure 5.4: Single crystals of the solid solutions, viewed under a microscope. From left to right: $\text{Co}_{75}\text{Ni}_{25}$, $\text{Co}_{50}\text{Ni}_{50}$ and $\text{Co}_{25}\text{Ni}_{75}$.

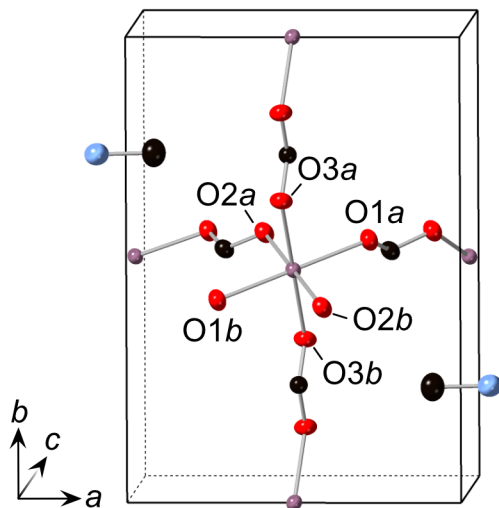


Figure 5.5: The connectivity of the metal-formate framework for $\text{Co}_{50}\text{Ni}_{50}$ measured with the D9 diffractometer (ILL) at ambient temperature. $\text{Co}_{75}\text{Ni}_{25}$ and $\text{Co}_{25}\text{Ni}_{75}$ are isostructural. The ellipsoids are shown with 50 % probability and the hydrogen atoms have been removed for clarity. At ambient temperature OXa and OXb , $X = 1, 2, 3$ are equivalent by symmetry. Metal = purple, O = red, C = black, N = blue.

From single crystal X-ray diffraction I found that the compounds are isostructural to the end-member methylammonium formate compounds $[\text{CH}_3\text{NH}_3]\text{Co}(\text{HCOO})_3$ and $[\text{CH}_3\text{NH}_3]\text{Ni}(\text{HCOO})_3$.^{163,325} At ambient temperature, they crystallise in the orthorhombic space group $Pnma$. Each metal site (Wyckoff site $4b$) is octahedrally coordinated and are bridged by formate anions in the *anti-anti* coordination mode resulting in a three-dimensional framework (Fig. 5.5). The carbon and nitrogen atoms of the methylammonium cations are positioned at $(x, 0.25, z)$ and $(x, 0.75, z)$, within the voids of the framework.

It is possible that there is site ordering of the metals. However, as cobalt and nickel have similar electron densities, it is difficult to definitively distinguish between them using an X-ray source. Therefore, to gain clearer information on the metal site orderings and the cobalt and nickel ratio in each crystal, neutron diffraction measurements were carried out using the D9 diffractometer (Institut Laue Langevin, ILL). Room temperature diffraction data were collected for a single crystal of $\text{Co}_{75}\text{Ni}_{25}$ ($1.5 \times 1.5 \times 1 \text{ mm}^3$), $\text{Co}_{50}\text{Ni}_{50}$ ($3 \times 2 \times 2 \text{ mm}^3$) and $\text{Co}_{25}\text{Ni}_{75}$ ($2 \times 1.5 \times 1.5 \text{ mm}^3$). The cobalt and nickel occupations were refined and were constrained such that the overall site occupancy was 1 and that the site positions and anisotropic displacement parameters were refined to equivalent values.

The neutron diffraction data suggests that the metal ordering is random. The symmetry for the solid solutions are the same as for the end members, $Pnma$, with no superlattice reflections observed or reflections corresponding to systematic absences in the $Pnma$ space group. These measurements were also ideal to determine the metal content for each crystal. For $\text{Co}_{75}\text{Ni}_{25}$ the refined metal ratio is 0.759(18) : 0.241(18) (Co : Ni).

The $\text{Co}_{50}\text{Ni}_{50}$ crystal has a measured ratio of 0.526(6) : 0.474(6) (Co : Ni), and for $\text{Co}_{25}\text{Ni}_{75}$ the metal content is 0.296(9) : 0.704(9) (Co : Ni). These values are close, although not always within error, of the stoichiometric quantities of metal chlorides used in the synthesis, suggesting that the compounds form with the expected proportions of the metals added.

By inspection under a microscope, it was observed that some of the $\text{Co}_{50}\text{Ni}_{50}$ crystals were in fact not uniformly dark green in colour. The crystals had regions of green and pink, arranged in stripes or concentric arcs (Fig. 5.4, centre image). The colouring might suggest that there is a strong local narcissistic ordering preference of the metals within the crystals. It is also possible the colouring is arising from fringes in the polarised light used in the microscope. Diffraction measurements consider the average structure, so it is not the ideal technique to explore this. However, if the crystals are biphasic, it should be detectable in the magnetometry measurements.

5.3.2 Magnetometry

Having confirmed I had synthesised solid solutions of the formate frameworks, I next looked at the bulk magnetic properties of the compounds. Field-cooled and zero-field-cooled susceptibility measurements were carried out on microcrystalline samples. The extent of field induced magnetisation was also explored at 2 K between $-5.00(1)$ and $5.00(1)$ T.

As $\text{Co}_{75}\text{Ni}_{25}$ is cooled, the field-cooled and zero-field-cooled susceptibilities split at the ordering temperature, $T_C = 19.7(5)$ K (Fig. 5.6a). The high-temperature Curie constant, C , was extracted from the value of χT at 300 K (Fig. 5.7a). $C = 2.625(1)$ emu K mol⁻¹, which is greater than the spin only value for the average magnetic site $C_{\text{spin only}} = 1.66$ emu K mol⁻¹ (approximating $C_{\text{Co}_{75}\text{Ni}_{25}} = 0.75 \times C_{\text{Co}} + 0.25 \times C_{\text{Ni}}$, Fig. 5.7a). Similarly, the effective moment, $\mu_{\text{eff.}} = 4.578(2)$ μ_B , is larger than the spin only value 3.61 μ_B . The Curie-Weiss temperature, obtained from a high temperature fit of the data $150 < T < 300$ K, is $\theta_{\text{CW}} = -43.6(5)$ K (Fig. 5.7d). Both Ni^{2+} and Co^{2+} ions have large orbital contributions to the magnetic moment, meaning that in all these formate compounds θ_{CW} varied greatly with the temperature range used to perform the fit.

The isothermal magnetisation measurements for $\text{Co}_{75}\text{Ni}_{25}$ show that as the field is increased, hysteresis is observed up to $3.04(1)$ T, where the magnetisation $M = 0.219(1)$ μ_B per metal (Fig. 5.8a). The remnant magnetisation is $M_{\text{rem.}} = 0.045(3)$ μ_B per metal, and the hysteresis has a coercive field of $H_C = 0.45(1)$ T. At the largest field measured, $5.00(1)$ T, the magnetisation reaches $M_{5\text{ T}} = 0.337(2)$ μ_B per metal, with no signs of a plateau. The degree of saturation is $M_{5\text{ T}}/M_{\text{sat.}} = 0.245$, where the saturation

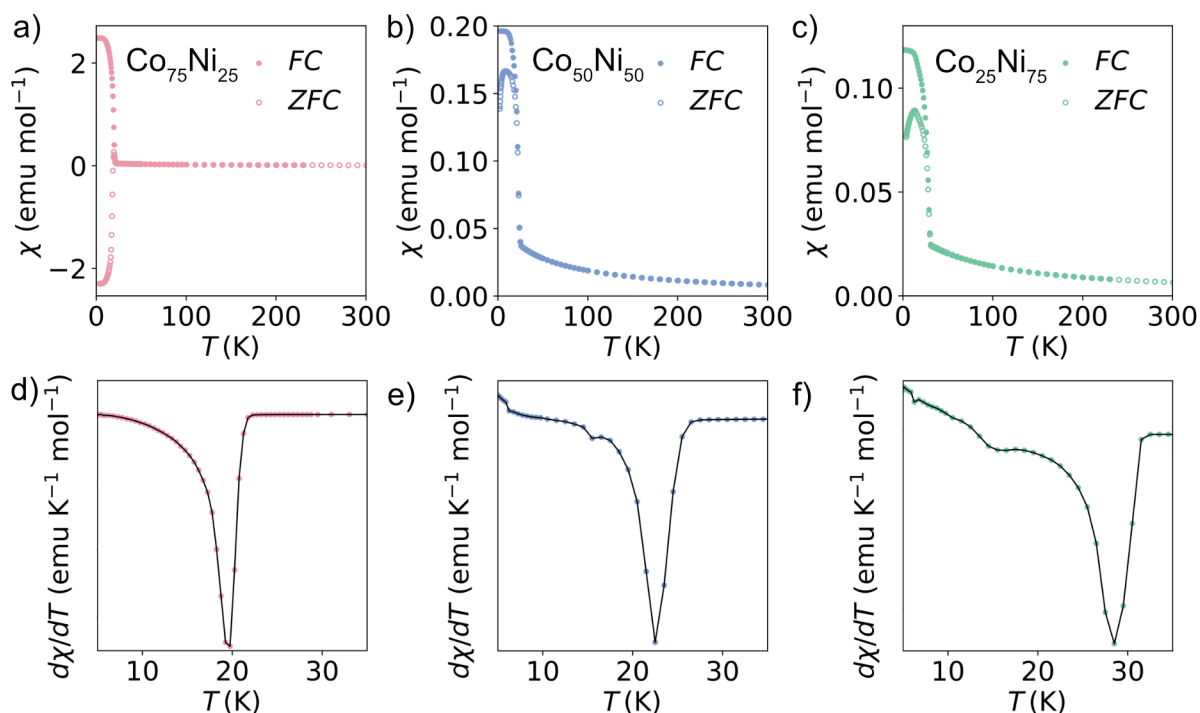


Figure 5.6: The field-cooled (*FC*, closed circles) and zero-field-cooled (*ZFC*, open circles) susceptibilities for a) $\text{Co}_{75}\text{Ni}_{25}$, b) $\text{Co}_{50}\text{Ni}_{50}$ and c) $\text{Co}_{25}\text{Ni}_{75}$. The derivative of the susceptibility for d) $\text{Co}_{75}\text{Ni}_{25}$, e) $\text{Co}_{50}\text{Ni}_{50}$ and f) $\text{Co}_{25}\text{Ni}_{75}$.

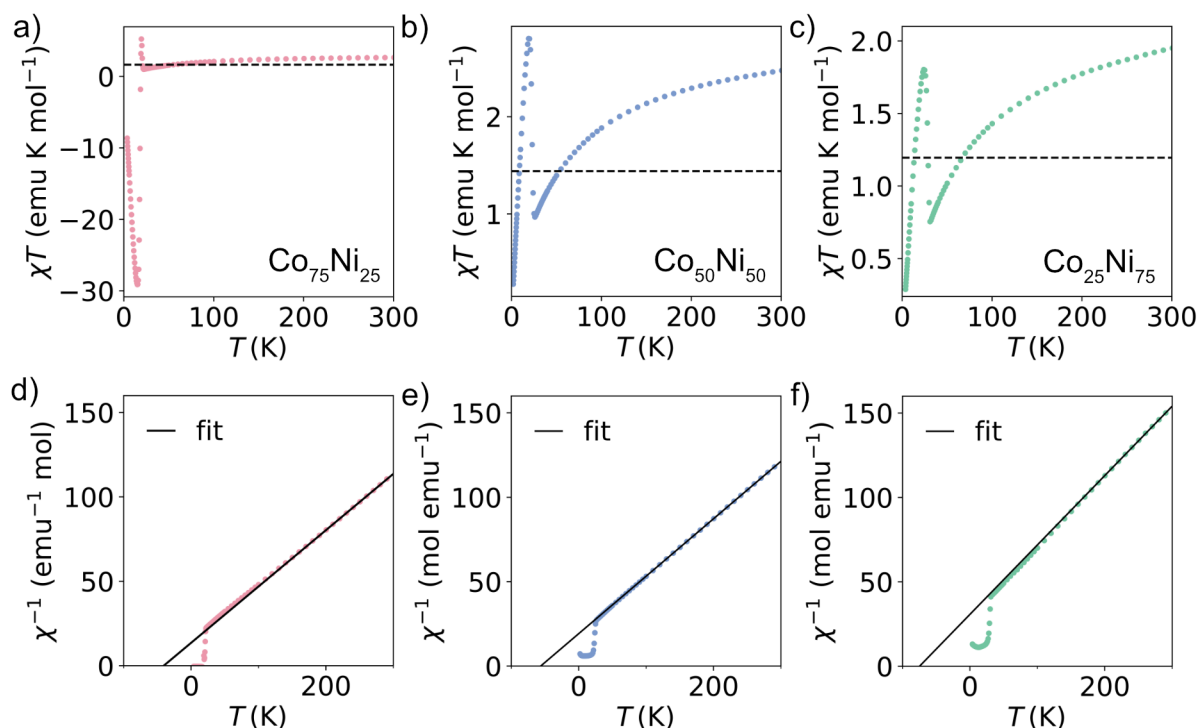


Figure 5.7: Plots of the of the variable temperature magnetic susceptibility product, with the high temperature spin only Curie value, $C_{\text{spin only}}$ indicated with a dashed line. a) $\text{Co}_{75}\text{Ni}_{25}$ ($C_{\text{spin only}} = 1.66 \text{ emu K mol}^{-1}$), b) $\text{Co}_{50}\text{Ni}_{50}$, $C_{\text{spin only}} = 1.44 \text{ emu K mol}^{-1}$ and c) $\text{Co}_{25}\text{Ni}_{75}$, $C_{\text{spin only}} = 1.21 \text{ emu K mol}^{-1}$. The inverse magnetic susceptibilities, with a Curie-Weiss fit (solid black line) for the temperature range $150 < T < 300$ K. d) $\text{Co}_{75}\text{Ni}_{25}$, $\theta_{\text{CW}} = -43.6(5) \text{ K}$, e) $\text{Co}_{50}\text{Ni}_{50}$, $\theta_{\text{CW}} = -56.3(1) \text{ K}$ and f) $\text{Co}_{25}\text{Ni}_{75}$, $\theta_{\text{CW}} = -70.8(7) \text{ K}$.

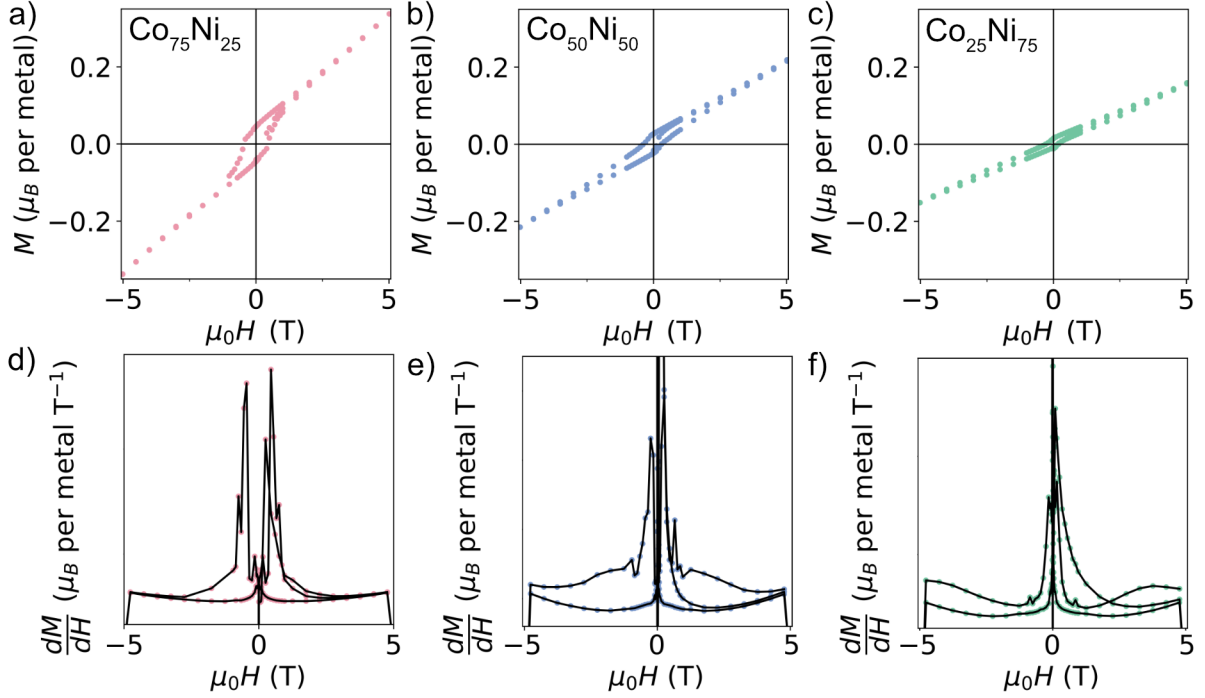


Figure 5.8: Isothermal magnetisation measurements for a) $\text{Co}_{75}\text{Ni}_{25}$, b) $\text{Co}_{50}\text{Ni}_{50}$ and c) $\text{Co}_{25}\text{Ni}_{75}$, measured at 2 K between $-5.00(1)$ and $5.00(1)$ T.

value $M_{\text{sat.}} = 1.375 \mu_{\text{B}}$ per metal.

For $\text{Co}_{50}\text{Ni}_{50}$, the field-cooled and zero-field-cooled susceptibilities diverge at the ordering temperature, $T_{\text{C}} = 22.5(7)$ K (Fig. 5.6b). $C = 2.461(1)$ emu K mol $^{-1}$, which is significantly higher than the spin only value $C_{\text{spin only}} = 1.44$ emu K mol $^{-1}$ (Fig. 5.7b). The effective magnetic moment $\mu_{\text{eff.}} = 4.436(2) \mu_{\text{B}}$ compared to $\mu_{\text{spin only}} = 3.35 \mu_{\text{B}}$. Fitting the inverse susceptibility to the Curie-Weiss Law, $\theta_{\text{CW}} = -56.3(1)$ K ($150 < T < 300$ K, Fig. 5.7e).

Hysteresis is observed in the magnetisation data of $\text{Co}_{50}\text{Ni}_{50}$, which closes at $5.0(2)$ T (Fig. 5.8b). The remnant magnetisation is $M_{\text{rem.}} = 0.027(1) \mu_{\text{B}}$ per metal, with a coercive field of $H_{\text{C}} = 0.30(1)$ T. The largest magnetisation measured is $M_{5\text{ T}} = 0.218(1) \mu_{\text{B}}$ per metal, which is lower than the saturation value $M_{\text{sat.}} = 1.25 \mu_{\text{B}}$ per metal ($M_{5\text{ T}}/M_{\text{sat.}} = 0.175$).

The susceptibility data for $\text{Co}_{25}\text{Ni}_{75}$ indicate an ordering temperature $T_{\text{C}} = 28.5(5)$ K (Fig. 5.6c, f). $C = 1.936(4)$ emu K mol $^{-1}$, which is larger than the spin only value $C_{\text{spin only}} = 1.21$ emu K mol $^{-1}$ (Fig. 5.7c). From the plot of χT , the effective moment is calculated to be $3.936(2) \mu_{\text{B}}$ in comparison to $\mu_{\text{spin only}} = 3.09 \mu_{\text{B}}$. The Curie-Weiss temperature $\theta_{\text{CW}} = -70.8(7)$ K ($150 < T < 300$ K, Fig. 5.7f).

The isothermal data, show hysteresis at all magnetic fields measured for $\text{Co}_{25}\text{Ni}_{75}$ (Fig. 5.8c). It exhibits a remnant magnetisation $M_{\text{rem.}} = 0.015(1) \mu_{\text{B}}$ per metal and

a coercive field of $H_C = 0.15(1)$ T. The magnetisation does not reach saturation, $M_{\text{sat.}} = 1.125(1) \mu_B$ per metal, with $M_{5\text{ T}} = 0.158(1) \mu_B$ per metal at $5.00(1)$ T ($M_{5\text{ T}}/M_{\text{sat.}} = 0.140$).

For all three compounds, the combination of a negative θ_{CW} and hysteresis in the isothermal data suggest weak ferromagnetic behaviour, in agreement with the magnetic ordering of the parent compounds. If the crystals were biphasic, rather than true solid solutions, it would be expected that there are two ordering temperatures observed in the magnetometry data, one for $[\text{CH}_3\text{NH}_3]\text{Co}(\text{HCOO})_3$ ($T_C = 16$ K) and one for $[\text{CH}_3\text{NH}_3]\text{Ni}(\text{HCOO})_3$ ($T_C = 34$ K). For the samples measured, essentially one ordering temperature is observed which incrementally increases between the Co and Ni ordering temperatures, dependent on the metal ratios used in the synthesis. This would support the X-ray and neutron diffraction data that there is no metal site ordering and the distribution of Co and Ni is random within the samples.

5.3.3 Temperature dependent structural evolutions

After collecting information of the bulk magnetic properties, I next looked to observe the temperature dependence of the nuclear structure. Single crystal Laue neutron diffraction was carried out for $\text{Co}_{75}\text{Ni}_{25}$, $\text{Co}_{50}\text{Ni}_{50}$ and $\text{Co}_{25}\text{Ni}_{75}$ with a wavelength range of 0.8–3.0 Å. The same crystals used to calculate the metal ratios were used for these measurements. The samples were heated between 10 and 120 K and the diffractograms were collected with a 3 K range per image. As only one diffractogram was obtained per temperature point (the crystal was not rotated), the reflections could not be integrated to determine the structures. However, approximate unit cells and orientation matrices could be used to calculate expected diffraction patterns, which were compared to the diffractograms to estimate the \mathbf{q} vectors.

Cooling from 120 K, the diffraction pattern for $\text{Co}_{75}\text{Ni}_{25}$ remains unchanged in the non-modulated $Pnma$ space group until 98(3) K where the emergence of satellite peaks can be observed (Fig. 5.9a, b). At 98(3) K, the main Bragg reflections match a calculated diffraction pattern for the $Pnma$ space group and the satellite peaks have a \mathbf{q} vector of $0.135(5)\mathbf{c}^*$, which continually decreases to $\mathbf{q} = 0.125(5)\mathbf{c}^*$ by 58(3) K. From 58(3) K a slow transition occurs over five diffractograms (approximately a 14(3) K temperature range, Fig. 5.9c). During the transition, the reflections reduce in intensity and are distributed over a larger pixel area. By 44(3) K, the reflections are again sharp intensities. The reflections no longer have satellite peaks, suggesting this is a non-modulated structure, and twinning can be observed by the appearance of a second Bragg reflection close in proximity to the main reflection (Fig. 5.9d). The reflections fit the monoclinic space

group $P2_1/n$, with the presence of calculated Bragg reflections, such as 320 present in the twinned low temperature phase, which is a systematic absence for the $Pnma$ space group (Fig. 5.9d, orange oval). At 18(3) K, certain reflections increase in intensity (Fig. 5.9d, purple arrow), indicating the onset of long-range magnetic ordering, which is in agreement with the ordering temperature determined by the magnetometry measurements ($T_C = 19.7(5)$ K). Since the magnetic reflections only appear as additional intensity to nuclear reflections, it likely has a propagation vector of $\mathbf{k} = (0, 0, 0)$.

When cooling, the $\text{Co}_{50}\text{Ni}_{50}$ crystal remains in a non-modulated $Pnma$ phase until 96(3) K, at which temperature satellite reflections appear and the main reflection reduces in intensity (Fig. 5.10b). The reflections can be modelled by the $Pnma$ space group, with $\mathbf{q} = 0.140(5)\mathbf{c}^*$. A sharp phase transition can be observed at 59(3) with a change in distance between the main and satellite reflections as well as the appearance of additional satellite reflections, which increase in intensity down to 33(3) K (Fig. 5.10c). The reflections can be matched to the $Pnma$ space group with $\mathbf{q} = 0.120(5)\mathbf{c}^*$. Below this temperature the position of the main and satellite reflections do not change further. Additional intensity to some reflections can be observed below 25(3) K, inline with the ordering temperature observed from the magnetisation data ($T_C = 22.5(7)$ K, Fig. 5.10d). This suggests the magnetic structure has a propagation vector of $\mathbf{k} = (0, 0, 0)$.

For the nickel rich compound, $\text{Co}_{25}\text{Ni}_{75}$, the crystal remains in the $Pnma$ space group on cooling until 85(3) K. At this temperature the satellite reflections are visible (Fig. 5.11b). The reflections match a calculated diffraction pattern for the $Pnma$ space group with $\mathbf{q} = 0.125(5)\mathbf{c}^*$. These reflections remain as the sample is cooled to 10 K, without observable alteration to the \mathbf{q} vector. The magnetic phase transition is unclear, without obvious additional intensity to any reflections appearing below the magnetic ordering temperature ($T_C = 28.5(5)$ K).

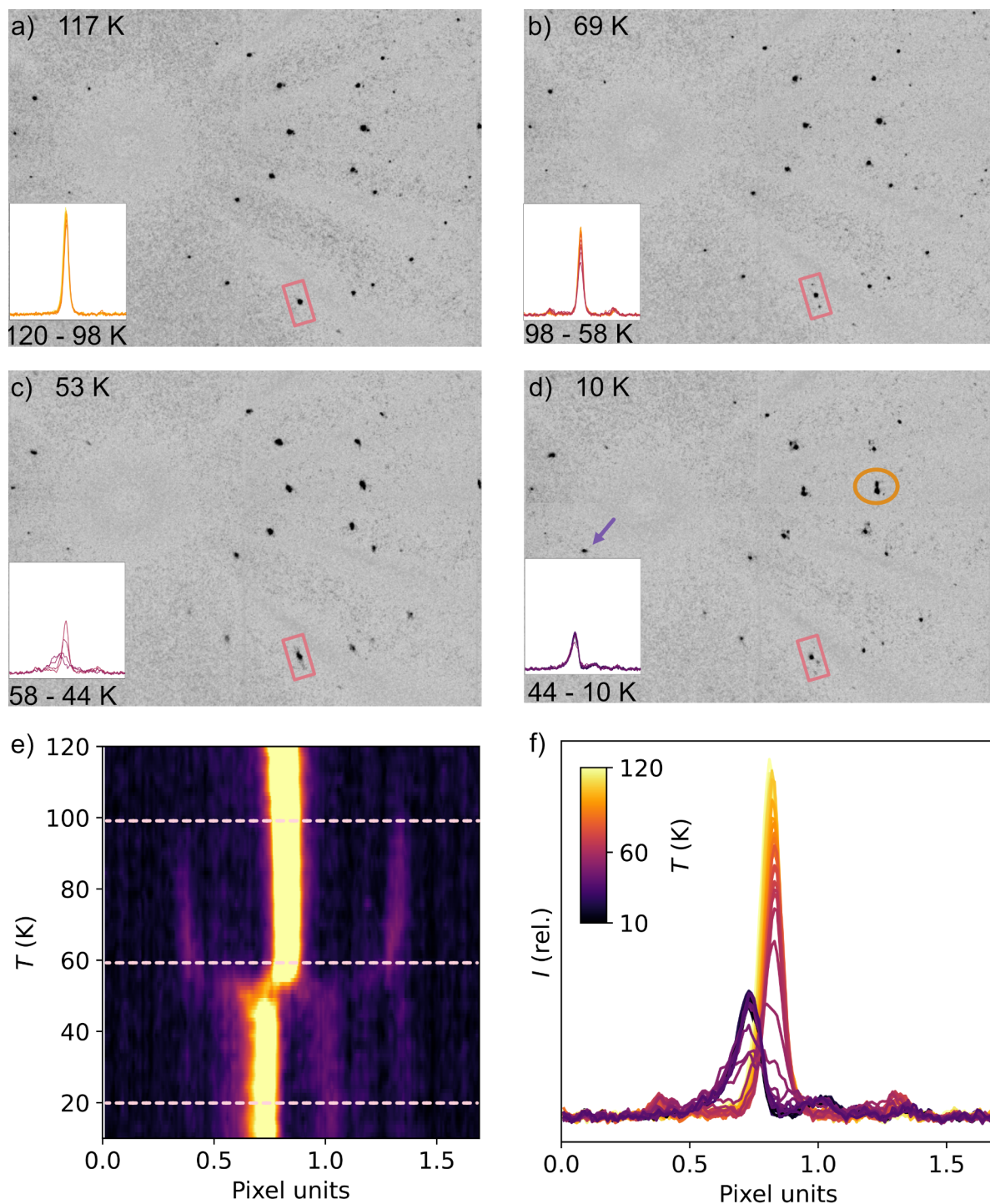


Figure 5.9: Laue neutron diffractograms (CYCLOPS, ILL), heating with a ramp of 3 K per image for $\text{Co}_{75}\text{Ni}_{25}$. The insets (in a, b, c and d) show the integrated intensity for the pixels in the box highlighted in pink, following the $\bar{1}3\bar{1}$ ($Pnma$) reflection over the temperature ranges specified below it. The displayed diffractograms were measured at a) 117 K showing the non-modulated phase. b) At 69 K, showing the modulated phase with weak satellite reflections visible. c) At 53 K, showing the slow phase transition. d) At 10 K showing the twinned, non-modulated $P2_1/n$ phase with the 112 reflection highlighted in pink and a magnetic reflection is indicated with a purple arrow. An orange oval indicates the 320 reflection. e) A heatmap over the temperature range 10–120 K for the pixel intensities in the pink box. The pink dashed lines indicate the approximate temperature of the phase transitions (structural and magnetic). f) A superposition of all the integrated intensities from the insets (a, b, c and d) over the temperature range 10–120 K.

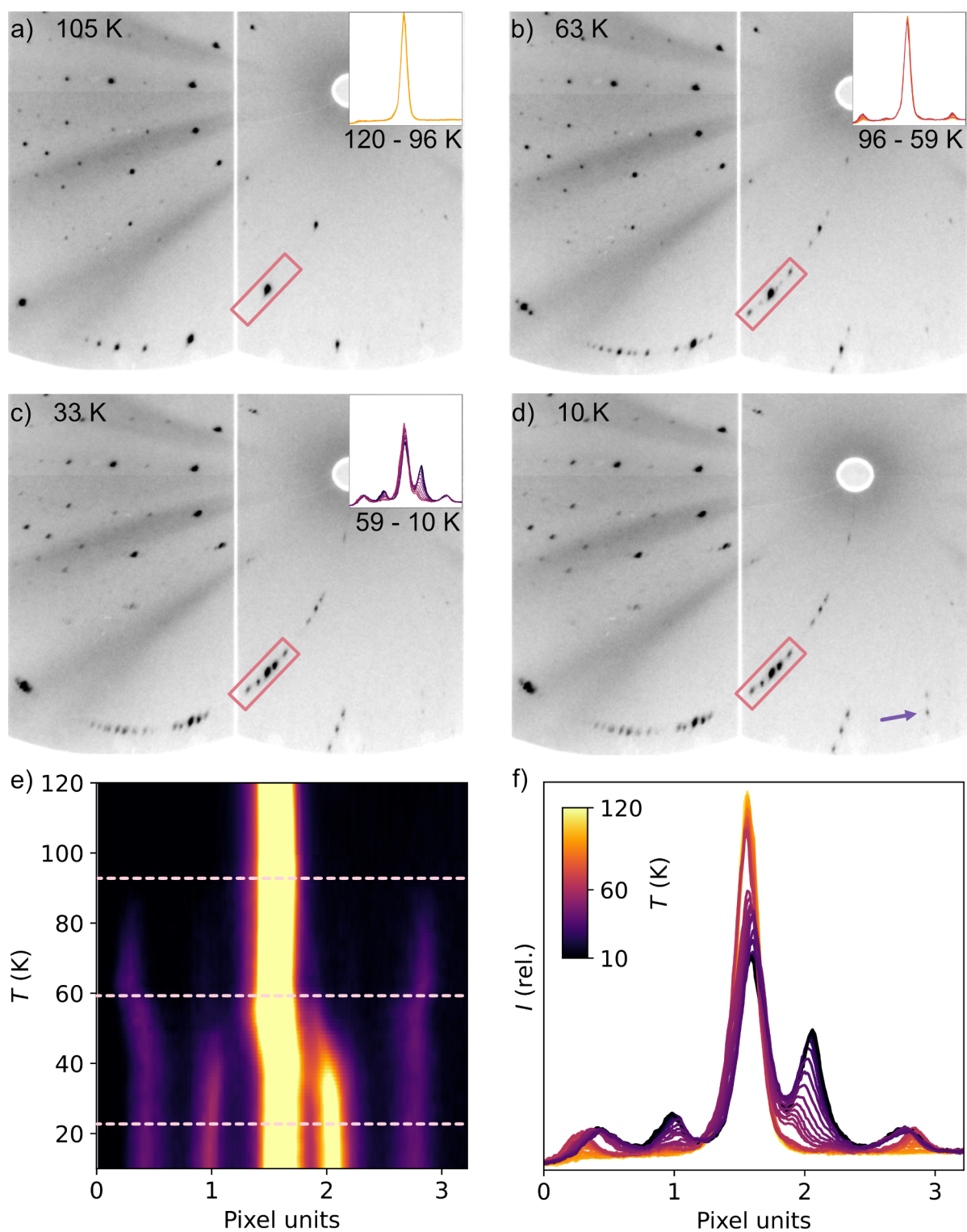


Figure 5.10: Laue neutron diffractograms (CYCLOPS, ILL), heating with a ramp of 3 K per image for $\text{Co}_{50}\text{Ni}_{50}$. The insets (in a, b, c and d) show the integrated intensity for the pixels in the box highlighted in pink, following the $03\bar{1}$ reflection over the temperature ranges specified below it. The displayed diffractograms were measured at a) 105 K, showing the non-modulated phase. b) At 63 K, showing the first modulated phase. c) At 33 K showing the second modulated phase. d) At 10 K where a visible magnetic reflection has been highlighted with a purple arrow. e) A heatmap over the temperature range 10–120 K for the pixel intensities in the pink box. The pink dashed lines indicate the approximate temperature of the phase transitions (structural and magnetic). f) A superposition of all the integrated intensities from the insets (a, b, c and d) over the temperature range 10–120 K.

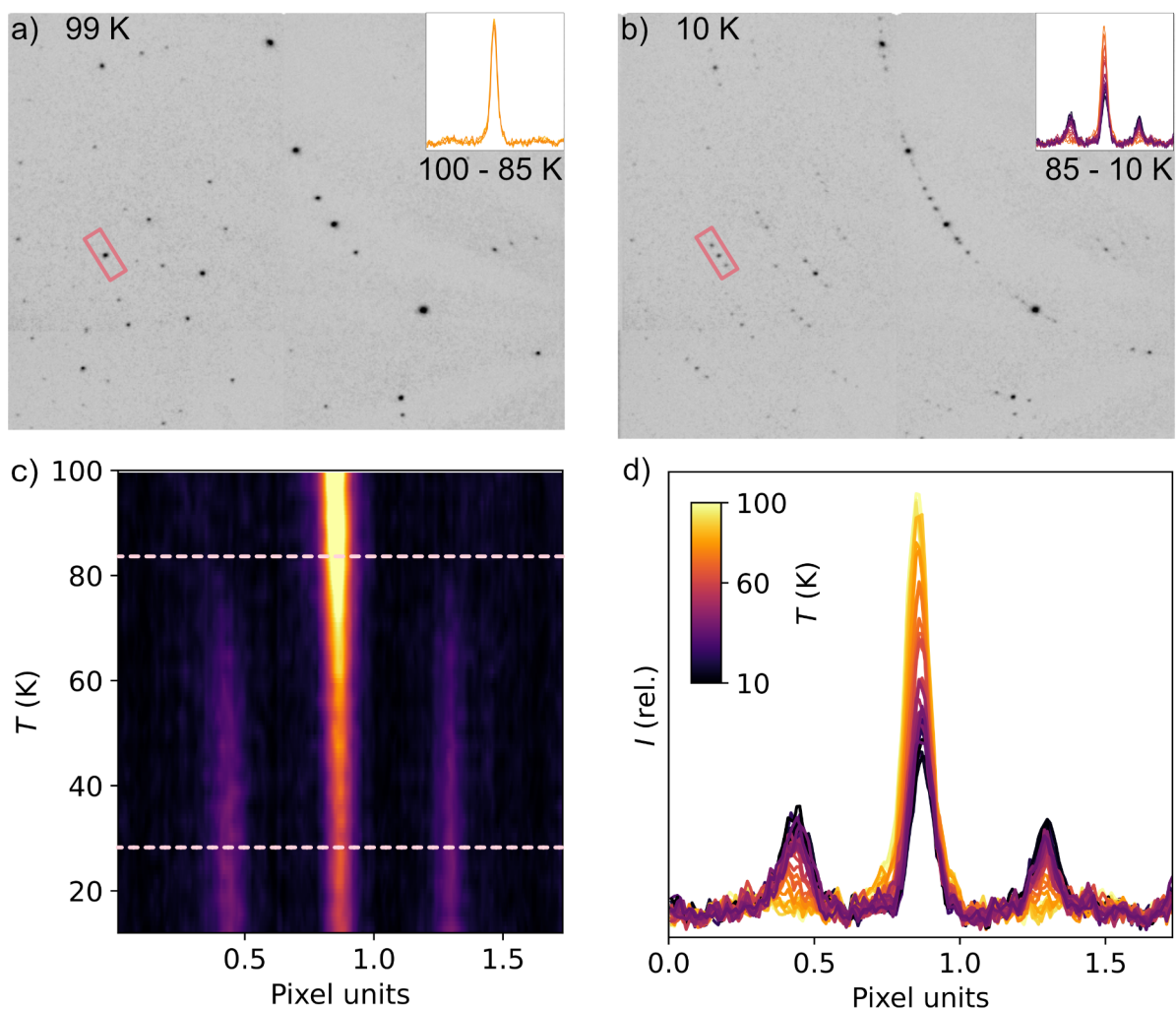


Figure 5.11: Laue neutron diffractograms (CYCLOPS, ILL), heating with a ramp of 3 K per image for $\text{Co}_{25}\text{Ni}_{75}$. The insets (in a and b) show the integrated intensity for the pixels in the box highlighted in pink, following the $14\bar{1}$ reflection over the temperature ranges specified below it. The displayed diffractograms were measured at a) 99 K, showing the non-modulated phase. b) At 10 K showing the modulated phase. No magnetic reflections were visible for these measurements. c) A heatmap over the temperature range 10–100 K for the pixel intensity in the pink box. The pink dashed lines indicate the approximate temperature of the phase transition (structural, and magnetic obtained from magnetometry data). f) A superposition of all the integrated intensities from the insets (a and b) over the temperature range 10–100 K.

5.3.4 Monochromatic neutron diffraction

The Laue diffraction data suggest that the cobalt-rich and nickel-rich solid solutions follow structural phase transitions similar to that of the end-member methylammonium formates. However, the evolution of the $\text{Co}_{50}\text{Ni}_{50}$ structure did not strictly follow the trend for either the Co or Ni analogue, encouraging a further neutron diffraction experiment to explain the observed behaviour.

A single crystal neutron diffraction experiment was carried out using the D19 diffractometer (ILL), using the same crystal which was used for the Laue neutron diffraction

experiment and for the diffraction measurement to obtain the metal ratios. Data were collected at 2 K and at 10 K intervals between 30 and 100 K. The orientation matrix was obtained for each data set to identify the temperature regimes for each phase. As a result, longer data acquisitions were made at 30 and 70 K. Refinements were carried out at 2, 30 and 70 K to determine the nuclear and magnetic structures of each phase. For the following refinements, the previously calculated metal ratio for this crystal was used (0.526 : 0.474, Co : Ni) and were fixed during the refinements.

At 96(3) K, $\text{Co}_{50}\text{Ni}_{50}$ undergoes a phase transition from the non-modulated, orthorhombic space group, $Pnma$ to a modulated structure. Integration of the data at 70 K found that the compound adopts the modulated superspace group $Pnma(00\gamma)0s0$ with a modulation vector $\mathbf{q} = 0.1429(2)\mathbf{c}^*$. Along the a and b axes the unit cell maintains its average periodicity, however, along the c axis it has a modulation length, $c/\mathbf{q} = 8.1153/0.1429 = 56.7990(11)$ Å, almost seven times the length of the average c axis.

Refinements of the amplitude displacements for the atoms show that the site displacement is largest along the b direction. For the metal site, the displacement is described by a sine term only (restricted by symmetry, Table 5.1), with a maximum displacement from its average position of 0.228(3) Å in the b direction (Fig. 5.12a, pink line). The modulation for each atom was refined independently to find the displacements. The modulation of all the atoms show similar results, with the b direction experiencing the largest displacement, on the same order of magnitude as the metal site. As a result of the asynchronous modulations of the atoms, the bond lengths also modulate. However, these variations are of two orders of magnitude smaller than the displacements experienced for the atoms. For example, the maximum distortion for $\text{M}-\text{O}3 = 0.006(3)$ Å. The $[\text{MO}_6]$ octahedra distort such that equivalent oxygens, e.g. the two O1 atoms, are no longer equivalent in a given unit cell, resulting in O1a and O1b (Fig. 5.13a). However, in the average structure, the O1 atoms remain equivalent.

The hydrogen bond interactions between the donor N–H methylammonium and acceptor O atoms vary in distance as the structure modulates. The $\text{H}2 \cdots \text{O}2$ interactions (atoms labelled as in Fig. 5.5) have an average distance of 1.806(3) Å (Fig. 5.12c). H1 hydrogen bonds to O3n, $n = a$ or b , with an average distance of 2.149(3) Å, however the distance

Table 5.1: The amplitude displacements for the sine term of the first order of the harmonics in the Fourier series of the metal site for $\text{Co}_{50}\text{Ni}_{50}$.

	70 K	30 K	2 K
x	0.00270(13)	−0.00283(19)	−0.0024(2)
y	−0.02035(19)	−0.03220(20)	−0.0338(3)
z	−0.00010(14)	0.00020(19)	0.0000(2)

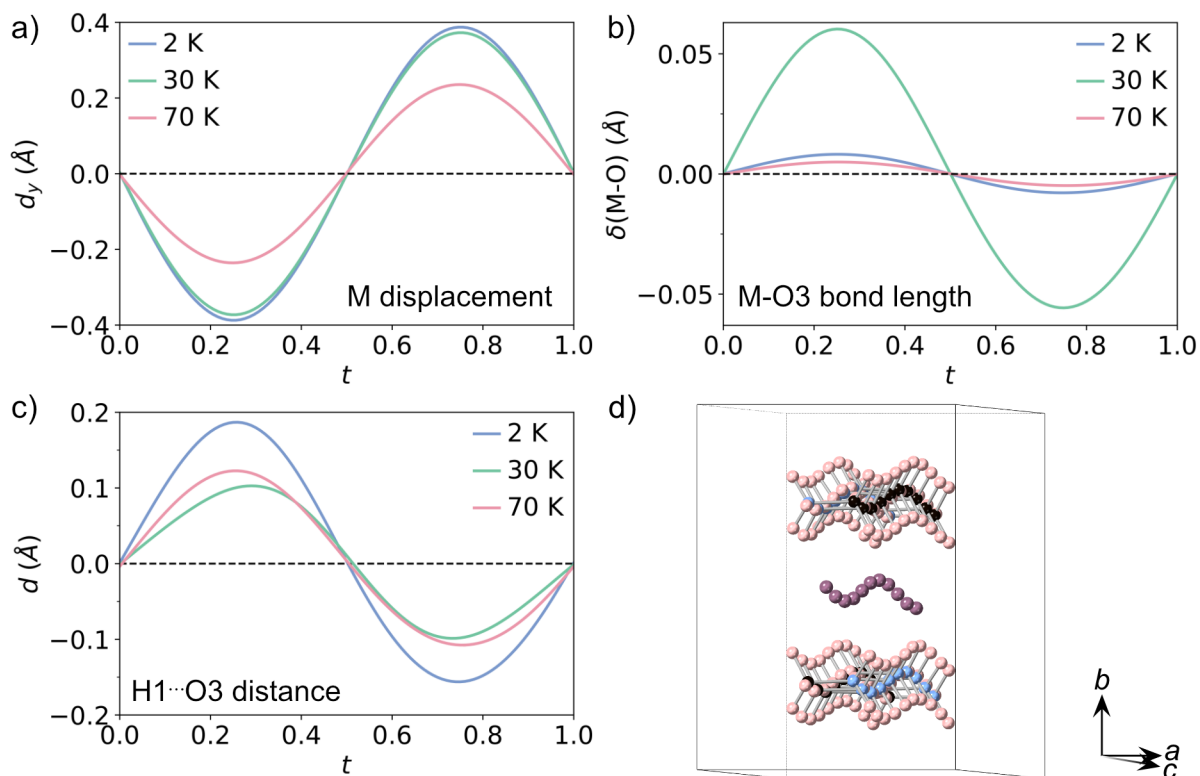


Figure 5.12: A summary of the modulations observed from the refinements of $\text{Co}_{50}\text{Ni}_{50}$ measured using the D19 diffractometer (ILL) at 2 K (blue lines), 30 K (green lines) and 70 K (pink lines). a) The modulation function of the metal site showing the displacement along y , d_y . b) The modulation of the H1 \cdots O3 distances. c) The modulation of the M–O3 bond lengths. d) The modulation for selected atoms (M-site and methylammonium cations) shown in a supercell 10 times the average unit cell length along the c axis to view at least one full modulation period. M = purple, C = black, O = red, N = blue, H = pink.

varies between 2.042(3) Å and 2.272(3) Å.

Decreasing in temperature, a second phase transition is observed between 40 and 30 K. This is slightly lower than the transition that was observed in the Laue diffraction data (between 59(3) and 44(3) K) where a slow transformation was observed. Potentially this discrepancy in the transition temperature is as a result of the temperature continually increasing as a function of time for the Laue diffraction measurements, whereas during these data collections the sample was allocated time to stabilise at each temperature point before starting the data collection.

At 30 K, the compound could be indexed by the superspace group $Pnma(00\gamma)0s0$, with a modulation vector, $\mathbf{q} = 0.1249(2)\mathbf{c}^*$. This describes a modulation length along c ($c/\mathbf{q} = 8.1133/0.1249$) of 64.9749(14) Å, slightly more than eight times the average c axis length. The metal site positions modulate with the largest contribution along the b direction (Table 5.1). This results in a displacement along the b axis from its average position of 0.373(3) Å (Fig. 5.12a, green line).

The M–O bond lengths show larger distortions from the average value at 30 K

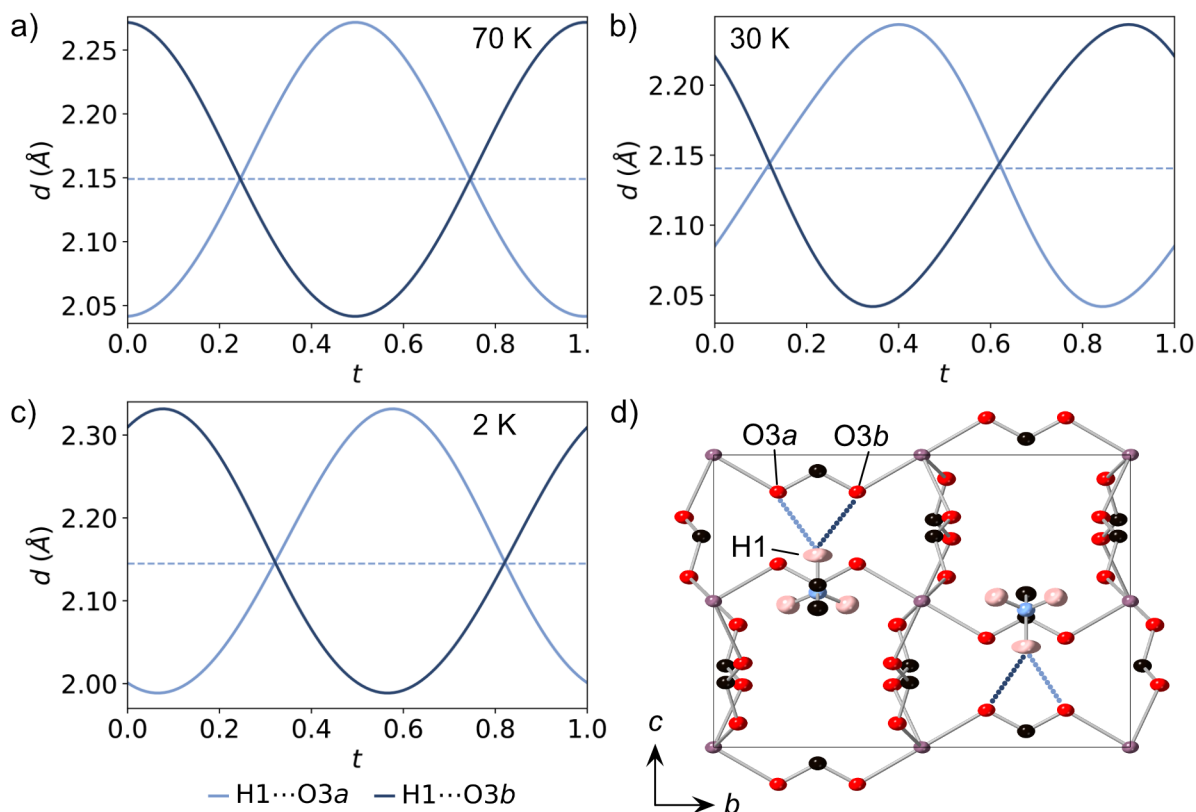


Figure 5.13: Modulation of the $H1 \cdots O3$ distances (solid lines) for a) 70 K, b) 30 K and c) 2 K. The dashed lines indicate the average distances. d) The average structure at 30 K, shown with 50 % thermal ellipsoids. Only the hydrogen atoms bonded to the nitrogen have been shown for clarity, to highlight the hydrogen bond interactions of $H1 \cdots O3$ (light and dark blue dashed lines). M = purple, C = black, O = red, N = blue, H = pink.

(Fig. 5.12b). This is particularly significant for $M-O1$ and $M-O3$. $M-O3$ coordinate to the metal sites along the b direction, with a maximum deviation from the average bond length of $0.069(3)$ Å. The $M-O1$ bonds are located in the ab plane with a maximum bond length variation of $0.061(3)$ Å. The difference in maximum bond length for $M-O2$ compared to its average value is an order of magnitude smaller, $0.007(3)$ Å. The $H2 \cdots O2$ atoms have an average distance of $1.823(3)$ Å and the $H1 \cdots O3n$ atoms has an average distance of $2.141(3)$ Å. The $H1 \cdots O3a$ and $H1 \cdots O3b$ modulations alternate, resulting in minimum and maximum distances at different points in the structure (Fig. 5.13b).

On further cooling to 2 K, additional reflections were observed, indicating the onset of magnetic ordering. The presence of the satellite reflections indicated that the structure remains in a modulated phase. However, initially it was unclear if the modulation arises from only the nuclear structure (improper incommensurate magnetic structure) or from a combination of the nuclear and magnetic structure (proper incommensurate magnetic structure). Refinements were carried out both where the Fourier components for the magnetic moments were refined and where the modulations were fixed to zero for the

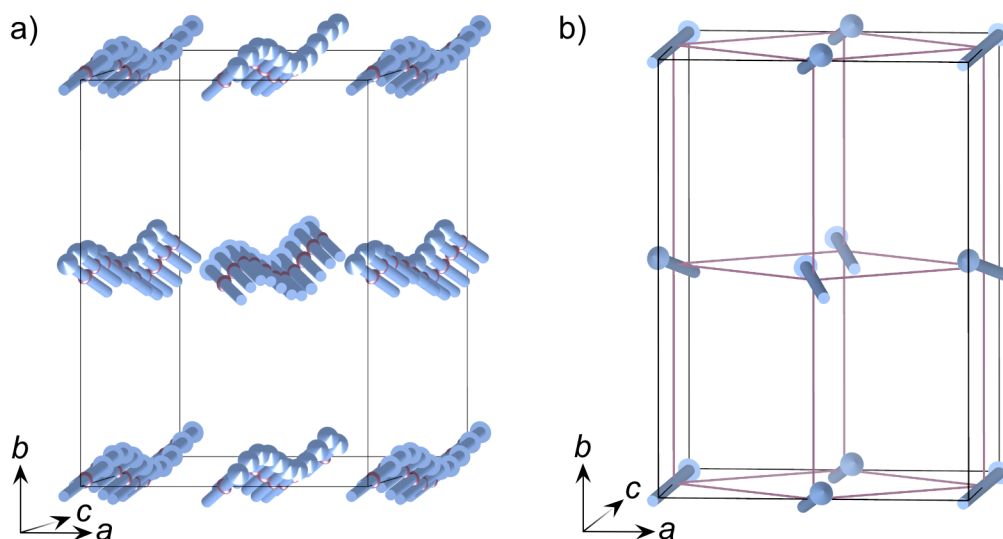


Figure 5.14: The magnetic structure of $\text{Co}_{50}\text{Ni}_{50}$ at 2 K measured with the D19 diffractometer (ILL). a) The position of the metal sites (purple spheres) and the magnetic moments (blue arrows), are shown in a supercell which is 10 times larger than the average unit cell to include at least a full modulation period. b) The average magnetic unit cell, showing the ordering of the moments without the modulation of the atom sites. The $[\text{M}(\text{HCOO})_3]^-$ framework is shown as a wireframe (purple lines) and the methylammonium cations and hydrogen atoms have been removed for clarity. The moments cant, with an uncompensated moment along the b axis.

moments. With equivalent refinement statistics obtained for the models, and no unequivocal evidence of additional intensities in the satellite reflections—only an increase in intensities of the main reflections—it was concluded the structure adopts an improper incommensurate magnetic structure.

From indexing the magnetic Bragg reflections, the propagation vector was determined to be $\mathbf{k} = (0, 0, 0)$. It orders with the magnetic superspace group $Pn'ma'(00\gamma)0s0$ with $\mathbf{q} = 0.1249(2)\mathbf{c}^*$, and a modulation length of $65.0092(14)$ Å. This model allows for a weak ferromagnetic arrangement of the moment, in agreement with the susceptibility data. The moment was fixed to have a magnitude of $2.5 \mu_{\text{B}}$, an average of high-spin Co^{2+} and Ni^{2+} moments. Each nearest neighbour, through $\text{M}-\text{OCO}-\text{M}$ superexchange pathways, has weak ferromagnetic correlations, with canting of the moments along the b axis at an angle of 137° ($0.575(91) \mu_{\text{B}}$, Fig. 5.14).

Since the magnetic component of the structure is non-modulated, the orientation and size of the moment does not change throughout the structure. The nuclear component, however, remains modulated. The metal site modulates and, accordingly, the position of the moment is displaced from the average structure, however, the magnitude and direction of the moments are not varied. The greatest displacement of the atom sites is along the b axis (Table 5.1), with a maximum displacement of $0.387(6)$ Å (Fig. 5.12a, blue line). The average hydrogen bond distances are $1.825(8)$ Å for $\text{H}2 \cdots \text{O}2$, the shorter interaction distance, and $2.145(8)$ Å for $\text{H}1 \cdots \text{O}3$ with a maximum deviation from the

average distance of 0.187(9) Å (Fig. 5.12c).

5.4 Discussion

The three solid solutions of $[\text{CH}_3\text{NH}_3]\text{Co}_x\text{Ni}_{1-x}(\text{HCOO})_3$, $x = 0.75, 0.50$ and 0.25 , show intermediate behaviours of their structural evolutions and magnetic properties compared to their two end members $[\text{CH}_3\text{NH}_3]\text{Co}(\text{HCOO})_3$ and $[\text{CH}_3\text{NH}_3]\text{Ni}(\text{HCOO})_3$. $\text{Co}_{0.75}\text{Ni}_{0.25}$ exhibits structural phase transitions similar to that of the Co analogue, transitioning through a modulated phase before adopting a twinned non-modulated structure by 44(3) K. On the other hand, the nickel-rich $\text{Co}_{0.25}\text{Ni}_{0.75}$ undergoes one non-modulated to modulated phase transition, which remains until 2 K. This behaviour follows the transitions observed by the Ni analogue. Both the $\text{Co}_{0.75}\text{Ni}_{0.25}$ and $\text{Co}_{0.25}\text{Ni}_{0.75}$ compounds show structural trends resembling the corresponding parent compounds, with the temperature at which

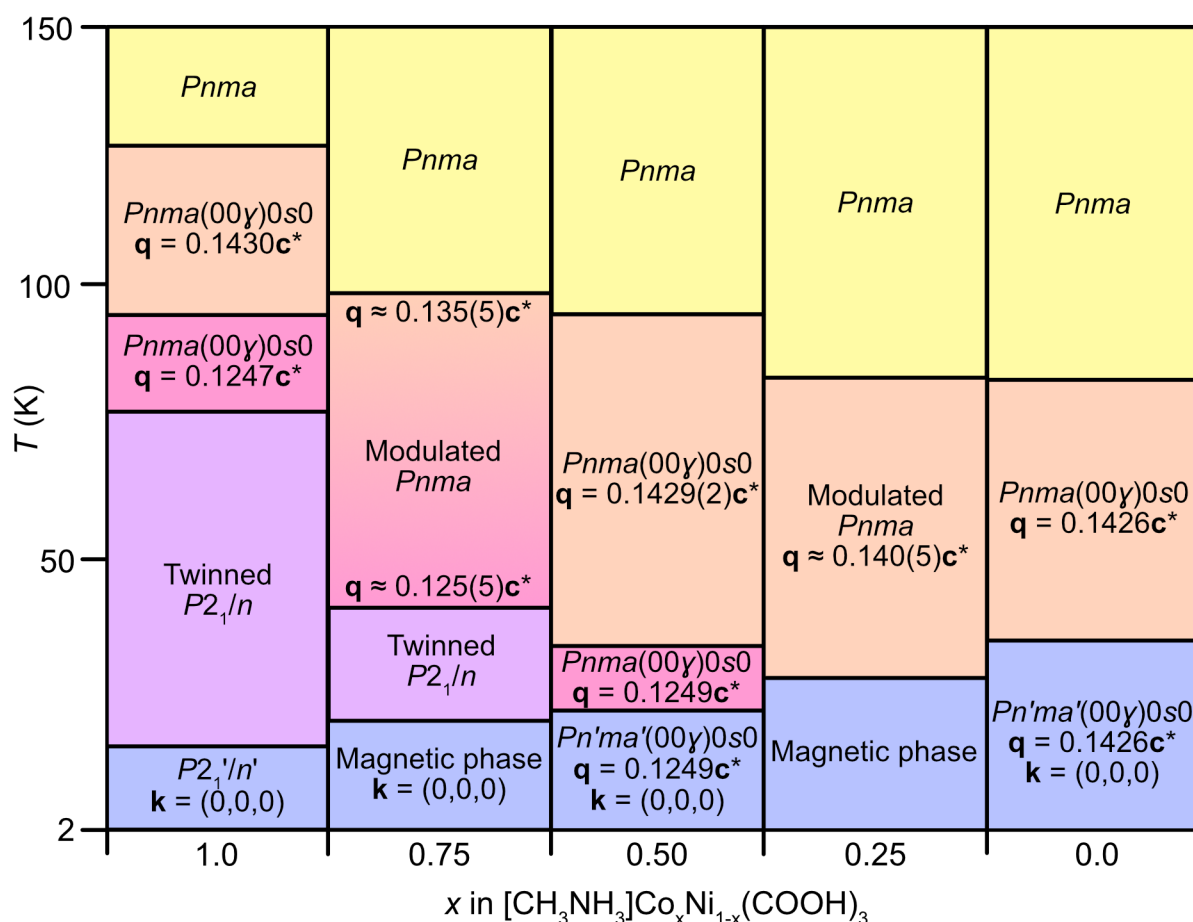


Figure 5.15: Summary of the structural and magnetic temperature dependent phase transitions in single crystal samples of $[\text{CH}_3\text{NH}_3]\text{Co}_x\text{Ni}_{1-x}(\text{HCOO})_3$, $x = 1, 0.75, 0.50, 0.25$ and 0 . For the solid solutions, $x = 0.75, 0.50, 0.25$, transition temperatures were obtained from Laue diffraction measurements, except where differences occur with respect to the monochromatic neutron diffraction data for $\text{Co}_{0.50}\text{Ni}_{0.50}$, in which case these values were used instead. The magnetic ordering temperatures are obtained from the magnetometry data, the magnetic phases are shown in blue.

the phase transitions altered so that they are broadly proportional to the ratio of Co and Ni in the compound (Fig. 5.15).

The structural behaviour of $\text{Co}_{50}\text{Ni}_{50}$ exhibits similarities to both the Co and Ni parent compounds, yet the series of phase transitions do not follow either compound directly. The first two phase transitions, between the non-modulated phase and a modulated phase with $\mathbf{q} = 0.1429(2)\mathbf{c}^*$, followed by an isomorphous phase transition to a structure with $\mathbf{q} = 0.1249(2)\mathbf{c}^*$, resembles that of the Co analogue, although occurring at lower temperatures. In comparison to the Co analogue, which transitions to a twinned, non-modulated, monoclinic structure that is retained with the onset of magnetic ordering, there is no low temperature non-modulated phase for $\text{Co}_{50}\text{Ni}_{50}$. It magnetically orders in the superspace group $Pn'ma'(00\gamma)0s0$ with $\mathbf{q} = 0.1249(2)\mathbf{c}^*$ and $\mathbf{k} = (0, 0, 0)$. The magnetic symmetry is similar to that of the Ni analogue, although with a smaller modulation vector and only the nuclear structure which contributes to the modulations, the magnetic ordering is non-modulated.

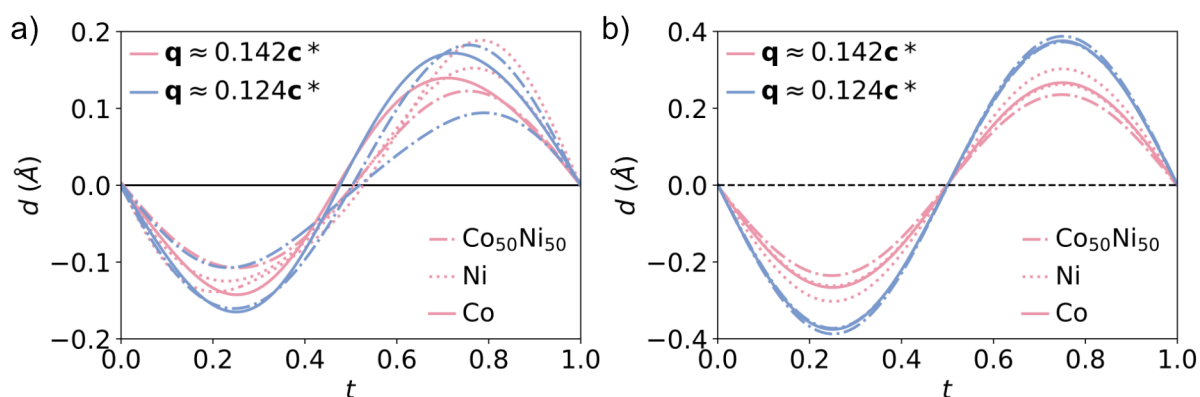


Figure 5.16: Summary of the a) H–O bond distances and b) metal displacement for $[\text{CH}_3\text{NH}_3]\text{Co}(\text{HCOO})_3$ (solid lines), $\text{Co}_{50}\text{Ni}_{50}$ (dot-dash lines) and $[\text{CH}_3\text{NH}_3]\text{Ni}(\text{HCOO})_3$ (dotted lines). The pink lines indicate the structures with the approximate wavevector, $\mathbf{q} = 0.142\mathbf{c}^*$ and the blue lines for the approximate wavevector $\mathbf{q} = 0.124\mathbf{c}^*$. $[\text{CH}_3\text{NH}_3]\text{Co}(\text{HCOO})_3$ data is plotted for structures obtained at $T = 106$ K (pink) and $T = 86$ K (blue), obtained from ref.¹⁸ $\text{Co}_{50}\text{Ni}_{50}$ data is plotted for $T = 70$ K (pink), $T = 30$ and 2 K (blue). $[\text{CH}_3\text{NH}_3]\text{Ni}(\text{HCOO})_3$ data is plotted for $T = 40$ and 5 K (pink), obtained from ref.¹⁹⁴

From the low temperature monochromatic neutron diffraction data, it is evident that the mechanism inducing the modulated phase transitions in $\text{Co}_{50}\text{Ni}_{50}$ is the competition of the hydrogen bonding interactions, akin to its parent compounds. The $\text{H}2 \cdots \text{O}2$ distance remains at values close to its average value, with only small deviations of up to $\pm 0.040(4)$ Å. $\text{H}1 \cdots \text{O}3$, which denotes the hydrogen bonding between the formate oxygens along the b axis, shows alternating distances between $\text{H}1 \cdots \text{O}3a$ and $\text{H}1 \cdots \text{O}3b$. There are certain zones in the structure where the $\text{H}1 \cdots \text{O}3a$ atoms have a shorter separation, whereas at other points, $\text{H}1 \cdots \text{O}3b$ has the shorter contact. This trend is observed at all three temperatures, driving the modulated phases. Comparing with the parent compounds, there is no clear trend between the changes in the hydrogen bond distances and either the

Table 5.2: Amplitude displacements along y of the metal site for $[\text{CH}_3\text{NH}_3]\text{Co}(\text{HCOO})_3$, $\text{Co}_{50}\text{Ni}_{50}$ and $[\text{CH}_3\text{NH}_3]\text{Ni}(\text{HCOO})_3$ for different modulation vectors, \mathbf{q}

M	\mathbf{q}	y	\mathbf{q}	y
Co	0.1430(2)	0.0229	0.1247(2)	0.0322
$\text{Co}_{50}\text{Ni}_{50}$	0.1429(2)	0.02035(19)	0.1249(2)	0.0338(3)
Ni	0.1426(2)	0.02274		

Table 5.3: Average bond length comparison for $[\text{CH}_3\text{NH}_3]\text{Co}(\text{HCOO})_3$ (45 K), $\text{Co}_{50}\text{Ni}_{50}$ (2 K) and $[\text{CH}_3\text{NH}_3]\text{Ni}(\text{HCOO})_3$ (5 K)

M	M–O1 (Å)	M–O2 (Å)	M–O3 (Å)
Co	2.081(2)	2.121(2)	2.105(2)
$\text{Co}_{50}\text{Ni}_{50}$	2.069(3)	2.087(3)	2.075(5)
Ni	2.054(3)	2.068(3)	2.057(6)

modulated structure that is adopted, or the composition of the compound (Fig. 5.16a).

The modulations are triggered by the hydrogen bond competition, however, the changes in the modulation vector can be observed by the resultant magnitude of displacement of the atom sites from the average structure. This can be followed through the y amplitude displacements of the metal site (Fig. 5.16b). There is a division between displacements observed for the shorter modulation length ($\mathbf{q} \approx 0.142\mathbf{c}^*$, pink lines) and the atom displacements observed for the larger modulation length ($\mathbf{q} \approx 0.124\mathbf{c}^*$, blue lines). This is more quantitatively conveyed in amplitude displacements along y for the atoms (Table 5.2). At 70 K, at which temperature $\text{Co}_{50}\text{Ni}_{50}$ has the modulation vector $\mathbf{q} = 0.1429(2)\mathbf{c}^*$, $y = 0.02035(19)$, which is similar to the displacement observed for the Co, $y = 0.0229$ (106 K), and Ni analogues, $y = 0.02274$ (40 K).^{18,194} The phase transition to the longer modulation length ($\mathbf{q} = 0.1249(2)\mathbf{c}^*$) coincides with increasing amplitude displacements in the metal site: for $\text{Co}_{50}\text{Ni}_{50}$ $y = 0.0338(3)$ (2 K), compared to the Co analogue $y = 0.0322(5)$ (86 K). It is proposed that the Co analogue undergoes its final structural transition to a monoclinic non-modulated phase as the continual increases in the amplitude displacements with temperature eventually result in a division into two non-modulated domains.¹⁸ It is possible that the shorter Ni–O bond lengths limit the atom displacement, preventing larger atomic displacement values from being reached. The M–O bond distances at 2 K for $\text{Co}_{50}\text{Ni}_{50}$ are intermediate of the Co–O and Ni–O values, as expected for a solid solution (Table 5.3).^{329,330} It is likely that this factor aids in dictating and limiting the phases accessible for each compound.

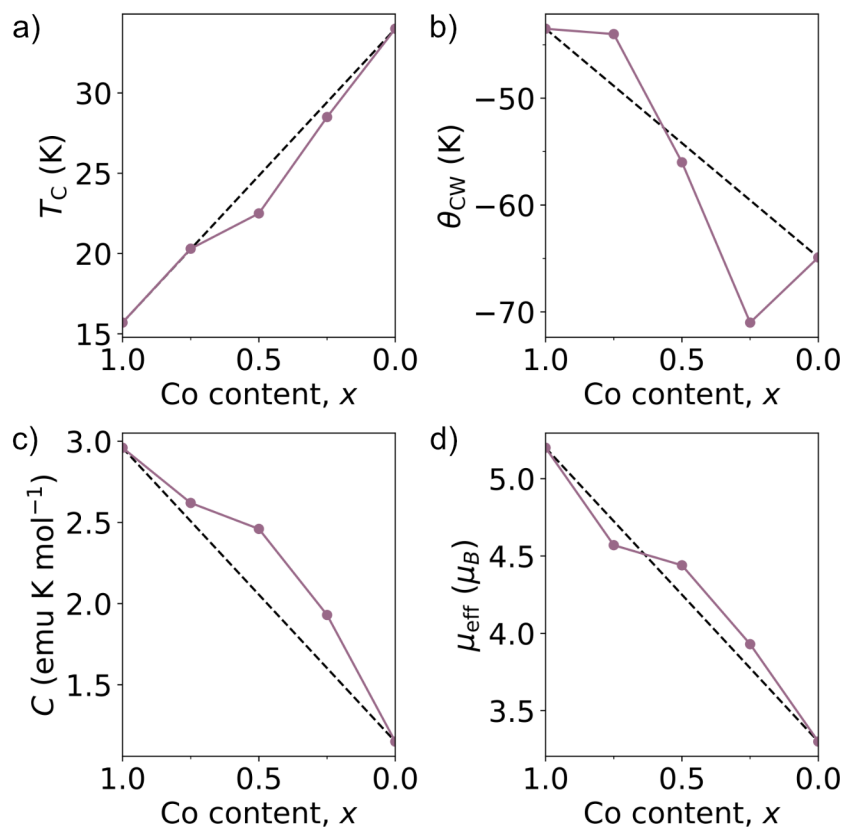


Figure 5.17: Summary of magnetometry values obtained from susceptibility measurements of $[\text{CH}_3\text{NH}_3]\text{Co}_x\text{Ni}_{1-x}(\text{HCOO})_3$ $x = 1.0, 0.75, 0.50, 0.25, 0.0$. a) The magnetic ordering temperatures, T_C , b) Curie-Weiss temperature, θ_{CW} , c) Curie constant, C and d) the effective magnetic moment, μ_{eff} . Values for $[\text{CH}_3\text{NH}_3]\text{Co}(\text{HCOO})_3$ and $[\text{CH}_3\text{NH}_3]\text{Ni}(\text{HCOO})_3$ are from their reported values.¹⁶³

The bulk magnetic properties of $\text{Co}_{75}\text{Ni}_{25}$, $\text{Co}_{50}\text{Ni}_{50}$ and $\text{Co}_{25}\text{Ni}_{75}$ show a continuous linear trend between the Co and Ni end members. This includes the increase in the ordering temperature and decrease in Curie constant and effective magnetic moment as the cobalt content decreases (Fig. 5.17). Cobalt-nickel solid solutions of molecular frameworks, such as dicyanamides³²⁹ and hypophosphites,³³¹ present similar trends, with the ordering temperatures increasing almost linearly towards the nickel parent compound. These are rationalised by the strengthening of superexchange interactions as a result of decreasing bond lengths with increasing nickel content.³²⁹ It is plausible that this can explain the magnetic properties observed for these formate compounds as well, where the bond lengths for $\text{Co}_{50}\text{Ni}_{50}$ follow this trend (Table 5.3) although a lack of structural data below the ordering temperature for $\text{Co}_{75}\text{Ni}_{25}$ and $\text{Co}_{25}\text{Ni}_{75}$ prevent full verification of this. It is possible, however, to observe the strength of the antiferromagnetic correlations in the isothermal magnetisation measurements. The degree of saturation at 5.00(1) T ($M_{5\text{T}}/M_{\text{sat.}}$) decreases from 0.24 for $\text{Co}_{75}\text{Ni}_{25}$, to 0.17 for $\text{Co}_{50}\text{Ni}_{50}$ and 0.14 for $\text{Co}_{25}\text{Ni}_{75}$. The decrease in the extent of saturation suggests that by increasing the nickel content, the antiferromagnetic correlations are strengthened.

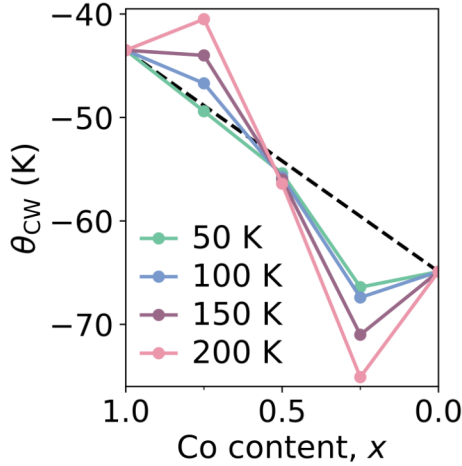


Figure 5.18: Comparison of Curie-Weiss values for $\text{Co}_{75}\text{Ni}_{25}$, $\text{Co}_{50}\text{Ni}_{50}$ and $\text{Co}_{25}\text{Ni}_{75}$ when using different temperature ranges for the fits. The starting temperatures are listed in the legend, fitting between these values and 300 K. The $[\text{CH}_3\text{NH}_3]\text{Co}(\text{HCOO})_3$ and $[\text{CH}_3\text{NH}_3]\text{Ni}(\text{HCOO})_3$ values are from ref.¹⁶³ which make Curie-Weiss fits between $20 < T < 300$ K for $[\text{CH}_3\text{NH}_3]\text{Co}(\text{HCOO})_3$ and $50 < T < 300$ K for $[\text{CH}_3\text{NH}_3]\text{Ni}(\text{HCOO})_3$.

The potential outlier to the trend in the magnetic properties is the Curie-Weiss temperature (Fig. 5.17b). Although the three values obtained for the solid solutions decrease (become more negative) with decreasing cobalt content, the $\text{Co}_{25}\text{Ni}_{75}$ and $\text{Co}_{75}\text{Ni}_{25}$ values are equal or larger than the values reported for the pure cobalt and nickel analogues. Co^{2+} experiences first order spin orbit coupling and, in addition, Ni^{2+} experiences second-order single ion anisotropy. These effects are temperature dependent and, therefore, will impact the values obtained when making the Curie-Weiss fits over different temperatures ranges. To observe the effect the temperature range has on the Curie-Weiss temperature, additional Curie-Weiss fits were performed using temperature ranges between $50 < T < 300$ K and $200 < T < 300$ K (Fig. 5.18). It is apparent that these additional contributions appear to be antagonistic, with $\theta_{\text{CW}, \text{Co}_{75}\text{Ni}_{25}}$ increasing (becoming less negative) with higher starting temperatures, whereas $\theta_{\text{CW}, \text{Co}_{25}\text{Ni}_{75}}$ decreases as only the higher temperature data points are fitted. The two effects almost negate each other in the $\text{Co}_{50}\text{Ni}_{50}$ compound, which shows nearly no variation in θ_{CW} over the temperature regime used for the fitting. The reported values for $[\text{CH}_3\text{NH}_3]\text{Co}(\text{HCOO})_3$ and $[\text{CH}_3\text{NH}_3]\text{Ni}(\text{HCOO})_3$ were fitted using $20 < T < 300$ K and $50 < T < 300$ K.¹⁶³ It is possible that at these temperatures the compounds are not completely in the paramagnetic state ($T_{\text{C}} = 15.7$ K for $\text{M} = \text{Co}$ and $T_{\text{C}} = 34$ K for $\text{M} = \text{Ni}$), which may also distort the Curie-Weiss values of the two end members. Without using more involved methods to calculate the Curie-Weiss temperatures which account for these additional effects, and also ensuring only the paramagnetic temperature regions are modelled, the Curie-Weiss temperatures for all the compounds should be taken with a degree of discretion. Nevertheless, these formate solid solutions follow the trend that the strength of the interactions increase with the nickel content, which is supported by the general negative trend in θ_{CW} .

Co₅₀Ni₅₀ magnetically orders at $T_C = 22.5(7)$ K in the magnetic superspace group $Pn'ma'(00\gamma)0s0$ with $\mathbf{q} = 0.1249(2)\mathbf{c}^*$. The moments show weak ferromagnetic ordering, with the uncompensated moment along the b axis. This ordering is broadly comparable to both the Co and Ni end members, which both show weak ferromagnetic superexchange with the nearest neighbours. Co₅₀Ni₅₀ orders in the same superspace group as the Ni analogue, although with a smaller modulation vector, $\mathbf{q} = 0.1249(2)\mathbf{c}^*$. Unlike the magnetic structure of the Ni compound, Co₅₀Ni₅₀ adopts an improper incommensurate magnetic structure. It has been reported that by applying a small external magnetic field, approximately 0.05 T, [CH₃NH₃]Ni(HCOO)₃ undergoes a transition to an improper incommensurate magnetic phase with collinear moments.³³² Perhaps, the weaker superexchange pathways deriving from coupling of the Co ions, or the modulation of the M–O–C bond angles, suppresses activation of any proper magnetic modulations in the structure.

5.5 Conclusions

Three solid solutions of [CH₃NH₃]Co _{x} Ni _{$1-x$} (HCOO)₃, $x = 0.25, 0.50, 0.75$, have been synthesised and their nuclear structures and magnetic properties identified through single crystal neutron diffraction and magnetisation measurements. Magnetometry data show that their bulk magnetic properties exhibit a linear continuum between the cobalt and nickel end members. The Laue neutron diffraction data permitted a practical method to track the structural behaviour of the compounds and identify the temperature regions of the low temperature modulated phases.

Monochromatic neutron diffraction data confirmed that, similar to the Co and Ni end members, the modulated phases for [CH₃NH₃]Co_{0.50}Ni_{0.50}(HCOO)₃ are induced by the competing hydrogen bond interactions. However, the structural evolution does not follow the same phases as either parent compound. This is likely as a result of the differing Co–O and Ni–O bond lengths which dictate the limits of the atom amplitude displacement modulations.

These solid solutions have shown that through doping of the metal site, the bulk magnetic properties, in particular the magnetic ordering temperature, of [CH₃NH₃]Co _{x} Ni _{$1-x$} (HCOO)₃ can be tuned through the metal ratios. In addition, both the transition temperatures and nature of the nuclear phase transitions can be manipulated *via* the nickel content.

Despite the sparsity of reported incommensurately modulated molecular frameworks, with understanding of the interactions which persuade the modulations, it presents the opportunity to consciously design molecular compounds with the propensity for incom-

mensurately modulated phases and finer control of their properties.

5.6 Experimental

5.6.1 Synthesis

The synthesis of $[\text{CH}_3\text{NH}_3]\text{Co}_{0.75}\text{Ni}_{0.25}(\text{HCOO})_3$, $[\text{CH}_3\text{NH}_3]\text{Co}_{0.50}\text{Ni}_{0.50}(\text{HCOO})_3$ and $[\text{CH}_3\text{NH}_3]\text{Co}_{0.25}\text{Ni}_{0.75}(\text{HCOO})_3$ were followed from reported methods for protonated amine metal formates.^{101,326} An example is provided for quantities and timescales used for the $[\text{CH}_3\text{NH}_3]\text{Co}_{0.50}\text{Ni}_{0.50}(\text{HCOO})_3$ synthesis.

Aqueous solutions of $\text{CoCl}_2 \cdot 6 \text{H}_2\text{O}$ (119 mg, 0.5 mmol, 1.5 mL), $\text{NiCl}_2 \cdot 6 \text{H}_2\text{O}$ (119 mg, 0.5 mmol, 1.5 mL), $\text{CH}_3\text{NH}_3\text{Cl}$ (68 mg, 1 mmol, 3 mL) and NaHCOO (204 mg, 3 mmol, 2 mL) were mixed with *N*-methylformamide (HCONHCH_3). The solution was sealed in an autoclave (43 mL) and heated at 413 K for 3 d. The solution was slowly cooled to ambient temperature (approximately 5 h), yielding dark green prismatic crystals ($3 \times 2 \times 2 \text{ mm}^3$). The crystals were filtered, and dried at room temperature.

Using an analogous method with stoichiometric ratios of $\text{CoCl}_2 \cdot 6 \text{H}_2\text{O}$ and $\text{NiCl}_2 \cdot 6 \text{H}_2\text{O}$ yield dark red crystals of $[\text{CH}_3\text{NH}_3]\text{Co}_{0.75}\text{Ni}_{0.25}(\text{HCOO})_3$ ($1.5 \times 1.5 \times 1 \text{ mm}^3$) and dark green crystals of $[\text{CH}_3\text{NH}_3]\text{Co}_{0.25}\text{Ni}_{0.75}(\text{HCOO})_3$ ($2 \times 1.5 \times 1.5 \text{ mm}^3$).

5.6.2 Single crystal X-ray diffraction

Single crystal X-ray measurements were carried out at ambient temperature using a Bruker D8 Venture diffractometer (Institut Laue Langevin, ILL, France) by Dr Laura Cañadillas Delgado (ILL), Dr Oscar Fabelo (ILL) and myself. A graphite monochromatic radiation source from Ag- $\text{K}\alpha$ radiation, $\lambda = 0.56086 \text{ \AA}$ was used. The samples were mounted on thin glass fibres attached to brass pins and mounted onto goniometer heads. Structure solution for $[\text{CH}_3\text{NH}_3]\text{Co}_{0.75}\text{Ni}_{0.25}(\text{HCOO})_3$ was carried out using SHELXT²⁷ and refinements were made with SHELXL, within the OLEX2^{268,269} graphical interfaces. The structural models for $[\text{CH}_3\text{NH}_3]\text{Co}_{0.25}\text{Ni}_{0.75}(\text{HCOO})_3$ and $[\text{CH}_3\text{NH}_3]\text{Co}_{0.50}\text{Ni}_{0.50}(\text{HCOO})_3$ were solved using the *SUPERFLIP* program²⁸ and refined using Jana2006.^{36,333} The non-hydrogen atoms were refined anisotropically with displacement parameters.

5.6.3 Magnetic measurements

Measurements of the magnetic susceptibility were carried by Dr Matthew Cliffe and Jem Pitcairn (University of Nottingham) out on samples of $[\text{CH}_3\text{NH}_3]\text{Co}_{0.75}\text{Ni}_{0.25}(\text{HCOO})_3$ (8.75 mg), $[\text{CH}_3\text{NH}_3]\text{Co}_{0.50}\text{Ni}_{0.50}(\text{HCOO})_3$ (12.50 mg) and $[\text{CH}_3\text{NH}_3]\text{Co}_{0.25}\text{Ni}_{0.75}(\text{HCOO})_3$ (12.45 mg) using a Quantum Design Magnetic Property Measurements System (MPMS) 3 Superconducting Quantum Interference Device (SQUID) magnetometer. The zero-field-cooled (ZFC) and field-cooled (FC) susceptibility were measured in an applied field of 0.01 T over the temperature range 2 – 300 K. As $M(H)$ is linear in this field, the small-field approximation for the susceptibility, $\chi(T) \simeq \frac{M}{H}$, where M is the magnetisation and H is the magnetic field intensity, was taken to be valid.

Isothermal magnetisation measurements were carried out at 2 K over the field range -5 to $+5$ T. Data were corrected for diamagnetism of the sample using Pascal’s constants.⁴¹

5.6.4 Laue neutron diffraction

The Laue neutron diffraction measurements were collected by Dr Laura Cañadillas Delgado, Dr Oscar Fabelo, Dr Matthew Cliffe and myself on the multiple CCD diffractometer CYCLOPS (Cylindrical CCD Laue Octagonal Photo Scintillator, at the ILL, France)³³⁴ which operates with thermal neutrons. A single crystal of $1.5 \times 1.5 \times 1$ mm³ ($[\text{CH}_3\text{NH}_3]\text{Co}_{0.75}\text{Ni}_{0.25}(\text{HCOO})_3$), $3 \times 2 \times 2$ mm³ ($[\text{CH}_3\text{NH}_3]\text{Co}_{0.50}\text{Ni}_{0.50}(\text{HCOO})_3$), $2 \times 1.5 \times 1.5$ mm³ ($[\text{CH}_3\text{NH}_3]\text{Co}_{0.25}\text{Ni}_{0.75}(\text{HCOO})_3$), was mounted on a vanadium pin and placed in a standard orange cryostat. The diffraction patterns were recorded in the temperature range 10 to 120 K, following a ramp of 0.1 K per 30 s. Each Laue diffraction pattern was collected over a period of 15 min with a temperature range of 3 K. The samples were centred on the neutron beam by maximisation of the intensity of several strong reflections in the x , y and z directions, after which, a specific orientation was selected and the temperature evolution was collected. Graphical visualisation of the Laue patterns was performed with the ESMERALDA software.³³⁵

5.6.5 Ambient temperature single crystal neutron diffraction (D9)

Hot neutron single crystal diffraction was performed by Dr Laura Cañadillas Delgado (ILL), Oscar Fabelo (ILL), Dr Matthew Cliffe and myself on the four-circle diffractometer D9 (ILL, France) for $[\text{CH}_3\text{NH}_3]\text{Co}_{0.75}\text{Ni}_{0.25}(\text{HCOO})_3$, $[\text{CH}_3\text{NH}_3]\text{Co}_{0.50}\text{Ni}_{0.50}(\text{HCOO})_3$ and $[\text{CH}_3\text{NH}_3]\text{Co}_{0.25}\text{Ni}_{0.75}(\text{HCOO})_3$. A monochromatic beam of wavelength $\lambda = 0.836$ Å was produced using the (220) plane of a Cu crystal in transmission geometry, and a small two-

dimensional area detector. Integrated intensities of structural Bragg peaks were collected with standard transverse scans (ω -scans). NOMAD software from the ILL was used for data collection.²²⁵

The structural models were solved using the *SUPERFLIP* program²⁸ and refined using Jana2006,^{36,333} refining the occupancies of the metal site to obtain the cobalt and nickel ratio of each crystal.

5.6.6 Low temperature single crystal neutron diffraction (D19)

Monochromatic single crystal neutron diffraction data were collected by Dr Laura Cañadillas Delgado (ILL), Dr Oscar Fabelo (ILL), Dr Matthew Cliffe and myself on the four-circle D19 diffractometer (ILL, France) for $[\text{CH}_3\text{NH}_3]\text{Co}_{0.50}\text{Ni}_{0.50}(\text{HCOO})_3$. Neutrons with a wavelength of 1.456 Å were provided by a flat Cu monochromator using the 220 reflection at $2\theta_M = 69.91^\circ$ take-off angle. The sample was placed in a closed-circuit displac cooling device, which was operated following a ramp of 2 K min⁻¹. Measurements were taken at 2 K, and at 10 K intervals between 30 and 100 K. NOMAD software from the ILL was used for data collection.²²⁵ Longer data acquisitions were made at 2, 30 and 70 K and were used for the nuclear and magnetic refinements.

Unit cell determinations were performed using PFIND and DIRAX programs, and processing of the raw data was applied using RETREAT, RAFD19 and Int3D programs.²²⁶⁻²²⁹ The data were corrected for the absorption of the low-temperature device using the D19ABSCAN program.²³⁰ Nuclear and magnetic models were solved by Dr Laura Cañadillas Delgado using the *SUPERFLIP* program²⁸ and refined using Jana2006.^{36,333}

5.7 Appendix

Table 5.4: Average bond lengths obtained from the refinement of $[\text{CH}_3\text{NH}_3]\text{Co}_{0.50}\text{Ni}_{0.50}(\text{HCOO})_3$ at 70 K for M–O bonds. The maximum, minimum and average bond lengths for M–O $_{xa}$ and M–O $_{xb}$ are equivalent

Bond	Average (Å)	Maximum (Å)	Minimum (Å)	Max. displacement (Å)
M–O1	2.0674(17)	2.072(2)	2.063(2)	+0.005(3), –0.004(3)
M–O2	2.0830(17)	2.089(2)	2.076(2)	+0.006(3), –0.007(3)
M–O3	2.0766(17)	2.083(2)	2.071(2)	+0.006(3), –0.006(3)

Table 5.5: Average bond lengths obtained from the refinement of $[\text{CH}_3\text{NH}_3]\text{Co}_{0.50}\text{Ni}_{0.50}(\text{HCOO})_3$ at 30 K for M–O bonds. The maximum, minimum and average bond lengths for M–O $_x$ a and M–O $_x$ b are equivalent

Bond	Average (Å)	Maximum (Å)	Minimum (Å)	Max. displacement (Å)
M–O1	2.070(2)	2.130(3)	2.014(3)	+0.061(4), –0.055(4)
M–O2	2.087(2)	2.094(3)	2.081(3)	+0.007(4), –0.006(4)
M–O3	2.078(2)	2.138(5)	2.009(5)	+0.060(5), –0.069(5)

Table 5.6: Average bond lengths obtained from the refinement of $[\text{CH}_3\text{NH}_3]\text{Co}_{0.50}\text{Ni}_{0.50}(\text{HCOO})_3$ at 2 K for M–O bonds. The maximum, minimum and average bond lengths for M–O $_x$ a and M–O $_x$ b are equivalent

Bond	Average (Å)	Maximum (Å)	Minimum (Å)	Max. displacement (Å)
M–O1	2.069(3)	2.076(3)	2.062(3)	+0.007(4), –0.007(4)
M–O2	2.086(3)	2.096(2)	2.077(3)	+0.010(4), –0.009(4)
M–O3	2.075(5)	2.090(6)	2.067(6)	+0.015(8), –0.008(8)

Table 5.7: Summary of the bulk magnetic properties for $[\text{CH}_3\text{NH}_3]\text{Co}_x\text{Ni}_{1-x}(\text{HCOO})_3$ $x = 0.75, 0.50, 0.25$, obtained from magnetisation measurements. C is calculated from the value of χT at 300 K. The θ_{CW} values are calculated from fits over the temperature ranges $150 < T < 300$ K

	$x = 1.0$	$x = 0.75$	$x = 0.50$	$x = 0.25$	$x = 0.0$
S	1.5	1.375	1.25	1.125	1.0
T_C (K)	15.7	19.7(5)	22.5(7)	28.5(5)	34
θ_{CW} (K)	–43.5	43.6(5)	56.3(1)	–70.8(7)	–64.9
C ($\text{cm}^3 \text{K mol}^{-1}$)	3.45	2.625(1)	2.461(1)	1.936(4)	1.40
$C_{\text{spin only}}$ ($\text{cm}^3 \text{K mol}^{-1}$)	1.87	1.633	1.41	1.195	1.0
$\mu_{\text{eff.}}$ (μ_B)	5.2	4.578(2)	4.436(2)	3.936(2)	3.3
$\mu_{\text{spin only}}$ (μ_B)	3.88	3.614	3.354	3.092	2.83
$M_{\text{rem.}}$ (μ_B per metal)		0.045(3)	0.27(1)	0.015(1)	
H_C (T)		0.45(1)	0.30(1)	0.15(1)	
$M_{5 \text{ T}}/M_{\text{sat.}}$		0.245	0.175	0.140	

Table 5.8: Calculated values of the Curie-Weiss temperature, θ_{CW} , for $\text{Co}_{75}\text{Ni}_{25}$, $\text{Co}_{50}\text{Ni}_{50}$ and $\text{Co}_{25}\text{Ni}_{75}$, when using varying temperature start temperatures over the region $x < T < 300$ K

x (K)	$\theta_{\text{CW}} \text{Co}_{75}\text{Ni}_{25}$ (K)	$\theta_{\text{CW}} \text{Co}_{50}\text{Ni}_{50}$ (K)	$\theta_{\text{CW}} \text{Co}_{25}\text{Ni}_{75}$ (K)
50	–66.4(2)	–55.4(1)	–49.4(2)
100	–67.4(5)	–55.77(8)	–46.7(4)
150	–70.8(7)	–56.2(1)	–43.7(5)
200	–75(1)	–56.4(4)	–40.5(5)

Table 5.9: Single crystal experimental details and crystallographic parameters for neutron diffraction of $\text{Co}_{50}\text{Ni}_{50}$ (D19, ILL) at 70 and 30 K

	$\text{C}_8\text{H}_{18}\text{CoNiNO}_{12}$	$\text{C}_8\text{H}_{18}\text{CoNiNO}_{12}$
Empirical formula	$\text{C}_8\text{H}_{18}\text{CoNiNO}_{12}$	$\text{C}_8\text{H}_{18}\text{CoNiNO}_{12}$
M_r	225.93	225.93
T (K)	70	30
Superspace group	$Pnma(00\gamma)0s0$	$Pnma(00\gamma)0s0$
a (Å)	8.2064(3)	8.2003(3)
b (Å)	11.5811(6)	11.5737(8)
c (Å)	8.1153(3)	8.1133(3)
V (Å ³)	771.27(6)	770.02(7)
Z	4	4
Modulation vector, \mathbf{q}	0.1429(2)	0.1249(2)
λ (Å)	1.4557	1.4557
$R_1, I > 3\sigma(I)$ (all)	0.0707 (0.0861)	0.1189 (0.1315)
$\omega R_2, I > 3\sigma(I)$ (all)	0.1439 (0.1786)	0.1900 (0.2034)
Main reflections: $R_1, I > 3\sigma(I)$ (all)	0.0594 (0.0597)	0.0842 (0.0861)
Main reflections: $\omega R_2, I > 3\sigma(I)$ (all)	0.1076 (0.1095)	0.1544 (0.1595)
First-order satellites: $R_1, I > 3\sigma(I)$ (all)	0.0831 (0.0895)	0.1400 (0.1432)
First-order satellites: $\omega R_2, I > 3\sigma(I)$ (all)	0.1583 (0.1691)	0.2025 (0.2072)
Second-order satellites: $R_1, I > 3\sigma(I)$ (all)	0.1222 (0.2800)	0.1765 (0.2436)
Second-order satellites: $\omega R_2, I > 3\sigma(I)$ (all)	0.1660 (0.2867)	0.2032 (0.2374)
Observed independent reflections (all)	2152 (3291)	2480 (3346)
Observed no. of main reflections (all)	673 (682)	655 (694)
Observed no. of first-order satellite reflections (all)	1094 (1230)	1149 (1250)
Observed no. of second-order satellite reflections (all)	385 (994)	676 (1402)

Chapter 6

A-site ordering and octahedral tilts in $[\square A]\text{Mn}\{\text{Bi}(\text{SCN})_6\}$

6.1 Summary

- Four manganese(II) bismuth(III) thiocyanate frameworks, nominally $[\square A]\text{Mn}\{\text{Bi}(\text{SCN})_6\}$ $A = \text{Cs}^+, \text{K}^+, \text{NH}_4^+$ and $\text{C}(\text{NH}_2)_3^+$, have been synthesised yielding single crystals and microcrystalline powders.
- The structures were solved through combinations of single crystal neutron diffraction, single crystal and powder X-ray diffraction and single crystal electron diffraction, depending on the quality and dimensions of the single crystals and powders obtained.
- All the compounds show cation ordering of the A- and M-sites, with unfamiliar A-site orderings for all the compounds. For $A = \text{NH}_4^+, \text{Cs}^+$ and $\text{C}(\text{NH}_2)_3^+$ unconventional A-site orderings and octahedral tilt sequences are also reported.

6.2 Introduction

The AMX_3 perovskite materials present a synthetic playground for scientists, tailoring compounds to exhibit specific physical properties through readily exchangeable A, M and X components.^{336,337} Species incorporated are generally selected with the aim of directing the overall functionality, for example, selecting a paramagnetic M ion to guide the magnetic properties. This can be compounded by altering the symmetry of the structure, for instance, by adopting a polar space group the coexistence of a second ordered state, such as ferroelectric ordering can be obtained.³³⁸

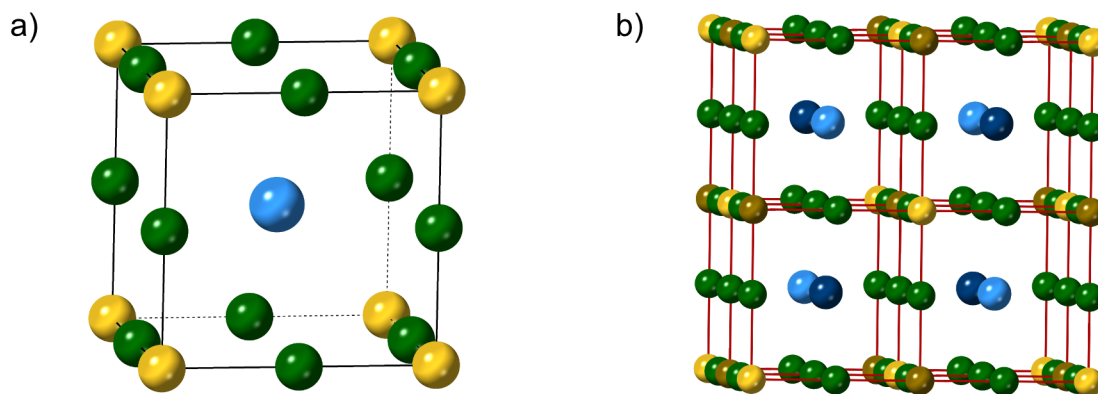


Figure 6.1: a) The aristotype $Pm\bar{3}m$ perovskite with AMX_3 stoichiometry. The black line indicates its unit cell. A = blue, M = yellow, X = green. b) A distorted double perovskite with $AA'MM'X_6$ stoichiometry and A- and M-site rocksalt orderings. The unit cell has doubled in length for all the axes, but the pseudocubic metal cage (red lines) are the same as the unit cell in a). A/A' = light and dark blue, M/M' = yellow and brown, X = green.

The aristotypic perovskite structure adopts the cubic $Pm\bar{3}m$ space group.¹³¹ To break the inversion centre, it is necessary to distort the structure. This can be systematically achieved by incorporating multiple species on a single site, forming $AA'M_2X_6$ or $A_2MM'X_6$ structures. The essential consideration is that A- or M- sites adopt an ordered arrangement. The most commonly observed ordering patterns are rocksalt, layered and columnar.¹⁴⁰

The M-site species commonly exhibit rocksalt ordering if there is a large difference in charges for M and M', as this distributes the higher charged cations equally.¹⁴⁰ In comparison, A-site cation ordering is not typically observed. For the small number of reported examples where A-site ordering is present, layered order is most common. This is because it permits the M–X bond lengths to distort, compensating for the strain created by the difference in A-cation sizes.³³⁹ However, A-site ordering can be strongly influenced by the octahedral tilt sequence of the framework, since the rotations distort the dimensions of the pseudocubic cage.¹³⁰ In this case, the A-site ordering is particularly directed by sterics, which is pertinent for mixed A-sites where one of the species are vacancies. The “metal cage” for each A-site is defined by the surrounding $[M_8X_{12}]$ cube. For an ideal perovskite, this is equivalent to its unit cell, whereas for compounds with ordered sites, the unit cell may be larger, and the $[M_8X_{12}]$ cube around the A-site is defined as a pseudocubic cage (Fig. 6.1).

The inclusion of molecular X anions has two immediate implications for the MX_3 framework, compared to atomic X components. The longer X^- linker means that the pseudocubic cell dimensions are extended and there is a larger volume to accommodate A-site species. In addition, the molecular anions permit unconventional tilt sequences created by the extra structural flexibility of the molecular components which cannot be

realised in atomic-only compounds. This can further lead to more unusual A-site ordering patterns.^{142,340,341}

Few thiocyanate perovskites have been reported, $\text{CsCd}(\text{NCS})_3$ ⁹⁶ and the double perovskites $(\text{NH}_4)_2\text{Ni}\{\text{Cd}(\text{SCN})_6\}$,⁹⁷ A-site ordered $[\square\text{A}]\text{Ni}\{\text{Bi}(\text{SCN})_6\}$, $\square = \text{vacancy}$, $\text{A} = \text{NH}_4^+$, K^+ , CH_3NH_3^+ , $\text{C}(\text{NH}_2)_3^{+98}$ and A-site vacant $\square_2\text{M}\{\text{Pt}(\text{SCN})_6\}$, $\text{M} = \text{Mn}$, Fe , Co , Ni , Cu ⁹⁹ and $\square_2\text{M}\{\text{Bi}(\text{SCN})_6\}$, $\text{M} = \text{Fe}$, Cr , Sc .⁷⁷ All the double perovskites show M-site rocksalt ordering, templated by the coordination preferences of the thiocyanate ligand so that there are $[\text{MN}_6]$ $\text{M} = \text{Ni}$, Fe , Cr , Sc , octahedra and $[\text{M}'\text{S}_6]$ $\text{M}' = \text{Cd}$, Bi , Pt , octahedra. The $[\square\text{A}]\text{Ni}\{\text{Bi}(\text{SCN})_6\}$ compounds also exhibit A-site order, which is predominately dictated by the tilt sequence, in addition to the size of the A species and electrostatic and hydrogen bond interactions.⁹⁸ The combination of A-site ordering and octahedral tilt patterns gives rise to an array of structures. $[\square\text{NH}_4]\text{Ni}\{\text{Bi}(\text{SCN})_6\}$ and $[\square\text{K}]\text{Ni}\{\text{Bi}(\text{SCN})_6\}$ are isostructural with columnar A-site order and $a^- a^- c^+$ tilt sequence (Glazer notation).¹⁴¹ $[\square\text{CH}_3\text{NH}_3]\text{Ni}\{\text{Bi}(\text{SCN})_6\}$ adopts a complex unconventional tilt sequence of $a^+ b^{+-} c^{+-}$ with the A-site cations ordering in $(1 \times 2 \times 3)$ blocks, surrounded by vacant cages. In addition, $[\square_9\text{Gua}_3]\text{Ni}_6\{\text{Bi}(\text{SCN})_6\}_5$ $\text{Gua} = \text{C}(\text{NH}_2)_3^+$, adopts a structure with M-site Bi vacancies, driven by the sterics of the larger Gua cations.

Octahedral tilt patterns are sensitive to the M-site species and by doping metals of different radii, the octahedral tilts can be tuned.^{342,343} The magnitude of the octahedral tilts plays a role in determining the A-site ordering, and, therefore, the overall structure. To date, the only double thiocyanate perovskites with both A- and M- site ordering are the $[\square\text{A}]\text{Ni}\{\text{Bi}(\text{SCN})_6\}$ compounds. To explore the effect of M-site composition on the tilt sequence and, consequently, A-site orderings, Ni^{2+} can be replaced with another first row transition metal, such as Mn^{2+} , which will readily coordinate with the N terminus of the thiocyanate as to maintain the rocksalt M-site ordering.

Here I present the synthesis, structure and magnetic data of four manganese(II) bismuth(III) thiocyanate frameworks, nominally $[\square\text{A}]\text{Mn}\{\text{Bi}(\text{SCN})_6\}$, $\text{A} = \text{K}^+$, Cs^+ , NH_4^+ and $\text{C}(\text{NH}_2)_3^+$ (guanidinium, Gua). The crystallographic analyses of the compounds take place through combinations of powder and single X-ray diffraction, single crystal neutron diffraction and electron diffraction data. The compounds show ordering of both the M-site and A-site species. Complex orderings for the A-site cations in combination with the octahedral tilt sequences observed result in unexpected structures, unlike their nickel analogues with equivalent A-site cations.

6.3 Results

6.3.1 Synthesis

The $[\square A]Mn\{Bi(SCN)_6\}$ compounds were synthesised from $Mn(NO_3)_2 \cdot 4H_2O$, $Bi(NO_3)_3 \cdot 5H_2O$ and $A(NCS)$ where $A = K^+$, Cs^+ , NH_4^+ and Gua, in the ratio 1 : 1 : 6, which were dissolved in butanone or acetone. On removal of the solvent, a red-orange microcrystalline powder was obtained for the synthesis with K^+ (KMnBi). Slow evaporation from their mother liquors yielded μm^3 sized crystals for $A = Gua$ ($Gua_2Mn_{17}Bi_{16}$) and mm^3 sized crystals of $A = NH_4^+$ (NH_4MnBi) and Cs^+ ($CsMnBi$).

Syntheses were also attempted for $A = CH_3NH_3^+$ and $H_2NNH_3^+$ (hydrazinium), however these either yielded wet solids or pastes that could not be dried under reduced pressure (using a rotary evaporator or a Schlenk line). On heating above $50^\circ C$, the samples began to melt, and below this temperature the solvent could not be removed by heating.

6.3.2 Structure

6.3.2.1 $[\square K]Mn\{Bi(SCN)_6\}$

From the synthesis of KMnBi an orange microcrystalline powder was obtained. Powder X-ray diffraction produced a diffractogram with well defined peaks. Le Bail fits of the data to other known thiocyanate structures, $[\square A]Ni\{Bi(SCN)_6\}$, $A = K$, CH_3NH_3 , Gua, and $\square_2Fe\{Bi(SCN)_6\}$, were attempted, however, these could not model the intensities at the positions observed. Slow evaporation recrystallisations from distilled H_2O or acetone did not produce crystals large enough for single crystal X-ray diffraction measurements.

With a crystalline powder, but no μm^3 sized crystals, it was possible to explore an alternative method of diffraction to determine the structure of KMnBi. Single crystal electron diffraction measurements were carried out by Dr Jakub Wojciechowski (Rigaku Europe SE), Dr Robert Bückler (Rigaku Europe SE) and Dr Stephen Argent (University of Nottingham). Nine data sets were collected on selected crystals from the bulk powder sample and the data were integrated to obtain a unit cell. Three data sets provided similar unit cell dimensions and symmetry, so these data were scaled and merged, providing one reflection file for the structure solution with a higher completeness and redundancy. The integrated unit cell is monoclinic Pn with the dimensions $a = 8.7(2) \text{ \AA}$, $b = 8.5(4) \text{ \AA}$, $c = 12.00(19) \text{ \AA}$, $\beta = 90.44(5)^\circ$. The minimum and maximum residual electron density peaks are $+0.4$ and -0.5 e\AA^{-3} .

During the refinement several restraints were employed for atoms of the thiocyanate ligands to maintain a stable model. This included hard restraints for the N–C, C–S and N···S distances and restraints to keep the average bond lengths between the symmetry distinct thiocyanate ligands approximately equivalent as well. Despite applying constraints to the anisotropic displacement parameters, it was not possible to refine these to physically meaningful values, so all atoms were refined isotropically. From these data, the connectivity of the thiocyanate framework and position of the K⁺ cations could be determined, however, the data quality does not allow for further analysis of specific atom positions and therefore bond distances and angles (Fig. 6.2a).

Having obtained a model from single crystal electron diffraction, the powder X-ray diffraction data could be fitted to verify the structure in the bulk microcrystalline sample and improve the precision of the unit cell parameters. Le Bail refinements were performed, refining freely the unit cell parameters ($R_{wp} = 35.0\%$). From this refinement, the unit cell parameters are $a = 8.8119(1)$ Å, $b = 8.61563(5)$ Å, $c = 12.1235(2)$ Å, $\beta = 90.364(1)^\circ$, within error equivalent to the electron diffraction data (Fig. 6.2b).

KMnBi crystallises in the monoclinic space group Pn . The M-site cations have rocksalt ordering, with Mn octahedrally coordinated to the nitrogen termini and Bi octahedrally coordinated to the sulfur of the thiocyanate anions (Fig. 6.2c). The pseudocubic cage axes are defined as $[1\bar{1}0]$, $[110]$ and $[001]$. The K⁺ A-site cations occupy half the metal cages, also with rocksalt ordering (Fig. 6.2d). Along the $[1\bar{1}0]$ and $[110]$ directions, the octahedra alternate their sense of rotation, and along $[001]$ all the octahedra rotate in the same direction. This is described as $a^-a^-c^+$ tilt sequence (Fig. 6.2e).

To confirm that KMnBi adopts a polar structure, FINDSYM from the ISOTROPY Software Suite^{344,345} was used to search for any potential higher symmetry space groups. No additional symmetry operators could be identified, suggesting that Pn is the correct space group for the crystal.

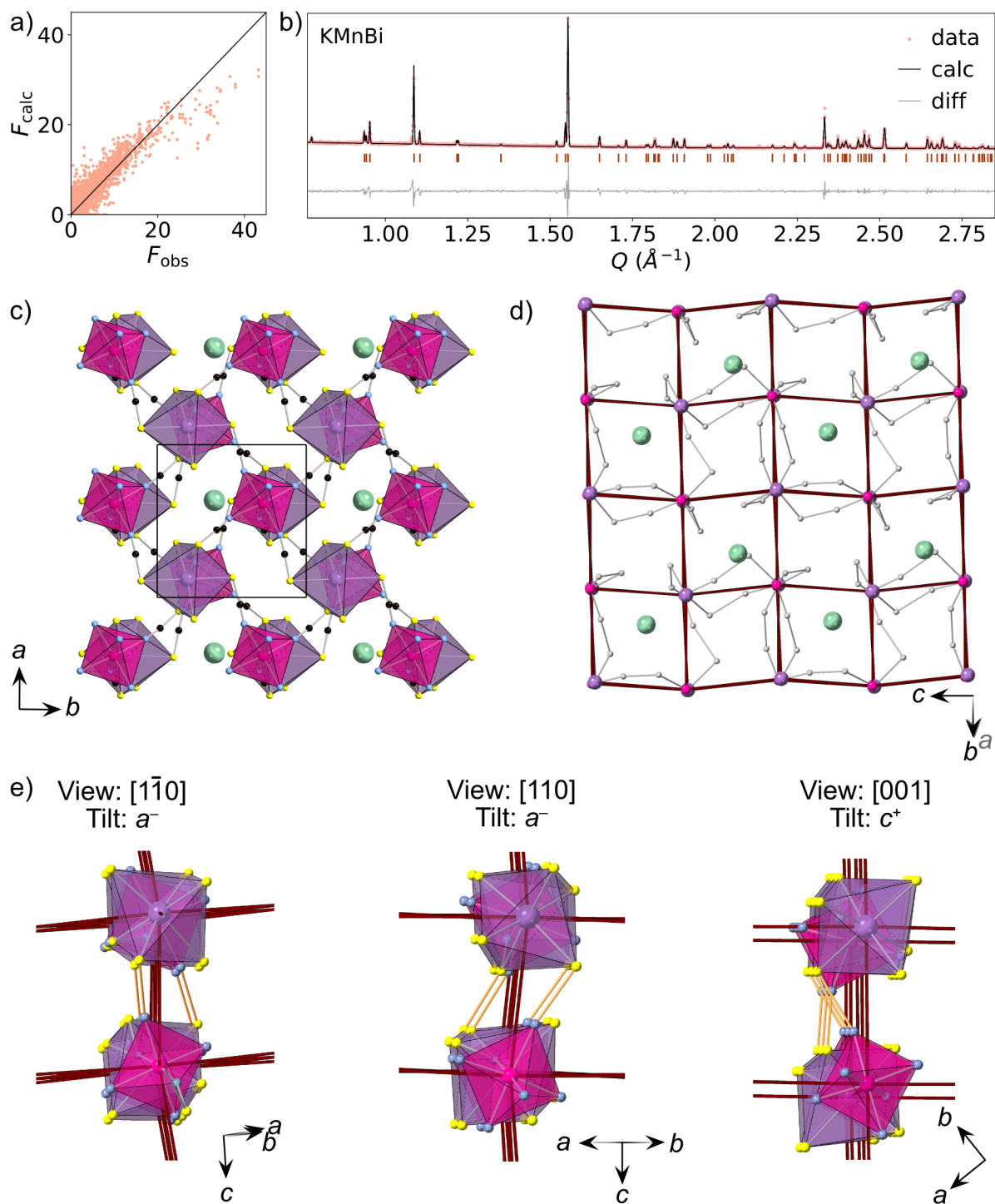


Figure 6.2: The structure of KMnBi in the Pn space group. a) F_{obs} against F_{calc} from refinements of the electron diffraction data. b) Le Bail refinement of the powder diffraction data using the model obtained from the electron diffraction refinement ($R_{\omega p} = 35.0\%$). c) The structure viewed along the $[001]$ direction. d) The A-site cation rocksalt ordering, viewed along $[110]$. The Mn and Bi atoms are joined by red lines, indicating the edges of the pseudocubic metal cages. e) The octahedral tilt patterns showing the N-S connections (pale pink) linking the neighbouring M-site metals. Where all the N-S connections alternate between being positioned to the left or right of the cage edge (red lines), the metals are rotating out-of-phase (a^-). Where the pale pink connections are on one side of the cage edge only, the metals show in-phase tilting (c^-). The C atoms have been removed for clarity. Mn = pink, Bi = purple, N = blue, C = black, S = yellow, K = pale green.

6.3.2.2 $[\square_{\frac{7}{8}}(\text{NH}_4)(\text{OH}_2)_x]\text{Mn}\{\text{Bi}(\text{SCN})_6\}$ ($2/8 \leq x \leq 2.5/8$)

From slow evaporation in butanone or acetone orange, dark red-orange, cuboid single crystals (100 to 200 μm length) were obtained. Single crystal X-ray diffraction (120 K) was carried out to determine the structure.

The integration of the reflections suggested a structure with tetragonal symmetry and a unit cell of $a = 12.4173(3)$ Å, $b = 24.4649(5)$ Å, $c = 24.4649(5)$ Å. Refinements were carried out in the $P4_2/mnm$ space group, and the manganese and bismuth atoms could be located. However, it was challenging to identify the atoms of the thiocyanate ligands or the ammonium ions due to the large spread of electron density which was not well localised. Since the given space group was not able to provide a suitable model to describe the electron densities observed, it was likely that the data were not integrated with the correct crystal symmetry. To check this, the symmetry of the model was reduced to triclinic. Structure solution and refinements were carried out in the $P1$ space group. From this, the connectivity of the $[\text{Mn}\{\text{Bi}(\text{SCN})_6\}]^-$ framework was identified, consisting of 16 unique Mn and Bi sites and 96 ligands (320 atoms in total). The NH_4^+ A-site cations could not be determined during these refinements.

From the structure of the framework the highest symmetry structure could be determined. FINDSYM from the ISOTROPY Software Suite^{344,345} was used to search for higher symmetry space groups, given the positions of the atoms in the unit cell. From this, it indicated that the framework adopts the orthorhombic $Pnmm$ space group.

Subsequently, the X-ray data were integrated with orthorhombic symmetry and the structure was solved and refined. The connectivity of the $[\text{Mn}\{\text{Bi}(\text{SCN})_6\}]^-$ framework could be identified. The Mn and Bi M-site ions have rocksalt ordering, with the nitrogens coordinating to the Mn^{2+} ions and the sulfurs coordinating to the Bi^{3+} ions. The pseudocubic cage axes are identical to that of the structure's unit cell (i.e. along the [100], [010] and [001] directions). The tilt sequence along [100] and [010] alternate between in-phase and out-of-phase rotations and octahedra along the [001] direction are all in phase: $a^+b^+c^+$ (Fig. 6.3c).

Although it was possible to identify the symmetry of the framework, it was not possible to locate the positions of all the NH_4^+ cations. Depending on the complexity of the cation orderings as well as the orientations of the NH_4^+ species, the A-site cations could further lower the overall symmetry from the $Pnmm$ space group obtained for the framework. In order to reliably determine the positions of nitrogen and hydrogen atoms, single crystal neutron diffraction was carried out at 20 K and 250 K (D19, Institut Laue Langevin).

The low temperature data at 20 K was integrated with orthorhombic symmetry in the

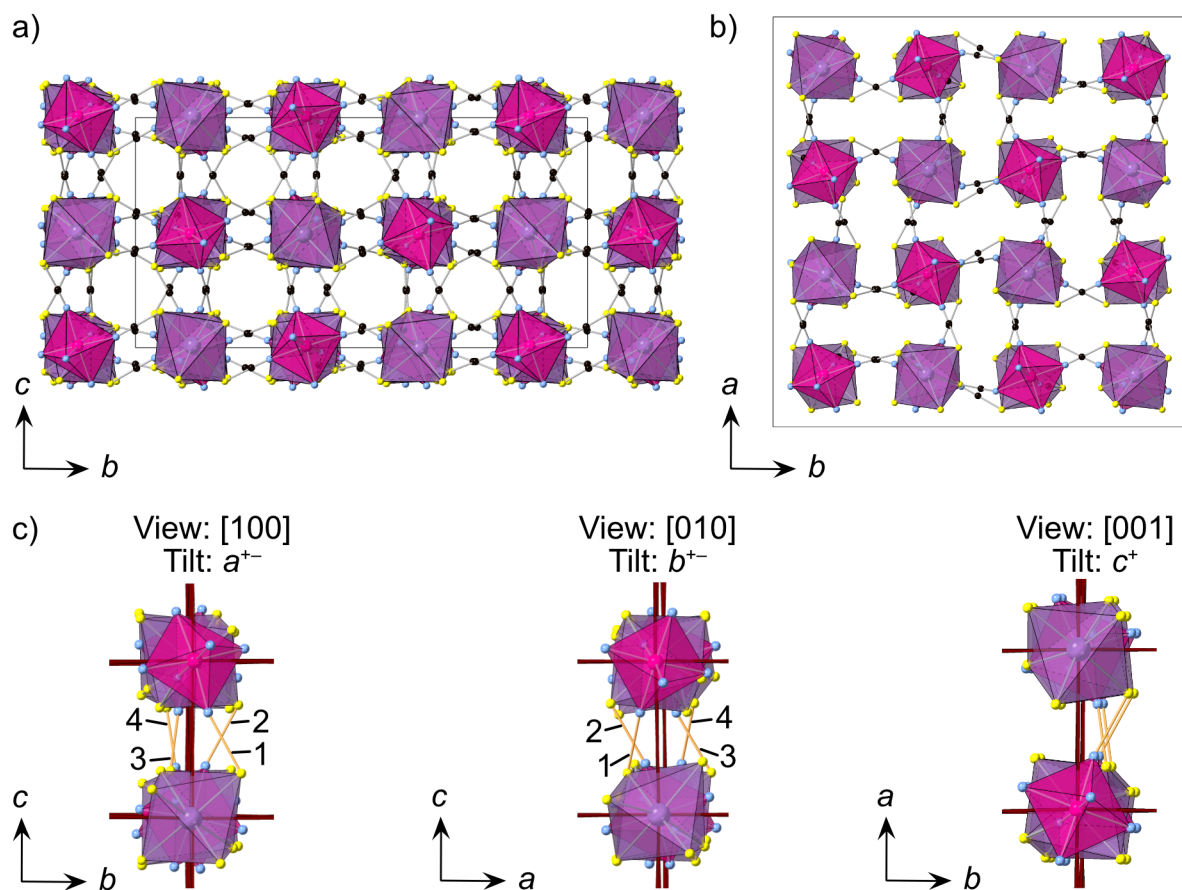


Figure 6.3: The $[\text{Mn}\{\text{Bi}(\text{SCN})_6\}]^-$ framework in the $Pn\bar{3}n$ space group (origin 1) for NH_4MnBi viewed along the a) a axis and b) c axis. c) The rotation sequences of the octahedra along the $[100]$ (left), $[010]$ (middle) and $[001]$ (right) directions. The N–S connections are shown in pale pink. The a^{+-} sequence observed along a and b axes have the bonds numbered moving from the front octahedra, backwards into the page to aid in viewing the progression. The Mn and Bi atoms are joined by red lines, indicating the edges of the pseudocubic metal cages. The C atoms have been removed for clarity. Mn = pink, Bi = purple, N = blue, C = black, S = yellow.

$Pn\bar{3}n$ space group, the same as was obtained for the $[\text{Mn}\{\text{Bi}(\text{SCN})_6\}]^-$ framework from X-ray diffraction. In addition, the position of the non-framework components could be located. There are four distinct, occupied A-site cages, identified as S1, S2, S3 and S4, roughly ordered in ascending complexity and disorder (Fig. 6.4a). Comparing to the residual electron density map for the X-ray data, the same atom positions could be identified (Fig. 6.4b).

From the low temperature neutron diffraction data, it was evident that S1 is an ammonium cation, with positive scattering density in the central position and four discrete positions of negative scattering density. The S1 ammonium has an occupancy of 1 and shows no signs of position or orientational disorder.

S2 was also identified as an ammonium, similarly with four positions of negative scattering density surrounding the central nitrogen atom. The scattering density is spread over a larger area, both from the nitrogen and hydrogen positions, suggesting that there may be

some variation in the position of the ammonium ions between unit cell. The symmetry of the crystal is such that there are two S2 NH_4^+ positions within a single cage, with a $\text{N}\cdots\text{N}$ separation of 2.453(3) Å. This is a short distance to observe two adjacent NH_4^+ species. The refinement was not stable if the atoms were assigned an occupancy of 1, and refined freely to 0.58(7). Therefore, based on the sterics and the refinement results, the occupancy of the cation (N and H atoms) was fixed to 0.5. In addition, the H–N–H bond angles and N–H distances were restrained to ensure a model with physical sense. Since the NH_4^+ cations have an occupancy of 0.5, only one of the positions is occupied within a given metal cage.

Having identified the S1 and S2 species as NH_4^+ , the compound composition was $(\text{NH}_4)_{0.75}[\text{Mn}\{\text{Bi}(\text{SCN})_6\}]^{0.25-}$, meaning that the overall compound was not neutral. The species occupying sites S3 and S4 must contribute a total positive charge of +0.25 per M-site. In both remaining A-site positions, it is evident that there is a significant amount

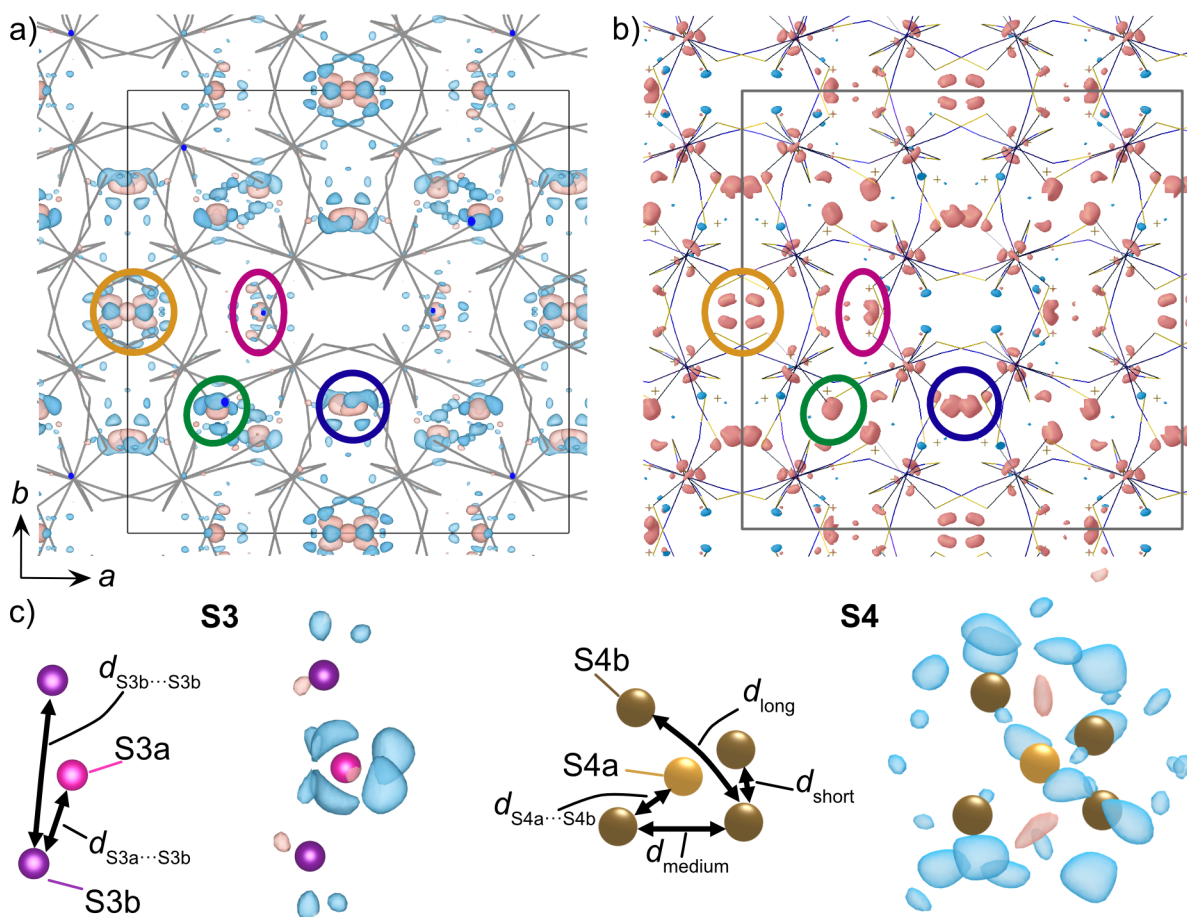


Figure 6.4: The scattering density difference maps after defining the $[\text{Mn}\{\text{Bi}(\text{SCN})_6\}]^-$ framework for NH_4MnBi , measured with a) neutrons (D19, Institut Laue Langevin, isosurface cut -1.1 to $+1.1$ $\text{e}\text{\AA}^{-3}$), b) X-rays (isosurface cut -1.4 to $+1.7$ $\text{e}\text{\AA}^{-3}$). The four A-sites are identified as S1 (green), S2 (blue), S3 (pink) and S4 (gold). Pink = positive scattering density and blue = negative scattering density. The framework is shown as a wireframe. c) The scattering density from neutron diffraction data where placeholder (dark pink, purple, orange and brown) atoms have been added to model the positive scattering density to highlight the spread of negative scattering density (blue) around the atoms for S3 (left) and S4 (right).

of disorder by the lack of well defined scattering density positions and the evidence for multiple site positions within the same cage.

It is possible that these A-site positions are partially occupied by NH_4^+ cations and partially occupied by a neutral species. Although it is common for solvent molecules to be incorporated into the voids within frameworks, the X-ray data were collected from a crystal synthesised and recrystallised from butanone ($\text{CH}_3\text{CH}_2\text{COCH}_3$), whilst the crystals measured with the neutron source used acetone (CH_3COCH_3). As the same atom positions could be observed in the scattering densities of the X-ray and neutron data, it was likely to be the same species. The scattered densities were not consistent with either acetone or butanone, so it was unlikely these had crystallised as part of the structure. The starting materials, $\text{Mn}(\text{NO}_3)_2 \cdot 4\text{H}_2\text{O}$ and $\text{Bi}(\text{NO}_3)_3 \cdot 5\text{H}_2\text{O}$ are both hydrated, and, in addition, neither the butanone or acetone was dry, so it is likely there was a significant amount of water present during the synthesis and recrystallisations.

The neutron data shows that within the S3 cage there are three positions of the A-site species (Fig. 6.4c). The central atom, S3a, is surrounded by significant negative scattering density, which is mostly grouped into four clusters. S3a was assigned as N with an occupancy of 0.5. This species is NH_4^+ , however, due to the spread of the negative scattering density surrounding S3a, it was not possible for hydrogen atoms to be added. In addition, there are two smaller positions of positive scattering density, S3b, at a distance from the central atom of $d_{\text{S3a}\cdots\text{S3b}} = 1.694(6)$ Å, and a distance of $d_{\text{S3b}\cdots\text{S3b}} = 3.190(5)$ Å from each other. Two possible atom assignments allowed for a stable refinement: The first, where S3b is a nitrogen from a NH_4^+ ion with an occupancy of 0.125. The second possibility is an oxygen atom from OH_2 with an occupancies of 0.25. It was not possible to obtain a stable refinement with S3b assigned as either N or O with an occupancy of 0.5. Based on the negative scattering density, S3b is more likely OH_2 molecules with two visible positions for H atoms. Assuming S3b are water molecules, the S3 site has an overall occupancy of 1.0, with three A-site positions.

The scattering density within the S4 cage is broad, suggesting there is position and orientational disorder over multiple sites. The five most prominent positive scattering sites are identified as the central atom, S4a, and the four surrounding atoms, S4b (Fig. 6.4c). The $\text{S4a}\cdots\text{S4b}$ distance is $1.387(4)$ Å and between the S4b species there are three distances, $d_{\text{S4b short}} = 1.986(5)$ Å, $d_{\text{S4b medium}} = 2.711(5)$ Å and $d_{\text{S4b long}} = 2.946(5)$ Å. $d_{\text{S4a}\cdots\text{S4b}}$ is a small separation, too close for non-bonding interactions to occur. To account for the steric bulk of the species, only S4a or S4b can be present within a cage, they cannot both be present within the same cage. $d_{\text{S4b medium}}$ is within the upper range reported for $\text{NH}_4^+\cdots\text{OH}_2$ hydrogen bond separations ($2.5 - 2.7$ Å), and $d_{\text{S4b long}}$ is similar to reported $\text{OH}_2\cdots\text{OH}_2$ hydrogen bond distances (2.9 Å).^{346,347} It is possible that more than

one S4b species is present within a given cage, therefore, the total occupancy of the S4 site could be greater than 1. Refinements were carried out with various combinations of N and O assignments in S4a and S4b positions, with varied occupancies (Table 6.1). The refinement results were inconclusive, however, S4a likely has an occupancy of 0.5. Generally the refinements were more stable with S4a and S4b assigned as O, which would suggest this is the predominant species occupying this site. It is likely S4a and S4b have a combination of NH_4^+ and OH_2 species. This matches with the large spread of negative scattering density, arising from the H atoms, as the species will likely show orientational disorder as well as position disorder.

Due to the degree of the disorder over the A-sites, from occupation, position and orientational disorder arising from both the NH_4^+ and OH_2 species, it was not possible to locate, or view the positions of all the hydrogen atoms in the scattering density maps. Including the additional A-site species gives the chemical formula $[\square_{\frac{7}{8}}(\text{NH}_4)(\text{OH}_2)_x]\text{MnBi}(\text{NCS})_6$, where $\frac{2}{8} \leq x \leq \frac{2.5}{8}$ ($0.25 \leq x \leq 0.313$) depending on OH_2 occupancy in the S4 site. $x = \frac{2}{8}$ if S3b is OH_2 and S4 has a total occupancy of 1, and $x = \frac{2.5}{8}$ if the S4 total occupancy is 2. The water content could be examined through further elemental analyses.

The A-site species are present within the framework as $(3 \times 3 \times 1)$ blocks, with the surrounding cages vacant (Fig. 6.5). In all the vacant cages, there are four thiocyanate ligands present. The cages occupied by A-site species range from having 0 thiocyanate ligands for S4, and increase relative to the positional disorder within the cage (Fig. 6.5c).

Table 6.1: Summary of selected refinement statistics for NH_4MnBi of various atom assignments (S4a and S4b) and occupancies (Occ) for site S4 (D19 diffractometer, Institut Laue Langevin).

Atom assignment				R_{obs} (%)
S4a	Occ	S4b	Occ	
N	0.5	O	0.25	14.80
N	0.5	O	0.125	14.81
O	0.5	N	0.25	14.88
O	0.5	N	0.125	14.82
N	0.25	O	0.25	Unstable
N	0.25	O	0.125	14.91
O	0.25	N	0.25	Unstable
O	0.25	N	0.125	Unstable
O	0.5	O	0.25	14.75
O	0.5	O	0.125	14.84

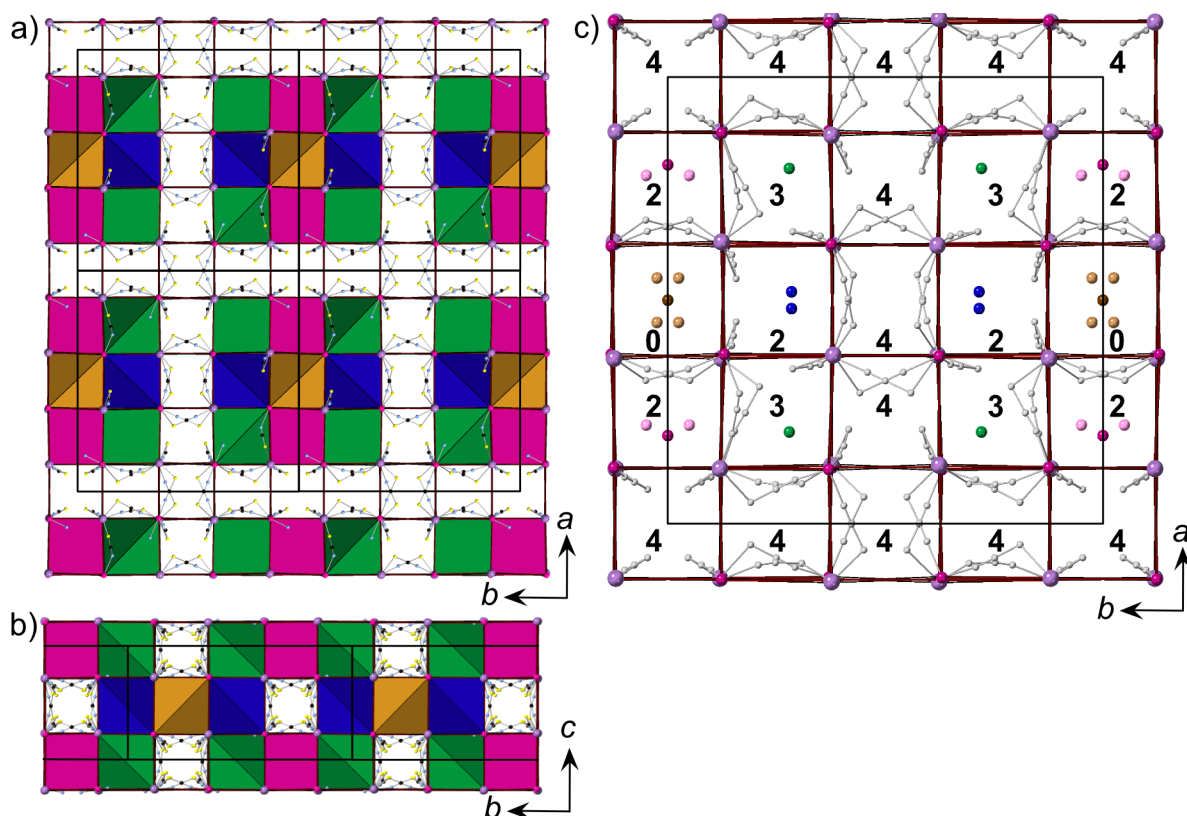


Figure 6.5: Ordering of the A-sites in NH_4MnBi , showing the $(3 \times 3 \times 1)$ blocks, viewed along the a) $[001]$ and b) $[100]$ directions. Where the cage is occupied, it is coloured corresponding to the A-site species present. S1 = green, S2 = blue, S3 = pink and S4 = gold. Red lines join the Mn and Bi atoms, acting as a guide to identify the pseudocubic metal cages. c) A single layer of metal cages showing the position of the thiocyanate ligands. The numbers indicate how many ligands are within the given cage. Where 4 ligands are positioned within the cage, no A-site species is present.

6.3.2.3 $[\square_{\frac{7}{8}}\text{Cs}(\text{OH}_2)_x]\text{Mn}\{\text{Bi}(\text{SCN})_6\}$ ($\frac{1}{8} \leq x \leq \frac{2}{8}$)

Orange cuboid single crystals were obtained from slow evaporation in butanone (up to dimensions of 2 mm). Single crystal X-ray diffraction (273 K) was carried out to determine the structure.

The Bragg reflections could be indexed by the orthorhombic space group $Pn\bar{1}n$ with the unit cell $a = 24.7803(7)$ Å, $b = 24.8038(7)$ Å, $c = 12.4386(4)$ Å, isostructural to NH_4MnBi (Fig. 6.6). The structure has been solved using origin 2, whereas NH_4MnBi was solved using origin 1. Origin 2 is related to origin 1 by the transformation $(a^{-1/4}, b^{-1/4}, c^{-1/4})$. The M-sites show rocksalt ordering with $[\text{MnN}_6]$ and $[\text{BiS}_6]$ octahedra. Three of the twelve crystallographically independent sulfur atoms are split over two sites, with refined occupancies of 0.76(7) : 0.24(7) (S10 a:b), 0.65(13) : 0.35(13) (S11 a:b) and 0.44(11) : 0.56(11) (S12 a:b). The octahedral tilt sequence is $a^{+-}b^{+-}c^+$.

The A-sites order in $3 \times 3 \times 1$ blocks, surrounded by empty cages. There are four distinct, occupied A-site sites S1–4, as described for NH_4MnBi (Fig. 6.6d, S1 = green, S2 = blue,

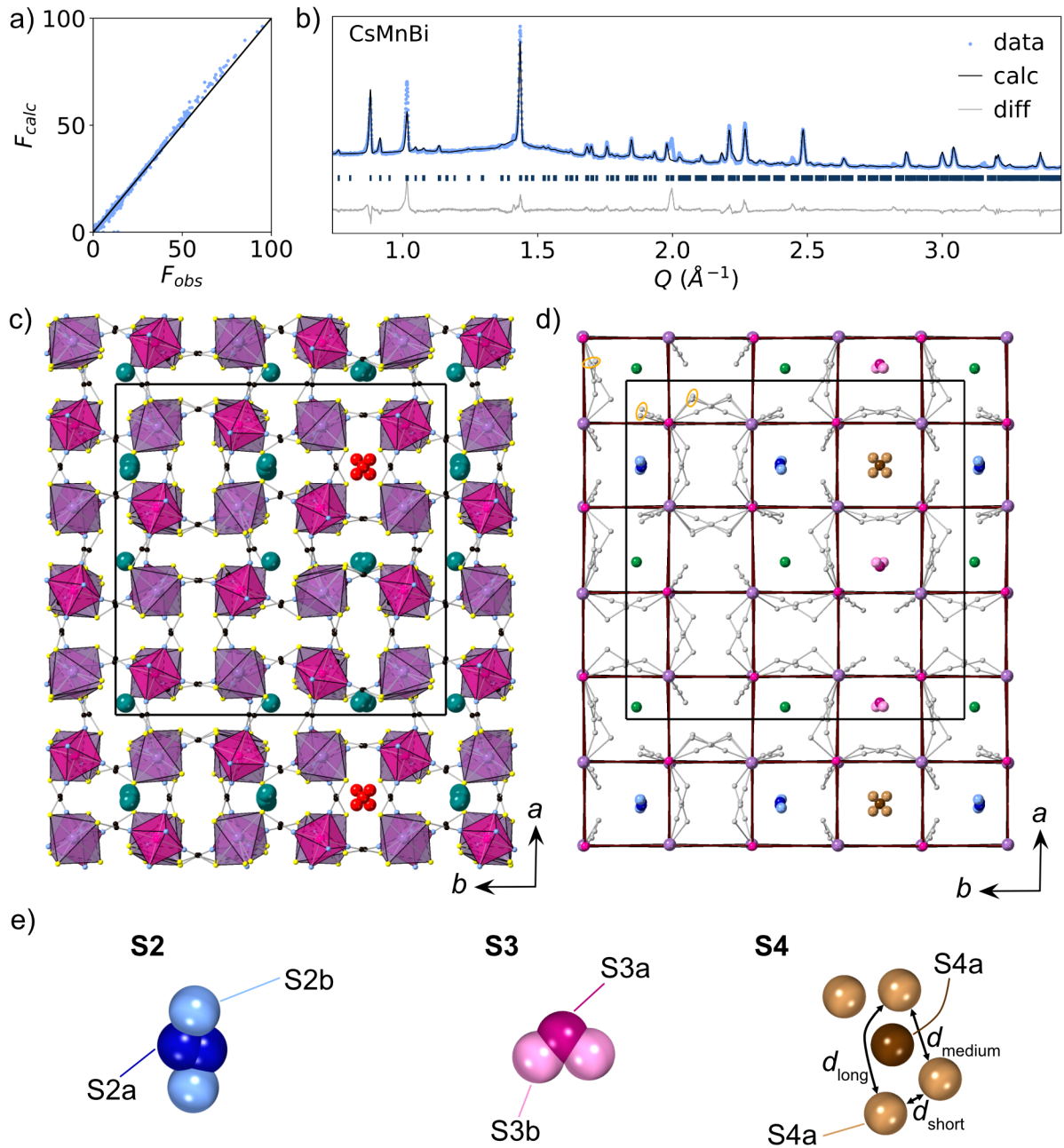


Figure 6.6: The structure of CsMnBi, obtained from single crystal X-ray diffraction data (273 K) in the $Pnnn$ space group (origin 2). a) F_{obs} against F_{calc} . b) Rietveld refinement of powder data using the model from the single crystal refinement. c) The framework connectivity viewed along the a axis. Only A-site cations with crystallographic atomic coordinates between $(0, y, z)$ and $(0.5, y, z)$ have been shown. d) The four A-site cages and crystallographically distinct A-site species. Colours match the designations for NH_4MnBi figures: S1 = green, S2 = blue, S3 = pink and S4 = brown. e) The atom labels for the crystallographically distinct Cs^+ positions in S2 and S3 and OH_2 positions and lengths in S4. The three S atoms with split atomic coordinates are circled (orange) in the first and second upper left metal cages, S10a/b, S11a/b and S12a/b. Mn = pink, Bi = purple, Cs = green, N = blue, C = black, S = yellow, O = red.

S3 = pink and S4 = brown). S1 is occupied by a single, ordered Cs⁺ cation. S2 is occupied by Cs⁺ cations, disordered over four positions, two with an occupancy of 0.32(3) (S2a) and two with an occupancy of 0.18(3) (S1b). The overall occupancy of S2 is 1. The S3 A-site contains Cs⁺ cations disordered over three positions. S3a and S3b have fixed occupancies of 0.5 and 0.25.

The water molecules could be distinguished from the Cs⁺ cations, and are located solely within the S4 cage: a central OH₂ with a fixed occupancy of 0.5 (S4a) and four outer OH₂ with an occupancy less than 0.4 (S4b), although this value could not be refined to a stable model without fixing the values. Between S4a and S4b the distance is 1.286(3) Å and the three distances between S4b OH₂ are $d_{\text{S4b short}} = 1.471(3)$ Å, $d_{\text{S4b medium}} = 2.331(3)$ Å and $d_{\text{S4b long}} = 2.373(3)$ Å. These distances are shorter than expected for OH₂ ··· OH₂ hydrogen bond interactions (approximately 2.9 Å).³⁴⁶ These distances will be verified by future neutron diffraction measurements, which will obtain the atom positions and distances at a lower temperature, and, ideally, the position of the H atoms will be located. Within the S4 cage, there may be an overall occupancy of 1 or greater than 1, depending on the positions and occupancies of the S4b OH₂ molecules. The overall structure is $[\square_7\text{Cs}(\text{OH}_2)_x]\text{Mn}\{\text{Bi}(\text{SCN})_6\}$, where $1/8 \leq x \leq 2/8$. $x = 1/8$ if the total occupancy in S4 is 1 and $x = 2/8$ if the occupancy is 2.

In addition, the structural model was fitted to the powder diffraction data, with $R_{\omega p} = 34.8$ %. There are several intensities, at 1.41, 1.99 and 2.44 Å⁻¹ in particular, which are not captured by the model. Refinements were carried out adding additional phases for unreacted starting materials (CsSCN, Bi(NO₃)₃ · xH₂O and Mn(NO₃)₂ · xH₂O), as well as side products (CsNO₃) in their dry and hydrated states. However, these could not account for the observed intensities. The additional peaks may arise from a small fraction of a second, unknown, polymorph of $[\square\text{Cs}]\text{Mn}\{\text{Bi}(\text{SCN})_6\}$.

6.3.2.4 $[\square_{24}\text{Gua}_{12}]\text{Mn}_{17}\{\text{Bi}(\text{SCN})_6(\text{OH}_2)_{\frac{5}{8}}\}_{16}$

A slow evaporation recrystallisation from butanone yielded dark red-orange, cuboid single crystals (100 to 200 μm length). To determine the structure of $\text{Gua}_{\frac{2}{3}}\text{Mn}_{\frac{17}{18}}\text{Bi}_{\frac{16}{18}}$, single crystal X-ray diffraction was performed.

When integrating the data, the majority of the reflections (30202 of 41455 total reflections) matched an orthorhombic unit cell with $a = 26.2090(5)$ Å, $b = 26.2159(6)$ Å and $c = 12.2143(3)$ Å, similar to that of NH₄MnBi and CsMnBi, although almost 2 Å larger along the a and b axes. However, a small number of superlattice reflections (5837 total reflections) were observed, occurring at $\frac{1}{2}a^*$, $\frac{1}{2}b^*$ and $\frac{1}{2}c^*$. To compare the difference between the smaller unit cell, and the larger superstructure, integrations were carried out

for both unit cells.

Despite the majority of the reflections fitting the smaller unit cell, it was not possible to solve the structure in with $Pn\bar{3}n$ symmetry, or with any other space group using this unit cell. Using the larger unit cell ($a = 52.4523(9)$ Å, $b = 52.4682(9)$ Å, $c = 24.4182(4)$ Å), the data was integrated and a structure solution was obtained in the orthorhombic space group $Fdd2$.

The framework shows rocksalt ordering of the M-sites, alternating between $[\text{MnN}_6]$ and $[\text{BiS}_6]$ octahedra. However, there are vacancies for both Mn^{2+} and Bi^{3+} sites, as well as for the thiocyanates surrounding the vacant Bi sites. Where the Mn vacancies are observed, 4 of the 6 surrounding thiocyanate anions are present. The metals which neighbour the vacancies have coordinating OH_2 molecules where the NCS^- ligands are absent. The metal ratio is 17 : 16 (1.06 : 1, Mn : Bi) and of $\text{Mn}_{17}[\text{Bi}(\text{NCS})_6(\text{OH}_2)_{0.75}]_{16}^{12-}$ for the framework (346 independent atoms).

The positions of two Gua cations could be located, identifying both the C and N atoms. A further two Gua cations could tentatively be identified, with a clear position for the C atom, but several possible positions for the N atoms. To obtain a stable refinement, the N atoms could be refined with an occupancy lower than 1 (Fig. 6.7a). It is likely there is orientational disorder about these two sites, meaning exact location of the N atoms were not possible for these Gua cations. With the four Gua cations in general positions (Wyckoff site 16b), this provides a charge of 8+ and, therefore, a formula of $\text{Gua}_8\text{Mn}_{17}\{\text{Bi}(\text{SCN})_6(\text{OH}_2)_{0.75}\}_{16}^{4-}$. The electron density map suggests that there are atoms positioned within the vacancies. It would be expected that the remaining Gua ions are located here, likely with orientational disorder (Fig. 6.7c). Therefore, the overall structure has the formula $[\square_{24}\text{Gua}_{12}]\text{Mn}_{17}\{\text{Bi}(\text{SCN})_6(\text{OH}_2)_{\frac{5}{8}}\}_{16}$, or $[\square_{\frac{4}{3}}\text{Gua}_{\frac{2}{3}}]\text{Mn}_{\frac{17}{18}}\{\text{Bi}_{\frac{16}{18}}(\text{S}_{\frac{16}{18}}\text{C}_{\frac{16}{18}}\text{N}_{\frac{16}{18}})_6(\text{OH}_2)_{\frac{10}{18}}\}$.

There are significant areas of residual electron density that can be viewed in the vacancies where the metal sites would be expected (Fig. 6.7c). It is possible that the metal sites are partially occupied with a small percentage of metal ions. Bi and Mn atoms were assigned to these positions and the occupancies were refined freely. This did not produce stable refinements, or resulted in refined occupancy values of less than 0. By fixing the occupancies of the additional Bi sites to 0.1 and Mn to 0.7 a stable refinement could be made. This would result in a metal ratio of 17.72 : 16.20 (1.09 : 1, Mn : Bi) and an approximate formula of $[\square_{24}\text{Gua}_{12}]\text{Mn}_{17.72}\{\text{Bi}(\text{SCN})_6(\text{OH}_2)_{0.625}\}_{16.2}$ or $[\square_{\frac{4}{3}}\text{Gua}_{\frac{2}{3}}]\text{Mn}_{\frac{17.72}{18}}\{\text{Bi}_{\frac{16.2}{18}}(\text{S}_{\frac{16.2}{18}}\text{C}_{\frac{16.2}{18}}\text{N}_{\frac{16.2}{18}})_6(\text{OH}_2)_{\frac{10.125}{18}}\}$. No additional thiocyanate ligands could be located around the partially occupied Bi sites, probably due to the low occupancy. For clarity to show the positions of the vacant sites, in Fig. 6.7 the structure is shown without the partially occupied metal sites.

The axes of the pseudocubic metal cages are defined by the $[\bar{1}10]$, $[110]$ and $[001]$ directions of the unit cell. Along the $[\bar{1}10]$ and $[110]$, the octahedra exhibit a tilt pattern of $+ - + - ++$, if no metal vacancies are present. Along the $[001]$ direction, all the octahedra tilt in-phase, giving a sequence of $a^{+++++}b^{+++++}c^+$ (Fig. 6.8).

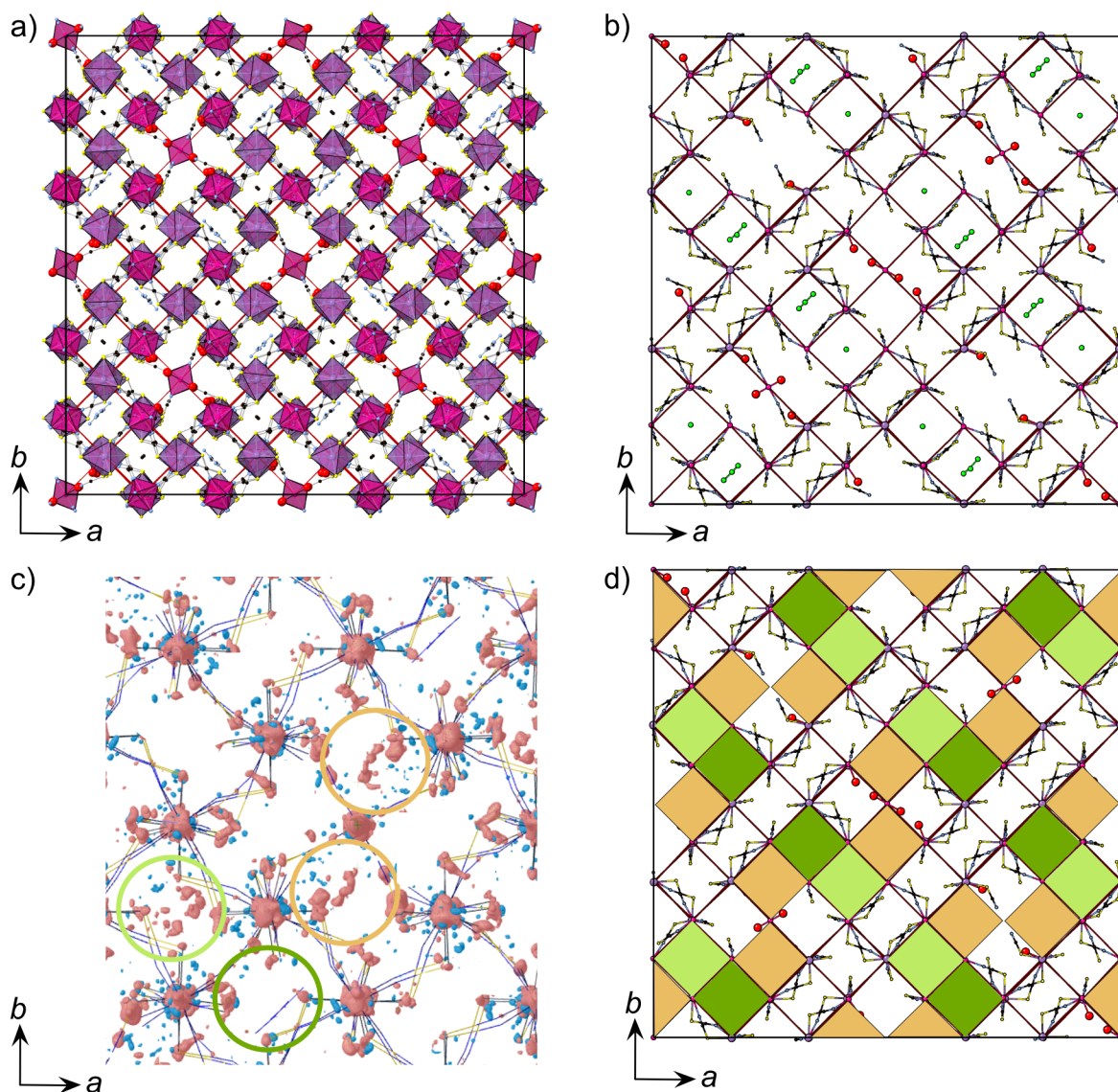


Figure 6.7: The structure of $\text{Gua}_{\frac{2}{3}}\text{Mn}_{\frac{17}{18}}\text{Bi}_{\frac{16}{18}}$ from single crystal X-ray diffraction (120 K). Partially occupied metal and ligand sites are shown as vacant. a) View along the c axis. b) One layer, showing the pseudocubic cages (red lines), where the Mn and Bi vacancies are observed in $(2 \times 2 \times 1)$ blocks. The Gua cations ($\text{C}(\text{NH}_2)_3^+$) have been identified in green, either the C and N atoms, or only the C atom. c) The difference electron density map from X-ray diffraction (isosurface cut -3.4 to $+1.05 \text{ e}\text{\AA}^{-3}$), showing a selected area of the unit cell. The identified cations are circled in green: dark green where C and N atoms have been located, and light green for only C atoms located. The orange circles identify sites within the pseudocubic cages with metal vacancies where the remaining A-site species are most likely located. Pink = positive scattering density, blue = negative scattering density. d) A view of one layer along the $[001]$ direction, showing the ordering of the A-site species. Green indicates the Gua cations which have been identified (dark = C and N atoms, light = C atoms only) and orange indicates the metal cages where the remaining Gua cations are likely positioned. Mn = pink, Bi = purple, N = blue, C = black, S = yellow, O = red, Gua cations $\text{C}(\text{NH}_2)_3^+$ = green. The hydrogen atoms could not be located.

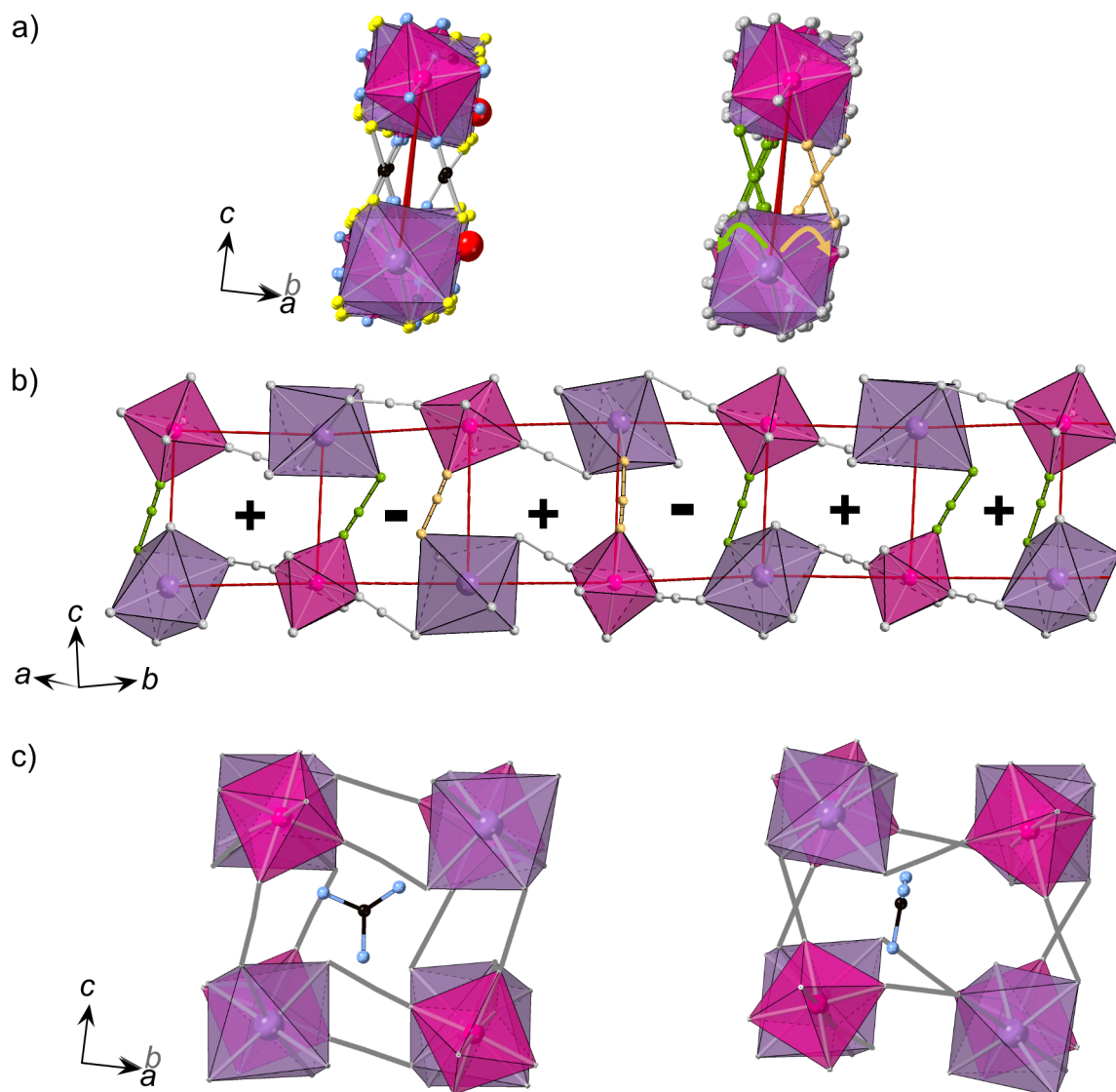


Figure 6.8: The octahedral tilt pattern of $\text{Gua}_{\frac{2}{3}}\text{Mn}_{\frac{17}{18}}\text{Bi}_{\frac{16}{18}}$ which is observed along the $[\bar{1}10]$ and $[110]$ directions, here viewed along the $[\bar{1}10]$ direction for a row of octahedra where no metal sites or thiocyanates are vacant. The red lines join the metal centres, denoting the edges of metal cages. a) Left: View of the octahedra along the $[\bar{1}10]$ direction. Mn = pink octahedra, Bi = purple octahedra, N = blue, C = black, S = yellow, O (water) = red. Right: same view, with the ligand atoms coloured grey except for the atoms participating in the rotation of octahedra along the $[110]$ direction. Octahedra that rotate clockwise (relative to the direction of view, tilting of the front Bi octahedron) have the ligands coloured beige, and anticlockwise rotations have ligands highlighted in green. b) The row of octahedra viewed along $[110]$. Where two adjacent ligands have the same colouring, the octahedra tilt in the same sense and are assigned "+" in Glazer notation. Adjacent beige and green ligands show neighbouring octahedra rotating in the opposite directions and are assigned "-" in Glazer notation. c) The two orientations of the Gua cations, perpendicular to the $[001]$ direction.

Within a layer of metal cages (for example between $(x, y, 0.12)$ and $(x, y, 0.38)$), the Gua cations are aligned along the $\{110\}$ planes. Shifting along the $[001]$ direction to adjacent layers (for example between $(x, y, 0.38)$ and $(x, y, 0.63)$), the Gua cations are parallel to the $\{\bar{1}10\}$ planes (Fig. 6.8c).

The A-sites order in “Z-blocks”, where the body are $(2 \times 1 \times 1)$ units (Fig. 6.7d, green squares), with $(1 \times 1 \times 1)$ head and tail units (Fig. 6.7d, orange squares) which are situated within the cages with metal vacancies. The rows of vacant cages occur once every three rows, separating each (2×2) row of Z-blocks.

6.3.3 Magnetisation

The bulk magnetic properties of KMnBi, NH_4MnBi and $\text{Gua}_2\text{Mn}_{\frac{17}{18}}\text{Bi}_{\frac{16}{18}}$ were explored through susceptibility measurements. In addition, isothermal magnetisation data were collected at 2 K for KMnBi and $\text{Gua}_2\text{Mn}_{\frac{17}{18}}\text{Bi}_{\frac{16}{18}}$.

KMnBi shows paramagnetic behaviour, with the susceptibility continually increasing as the temperature is decreased (Fig. 6.9a). The high temperature Curie constant $C = 4.5(2)$ emu K mol⁻¹, which is slightly larger than the spin-only value $C_{\text{spin only}} = 4.375$ emu K mol⁻¹ for Mn²⁺ ions (Fig. 6.9b). Fitting the Curie-Weiss Law to the inverse of the susceptibility ($T > 150$ K) gives a Curie-Weiss temperature of $\theta_{\text{CW}} = -6.9(5)$ K (Fig. 6.9c). There is no observable evidence of hysteresis in the isothermal magnetisation data for KMnBi, with saturation being reached by $M_{5\text{T}} = 4.45(3)$ μ_{B} per Mn (Fig. 6.10a). This is suggestive of very weak antiferromagnetic interactions.

The susceptibility data for NH_4MnBi show no evidence of long-range magnetic ordering as the temperature is decreased, as the susceptibility increases showing no variation between the field-cooled and zero-field-cooled data (Fig. 6.9d). This suggests NH_4MnBi behaves as a paramagnet down to 2 K. From the high temperature-magnetic susceptibility product, $C = 4.7(4)$ emu K mol⁻¹, which is larger than the spin-only value for Mn²⁺ ions (Fig. 6.9e). The Curie-Weiss temperature, $\theta_{\text{CW}} = +3.0(2)$ K (fitting $T > 150$ K), which is close to the expected value of $\theta_{\text{CW}} = 0$ K for a paramagnet (Fig. 6.9f).

The susceptibility of $\text{Gua}_2\text{Mn}_{\frac{17}{18}}\text{Bi}_{\frac{16}{18}}$ increases as the temperature is lowered showing no cusp and no variation between the field-cooled and zero-field-cooled data, indicating paramagnetic behaviour on cooling to 2 K. The Curie constant $C = 3.9(2)$ emu K mol⁻¹, which is slightly smaller than the spin-only value for Mn²⁺ ions (Fig. 6.9h). Fitting the Curie-Weiss Law to the high temperature data ($T > 150$ K) gives $\theta_{\text{CW}} = +3.3(2)$ K (Fig. 6.9i). There is no observable evidence of hysteresis in the isothermal magnetisation data of $\text{Gua}_2\text{Mn}_{\frac{17}{18}}\text{Bi}_{\frac{16}{18}}$, with saturation being reached at $M_{5\text{T}} = 4.92(3)$ μ_{B} per Mn

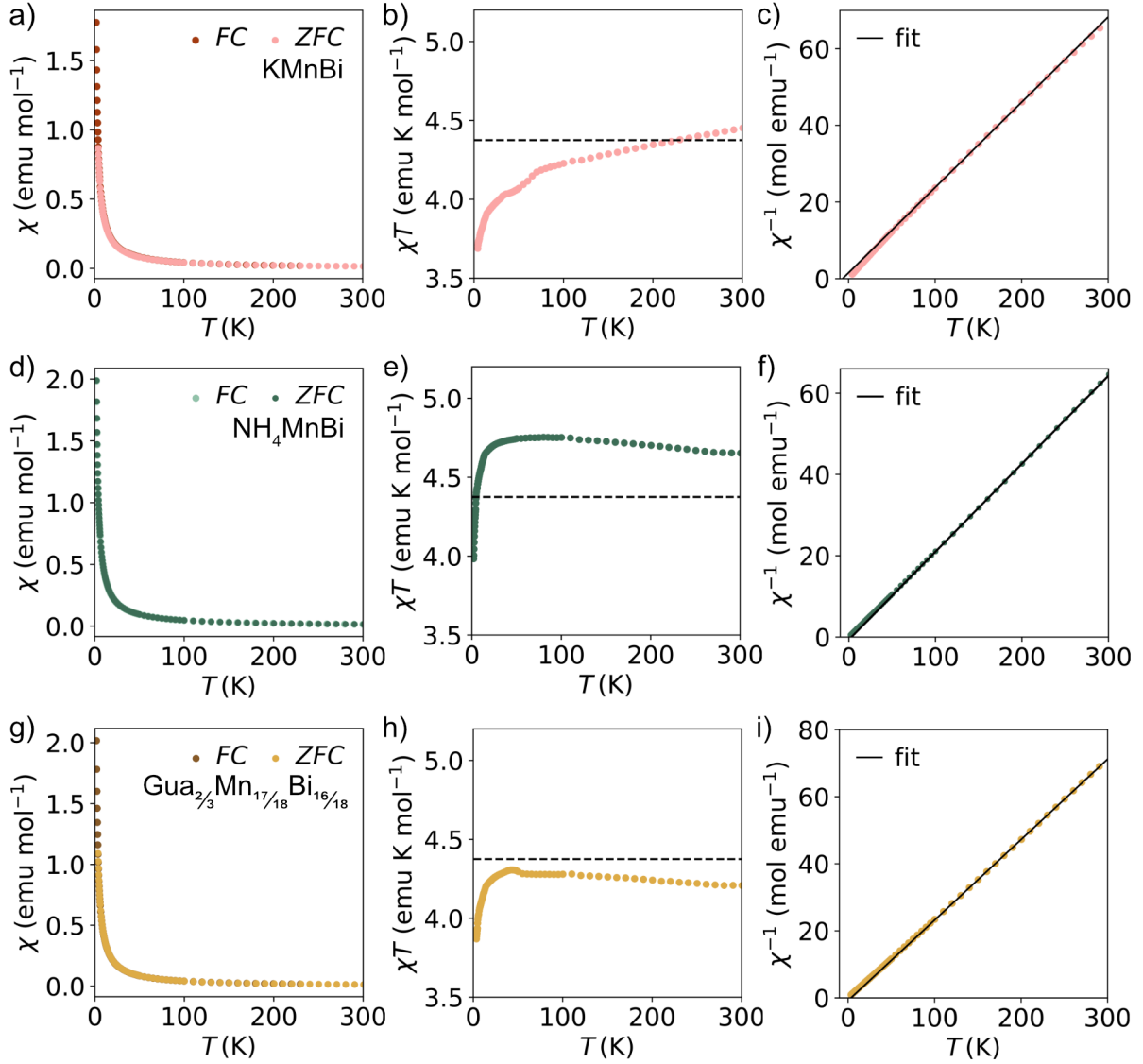


Figure 6.9: The magnetometry results for KMnBi (a, b and c), NH_4MnBi (d, e and f) and $\text{Gua}_{\frac{2}{3}}\text{Mn}_{\frac{17}{18}}\text{Bi}_{\frac{16}{18}}$ (g, h and i). a), d) and g) are plots of the susceptibility under field-cooled (*FC*) and zero-field-cooled (*ZFC*) conditions. The temperature-magnetic susceptibility product in b), e) and h) are shown with the high temperature spin-only Curie constant $C_{\text{spin only}} = 4.375 \text{ emu K mol}^{-1}$ (dashed line). c), f) and i) The inverse magnetic susceptibilities with a Curie-Weiss fit (solid black line) for the temperature range $100 < T < 300 \text{ K}$, with calculated Curie-Weiss temperatures, θ_{CW} , of c) $\theta_{\text{CW}} = -6.9(5) \text{ K}$, f) $\theta_{\text{CW}} = +3.0(2) \text{ K}$ and i) $\theta_{\text{CW}} = +3.3(2) \text{ K}$.

(Fig. 6.10b).

For the three compounds, the magnetometry data suggest that there is no long-range magnetic ordering occurring down to 2 K, with the Mn^{2+} ions behaving as paramagnets. The discrepancies between the measured C and the expected $C_{\text{spin only}}$ values are likely to arise from mass errors when preparing the samples for the measurements. The irregular changes to χT for KMnBi and $\text{Gua}_{\frac{2}{3}}\text{Mn}_{\frac{17}{18}}\text{Bi}_{\frac{16}{18}}$ below 100 K (Fig. 6.9b, h), are possibly caused by the freezing of atmospheric oxygen.³⁴⁸

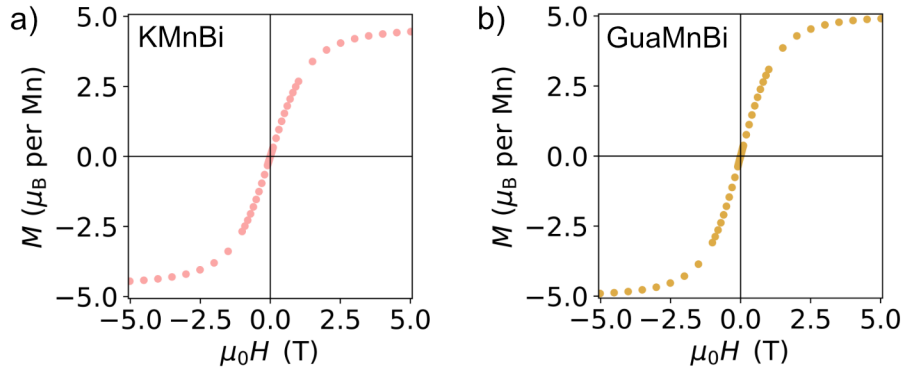


Figure 6.10: The isothermal magnetisation data, measured at 2 K, for a) KMnBi and b) $\text{Gua}_{\frac{2}{3}}\text{Mn}_{\frac{17}{18}}\text{Bi}_{\frac{16}{18}}$.

6.4 Discussion

From diffraction measurements, several new structures have been identified for the AMnBi compounds, $\text{A} = \text{K}^+, \text{NH}_4^+, \text{Cs}^+, \text{Gua}$. A common feature of all the frameworks is the M-site rocksalt ordering. The arrangement is likely driven by the thiocyanate ligand, which acts as a template for the metal positions, as a result of the alternate reactivities of the N and S termini. Thiocyanate frameworks do not tend to exhibit ligand orientational disorder, even if there is one only M-site species present.^{78,80,81} However, where there is a mix of M-site species, such as in AMnBi , $[\text{NH}_4]_2\text{Ni}\{\text{Cd}(\text{SCN})_6\}$,⁹⁷ $[\square\text{A}]\text{Ni}\{\text{Bi}(\text{SCN})_6\}$ ⁹⁸ or $\text{Mn}\{\text{Pt}(\text{SCN})_6\}$,⁹⁹ the first row transition metals coordinate with $[\text{MN}_6]$ octahedra $\text{M} = \text{Mn}, \text{Ni}$, and the metals with more diffuse electron density coordinate as $[\text{M}'\text{S}_6]$ octahedra, $\text{M}' = \text{Bi}, \text{Cd}, \text{Pt}$. M-site rocksalt ordering is commonly observed in atomic-based double perovskites, with abundant examples within the oxide and halide families.^{349–351}

Generally, to encourage rocksalt ordering, large differences in the M/M' electron densities are required.¹⁴⁰ For the thiocyanate frameworks, the ordering pattern is dictated by the ligand coordination requirements rather than inherent charge variances of M/M' .

Despite the similarity in topology and M-site ordering of the AMnBi compounds, the overall structures show variations. The determination of the structures, relies on the A-site cations and octahedral tilt patterns. A-site ordering is typically not observed in perovskite structures, but usually adhere to layered ordering when present to reduce strain of the $[\text{MX}_6]$ octahedra which distort as a result,¹⁴⁰ such as $\square_{\frac{2}{3}}\text{Ln}_{\frac{1}{3}}\text{TaO}_3$ $\text{Ln} = \text{lanthanides}, \text{La to Yb}$,¹³⁶ or $\square_{\frac{2}{3}}\text{La}_{\frac{1}{3}}\text{NbO}_3$.³⁵² Similar to the AMnBi compounds, the A-site ordering occurs between species and vacancies. With the exception of KMnBi which exhibits rocksalt ordering, the A-site orderings for AMnBi are complex, with the cations arranging in two-dimensional blocks.

The A-site ordering of NH_4MnBi and CsMnBi occur as $3 \times 3 \times 1$ blocks. Block ordering is unusual, having only been reported for the Ni analogue $[\square\text{MA}]\text{Ni}\{\text{Bi}(\text{SCN})_6\}$ $\text{MA} =$

CH_3NH_3^+ , which adopts $1 \times 2 \times 3$ blocks of occupied A-sites.⁹⁸ Although, the size of the cation is an important factor in predicting the structure, for thiocyanate perovskites, the radius of the A-site species cannot be used as the only indicator to predict the structure of the compounds. It is common to observe isostructural compounds with NH_4^+ and K^+ A-site species, as reported in thiocyanates,⁹⁸ and formates³⁵³ as well as for other molecular frameworks^{354,355} and atomic compounds.³⁵⁶ NH_4MnBi ($r_{\text{NH}_4^+} = 1.46 \text{ \AA}$)³⁵⁷ and KMnBi ($r_{\text{K}^+} = 1.38 \text{ \AA}$)³⁵⁸ have similar radii, which is attributed to the formation of the isostructural compounds. Similarity in the structures of NH_4MnBi and CsMnBi ($r_{\text{Cs}^+} = 1.81 \text{ \AA}$)³⁵⁹ is likely related to the additional OH_2 molecules present in the A-sites. OH_2 ($r_{\text{OH}_2} = 2.8 \text{ \AA}$)³⁶⁰ is a larger cation, and possibly has an occupation greater than 1 in some of the A-sites, which would increase the effective radius of the A-site species further.

The combination of site ordering and tilt sequences can systematically lower the symmetry from the aristotype $Pm\bar{3}m$ perovskite. For KMnBi and $\text{Gua}_{\frac{2}{3}}\text{Mn}_{\frac{17}{18}}\text{Bi}_{\frac{16}{18}}$ this results in the structures adopting non-centrosymmetric space groups, the only polar thiocyanate perovskites to be reported. KMnBi crystallises in the monoclinic space group Pn . The $a^-a^-c^+$ tilt sequence is the most commonly reported pattern in atomic perovskites,¹⁴⁰ and is also observed in perovskites with molecular ligands including $\text{AMn}(\text{HCOO})_3$ $A = \text{CH}_3\text{NH}_3^+$ and $(\text{CH}_2)_3\text{NH}_2^+$.^{100,361} In double oxide perovskites, $\text{AA}'\text{MM}'\text{O}_6$ with M-site rocksalt ordering and the absence of A-site order, the $a^-a^-c^+$ tilt sequence leads to $P2_1$ symmetry.³⁶² This has been reported for $\text{La}_2\text{LiSbO}_6$ ³⁶³ and $\text{Sr}_2\text{NbBiO}_6$.³⁶⁴ For KMnBi , the A-site rocksalt ordering further lowers the symmetry to Pn . It is a common perovskite-design strategy to access polarity by incorporating polar A-site cations which remove inversion centres as the ions lose their dynamic disorder at low temperatures, such as $[\text{C}_5\text{H}_{13}\text{NBr}]\text{Mn}(\text{dca})_3$ $\text{dca} = \text{N}(\text{CN})_2$ ¹²⁵ and $[(\text{CH}_3)_2\text{NH}_2]\text{Zn}(\text{HCOO})_3$.¹¹⁴ However, for KMnBi the spherical K^+ cation does not inherently activate the polar symmetry, instead it is the combination A-site and M-site orderings which realises this structure.

The significance of the A-site ordering can also be observed by comparing KMnBi to $[\square\text{K}]\text{Ni}\{\text{Bi}(\text{SCN})_6\}$ which exhibits columnar A-site order. The M-site ordering and tilt sequence are the same in both compounds, possibly suggesting that it is the extent of tilting, i.e. the Bi-Ni-N and Ni-Bi-S bond angles compared to Bi-Mn-N and Mn-Bi-S , that might drive the A-site ordering, such as is observed for $\text{CaFeTi}_2\text{O}_6$.³⁴³ Within the limits of the electron diffraction data, the bond angles cannot be quantitatively discussed for KNiBi , it would be necessary to obtain a model from higher resolution single crystal diffraction data to confirm this.

It is unusual to observe two species occupying a single cage, such as is potentially observed for the S4 sites in NH_4MnBi and CsMnBi . The dimensions of the pseudocubic cage are

related to the length (or radius for atomic compounds) of the X species. Atomic-only perovskites likely have pseudocubic cages which are too small to accommodate more than one A-site cation. However, this has not been knowingly reported for other thiocyanate or formate frameworks,^{98,102} yet, both a cation and a co-crystal are observed within the framework of $[\text{NBu}_4]\text{Mn}(\text{Au}(\text{CN})_2)_3$, $\text{NBu}_4 = \text{N}(\text{C}_4\text{H}_9)_4^+$.³⁶⁵ The inclusion of the additional extra-framework components are believed to occur from a size mismatch between the large $[\text{Mn}_8(\text{Au}(\text{CN})_2)_{12}]$ pseudocubic cage, and the significantly smaller NBu_4 cation. Water uptake has been reported for the A-site vacant $\square_2\text{Cr}\{\text{Bi}(\text{SCN})_6\}$ to $[\square(\text{H}_2\text{O})]\text{Cr}\{\text{Bi}(\text{SCN})_6\}$ where half the A-sites are occupied by water.⁷⁷ Although this is a reversible process, it suggests that the thiocyanate perovskites show a propensity for reducing the volume of empty space within the framework. In both NH_4MnBi and CsMnBi , the additional OH_2 molecules result in fewer (7/8) vacant A-sites than the expected (8/8).

The cation ordering of $\text{Gua}_{\frac{2}{3}}\text{Mn}_{\frac{17}{18}}\text{Bi}_{\frac{16}{18}}$ is complex, with Z-block A-site ordering, and additional A-site vacancies which are charge balanced by the removal of Mn and Bi M-sites. If $\text{Gua}_{\frac{2}{3}}\text{Mn}_{\frac{17}{18}}\text{Bi}_{\frac{16}{18}}$ had no metal site or thiocyanate deficiencies, the expected number of Gua cations would be 18. As a consequence of the additional M-site vacancies, the compound has $\frac{2}{3}$ the expected A-site occupancy. This bears resemblance to the Ni analogue $\text{Gua}_3\text{Ni}_6[\text{Bi}(\text{NCS})_6]_5$,⁹⁸ however, here only Bi and ligand vacancies are observed. This appears to be a feature of thiocyanate perovskite frameworks with Gua cation, as opposed to all molecular-based frameworks, since compounds such as $\text{GuaM}(\text{HCOO})_3$ $\text{M} = \text{Mn}, \text{Fe}, \text{Co}, \text{Ni}, \text{Cu}, \text{Zn}$ ⁸ and $\text{GuaMn}(\text{H}_2\text{POO})_3$ ³⁴⁰ do not exhibit M-site or ligand vacancies.

It was noted for $\text{Gua}_3\text{Ni}_6[\text{Bi}(\text{NCS})_6]_5$ that the M- and X-site vacancies and reduction in Gua cations result in a lower volume than expected given the Gua radius.⁹⁸ The averaged $\text{M}_8(\text{NCS})_{12}$ pseudocubic cage dimension reported for $\text{Gua}_3\text{Ni}_6[\text{Bi}(\text{NCS})_6]_5$, a_{pc} , is 6.0626 Å, and a pseudocubic volume, v_{pc} of 222.836 Å³.⁹⁸ $\text{Gua}_{\frac{2}{3}}\text{Mn}_{\frac{17}{18}}\text{Bi}_{\frac{16}{18}}$ has notably similar dimensions, $a_{\text{pc}} = 6.07(3)$ Å and $v_{\text{pc}} = 223.3(2)$ Å³. It is possible that the Mn analogue adopts a structure with additional M-site vacancies to achieve the lowered volume whilst accounting for the typically longer Mn–N bond lengths compared to Ni–N observed in thiocyanate frameworks.⁸⁰ For comparison, the pseudocubic cage and volume for $\text{GuaMn}(\text{HCOO})_3$ are of similar dimensions, $a_{\text{pc}} = 6.14$ Å and $v_{\text{pc}} = 231.6$ Å³,⁸ potentially demonstrating the lack of need for vacancies in the compound. The other reported compounds, NH_4MnBi , CsMnBi and KMnBi , adopt frameworks with similar pseudocubic dimensions of $a_{\text{pc}} = 6.11(3)$ Å, 6.17(3) Å and 6.09(3) Å.

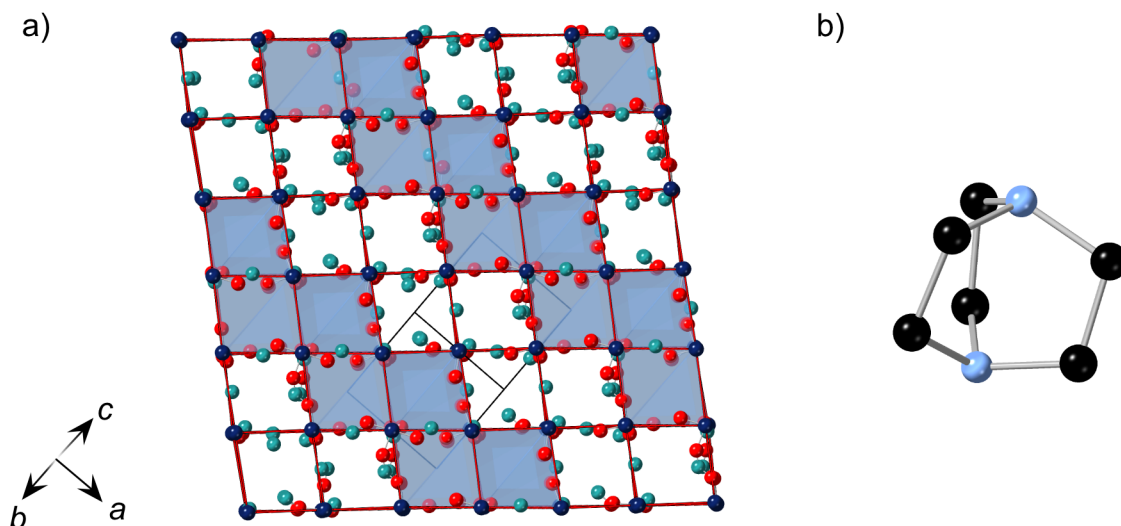


Figure 6.11: a) The A-site order of $[DAB]Mn_2(H_2POO)_6$.³⁴⁰ The pseudocubic cages, edges represented by red lines, shaded blue to show the occupied cages. Due to the flexibility of the H_2POO^- ligands, some atoms of a ligand are positioned within one cage, and other atoms within the adjacent cage, leading to some of the ligands being only partially visible in the figure. b) The DAB (1,4-diazabicyclo[2.2.2]octane-1,4-dium) cation. Mn = navy blue, O = red, P = green, C = black, N = blue. Hydrogen atoms have been removed for clarity.

Complex A-site order has also been reported for complexes with large, doubly charged cations in perovskites, such as the DAB cation (DAB = 1,4-diazabicyclo[2.2.2]octane-1,4-dium, in $HN(C_2H_4)_3NH^{2+}$) in $[DAB]Mn_2(H_2POO)_6$ ³⁴⁰ and $TPCn$ ($[(C_3H_7)_3N(CH_2)_n-N(C_3H_7)_3]^{2+}$, $n = 4, 5$) in $[TPC]_nMn_2(dca)_6$.³⁶⁶ These divalent cations are large enough to straddle two pseudocubic cages, ordering with a head-to-tail or herringbone pattern, which is directly dependent on the length of the A-site species (proportional to n).³⁶⁶ To the best of my knowledge, the closest complex A-site ordering to $Gua_{\frac{2}{3}}Mn_{\frac{17}{18}}Bi_{\frac{16}{18}}$ is reported for $[DAB]Mn_2(H_2POO)_6$. The A-site ordering follows corrugated, stair-like rows, diagonal to the pseudocubic cage axes, alternating between filled and vacant rows (Fig. 6.11). It is suggested the hypophosphite adopts this ordering due to the bulkier A-site cation, as this ordering permits $N-H \cdots O$ hydrogen bond interactions. It is also noted that, similar to the double perovskite thiocyanate frameworks, the vacant cages have the H_2POO^- ligands pointing within the cage.⁹⁸

6.5 Conclusion

This work has demonstrated the synthesis and determination of crystal structures for four manganese(II) bismuth(III) thiocyanate frameworks. The structural analysis employed a range of diffraction techniques, for NH_4MnBi single crystals of suitable dimensions were obtained to allow for neutron diffraction measurements. In addition, $Gua_{\frac{2}{3}}Mn_{\frac{17}{18}}Bi_{\frac{16}{18}}$ and $CsMnBi$ were determined with single crystal X-ray diffraction. Although large single crys-

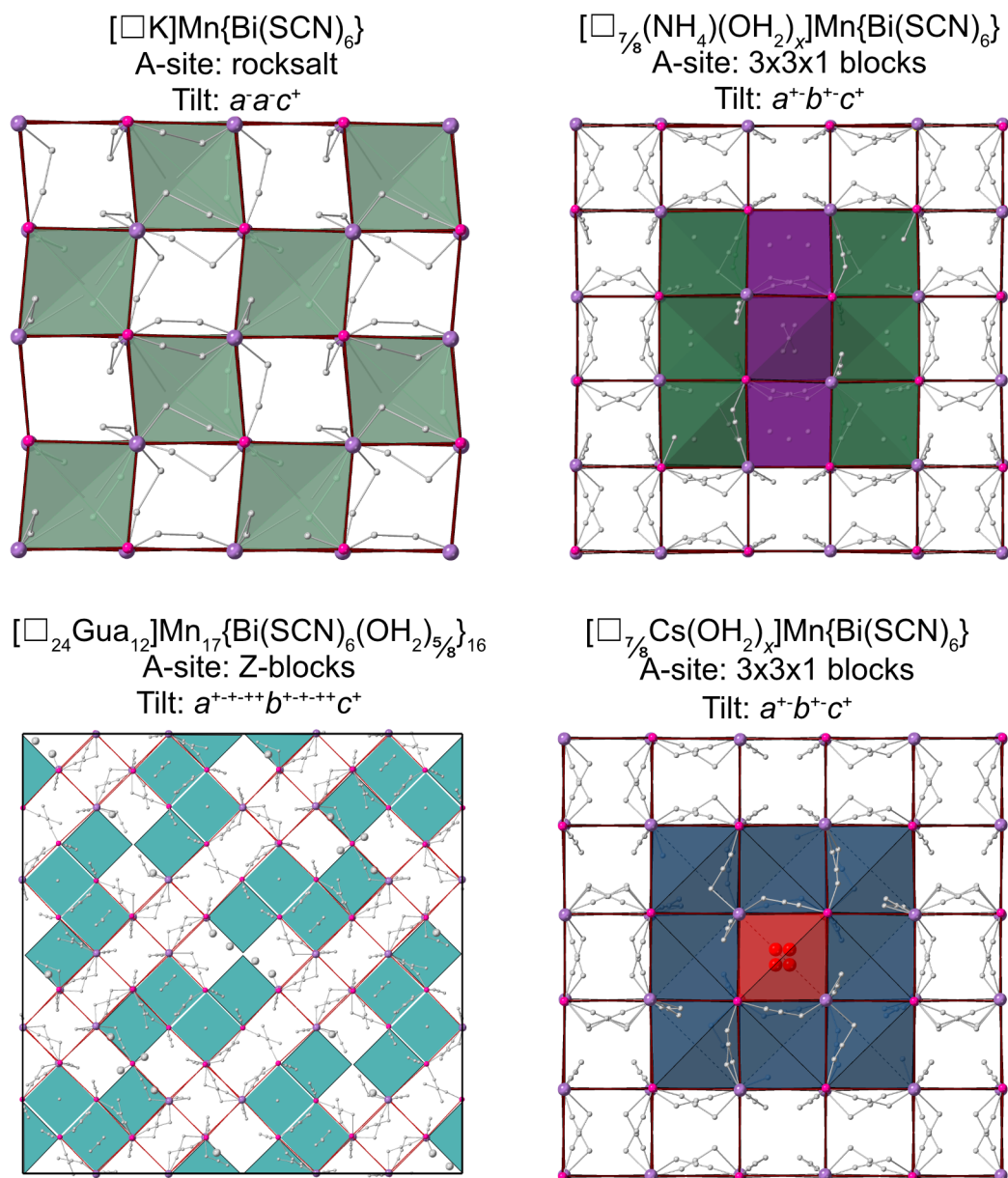


Figure 6.12: A summary of the A-site cation ordering and octahedral tilt sequences for $[\square\text{A}]\text{Mn}\{\text{Bi}(\text{SCN})_6\}$ compounds. Red lines connect the Mn and Bi atoms, indicating edges of the pseudocubic cages. Filled cages indicate occupied A-sites. For NH_4MnBi , the green cages represent A-sites occupied by only NH_4^+ cations and purple cages show mixed NH_4^+ and OH_2 occupation. For CsMnBi , teal cages show A-site Cs^+ cations and the red cage for OH_2 A-sites. The thiocyanate ligands are shown in grey, Mn = pink, Bi = purple.

tals were not grown for KMnBi the structure was solved through single crystal electron diffraction refinements.

Despite the chemical similarities between Mn and Ni, these compounds are not isostructural to their Ni analogues. The M-sites consistently exhibit rocksalt ordering, templated by the thiocyanate anions, however, the overall structures are dictated by the combination of the A-site cation incorporated and the octahedral tilt sequence. A-site cation ordering is present in all of the compounds with several complex orderings reported for

NH_4MnBi , $\text{Gua}_{\frac{2}{3}}\text{Mn}_{\frac{17}{18}}\text{Bi}_{\frac{16}{18}}$ and CsMnBi . Moreover, NH_4MnBi and $\text{Gua}_{\frac{2}{3}}\text{Mn}_{\frac{17}{18}}\text{Bi}_{\frac{16}{18}}$ exhibit octahedral tilt sequences which have not knowingly been reported previously.

Unlike most atomic perovskites, synthesising thiocyanate-based perovskite frameworks permit multiple site orderings. These orderings, A-site, M-site and octahedral tilt patterns, welcome control over the structure, and, in some cases such as KMnBi and $\text{Gua}_{\frac{2}{3}}\text{Mn}_{\frac{17}{18}}\text{Bi}_{\frac{16}{18}}$, adopt polar structures, without the need for A-site orientational order-disorder phase transitions to occur.

6.6 Experimental

6.6.1 Synthesis

$\text{Bi}(\text{NO}_3)_3 \cdot 5\text{H}_2\text{O}$ (251 mg, 1 mmol) was suspended in butanone ($\text{CH}_3\text{COC}_2\text{H}_5$, 5 mL) and KNCS (583 mg, 6 mmol) was added, forming an opaque yellow-orange solution with a white precipitate. $\text{Mn}(\text{NO}_3)_2 \cdot 4\text{H}_2\text{O}$ (251 mg, 1 mmol) was added and the mixture was stirred overnight. The mixture was filtered and the yellow-orange solution was removed *in vacuo*, yielding an orange microcrystalline powder of $\text{KMn}\{\text{Bi}(\text{SCN})_6\}$.

Analogous syntheses were carried out for the other A-site cations, replacing KNCS with the appropriate thiocyanate salt. CsMnBi was synthesised from CsNCS (1146 mg, 6 mmol), NH_4MnBi from NH_4NCS (457 mg, 6 mmol) and $\text{Gua}_{\frac{2}{3}}\text{Mn}_{\frac{17}{18}}\text{Bi}_{\frac{16}{18}}$ from GuaNCS (709 mg, 6 mmol). The synthesis of NH_4MnBi for neutron diffraction measurements and CsMnBi were synthesised using acetone (CH_3COCH_3) as the solvent.

Single crystals of NH_4MnBi , CsMnBi and $\text{Gua}_{\frac{2}{3}}\text{Mn}_{\frac{17}{18}}\text{Bi}_{\frac{16}{18}}$ were obtained by slow evaporation recrystallisations from their mother liquor for a duration of 2 to 7 months.

6.6.2 Powder X-ray diffraction

Powder X-ray diffraction data were collected for CsMnBi by myself using a Malvern PANalytical Xpert MPD (University of Nottingham) operating in Bragg-Brentano geometry equipped with PIXcel area detector and a sealed tube Cu source operating at 40 kV and 40 mA. A Johansson focussing beam monochromator selected pure $\text{K}\alpha_1$ radiation ($\lambda = 1.542 \text{ \AA}$). The incident and diffracted beam path passes through a pair of 0.04 rad Soller slits to reduce axial beam divergence. A fixed 1° anti-scatter slit were used in the incident beam path.

Data were collected with a step size of 0.013° in continuous mode and a scan speed of

26 seconds per step. Four repeated scans were measured and summed after inspection to ensure no sample degradation had occurred. The sample holder was spun with a duration per spin of 8 seconds. Structural refinements were carried out using the FullProf program.³⁷

Powder X-ray diffraction data were collected for KMnBi by myself using a Panalytical Empyrean X-ray diffractometer (Institut Laue Langevin) equipped with GaliPIX3D area detector and a sealed tube Cu source ($\lambda = 1.542 \text{ \AA}$) operating at 40 kV and 40 mA. The incident and diffracted beam path passes through a pair of 0.04 rad Soller slits to reduce axial beam divergence. The sample was prepared between two layers of Kapton film.

Data were collected with a step size of 0.02° in continuous mode and a scan speed of 15 seconds per step. Repeated scans were measured and merged after inspection to ensure no sample degradation had occurred. The sample holder was spun with a duration per spin of 4 seconds. Structural refinements were carried out using the FullProf program.³⁷

6.6.3 Single crystal X-ray diffraction

Single crystal X-ray diffraction was carried out for NH_4MnBi and $\text{Gua}_{\frac{2}{3}}\text{Mn}_{\frac{17}{18}}\text{Bi}_{\frac{16}{18}}$ by myself. Single crystals were selected and mounted using Fomblin® (YR-1800 perfluoropolyether oil) on a polymer-tipped MiTeGen MicroMount™ and cooled rapidly to 120 K in a stream of cold N_2 using an Oxford Cryosystems open flow cryostat.²⁶⁶ Single crystal X-ray diffraction data were collected on an Oxford Diffraction GV1000 (AtlasS2 CCD area detector, mirror-monochromated Mo- $K\alpha$ radiation source; $\lambda = 0.71073 \text{ \AA}$; ω scans, University of Nottingham). Cell parameters were refined from the observed positions of all strong reflections and absorption corrections were applied using a Gaussian numerical method with beam profile correction (CrysAlisPro).²⁶⁷

The structures were solved within Olex2²⁶⁸ by dual space iterative methods (SHELXT),²⁷ least squares refinement of the structural model was carried using (SHELXL).²⁶⁹

Single crystal X-ray measurements were carried out for CsMnBi at ambient temperature using a Bruker D8 Venture diffractometer by Dr Laura Cañadillas Delgado (Institut Laue Langevin, ILL) and Dr Oscar Fabelo (ILL). A graphite monochromatic radiation source from Ag- $K\alpha$ radiation, $\lambda = 0.56086 \text{ \AA}$ was used. The samples were mounted on thin glass fibres attached to brass pins and mounted onto goniometer heads. Data were collected at 273 K. Cell parameters were refined from the observed positions of all strong reflections and absorption corrections were applied using a Gaussian numerical method with beam profile correction (APEX2).³⁶⁷

Structure solution for CsMnBi was carried out using SHELXT²⁷ and refinements were

made with SHELXL²⁶⁹ by Dr Laura Cañadillas Delgado. The non-hydrogen atoms were refined anisotropically with displacement parameters.

6.6.4 Single crystal electron diffraction

Microcrystal electron diffraction data were collected for KMnBi by Dr Jakub Wojciechowski (Rigaku Europe SE, Germany), Dr Robert Bücke (Rigaku Europe SE, Germany) and Dr Stephen Argent (University of Nottingham) using the Rigaku XtaLAB Synergy-ED electron diffractometer.³⁶⁸ A JEOL 200 kV electron source ($\lambda = 0.02510 \text{ \AA}$) was used with a Rigaku HyPix-ED hybrid-pixel detector. A total of 9 different crystals were measured. Individual datasets of each crystal were collected at room temperature. For all datasets, indexing, integration and space group determination were performed using CrysAlisPro version 43.62a.³⁶⁹ Datasets with similar unit cells and symmetry were scaled and merged (three datasets) using CrysAlisPro to obtain more complete and redundant data.

The integrated data were solved by Dr Stephen Argent and myself using direct methods with SHELXT,²⁷ and refinements were made with SHELXT and SHELXL within the OLEX2 graphical interfaces.^{268,269} Rigid bond, atom distance and anisotropic displacement parameter restraints were applied to all N, C and S atoms during the refinements.

6.6.5 Single crystal neutron diffraction

Monochromatic single crystal neutron diffraction data for NH_4MnBi were collected by Dr Laura Cañadillas Delgado (Institut Laue Langevin, ILL), Dr Oscar Fabelo (ILL), Dr Matthew Cliffe (University of Nottingham) and myself on the four-circle D19 diffractometer (ILL). Neutrons with a wavelength of 1.458 \AA were used, provided by a flat Cu monochromator using the 220 reflection at $2\theta_M = 69.91^\circ$ take-off angle. The samples were each placed in a closed-circuit displax cooling device, which was operated following a ramp of 2 K min^{-1} . Measurements were taken at 20 K and at 250 K. An additional crystal was measured at 20 K as well. NOMAD software from the Institut Laue Langevin was used for data collection.²²⁵

Unit cell determinations were performed using PFIND and DIRAX programs, and processing of the raw data was applied using RETREAT, RAFD19 and Int3D programs.^{226–229} The data were corrected for the absorption of the low-temperature device using the D19ABSCAN program.²³⁰ The structure was solved using *SUPERFLIP*²⁸ and refined using Jana2006.³⁶

6.6.6 Magnetometry

Measurements of the magnetic susceptibility were carried out by Dr Matthew Cliffe and myself for KMnBi , NH_4MnBi and $\text{Gua}_{\frac{2}{3}}\text{Mn}_{\frac{17}{18}}\text{Bi}_{\frac{16}{18}}$ using a Quantum Design Magnetic Property Measurements System (MPMS) 3 Superconducting Quantum Interference Device (SQUID) magnetometer. The zero-field-cooled and field-cooled susceptibility was measured in an applied field of 0.01 T over the temperature range 2 – 300 K. As $M(H)$ is linear in this field, the small-field approximation for the susceptibility, $\chi(T) \simeq \frac{M}{H}$, where M is the magnetisation and H is the magnetic field intensity, was taken to be valid.

Isothermal magnetisation measurements were carried out at 2 K over the field range -5 to $+5$ T. Data were corrected for diamagnetism of the sample using Pascal's constants.⁴¹

6.7 Appendix

Table 6.2: Summary of the different site orderings (A-site, M-site and octahedral tilt sequences) observed for the series of $[\square\text{A}]\text{Mn}\{\text{Bi}(\text{SCN})_6\}$ compounds

Ordering	K	Cs	NH_4	Gua
A-site	Rocksalt	$3 \times 3 \times 1$ blocks	$3 \times 3 \times 1$ blocks	Z-blocks
M-site	Rocksalt	Rocksalt	Rocksalt	Rocksalt
Tilt	$a^- a^- c^+$	$a^{+-} b^{+-} c^+$	$a^{+-} b^{+-} c^+$	$a^{+---} b^{+---} c^+$

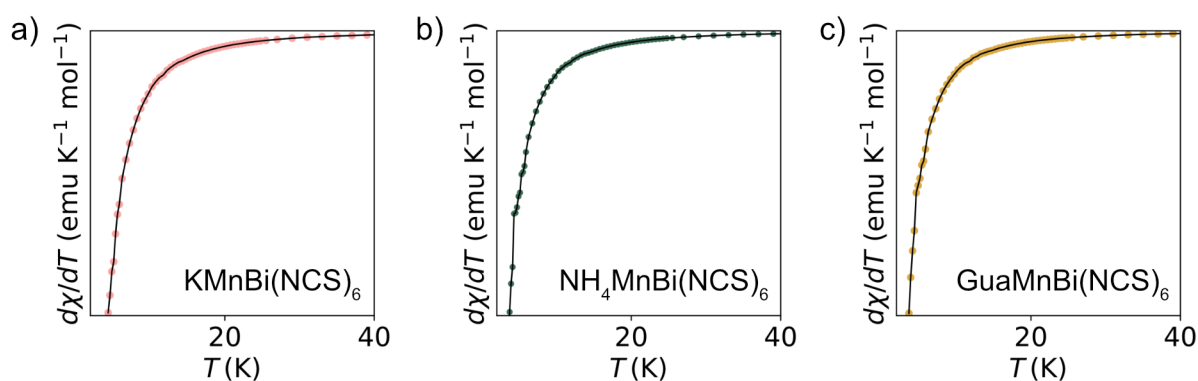


Figure 6.13: The derivative of the susceptibility for a) KMnBi , b) NH_4MnBi and c) $\text{Gua}_{\frac{2}{3}}\text{Mn}_{\frac{17}{18}}\text{Bi}_{\frac{16}{18}}$, with no obvious cusp, suggesting long-range magnetic ordering does not take place down to 2 K.

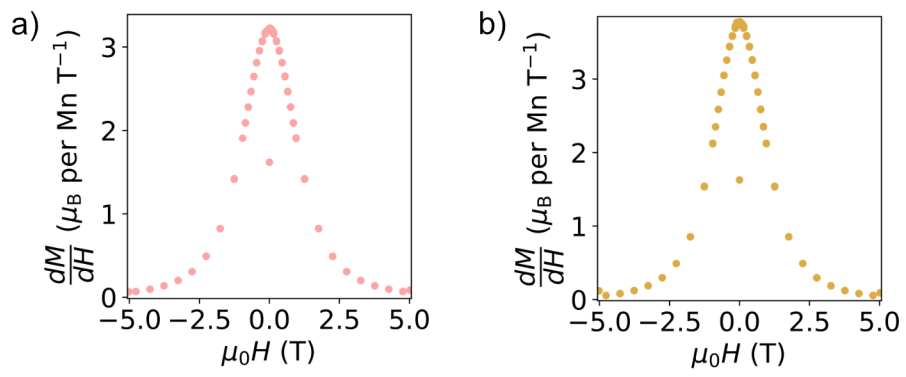


Figure 6.14: The derivative of the magnetisation at 2 K for a) KMnBi and b) $\text{Gua}_{\frac{2}{3}}\text{Mn}_{\frac{17}{18}}\text{Bi}_{\frac{16}{18}}$.

Table 6.3: Single crystal experimental details for $\text{Gua}_{\frac{2}{3}}\text{Mn}_{\frac{17}{18}}\text{Bi}_{\frac{16}{18}}$ (X-ray data) and NH_4MnBi (neutron data). OH_2 content has been estimated to be $x = 2/8$. $S =$ "Goodness of fit"

Crystal data	$\text{Gua}_{\frac{2}{3}}\text{Mn}_{\frac{17}{18}}\text{Bi}_{\frac{16}{18}}$	NH_4MnBi
Chemical formula	$\text{Bi}_{16}\text{C}_{106}\text{H}_{96}\text{Mn}_{17}\text{N}_{130}\text{O}_{12}\text{S}_{94}$	$\text{C}_6\text{H}_{5.5}\text{Bi}_1\text{Mn}_1\text{N}_7\text{O}_{0.75}\text{S}_6$
M_r	10674.50	643.965
Temperature (K)	120	20
λ (Å)	0.71073	1.458
Radiation type	Mo- $K\alpha$ X-rays	Neutron
Crystal system	Orthorhombic	Orthorhombic
Space group	$Fdd2$	$Pnnn$
a (Å)	52.4523(9)	24.371(3)
b (Å)	52.4682(9)	24.422(3)
c (Å)	24.4182(4)	12.4418(17)
V (Å ³)	67201(2)	7405.1(17)
Z	128	16
μ (mm ⁻¹)	9.93	0.003
Crystal size (mm)	$0.10 \times 0.05 \times 0.03$	$3 \times 3 \times 1$
Data collection		
Diffractometer	GV1000, AtlasS2	D19 (ILL)
No. of measured reflections	453600	24833
No. of independent reflections	60468	3874
No. of observed [$I > 2\sigma(I)$] reflections	41455	2086
R_{int}	0.1005	0.099
$(\sin \theta/\lambda)_{\text{max}}$ (Å ⁻¹)	0.650	0.599
Data completeness	0.997	0.94
Refinement		
$R[F^2 > 2\sigma(F^2)]$	0.1494	0.1481
$\omega R(F^2)$	0.3027	0.1469
S	1.02	3.68
No. of parameters	1443	392
$\Delta\rho >_{\text{max}}, \Delta\rho >_{\text{min}}$ (e Å ⁻³)	+7.4, -3.6	—

Table 6.4: Single crystal X-ray diffraction experimental details for CsMnBi. OH₂ content has been estimated to be $x = 2/8$. S = "Goodness of fit"

Chemical formula	C ₆ H _{5.5} Bi ₁ Mn ₁ N ₆ O _{0.25} S ₆
M_r	749.51
Temperature (K)	273
λ (Å)	0.56086
Radiation type	Ag- $K\alpha$ X-rays
Crystal system	Orthorhombic
Space group	$Pn\bar{m}n$
a (Å)	24.7803(7)
b (Å)	24.8038(7)
c (Å)	12.4386(4)
V (Å ³)	7645.3(4)
Z	16
μ (mm ⁻¹)	6.64
Crystal size (mm)	$3 \times 3 \times 1$
Data collection	
Diffractometer	Bruker D8 Venture
No. of measured reflections	235994
No. of independent reflections	18782
No. of observed [$I > 2\sigma(I)$] reflections	10132
R_{int}	0.0799
$(\sin \theta / \lambda)_{\text{max}}$ (Å ⁻¹)	0.60
Data completeness	0.999
Refinement	
$R[F^2 > 2\sigma(F^2)]$	0.0632
$\omega R(F^2)$	0.213
S	1.05
No. of parameters	454
$\Delta\rho >_{\text{max}}, \Delta\rho >_{\text{min}}$ (e Å ⁻³)	+8.63, -3.58

Chapter 7

Conclusions and Outlook

The aim of this thesis was to explore the interplay between crystallographic and magnetic properties in molecular-based frameworks. This was accomplished through the synthesis of unreported thiocyanate and formate-based framework compounds, and performing structural and magnetic characterisations. In particular, the use of neutron diffraction was employed to simultaneously probe the nuclear and magnetic structures.

By tuning the composition of AMX_n compounds, the thesis has demonstrated that a diverse range of topologies exist. The crystallographic structures can show profound changes as the composition is altered. Although this is well-trodden ground for compounds with atomic components, where many compounds can be reliably predicted using radius ratio of the components,^{5,6} this does not follow for molecular-based compounds. Due to the flexibility in the coordination angles of the thiocyanate ligand and the additional A-site volume induced by the longer ligand, these molecular frameworks studied show the versatility of molecular ligands. Structures have been attained that are difficult to synthesise using atomic ligands, such as molecular-based post-perovskites (Chapter 3) and can incorporate a larger A-site cations (Chapter 2). With varied site composition, combined with the inherent flexibility of the framework, unconventional structural orderings (Chapter 6) and modulated structures (Chapter 5) can be identified. Expanding the range of structures and framework topologies broadens the understanding of the complex harmony between the composition and the structure of molecular compounds.

Conversely, it is not a necessity to augment the crystal structure to prompt marked changes to the magnetic behaviour of compounds. Magnetic materials are promising candidates to integrate in future spintronic devices. In order to make these materials functional, it is necessary to harness the magnetic properties in a manner that can be simply tuned and selected as requested. The magnetic ordering temperature can be controlled through metal substitution (Chapter 5), or through external stimuli (pressure,

Chapter 4). More drastically, the magnetic structure can be altered through metal substitution (Chapter 3), with non-collinear magnetic structures currently being held in high regard as materials to be employed in functional devices a result of their more robust nature against external magnetic fields.³⁷⁰

Following this work presented, I would recommend expanding the scope of, in particular, thiocyanate-based frameworks, to incorporate 4d transition metals as M-site components. With more diffuse valence orbitals than metals in the 3rd period, the 4d transition metals can exhibit greater efficiency in orbital overlap and a wider range of metal–ligand bonding angles,³⁷¹ potentially giving rise to unusual structural orders. From a magnetic perspective, strong spin-orbit coupling is exhibited in 4d metals, which shows promise in promoting complex spin textures and non-collinear magnetic orderings.^{372,373}

In conclusion, this thesis has demonstrated there is a careful balance between the chemical composition and the structural and magnetic behaviours of molecular-based frameworks. Unexpected and unconventional structures and characteristics should be enjoyed as further chemical space is explored. Our knowledge is broadened by the simultaneous investigations of new crystallographic structures and their physical properties, and as our understanding of molecular-based frameworks continues to be consolidated, their future utility as functional materials is necessarily progressed.

Bibliography

1. Ogawa, S. Magnetic properties of 3d transition-metal dichalcogenides with the pyrite structure. *Journal of Applied Physics* **50**, 2308–2311 (1979).
2. Ishihara, T. Structure and Properties of Perovskite Oxides. in *Perovskite Oxide for Solid Oxide Fuel Cells* (ed. Ishihara, T.) 1–16 (Springer US, 2009). doi:10.1007/978-0-387-77708-5_1.
3. Ramsdell, L. S. The crystal structure of some metallic sulfides. *American Mineralogist: Journal of Earth and Planetary Materials* **10**, 281–304 (1925).
4. Gulamova, D. & Novoselova, S. Polymorphism of calcium titanate. *Russian Journal of Inorganic Chemistry* **36**, 637–639 (1991).
5. Goldschmidt, V. M. Die Gesetze der Krystallochemie. *Naturwissenschaften* **14**, 477–485 (1926).
6. Kieslich, G., Sun, S. & Cheetham, A. K. An extended Tolerance Factor approach for organic-inorganic perovskites. *Chemical Science* **6**, 3430–3433 (2015).
7. Ichiraku, Y. *et al.* Magnetic Phase Diagram and Chiral Soliton Phase of Chiral Antiferromagnet $[\text{NH}_4][\text{Mn}(\text{HCOO})_3]$. *Journal of the Physical Society of Japan* **88**, 094710 (2019).
8. Hu, K.-L., Kurmoo, M., Wang, Z. & Gao, S. Metal-Organic Perovskites: Synthesis, Structures, and Magnetic Properties of $[\text{C}(\text{NH}_2)_3][\text{M}^{\text{II}}(\text{HCOO})_3]$ (M = Mn, Fe, Co, Ni, Cu, and Zn; $\text{C}(\text{NH}_2)_3$ = Guanidinium). *Chemistry - A European Journal* **15**, 12050–12064 (2009).
9. International Union of Crystallography. Report of the Executive Committee for 1991. *Acta Crystallographica Section A Foundations of Crystallography* **48**, 922–946 (1992).
10. Oppenheim, J. J., Skorupskii, G. & Dincă, M. Aperiodic metal-organic frameworks. *Chemical Science* **11**, 11094–11103 (2020).
11. *International Tables for Crystallography: X-ray absorption spectroscopy and related techniques*. vol. I (International Union of Crystallography, 2020).
12. Aroyo, M. I. *et al.* Crystallography online: Bilbao crystallographic server. *Bulg. Chem. Commun* **43**, 183–197 (2011).
13. Aroyo, M. I. *et al.* Bilbao Crystallographic Server: I. Databases and crystallographic computing programs. *Zeitschrift für Kristallographie - Crystalline Materials* **221**, 15–27 (2006).
14. Sánchez-Andújar, M. *et al.* Characterization of the Order–Disorder Dielectric Transition in the Hybrid Organic–Inorganic Perovskite-Like Formate $\text{Mn}(\text{HCOO})_3[(\text{CH}_3)_2\text{NH}_2]$. *Inorganic Chemistry* **49**, 1510–1516 (2010).
15. Yang, J. *et al.* Coexistence of piezoelectricity and magnetism in two-dimensional vanadium dichalcogenides. *Physical Chemistry Chemical Physics* **21**, 132–136 (2019).

16. Triki, H., Nagy, B., Overgaard, J., Jensen, F. & Kamoun, S. Structure, DFT based investigations on vibrational and nonlinear optical behavior of a new guanidinium cobalt thiocyanate complex. *Structural Chemistry* **31**, 103–114 (2020).
17. Mamontova, E. *et al.* Enantioselective separation under humid conditions by chiral Hofmann clathrates: New opportunities for vintage materials. *Inorganic Chemistry Frontiers* **6**, 3245–3254 (2019).
18. Cañadillas-Delgado, L., Mazzuca, L., Fabelo, O., Rodriguez-velamazan, J. A. & Rodriguez-carvajal, J. Incommensurate structures of the $[\text{CH}_3\text{NH}_3][\text{Co}(\text{COOH})_3]$ compound. *International Union of Crystallography* **6**, 105–115 (2019).
19. Sanjuan-Szklarz, W. F. *et al.* On the accuracy and precision of X-ray and neutron diffraction results as a function of resolution and the electron density model. *IUCrJ* **7**, 920–933 (2020).
20. Gruene, T. & Mugnaioli, E. 3D Electron Diffraction for Chemical Analysis: Instrumentation Developments and Innovative Applications. *Chemical Reviews* **121**, 11823–11834 (2021).
21. Boothroyd, A. T. Interaction with Matter: The Nuclear Interaction. in *Principles of neutron scattering from condensed matter* 10–11 (Oxford University Press, 2020).
22. Gemmi, M. *et al.* 3D Electron Diffraction: The Nanocrystallography Revolution. *ACS Central Science* **5**, 1315–1329 (2019).
23. Saha, A., Nia, S. S. & Rodríguez, J. A. Electron Diffraction of 3D Molecular Crystals. *Chemical Reviews* **122**, 13883–13914 (2022).
24. Powell, C. J., Jablonski, A., Salvat, F. & Lee, A. Y. *NIST Electron Elastic-Scattering Cross-Section Database, Version 4.0*. NIST NSRDS 64 <https://nvlpubs.nist.gov/nistpubs/NSRDS/NIST.NSRDS.64.pdf> (2016) doi:10.6028/NIST.NSRDS.64.
25. Truong, K.-N. *et al.* Making the Most of 3D Electron Diffraction: Best Practices to Handle a New Tool. *Symmetry* **15**, 1555 (2023).
26. Isaacs, N. & Taylor, M. R. *Crystallographic Computing 4: Techniques and New Technologies: Papers Presented at the International School of Crystallographic Computing Held at the Flinders University of South Australia, Adelaide, Australia, August 22-29, 1987*. vol. 3 (International Union of Crystallography, 1988).
27. Sheldrick, G. M. SHELXT - Integrated space-group and crystal-structure determination. *Acta Crystallographica Section A: Foundations of Crystallography* **71**, 3–8 (2015).
28. Palatinus, L. & Chapuis, G. SUPERFLIP – a computer program for the solution of crystal structures by charge flipping in arbitrary dimensions. *Journal of Applied Crystallography* **40**, 786–790 (2007).
29. Spek, A. L. *checkCIF* validation ALERTS: What they mean and how to respond. *Acta Crystallographica Section E Crystallographic Communications* **76**, 1–11 (2020).
30. Dubler, E., Reller, A. & Oswald, H. R. Intermediates in thermal decomposition of nickel(II) complexes: The crystal structures of $\text{Ni}(\text{SCN})_2(\text{NH}_3)_2$ and $\text{Ni}(\text{SCN})_2$. *Zeitschrift für Kristallographie* **161**, 265–277 (1982).
31. Rietveld, H. M. A profile refinement method for nuclear and magnetic structures. *Journal of Applied Crystallography* **2**, 65–71 (1969).
32. Pawley, G. S. Unit-cell refinement from powder diffraction scans. *Journal of Applied Crystallography* **14**, 357–361 (1981).
33. Le Bail, A., Duroy, H. & Fourquet, J. L. Ab-initio structure determination of LiSbWO_6 by X-ray powder diffraction. *Materials Research Bulletin* **23**, 447–452 (1988).

34. Li, C., Pramana, S. S. & Skinner, S. J. Room temperature structure and transport properties of the incommensurate modulated $\text{LaNb}_{0.88}\text{W}_{0.12}\text{O}_{4.06}$. *Dalton Transactions* **48**, 1633–1646 (2019).
35. Yamamoto, A. Crystallography of Quasiperiodic Crystals. *Acta Crystallographica Section A Foundations of Crystallography* **52**, 509–560 (1996).
36. Petříček, V., Dušek, M. & Palatinus, L. Crystallographic computing system JANA2006: General features. *Zeitschrift für Kristallographie-Crystalline Materials* **5**, 345–352 (2014).
37. Rodríguez-Carvajal, J. Recent advances in magnetic structure determination by neutron powder diffraction. *Physica B: Condensed Matter* **192**, 55–69 (1993).
38. Goossens, D. J., Wildes, A. R., Ritter, C. & Hicks, T. J. Ordering and the nature of the spin flop phase transition in MnPS_3 . *Journal of Physics: Condensed Matter* **12**, 1845–1854 (2000).
39. Matsukura, F., Tokura, Y. & Ohno, H. Control of magnetism by electric fields. *Nature Nanotechnology* **10**, 209–220 (2015).
40. Blundell, S. Magnetic susceptibility. in *Magnetism in Condensed Matter* 19–20 (Oxford University Press, 2001).
41. Bain, G. A. & Berry, J. F. Diamagnetic Corrections and Pascal’s Constants. *Journal of Chemical Education* **85**, 532 (2008).
42. Mugiraneza, S. & Hallas, A. M. Tutorial: A beginner’s guide to interpreting magnetic susceptibility data with the Curie-Weiss law. *Communications Physics* **5**, 95 (2022).
43. Landee, C. P. & Turnbull, M. M. Review: A gentle introduction to magnetism: Units, fields, theory, and experiment. *Journal of Coordination Chemistry* **67**, 375–439 (2014).
44. Brown, P. J., Fox, A. G., Maslen, E. N., O’Keefe, M. A. & Willis, B. T. M. Intensity of diffracted intensities. in *International Tables for Crystallography* (eds. Fuess, H. et al.) vol. C 554–595 (International Union of Crystallography, 2006).
45. Boothroyd, A. T. Magnetization and the magnetic interaction. in *Principles of neutron scattering from condensed matter* 106–108 (Oxford University Press, 2020).
46. Litvin, D. B. Magnetic Group Tables 1-, 2- and 3-dimensional magnetic subperiodic groups and magnetic space groups. in *Magnetic Group Tables 1-, 2- and 3-dimensional magnetic subperiodic groups and magnetic space groups* 35–37 (International Union of Crystallography, 2013).
47. Belov, N. The 1651 shubnikov groups. *Kristallografiya* **2**, 315–325 (1957).
48. Opechowski, W. & Guccione, R. *Magnetic Symmetry. Magnetism a treatise on modern theory and materials, vol. IIA.* vol. IIA (Academic Press, 1965).
49. Campbell, B. J., Stokes, H. T., Perez-Mato, J. M. & Rodríguez-Carvajal, J. Introducing a unified magnetic space-group symbol. *Acta Crystallographica Section A Foundations and Advances* **78**, 99–106 (2022).
50. Schweika, W. XYZ-polarisation analysis of diffuse magnetic neutron scattering from single crystals. *Journal of Physics: Conference Series* **211**, 012026 (2010).
51. Perez-Mato, J. M. *et al.* Symmetry-Based Computational Tools for Magnetic Crystallography. *Annual Review of Materials Research* **45**, 217–248 (2015).
52. Campbell, B. J., Stokes, H. T., Tanner, D. E. & Hatch, D. M. *ISODISPLACE*: A web-based tool for exploring structural distortions. *Journal of Applied Crystallography* **39**, 607–614 (2006).

53. Stokes, H. T., Hatch, D. M. & Campbell, B. J. *ISODISTORT*, ISOTROPY Software Suite. (2023).
54. Cortie, D. L. *et al.* Two-Dimensional Magnets: Forgotten History and Recent Progress towards Spintronic Applications. *Advanced Functional Materials* **30**, 1901414 (2020).
55. Fruchart, O. & Thiaville, A. Magnetism in reduced dimensions. *Comptes Rendus Physique* **6**, 921–933 (2005).
56. Blundell, S. Chapter 6 Phase Transitions. in *Magnetism in Condensed Matter* 119–121 (Oxford University Press, 2001).
57. Köbler, U. & Hoser, A. Critical magnetic behaviour in one and two dimensions. *Journal of Magnetism and Magnetic Materials* **311**, 523–529 (2007).
58. Brooks, N. J. *et al.* Automated high pressure cell for pressure jump x-ray diffraction. *Review of Scientific Instruments* **81**, 064103 (2010).
59. Shen, G. & Mao, H. K. High-pressure studies with x-rays using diamond anvil cells. *Reports on Progress in Physics* **80**, 016101 (2017).
60. Klotz, S., Chervin, J.-C., Munsch, P. & Le Marchand, G. Hydrostatic limits of 11 pressure transmitting media. *Journal of Physics D: Applied Physics* **42**, 075413 (2009).
61. Anzellini, S. *et al.* Quasi-hydrostatic equation of state of silicon up to 1 megabar at ambient temperature. *Scientific reports* **9**, 15537 (2019).
62. Eiling, A. & Schilling, J. S. Pressure and temperature dependence of electrical resistivity of Pb and Sn from 1-300K and 0-10 GPa-use as continuous resistive pressure monitor accurate over wide temperature range; superconductivity under pressure in Pb, Sn and In. *Journal of Physics F: Metal Physics* **11**, 623–639 (1981).
63. Liu, J. High pressure x-ray diffraction techniques with synchrotron radiation. *Chinese Physics B* **25**, 076106 (2016).
64. Lertkiattrakul, M., Evans, M. L. & Cliffe, M. J. PASCAL Python: A Principal Axis Strain Calculator. *Journal of Open Source Software* **8**, 5556 (2023).
65. Goodwin, A. L., Keen, D. A. & Tucker, M. G. Large negative linear compressibility of $\text{Ag}_3[\text{Co}(\text{CN})_6]$. *Proceedings of the National Academy of Sciences* **105**, 18708–18713 (2008).
66. Birch, F. Finite Elastic Strain of Cubic Crystals. *Physical Review* **71**, 809–824 (1947).
67. Dokukin, M. E. & Sokolov, I. On the Measurements of Rigidity Modulus of Soft Materials in Nanoindentation Experiments at Small Depth. *Macromolecules* **45**, 4277–4288 (2012).
68. Gilman, J. J., Cumberland, R. W. & Kaner, R. B. Design of hard crystals. *International Journal of Refractory Metals and Hard Materials* **24**, 1–5 (2006).
69. Wang, Z. *et al.* Understanding the Diverse Coordination Modes of Thiocyanate Anion on Solid Surfaces. *Journal of Physical Chemistry C* **123**, 9282–9291 (2019).
70. Neumann, T., Gallo, G., Dinnebier, R. E. & Näther, C. Synthesis, Crystal Structures, and Properties of $\text{Mn}(\text{NCS})_2$ Coordination Compounds with 4-Picoline as Coligand and Crystal Structure of $\text{Mn}(\text{NCS})_2$. *Zeitschrift für anorganische und allgemeine Chemie* **646**, 88–94 (2020).
71. Bie, H.-Y. *et al.* Synthesis, structure and non-linear optical property of a copper(II) thiocyanate three-dimensional supramolecular compound. *Journal of Molecular Structure* **660**, 107–112 (2003).

72. Pearson, R. G. Hard and Soft Acids and Bases. *Journal of the American Chemical Society* **85**, 3533–3539 (1963).
73. Böhland, H., Härtung, H., Baumeister, U., König, G. & Matthäus, R. Preparation, characterization and crystal structure of $\text{Na}_4[\text{Mn}(\text{NCS})_6] \cdot 13\text{H}_2\text{O}$. *Mikrochimica Acta* **125**, 149–152 (1997).
74. Vijayakanth, T., Ram, F., Praveenkumar, B., Shanmuganathan, K. & Boomishankar, R. Piezoelectric Energy Harvesting from a Ferroelectric Hybrid Salt $[\text{Ph}_3\text{MeP}]_4[\text{Ni}(\text{NCS})_6]$ Embedded in a Polymer Matrix. *Angewandte Chemie International Edition* **59**, 10368–10373 (2020).
75. Ha, K. Crystal structure of bis(1,10-phenanthroline) hexakis(thiocyanato-kS)platinate(IV), $(\text{C}_{12}\text{H}_9\text{N}_2)_2[\text{Pt}(\text{SCN})_6]$. *Zeitschrift für Kristallographie - New Crystal Structures* **225**, 699–700 (2010).
76. Maniukiewicz, W., Sieron, L., Bukowska-Strzyzewska, M. & Turek, A. Triaqua-hexathiocyanatobismuth-lanthanum dihydrate, $[\text{Bi}(\text{SCN})_6\text{La}(\text{H}_2\text{O})_3] \cdot 2\text{H}_2\text{O}$, and triaqua-hexathiocyanatobismuth-neodymium dihydrate, $[\text{Bi}(\text{SCN})_6\text{Nd}(\text{H}_2\text{O})_3] \cdot 2\text{H}_2\text{O}$. *Acta Crystallographica Section C: Crystal Structure Communications* **52**, 753–757 (1996).
77. Cliffe, M. J. *et al.* Strongly coloured thiocyanate frameworks with perovskite-analogue structures. *Chemical Science* **10**, 793–801 (2019).
78. Fleck, M. Thiocyanates of nickel and caesium: $\text{Cs}_2\text{NiAg}_2(\text{SCN})_6 \cdot 2\text{H}_2\text{O}$ and $\text{CsNi}(\text{SCN})_3$. *Acta Crystallographica* **C60**, i63–i65 (2004).
79. Suckert, S. *et al.* Synthesis, structures, magnetic, and theoretical investigations of layered Co and Ni thiocyanate coordination polymers. *Dalton Transactions* **45**, 18190–18201 (2016).
80. Bassey, E. N. *et al.* Strengthening the Magnetic Interactions in Pseudobinary First-Row Transition Metal Thiocyanates, $\text{M}(\text{NCS})_2$. *Inorganic Chemistry* **59**, 11627–11639 (2020).
81. Biedermann, M., Hartung, H., Böhland, H. & Matthäus, R. Koordinationsambidenz des thiocyanations inalkalitrithiocyanatomanganat(II)-hydraten. *Zeitschrift für Naturforschung - Section B Journal of Chemical Sciences* **53**, 416–422 (1998).
82. Magnetism in Condensed Matter: Exchange interaction. in *Magnetism in Condensed Matter* 77–79 (Oxford University Press, 2001).
83. Anderson, P. W. Antiferromagnetism. Theory of Superexchange. *Physical Review* **79**, 350–356 (1950).
84. Miller, J. S. & Drillon, M. Antiferromagnetic coupling between neighbors along a chain. in *Magnetism: Molecules IV* 62 (Wiley Online Library, 2002).
85. Snively, L. O., Tuthill, G. F. & Drumheller, J. E. Measurement and calculation of the superexchange interaction through the two-halide bridge in the eclipsed layered compounds $[\text{NH}_3(\text{CH}_2)_n\text{NH}_3]\text{CuX}$ for $n = 2-5$ and $\text{X} = \text{Cl}_4$ and $\text{Cl}_2 \text{Br}_2$. *Physical Review B* **24**, 5349 (1981).
86. Lappas, A., Wills, A. S., Green, M. A., Prassides, K. & Kurmoo, M. Magnetic ordering in the rutile molecular magnets $\text{M}^{\text{II}}[\text{N}(\text{CN})_2]_2$ ($\text{M} = \text{Ni}, \text{Co}, \text{Fe}, \text{Mn}, \text{Ni}_{0.5}\text{Co}_{0.5}, \text{and Ni}_{0.5}\text{Fe}_{0.5}$). *Physical Review B* **67**, 144406 (2003).
87. Raebiger, J. W. *et al.* 1-D and 2-D Homoleptic Dicyanamide Structures, $[\text{Ph}_4\text{P}]_2\{\text{Co}^{\text{II}}[\text{N}(\text{CN})_2]_4\}$ and $[\text{Ph}_4\text{P}]\{\text{M}[\text{N}(\text{CN})_2]_3\}$ ($\text{M} = \text{Mn}, \text{Co}$). *Inorganic Chemistry* **40**, 2578–2581 (2001).
88. Fedorov, P. P., Sobolev, B. P. & Trncova, V. Ionic conductivity and dielectric relaxation of scandium fluoride. *Crystallography Reports* **40**, (1995).
89. Tsui, K. Y., Onishi, N. & Berger, R. F. Tolerance Factors Revisited: Geometrically Designing the Ideal Environment for Perovskite Dopants. *The Journal of Physical Chemistry C* **120**, 23293–23298 (2016).

90. Matsui, T. Thermodynamic properties of ternary barium oxides. *Thermochimica Acta* **253**, 155–165 (1995).
91. Aoba, T., Tiittanen, T., Suematsu, H. & Karppinen, M. Pressure-induced phase transitions of hexagonal perovskite-like oxides. *Journal of Solid State Chemistry* **233**, 492–496 (2016).
92. Bartel, C. J. *et al.* New tolerance factor to predict the stability of perovskite oxides and halides. *Science Advances* **5**, eaav0693 (2019).
93. Burger, S., Ehrenreich, M. G. & Kieslich, G. Tolerance factors of hybrid organic-inorganic perovskites: Recent improvements and current state of research. *Journal of Materials Chemistry A* **6**, 21785–21793 (2018).
94. Peppel, T. & Köckerling, M. Poly[1-ethyl-3-methylimidazolium [tri-isothiocyanato-manganate(II)]]. *IUCrData* **4**, x191659 (2019).
95. Kristallstrukturen, D. Die Kristallstrukturen der Trithiocyanatomercurate $\text{RbHg}(\text{SCN})_3$, und $\text{CsHg}(\text{SCN})_3$. **36**, (1996).
96. Thiele, G. & Messer, D. S-Thiocyanato- und N-Isouthiocyanato-Bindungsisomerie in den Kristallstrukturen von $\text{RbCd}(\text{SCN})_3$ und $\text{CsCd}(\text{SCN})_3$. *Zeitschrift für Anorganische und Allgemeine Chemie* **464**, 255–267 (1980).
97. Xie, K.-P. *et al.* Order–disorder phase transition in the first thiocyanate-bridged double perovskite-type coordination polymer: $[\text{NH}_4]_2[\text{NiCd}(\text{SCN})_6]$. *CrystEngComm* **18**, 4495–4498 (2016).
98. Lee, J. Y. *et al.* Controlling multiple orderings in metal thiocyanate molecular perovskites $\text{A}_x\{\text{Ni}[\text{Bi}(\text{SCN})_6]\}$. *Chemical Science* **12**, 3516 (2021).
99. Tabe, H., Matsushima, M., Tanaka, R. & Yamada, Y. Creation and stabilisation of tuneable open metal sites in thiocyanato-bridged heterometallic coordination polymers to be used as heterogeneous catalysts. *Dalton Transactions* **48**, 17063–17069 (2019).
100. Wang, Z. *et al.* Anionic NaCl-type frameworks of $[\text{Mn}^{\text{II}}(\text{HCOO})_3^-]$, templated by alkylammonium, exhibit weak ferromagnetism. *Dalton Trans.* 2209–2216 (2004) doi:10.1039/B404466E.
101. Wang, X.-Y., Gan, L., Zhang, S.-W. & Gao, S. Perovskite-like Metal Formates with Weak Ferromagnetism and as Precursors to Amorphous Materials. *Inorganic Chemistry* **43**, 4615–4625 (2004).
102. Wang, Z. *et al.* Occurrence of a Rare $4^9 \cdot 6^6$ Structural Topology, Chirality, and Weak Ferromagnetism in the $[\text{NH}_4][\text{M}^{\text{II}}(\text{HCOO})_3]$ (M = Mn, Co, Ni) Frameworks. *Inorganic Chemistry* **46**, 437–445 (2007).
103. Li, M., Kurmoo, M., Wang, Z. & Gao, S. Metal-Organic Niccolite: Synthesis, Structures, Phase Transition, and Magnetic Properties of $[\text{CH}_3\text{NH}_2(\text{CH}_2)_2\text{NH}_2\text{CH}_3][\text{M}_2(\text{HCOO})_6]$ (M = divalent Mn, Fe, Co, Ni, Cu and Zn). *Chemistry – An Asian Journal* **6**, 3084–3096 (2011).
104. Mączka, M. *et al.* Phase Transitions and Coexistence of Magnetic and Electric Orders in the Methylhydrazinium Metal Formate Frameworks. *Chemistry of Materials* **29**, 2264–2275 (2017).
105. García-Ben, J. *et al.* Narrowing the tolerance factor limits for hybrid organic-inorganic dicyanamide-perovskites. *Journal of Solid State Chemistry* **316**, 123635 (2022).
106. Burger, S., Kronawitter, S., Boström, H. L. B., Zareba, J. K. & Kieslich, G. A new polar perovskite coordination network with azaspirodecane as A-site cation. *Dalton Transactions* **49**, 10740–10744 (2020).

107. García-Ben, J., McHugh, L. N., Bennett, T. D. & Bermúdez-García, J. M. Dicyanamide-perovskites at the edge of dense hybrid organic–inorganic materials. *Coordination Chemistry Reviews* **455**, 214337 (2022).
108. Werff, P. M. van der *et al.* Structure and magnetism of anionic dicyanamidometallate extended networks of types $(\text{Ph}_4\text{As})[\text{M}^{\text{II}}(\text{dca})_3]$ and $(\text{Ph}_4\text{As})_2[\text{M}_2^{\text{II}}(\text{dca})_6(\text{H}_2\text{O})] \cdot \text{H}_2\text{O} \cdot x\text{CH}_3\text{OH}$, where $\text{dca} = \text{N}(\text{CN})_2^-$ and $\text{M}^{\text{II}} = \text{Co}, \text{Ni}$. *Polyhedron* **20**, 1129–1138 (2001).
109. Evans, H. A., Wu, Y., Seshadri, R. & Cheetham, A. K. Perovskite-related ReO_3 -type structures. *Nature Reviews Materials* 1–18 (2020) doi:10.1038/s41578-019-0160-x.
110. Beauchamp, A. L. & Goutier, D. Structure cristalline et moléculaire du thiocyanate mercurique. *Canadian Journal of Chemistry* **50**, 977–981 (1972).
111. Ferrari, A., Braibanti, A. & Bigliardi, G. Refinement of the crystal structure of NiCl_2 and of unit-cell parameters of some anhydrous chlorides of divalent metals. *Acta Crystallographica* **16**, 846–847 (1963).
112. Manson, J. L. *et al.* Structure and Magnetic Ordering of $\text{M}^{\text{II}}[\text{N}(\text{CN})_2]_2$ ($\text{M} = \text{Co}, \text{Ni}$). *Chemistry of Materials* **10**, 2552–2560 (1998).
113. Batten, S. R. *et al.* Structure and molecular magnetism of the rutile-related compounds $\text{M}(\text{dca})_2$, $\text{M} = \text{Co}^{\text{II}}, \text{Ni}^{\text{II}}, \text{Cu}^{\text{II}}$, $\text{dca} = \text{dicyanamide}, \text{N}(\text{CN})_2^-$. *Chemical Communications* 439–440 (1998) doi:10.1039/a707264c.
114. Jain, P., Dalal, N. S., Toby, B. H., Kroto, H. W. & Cheetham, A. K. Order–Disorder Antiferroelectric Phase Transition in a Hybrid Inorganic–Organic Framework with the Perovskite Architecture. *Journal of the American Chemical Society* **130**, 10450–10451 (2008).
115. Mikolajick, T., Schroeder, U. & Slesazek, S. The Past, the Present, and the Future of Ferroelectric Memories. *IEEE Transactions on Electron Devices* **67**, 1434–1443 (2020).
116. Sekine, T. *et al.* Fully Printed Wearable Vital Sensor for Human Pulse Rate Monitoring using Ferroelectric Polymer. *Scientific Reports* **8**, 4442 (2018).
117. Mączka, M. *et al.* Structural, thermal, dielectric and phonon properties of perovskite-like imidazolium magnesium formate. *Physical Chemistry Chemical Physics* **18**, 13993–14000 (2016).
118. Mączka, M. *et al.* Perovskite Metal Formate Framework of $[\text{NH}_2\text{-CH}^+\text{-NH}_2]\text{Mn}(\text{HCOO})_3$: Phase Transition, Magnetic, Dielectric, and Phonon Properties. *Inorganic Chemistry* **53**, 5260–5268 (2014).
119. Shang, R., Xu, G., Wang, Z. & Gao, S. Phase Transitions, Prominent Dielectric Anomalies, and Negative Thermal Expansion in Three High Thermally Stable Ammonium Magnesium–Formate Frameworks. *Chemistry – A European Journal* **20**, 1146–1158 (2014).
120. Fu, D. *et al.* A Multiferroic Perdeutero Metal–Organic Framework. *Angewandte Chemie International Edition* **50**, 11947–11951 (2011).
121. Jain, P. *et al.* Multiferroic Behavior Associated with an Order–Disorder Hydrogen Bonding Transition in Metal–Organic Frameworks (MOFs) with the Perovskite ABX_3 Architecture. *Journal of the American Chemical Society* **131**, 13625–13627 (2009).
122. Ptak, M. *et al.* Experimental and theoretical studies of structural phase transition in a novel polar perovskite-like $[\text{C}_2\text{H}_5\text{NH}_3][\text{Na}_{0.5}\text{Fe}_{0.5}(\text{HCOO})_3]$ formate. *Dalton Transactions* **45**, 2574–2583 (2016).
123. Chen, S., Shang, R., Hu, K.-L., Wang, Z.-M. & Gao, S. $[\text{NH}_2\text{NH}_3][\text{M}(\text{HCOO})_3]$ ($\text{M} = \text{Mn}^{2+}, \text{Zn}^{2+}, \text{Co}^{2+}$ and Mg^{2+}): Structural phase transitions, prominent dielectric anomalies and negative thermal expansion, and magnetic ordering. *Inorg. Chem. Front.* **1**, 83–98 (2014).

124. Wang, S.-S. *et al.* Temperature-Induced Structural Phase Transitions in Two New Postperovskite Coordination Polymers. *Crystal Growth & Design* **19**, 1111–1117 (2019).
125. Wang, S.-S. *et al.* Unique Freezing Dynamics of Flexible Guest Cations in the First Molecular Postperovskite Ferroelectric: $(\text{C}_5\text{H}_{13}\text{NBr})[\text{Mn}(\text{N}(\text{CN})_2)_3]$. *CCS Chemistry* **1**, 448–454 (2019).
126. Wang, W. *et al.* Magnetolectric coupling in the paramagnetic state of a metal-organic framework. *Scientific Reports* **3**, 2024 (2013).
127. Xin, L. *et al.* Strain Coupling and Dynamic Relaxation in a Molecular Perovskite-Like Multiferroic Metal-Organic Framework. *Advanced Functional Materials* **28**, 1806013 (2018).
128. Kimura, T., Lashley, J. C. & Ramirez, A. P. Inversion-symmetry breaking in the noncollinear magnetic phase of the triangular-lattice antiferromagnet CuFeO_2 . *Physical Review B* **73**, 220401 (2006).
129. Liu, M. *et al.* Two-Step Antiferromagnetic Transitions and Ferroelectricity in Spin-1 Triangular-Lattice Antiferromagnetic $\text{Sr}_3\text{NiTa}_2\text{O}_9$. *Inorganic Chemistry* **55**, 2709–2716 (2016).
130. Woodward, P. M. Octahedral Tilting in Perovskites. II. Structure Stabilizing Forces. *Acta Crystallographica Section B Structural Science* **53**, 44–66 (1997).
131. Woodward, P. M. Octahedral Tilting in Perovskites. I. Geometrical Considerations. *Acta Crystallographica Section B: Structural Science* **53**, 32–43 (1997).
132. Zheng, K. & Świerczek, K. Physicochemical properties of rock salt-type ordered Sr_2MMoO_6 (M = Mg, Mn, Fe, Co, Ni) double perovskites. *Journal of the European Ceramic Society* **34**, 4273–4284 (2014).
133. García-Ben, J. *et al.* Structural, Thermal and Functional Properties of a Hybrid Dicyanamide-Perovskite Solid Solution. *Crystals* **12**, 860 (2022).
134. Shang, R., Sun, X., Wang, Z. & Gao, S. Zinc-Diluted Magnetic Metal Formate Perovskites: Synthesis, Structures, and Magnetism of $[\text{CH}_3\text{NH}_3][\text{Mn}_x\text{Zn}_{1-x}(\text{HCOO})_3]$ ($x = 0-1$). *Chemistry – An Asian Journal* **7**, 1697–1707 (2012).
135. Salak, A. N., Vyshatko, N. P., Khalyavin, D. D., Prokhnenko, O. & Ferreira, V. M. Low-temperature structural and dielectric phenomena in $\text{La}_{1/3}\text{NbO}_3$ and $\text{La}_{1/3}\text{TaO}_3$: Comparative study. *Applied Physics Letters* **93**, 162903 (2008).
136. Zhou, Q. *et al.* Crystal Structures and Phase Transitions in A-Site Deficient Perovskites $\text{Ln}_{1/3}\text{TaO}_3$. *Chemistry of Materials* **20**, 6666–6676 (2008).
137. Zhang, Z., Howard, C. J., Kennedy, B. J., Knight, K. S. & Zhou, Q. Crystal structure of $\text{Ln}_{1/3}\text{NbO}_3$ (Ln=Nd, Pr) and phase transition in $\text{Nd}_{1/3}\text{NbO}$. *Journal of Solid State Chemistry* **180**, 1846–1851 (2007).
138. Ducau, M., Suh, K. S., Senegas, J. & Darriet, J. Crystal structure and NMR studies of a cubic perovskite. *Materials Research Bulletin* **27**, 1115–1123 (1992).
139. Darriet, J., Mayorga, S. & Tressaud, A. Crystal Structure of $\text{Na}_2\text{BaFe}_4\text{F}_{12}$: A New Ordered Perovskite-Like Fluoride. *European Journal of Solid State Inorganic Chemistry* **27**, 783–790 (1990).
140. King, G. & Woodward, P. M. Cation ordering in perovskites. *Journal of Materials Chemistry* **20**, 5785 (2010).
141. Glazer, A. M. The classification of tilted octahedra in perovskites. *Acta Crystallographica Section B Structural Crystallography and Crystal Chemistry* **28**, 3384–3392 (1972).
142. Boström, H. L. B. Tilts and shifts in molecular perovskites. *CrystEngComm* **22**, 961–968 (2020).

143. Collings, I. E. *et al.* Disorder-order transitions in the perovskite metal-organic frameworks $[(\text{CH}_3)_2\text{NH}_2][\text{M}(\text{HCOO})_3]$ at high pressure. *CrystEngComm* **20**, 3512–3521 (2018).
144. Zhao, X.-H. *et al.* Cation-Dependent Magnetic Ordering and Room-Temperature Bistability in Azido-Bridged Perovskite-Type Compounds. *Journal of the American Chemical Society* **135**, 16006–16009 (2013).
145. Jenkins, S. *et al.* Breaking through the Mermin-Wagner limit in 2D van der Waals magnets. *Nature Communications* **13**, 6917 (2022).
146. Palle, G. & Sunko, D. K. Physical limitations of the Hohenberg–Mermin–Wagner theorem. *Journal of Physics A: Mathematical and Theoretical* **54**, 315001 (2021).
147. Elahi, E. *et al.* A review on two-dimensional (2D) magnetic materials and their potential applications in spintronics and spin-caloritronic. *Computational Materials Science* **213**, 111670 (2022).
148. Moore, M. W. & Day, P. Magnetic phase diagrams and helical magnetic phases in $\text{M}_x\text{Ni}_{1-x}\text{Br}_2$ (M = Fe, Mn): A neutron diffraction and magneto-optical study. *Journal of Solid State Chemistry* **59**, 23–41 (1985).
149. Cable, J. W., Wilkinson, M. K., Wollan, E. O. & Koehler, W. C. Neutron Diffraction Investigation of the Magnetic Order in MnI_2 . *Physical Review* **125**, 1860–1864 (1962).
150. Kuindersma, S. R., Sanchez, J. P. & Haas, C. Magnetic and structural investigations on NiI_2 and CoI_2 . *Physica B+C* **111**, 231–248 (1981).
151. Cable, J. W., Wilkinson, M. K., Wollan, E. O. & Koehler, W. C. Neutron-Diffraction Study of Antiferromagnetic FeCl_3 . *Physical Review* **127**, 714–717 (1962).
152. Wu, X. *et al.* Magnetic ordering and multiferroicity in MnI_2 . *Physical Review B* **86**, 134413 (2012).
153. Gelard, J., Fert, A. R., Meriel, P. & Allain, Y. Magnetic structure of FeI_2 by neutron diffraction experiments. *Solid State Communications* **14**, 187–189 (1974).
154. Jung, J. H., Park, C.-H. & Ihm, J. A Rigorous Method of Calculating Exfoliation Energies from First Principles. *Nano Letters* **18**, 2759–2765 (2018).
155. Velický, M. *et al.* Exfoliation of natural van der Waals heterostructures to a single unit cell thickness. *Nature Communications* **8**, 14410 (2017).
156. Song, T. *et al.* Switching 2D magnetic states via pressure tuning of layer stacking. *Nature Materials* **18**, 1298–1302 (2019).
157. Lee, J.-U. *et al.* Ising-type magnetic ordering in atomically thin FePS_3 . *Nano letters* **16**, 7433–7438 (2016).
158. O’Hara, D. J. *et al.* Room temperature intrinsic ferromagnetism in epitaxial manganese selenide films in the monolayer limit. *Nano letters* **18**, 3125–3131 (2018).
159. Deng, Y. *et al.* Gate-tunable room-temperature ferromagnetism in two-dimensional Fe_3GeTe_2 . *Nature* **563**, 94–99 (2018).
160. Tan, C. *et al.* Hard magnetic properties in nanoflake van der Waals Fe_3GeTe_2 . *Nature Communications* **9**, 1554 (2018).
161. Huang, B. *et al.* Layer-dependent ferromagnetism in a van der Waals crystal down to the monolayer limit. *Nature* **546**, 270–273 (2017).
162. Tudu, B. & Tiwari, A. Recent Developments in Perpendicular Magnetic Anisotropy Thin Films for Data Storage Applications. *Vacuum* **146**, 329–341 (2017).

163. Pato-Doldán, B. *et al.* Magnetic transitions and isotropic: Versus anisotropic magnetic behaviour of $[\text{CH}_3\text{NH}_3][\text{M}(\text{HCOO})_3]$ $\text{M} = \text{Mn}^{2+}, \text{Co}^{2+}, \text{Ni}^{2+}, \text{Cu}^{2+}$ metal-organic perovskites. *Journal of Materials Chemistry C* **4**, 11164–11172 (2016).
164. Zhao, J. P. *et al.* Magnetic behavior control in niccolite structural metal formate frameworks $[\text{NH}_2(\text{CH}_3)_2][\text{Fe}^{\text{III}}\text{M}^{\text{II}}(\text{HCOO})_6]$ ($\text{M} = \text{Fe}, \text{Mn}, \text{and Co}$) by varying the divalent metal ions. *Inorganic Chemistry* **49**, 10390–10399 (2010).
165. Shurdha, E. *et al.* Extended network thiocyanate- and tetracyanoethanide-based first-row transition metal complexes. *Inorganic Chemistry* **51**, 9655–9665 (2012).
166. Billerey, D., Terrier, C., Pointon, A. J. & Redoules, J. P. Low-field magnetic properties of anhydrous NiCl_2 . *Journal of Magnetism and Magnetic Materials* **21**, 187–190 (1980).
167. Wilkinson, M. K., Cable, J. W., Wollan, E. O. & Koehler, W. C. Neutron Diffraction Investigations of the Magnetic Ordering in FeBr_2 , CoBr_2 , FeCl_2 , and CoCl_2 . *Physical Review* **113**, 497–507 (1959).
168. Pollard, R. J., McCann, V. H. & Ward, J. B. Electronic and magnetic properties of ^{57}Fe in NiCl_2 , NiBr_2 , NiI_2 and CoI_2 from Mossbauer spectroscopy. *Journal of Physics C: Solid State Physics* **15**, 6807–6822 (1982).
169. Botana, A. S. & Norman, M. R. Electronic structure and magnetism of transition metal dihalides: Bulk to monolayer. *Physical Review Materials* **3**, 044001 (2019).
170. Chemistry of transition metal cyanide compounds: Modern perspectives. in *Chemistry of transition metal cyanide compounds: Modern perspectives* (ed. Karlin, K. D.) vol. 45 123 (Wiley, 1997).
171. Manson, J. L., Kmety, C. R., Epstein, A. J. & Miller, J. S. Spontaneous Magnetization in the $\text{M}[\text{N}(\text{CN})_2]_2$ ($\text{M} = \text{Cr}, \text{Mn}$) Weak Ferromagnets. *Inorganic Chemistry* **38**, 2552–2553 (1999).
172. Kurmoo, M. & Kepert, C. J. Hard magnets based on transition metal complexes with the dicyanamide anion, $\{\text{N}(\text{CN})_2\}^-$. *New Journal of Chemistry* **22**, 1515–1524 (1998).
173. Mondal, S. *et al.* Effect of hydrostatic pressure on ferromagnetism in two-dimensional CrI_3 . *Physical Review B* **99**, 180407 (2019).
174. Sun, Y. *et al.* Effects of hydrostatic pressure on spin-lattice coupling in two-dimensional ferromagnetic $\text{Cr}_2\text{Ge}_2\text{Te}_6$. *Applied Physics Letters* **112**, 072409 (2018).
175. Kmety, C. R. *et al.* Noncollinear antiferromagnetic structure of the molecule-based magnet $\text{Mn}[\text{N}(\text{CN})_2]_2$. *Physical Review B* **62**, 5576–5588 (2000).
176. Ribas, J. *et al.* Two New Antiferromagnetic Nickel(II) Complexes Bridged by Azido Ligands in the *cis* Position. Effect of the Counteranion on the Crystal Structure and Magnetic Properties. *Inorganic Chemistry* **35**, 864–868 (1996).
177. Balents, L. Spin liquids in frustrated magnets. *Nature* **464**, 199–208 (2010).
178. Escuer, A. *et al.* Synthesis, Structural Characterization, and Monte Carlo Simulation of the Magnetic Properties of Two New Alternating Mn^{II} Azide 2-D Honeycombs. Study of the Ferromagnetic Ordered Phase below 20 K. *Inorganic Chemistry* **39**, 4688–4695 (2000).
179. Gao, E.-Q., Wang, Z.-M. & Yan, C.-H. From manganese(ii)-azido layers to a novel three-dimensional molecular magnet: Spin canting and metamagnetism. *Chemical Communications* 1748 (2003) doi:10.1039/b304536f.
180. Wang, X.-Y., Wang, L., Wang, Z.-M. & Gao, S. Solvent-Tuned Azido-Bridged Co^{2+} Layers: Square, Honeycomb, and *kagomé*. *Journal of the American Chemical Society* **128**, 674–675 (2006).

181. Li, W. *et al.* Phase transitions and thermodynamics of the two-dimensional Ising model on a distorted kagome lattice. *Physical Review B* **82**, 134434 (2010).
182. Böhme, M. *et al.* Variation of the Chain Geometry in Isomeric 1D Co(NCS)₂ Coordination Polymers and Their Influence on the Magnetic Properties. *Inorganic Chemistry* **59**, 5325–5338 (2020).
183. Yang, Q., Zhao, J.-P., Hu, B.-W., Zhang, X.-F. & Bu, X.-H. New Manganese(II) Azido Coordination Polymers with Nicotinic/Isonicotinic Acids as Coligands: Synthesis, Structure, and Magnetic Properties. *Inorganic Chemistry* **49**, 3746–3751 (2010).
184. Zhao, J.-P. *et al.* A chiral 2p–3d heterometallic azido complex with 2,6-pyridinedicarboxylate as the co-ligand showing magnetic order. *Dalton Transactions* **42**, 8201 (2013).
185. Wang, Y.-Q., Zhang, X.-M., Li, X.-B., Wang, B.-W. & Gao, E.-Q. Magnetic Systems with Mixed Carboxylate and Azide Bridges: Slow Relaxation in Co(II) Metamagnet and Spin Frustration in Mn(II) Compound. *Inorganic Chemistry* **50**, 6314–6322 (2011).
186. Bordallo, H. N. *et al.* S = 1/2 Ising behavior in the two-dimensional molecular magnet Fe(NCS)₂(pyrazine)₂. *Physical Review B* **69**, 224405 (2004).
187. Lloret, F. *et al.* Spin Polarization and Ferromagnetism in Two-Dimensional Sheetlike Cobalt(II) Polymers: [Co(L)₂(NCS)₂] (L= Pyrimidine or Pyrazine). *Angewandte Chemie International Edition* **37**, 135–138 (1998).
188. Wriedt, M., Sellmer, S. & Näther, C. Thermal Decomposition Reactions as Tool for the Synthesis of New Metal Thiocyanate Diazine Coordination Polymers with Cooperative Magnetic Phenomena. *Inorganic Chemistry* **48**, 6896–6903 (2009).
189. Wellm, C., Rams, M., Neumann, T., Ceglarska, M. & Näther, C. Tuning of the Critical Temperature in Magnetic 2D Coordination Polymers by Mixed Crystal Formation. *Crystal Growth & Design* **18**, 3117–3123 (2018).
190. Wellm, C., Rams, M., Ceglarska, M. & Näther, C. Synthesis and Magnetic Properties of the Layered Compound [Fe(NCS)₂(4-acetylpyridine)₂]_n and Its Mixed Crystals with the Ni(II) Analogue. *Crystal Growth and Design* **20**, 2508–2515 (2020).
191. Näther, C., Jess, I., Krebs, C. & Poschmann, M. P. M. Synthesis, Crystal Structure and Properties of a new Hydrate of Manganese Thiocyanate with the Composition Mn(NCS)₂(H₂O)₂. *Zeitschrift für anorganische und allgemeine Chemie* **648**, e202200023 (2022).
192. Shurdha, E. *et al.* First row transition metal(II) thiocyanate complexes, and formation of 1-, 2-, and 3-dimensional extended network structures of M(NCS)₂(solvent)₂ (M = Cr, Mn, Co) composition. *Inorganic Chemistry* **52**, 10583–10594 (2013).
193. McElearney, J. N., Balagot, L. L., Muir, J. A. & Spence, R. D. Structural and magnetic properties of Mn(SCN)₂(C₂H₅OH)₂, a new two-dimensional Heisenberg magnet. *Physical Review B* **19**, 306–317 (1979).
194. Cañadillas-Delgado, L., Mazzuca, L., Fabelo, O., Rodríguez-Carvajal, J. & Petricek, V. Experimental Evidence of the Coexistence of Proper Magnetic and Structural Incommensurability on the [CHNH₃][Ni(COOH)₃] Compound. *Inorganic Chemistry* **59**, 17896–17905 (2020).
195. Deng, Y. *et al.* All-electrical switching of a topological non-collinear antiferromagnet at room temperature. *National Science Review* **10**, 154 (2023).
196. Gao, F. *et al.* Noncollinear commensurate antiferromagnetic structure in metallic Pr₂PdAl₇Ge₄. *Physical Review B* **107**, 214435 (2023).

197. Sosnowska, I. Comments on the unusual magnetic structure of BiFeO₃. *Ferroelectrics* **79**, 127–130 (1988).
198. Sears, J. A. *et al.* Magnetic order in RuCl₃: A honeycomb-lattice quantum magnet with strong spin-orbit coupling. *Physical Review B* **91**, 144420 (2015).
199. Gao, S. *et al.* Spiral Spin Liquid on a Honeycomb Lattice. *Physical Review Letters* **128**, 227201 (2022).
200. Tsubokawa, I. On the Magnetic Properties of a CrBr₃ Single Crystal. *Journal of the Physical Society of Japan* **15**, 1664–1668 (1960).
201. McGuire, M. A., Dixit, H., Cooper, V. R. & Sales, B. C. Coupling of Crystal Structure and Magnetism in the Layered, Ferromagnetic Insulator CrI₃. *Chemistry of Materials* **27**, 612–620 (2015).
202. Cable, J. W., Wilkinson, M. K. & Wollan, E. O. Neutron diffraction investigation of antiferromagnetism in CrCl₃. *Journal of Physics and Chemistry of Solids* **19**, 29–34 (1961).
203. Cole, A. *et al.* Extreme sensitivity of the magnetic ground state to halide composition in FeCl_{3-x}Br_x. *Physical Review Materials* **7**, 064401 (2023).
204. Fedoseeva, N., Spevakova, I., Petrakovskii, G., Chuev, V. & Petrov, S. Magnetic structure and magnetic field behaviour of NaMnCl₃. *1980 15-18, Part 1*, 539–541 (1980).
205. Liu, J., Sun, Q., Kawazoe, Y. & Jena, P. Exfoliating biocompatible ferromagnetic Cr-trihalide monolayers. *Physical Chemistry Chemical Physics* **18**, 8777–8784 (2016).
206. Zhong, D. *et al.* Van der Waals engineering of ferromagnetic semiconductor heterostructures for spin and valleytronics. *Science Advances* **3**, e1603113 (2017).
207. Zhang, W.-B., Qu, Q., Zhu, P. & Lam, C.-H. Robust intrinsic ferromagnetism and half semiconductivity in stable two-dimensional single-layer chromium trihalides. *Journal of Materials Chemistry C* **3**, 12457–12468 (2015).
208. Li, H. *et al.* Highly Selective Sorption and Luminescent Sensing of Small Molecules Demonstrated in a Multifunctional Lanthanide Microporous Metal–Organic Framework Containing 1D Honeycomb-Type Channels. *Chemistry – A European Journal* **19**, 3358–3365 (2013).
209. Henke, S. & Fischer, R. A. Gated Channels in a Honeycomb-like Zinc–Dicarboxylate–Bipyridine Framework with Flexible Alkyl Ether Side Chains. *Journal of the American Chemical Society* **133**, 2064–2067 (2011).
210. Gao, C. *et al.* Synthesis and structure study of a novel 2D network polymeric cadmium(II) complex bridged by thiocyanate. *Inorganic Chemistry Communications* **11**, 985–987 (2008).
211. Lai, L.-L. *et al.* Polypseudorotaxane architecture of poly-bis[4-(N-benzyl-pyridinium)]piperazine-hexathiocyanato-di-cadmium(ii) with 2-D honeycomb-like [Cd(SCN)₃]_{n⁻} anionic polymeric framework. *CryStEngComm* **9**, 345 (2007).
212. Greenspan, L. Humidity fixed points of binary saturated aqueous solutions. *Journal of Research of the National Bureau of Standards Section A: Physics and Chemistry* **81A**, 89 (1977).
213. O’Brien, F. E. M. The Control of Humidity by Saturated Salt Solutions. *Journal of Scientific Instruments* **25**, 73–76 (1948).
214. Gallego, S. V., Tasci, E. S., Flor, G. de la, Perez-Mato, J. M. & Aroyo, M. I. Magnetic symmetry in the Bilbao Crystallographic Server: A computer program to provide systematic absences of magnetic neutron diffraction. *Journal of Applied Crystallography* **45**, 1236–1247 (2012).
215. Blundell, S. *Magnetism in Condensed Matter*. (Oxford University Press, 2001).

216. Loon, C. J. J. van & Verschoor, G. C. The crystal structure of NaMnCl₃. *Acta Crystallographica Section B Structural Crystallography and Crystal Chemistry* **29**, 1224–1228 (1973).
217. Johnson, R. D. *et al.* Monoclinic crystal structure of RuCl₃ and the zigzag antiferromagnetic ground state. *Physical Review B* **92**, 235119 (2015).
218. Shusharina, E. A., Zadesenets, A. V. & Gromilov, S. A. Crystal structure and thermal properties of Na₂[ReCl₆] · 6H₂O. *Journal of Structural Chemistry* **52**, 439–442 (2011).
219. Bonamico, M. & Dessey, G. Atti della Accademia Nazionale dei Lincei. *Rendiconti della Classe di scienze fisiche, matematiche e naturali* **39**, 504–509 (1965).
220. Yoshida, H., Chiba, J., Kaneko, T., Fujimori, Y. & Abe, S. Pressure effect on the Curie temperature of CrBr₃. *Physica B: Condensed Matter* **237–238**, 525–526 (1997).
221. Lindgard, P. A., Birgeneau, R. J., Guggenheim, H. J. & Als-Nielsen, J. Spin-wave dispersion and sublattice magnetization in NiCl₂. *Journal of Physics C: Solid State Physics* **8**, 1059–1069 (1975).
222. Yelon, W. B. & Birgeneau, R. J. Magnetic Properties of FeCl₂ in Zero Field. II. Long-Range Order. *Physical Review B* **5**, 2615–2621 (1972).
223. Khomskii, D. Classifying multiferroics: Mechanisms and effects. *Physics* **2**, 20 (2009).
224. Lee, M. *et al.* Magnetic phase diagram and multiferroicity of Ba₃MnNb₂O₉: A spin-5/2 triangular lattice antiferromagnet with weak easy-axis anisotropy. *Physical Review B* **90**, 224402 (2014).
225. Mutti, P. *et al.* Nomad more than a simple sequencer. in *Proc. ICALEPCS* (2011).
226. Duisenberg, A. J. M. Indexing in single-crystal diffractometry with an obstinate list of reflections. *Journal of Applied Crystallography* **25**, 92–96 (1992).
227. McIntyre, G. J. & Stansfield, R. F. D. A general Lorentz correction for single-crystal diffractometers. *Acta Crystallographica Section A Foundations of Crystallography* **44**, 257–262 (1988).
228. Wilkinson, C., Khamis, H. W., Stansfield, R. F. D. & McIntyre, G. J. Integration of single-crystal reflections using area multidetectors. *Journal of Applied Crystallography* **21**, 471–478 (1988).
229. Katcho, N. A., Cañadillas-Delgado, L., Fabelo, O., Fernández-Díaz, M. T. & Rodríguez-Carvajal, J. Int3D: A Data Reduction Software for Single Crystal Neutron Diffraction. *Crystals* **11**, 897 (2021).
230. Matthewman, J. C., Thompson, P. & Brown, P. J. The Cambridge Crystallography Subroutine Library. *Journal of Applied Crystallography* **15**, 167–173 (1982).
231. Vishnoi, P. *et al.* Structural Diversity and Magnetic Properties of Hybrid Ruthenium Halide Perovskites and Related Compounds. *Angewandte Chemie International Edition* **59**, 8974–8981 (2020).
232. Jaffe, A. *et al.* High Compression-Induced Conductivity in a Layered Cu–Br Perovskite. *Angewandte Chemie International Edition* **59**, 4017–4022 (2020).
233. Kojima, A., Teshima, K., Shirai, Y. & Miyasaka, T. Organometal Halide Perovskites as Visible-Light Sensitizers for Photovoltaic Cells. *Journal of the American Chemical Society* **131**, 6050–6051 (2009).
234. Xu, J. *et al.* Halide Perovskites for Nonlinear Optics. *Advanced Materials* **32**, 1806736 (2020).
235. Oganov, A. R. & Ono, S. Theoretical and experimental evidence for a post-perovskite phase of MgSiO₃ in Earth’s D” layer. *Nature* **430**, 445–448 (2004).
236. Murakami, M., Hirose, K., Kawamura, K., Sata, N. & Ohishi, Y. Post-Perovskite Phase Transition in MgSiO₃. *Science* **304**, 855–858 (2004).

237. Ohgushi, K. *et al.* CaPtO₃ as a novel post-perovskite oxide. *Physics and Chemistry of Minerals* **35**, 189–195 (2008).
238. Yamaura, K. *et al.* Synthesis and Magnetic and Charge-Transport Properties of the Correlated 4d Post-Perovskite CaRhO₃. *Journal of the American Chemical Society* **131**, 2722–2726 (2009).
239. Rodi, F. & Babel, D. Ternare Oxide der Übergangsmetalle. IV. Erdalkaliiridium(IV)-oxide: Kristallstruktur von CaIrO₃. *Zeitschrift für Anorganische und Allgemeine Chemie* **336**, 17–23 (1965).
240. Bremholm, M., Dutton, S. E., Stephens, P. W. & Cava, R. J. NaIrO₃—A pentavalent post-perovskite. *Journal of Solid State Chemistry* **184**, 601–607 (2011).
241. Martin, C. D. *et al.* Rietveld structure refinement of perovskite and post-perovskite phases of NaMgF₃ (Neighborite) at high pressures. *American Mineralogist* **91**, 1703–1706 (2006).
242. Shirako, Y. *et al.* High-pressure stability relations, crystal structures, and physical properties of perovskite and post-perovskite of NaNiF₃. *Journal of Solid State Chemistry* **191**, 167–174 (2012).
243. Dobson, D. P., Hunt, S. A., Lindsay-Scott, A. & Wood, I. G. Towards better analogues for MgSiO₃ post-perovskite: NaCoF₃ and NaNiF₃, two new recoverable fluoride post-perovskites. *Physics of the Earth and Planetary Interiors* **189**, 171–175 (2011).
244. Lindsay-Scott, A. *et al.* Time-of-flight neutron powder diffraction with milligram samples: The crystal structures of NaCoF₃ and NaNiF₃ post-perovskites. *Journal of Applied Crystallography* **47**, 1939–1947 (2014).
245. Bernal, F. L. *et al.* Perovskite to Postperovskite Transition in NaFeF₃. *Inorganic Chemistry* **53**, 12205–12214 (2014).
246. Ohgushi, K. *et al.* Resonant X-ray Diffraction Study of the Strongly Spin-Orbit-Coupled Mott Insulator CaIrO₃. *Physical Review Letters* **110**, 217212 (2013).
247. Ijjaali, I., Mitchell, K., Huang, F. Q. & Ibers, J. A. Syntheses and characterization of the actinide manganese selenides ThMnSe₃ and UMnSe₃. *Journal of Solid State Chemistry* **177**, 257–261 (2004).
248. Noël, H. & Padiou, J. Structure cristalline de FeUS₃. *Acta Crystallographica* **B32**, 1593–1595 (1976).
249. Lin, W. *et al.* Inorganic Halide Perovskitoid TIPbI₃ for Ionizing Radiation Detection. *Advanced Functional Materials* **31**, 2006635 (2021).
250. Bogdanov, N. A., Katukuri, V. M., Stoll, H., Brink, J. van den & Hozoi, L. Post-perovskite CaIrO₃: A $j = 1/2$ quasi-one-dimensional antiferromagnet. *Physical Review B* **85**, 235147 (2012).
251. Jia, F. *et al.* Persistent Spin-texture and Ferroelectric Polarization in 2D Hybrid Perovskite Benzylammonium Lead-halide. *The Journal of Physical Chemistry Letters* **11**, 5177–5183 (2020).
252. Tokura, Y. & Kanazawa, N. Magnetic Skyrmion Materials. *Chemical Reviews* **121**, 2857–2897 (2021).
253. Li, S., Wang, Y., Wang, Y., Sanvito, S. & Hou, S. High-Performance Spin Filters Based on 1,2,4,5-Tetrahydroxybenzene Molecules Attached to Bulk Nickel Electrodes. *The Journal of Physical Chemistry C* **125**, 6945–6953 (2021).
254. Werff, P. M. van der, Batten, S. R., Jensen, P., Moubaraki, B. & Murray, K. S. Cation Templatation of Anionic Metal Dicyanamide Networks. *Inorganic Chemistry* **40**, 1718–1722 (2001).
255. Mączka, M., Gağor, A., Ptak, M., Stefańska, D. & Sieradzki, A. Temperature-dependent studies of a new two-dimensional cadmium dicyanamide framework exhibiting an unusual temperature-induced irreversible phase transition into a three-dimensional perovskite-like framework. *Physical Chemistry Chemical Physics* **20**, 29951–29958 (2018).

256. Biswas, M., Batten, S. R., Jensen, P. & Mitra, S. Retention of (4,4) Connectivity in the Absence of $\pi\cdots\pi$ Interactions in a Cadmium tris-Dicyanamide Compound. *Australian Journal of Chemistry* **59**, 115 (2006).
257. Wang, H.-T., Zhou, L. & Wang, X. L. A two-dimensional anionic Cd^{II} polymer constructed through dicyanamide coordination bridges. *Acta Crystallographica* **C71**, 717–720 (2015).
258. Liu, S., Wang, B.-W., Wang, Z.-M. & Gao, S. Magnetic layered perovskites of [CH₃C(NH₂)₂]₂[M(HCOO)₄] (M = Co²⁺ and Ni²⁺): Synthesis, structures and properties. *Dalton Transactions* **47**, 11925–11933 (2018).
259. Curley, S. P. M. *et al.* Magnetic ground state of the one-dimensional ferromagnetic chain compounds M(NCS)₂(thiourea)₂ (M = Ni, Co). *Physical Review Materials* **5**, 034401 (2021).
260. Cliffe, M. J. *et al.* Low-dimensional quantum magnetism in Cu(NCS)₂: A molecular framework material. *Physical Review B* **97**, 144421 (2018).
261. DeFotis, G. C., Dell, K. D., Krovich, D. J. & Brubaker, W. W. Antiferromagnetism of Ni(SCN)₂. *Journal of Applied Physics* **73**, 5386–5388 (1993).
262. Ohgushi, K. *et al.* Metal-insulator transition in Ca_{1-x}Na_xIrO₃ with post-perovskite structure. *Physical Review B* **74**, 241104 (2006).
263. Shirako, Y. *et al.* Magnetic properties of high-pressure phase of CaRuO₃ with post-perovskite structure. *Journal of Physics: Conference Series* **215**, 012038 (2010).
264. Cliffe, M. J., Fabelo, O. & Cañadillas-Delgado, L. Magnetic order in a metal thiocyanate perovskite-analogue. *CrystEngComm* **24**, 7250–7254 (2022).
265. Weingart, C., Spaldin, N. & Bousquet, E. Noncollinear magnetism and single-ion anisotropy in multiferroic perovskites. *Physical Review B* **86**, 094413 (2012).
266. Cosier, J. & Glazer, A. M. A nitrogen-gas-stream cryostat for general X-ray diffraction studies. *Journal of Applied Crystallography* **19**, 105–107 (1986).
267. Diffraction, R. O. CrysAlisPro Software system, version 1.171.40.45a. (2018).
268. Dolomanov, O. V., Bourhis, L. J., Gildea, R. J., Howard, J. A. K. & Puschmann, H. OLEX2 : A complete structure solution, refinement and analysis program. *Journal of Applied Crystallography* **42**, 339–341 (2009).
269. Sheldrick, G. M. Crystal structure refinement with *SHELXL*. *Acta Crystallographica Section C Structural Chemistry* **71**, 3–8 (2015).
270. Orench, I. P. *et al.* The new powder diffractometer D1B of the Institut Laue Langevin. *Journal of Physics: Conference Series* **549**, 012003 (2014).
271. Grimme, S., Antony, J., Ehrlich, S. & Krieg, H. A consistent and accurate *ab initio* parametrization of density functional dispersion correction (DFT-D) for the 94 elements H-Pu. *The Journal of Chemical Physics* **132**, 154104 (2010).
272. Kresse, G. & Furthmüller, J. Efficient iterative schemes for *ab initio* total-energy calculations using a plane-wave basis set. *Physical Review B* **54**, 11169–11186 (1996).
273. Pickett, W. E., Erwin, S. C. & Ethridge, E. C. Reformulation of the LDA + U method for a local-orbital basis. *Physical Review B* **58**, 1201–1209 (1998).
274. Zhou, F., Cococcioni, M., Marianetti, C. A., Morgan, D. & Ceder, G. First-principles prediction of redox potentials in transition-metal compounds with LDA + U. *Physical Review B* **70**, 235121 (2004).

275. Perdew, J. P., Burke, K. & Ernzerhof, M. Generalized Gradient Approximation Made Simple. *Physical Review Letters* **77**, 3865–3868 (1996).
276. Blöchl, P. E. Projector augmented-wave method. *Physical Review B* **50**, 17953–17979 (1994).
277. Hobbs, D., Kresse, G. & Hafner, J. Fully unconstrained noncollinear magnetism within the projector augmented-wave method. *Physical Review B* **62**, 11556–11570 (2000).
278. Coak, M. J. *et al.* Emergent Magnetic Phases in Pressure-Tuned van der Waals Antiferromagnet FePS₃. *Physical Review X* **11**, 011024 (2021).
279. Pasternak, M. P. *et al.* Pressure-induced magnetic and electronic transitions in the layered Mott insulator FeI₂. *Physical Review B* **65**, 035106 (2001).
280. Wang, Y. *et al.* Emergent superconductivity in an iron-based honeycomb lattice initiated by pressure-driven spin-crossover. *Nature Communications* **9**, 1914 (2018).
281. Quintero, P. A. *et al.* Pressure-induced enhancement of the magnetic anisotropy in Mn(N(CN)₂)₂. *Physical Review B* **91**, 014439 (2015).
282. Pasternak, M. P. *et al.* Pressure-induced metallization and the collapse of the magnetic state in the antiferromagnetic insulator NiI₂. *Physical Review Letters* **65**, 790–793 (1990).
283. Molnár, G. *et al.* Raman Spectroscopic Study of Pressure Effects on the Spin-Crossover Coordination Polymers Fe(Pyrazine[M(CN₄)] · 2H₂O (M = Ni, Pd, Pt). First Observation of a Piezo-Hysteresis Loop at Room Temperature. *The Journal of Physical Chemistry B* **107**, 3149–3155 (2003).
284. Barreda-Argüeso, J. A. *et al.* Pressure-induced spin transition and site-selective metallization in CoCl₂. *Scientific Reports* **9**, 5448 (2019).
285. Kuo, C.-T. *et al.* Exfoliation and Raman Spectroscopic Fingerprint of Few-Layer NiPS₃ Van der Waals Crystals. *Scientific Reports* **6**, 20904 (2016).
286. Bedoya-Pinto, A. *et al.* Intrinsic 2D-XY ferromagnetism in a van der Waals monolayer. *Science* **374**, 616–620 (2021).
287. Xu, W. M. & Pasternak, M. P. Magnetism in FeCl₂ at High Pressures. *Mössbauer Spectroscopy* 175–181 (2003) doi:10.1007/978-94-010-0045-1_16.
288. Rozenberg, G. Kh., Xu, W. & Pasternak, M. P. The Mott insulators at extreme conditions; structural consequences of pressure-induced electronic transitions. *Zeitschrift für Kristallographie – Crystalline Materials* **229**, 210–222 (2014).
289. Rozenberg, G. Kh. *et al.* Pressure-induced structural, electronic, and magnetic phase transitions in FeCl₂ studied by x-ray diffraction and resistivity measurements. *Physical Review B* **79**, 214105 (2009).
290. Serra-Crespo, P. *et al.* Experimental evidence of negative linear compressibility in the MIL-53 metal–organic framework family. *CrystEngComm* **17**, 276–280 (2015).
291. Wu, H., Yildirim, T. & Zhou, W. Exceptional Mechanical Stability of Highly Porous Zirconium Metal–Organic Framework UiO-66 and Its Important Implications. *The Journal of Physical Chemistry Letters* **4**, 925–930 (2013).
292. Kaneko, W., Mito, M., Kitagawa, S. & Ohba, M. Interpenetrated Three-Dimensional Mn^{II}M^{III} Ferromagnets, [Mn(4-dmap)₄]₃[M(CN)₆]₂ · 10 H₂O (M = Cr, Mn): Structures, Magnetic Properties, and Pressure-Responsive Magnetic Modulation. *Chemistry - A European Journal* **14**, 3481–3489 (2008).

293. Shum, W. W., Her, J.-H., Stephens, P. W., Lee, Y. & Miller, J. S. Observation of the Pressure Dependent Reversible Enhancement of t_c and Loss of the Anomalous Constricted Hysteresis for $[\text{Ru}_2(\text{O}_2\text{CMe})_4]_3[\text{Cr}(\text{CN})_6]$. *Advanced Materials* **19**, 2910–2913 (2007).
294. Nuttall, C. J., Takenobu, T., Iwasa, Y. & Kurmoo, M. Pressure Dependence of the Magnetization of $\text{M}^{\text{II}}(\text{N}(\text{CN})_2)_2$: Mechanism for the Long Range Magnetic Ordering. *Molecular Crystals and Liquid Crystals Science and Technology. Section A. Molecular Crystals and Liquid Crystals* **343**, 227–234 (2000).
295. López-Cabrelles, J. *et al.* Isoreticular two-dimensional magnetic coordination polymers prepared through pre-synthetic ligand functionalization. *Nature Chemistry* **10**, 1001–1007 (2018).
296. Perlepe, P. *et al.* Metal-organic magnets with large coercivity and ordering temperatures up to 242°C. *Science* **370**, 587–592 (2020).
297. Ketelaar, J. A. A. Die Kristallstruktur des Nickelbromids und -jodids. *Zeitschrift für Kristallographie - Crystalline Materials* **88**, 26–34 (1934).
298. Tassini, L., Gorelli, F. & Ulivi, L. High temperature structures and orientational disorder in compressed solid nitrogen. *The Journal of Chemical Physics* **122**, 074701 (2005).
299. Gorelli, F. A., Santoro, M., Ulivi, L. & Hanfland, M. Crystal structure of solid Oxygen at high pressure and low temperature. *Physical Review B* **65**, 172106 (2002).
300. Ahmad, A. S. *et al.* Pressure-driven switching of magnetism in layered CrCl_3 . *Nanoscale* **12**, 22935–22944 (2020).
301. Haines, C. R. S. *et al.* Pressure-Induced Electronic and Structural Phase Evolution in the van der Waals Compound FePS_3 . *Physical Review Letters* **121**, 266801 (2018).
302. Wang, X. *et al.* Pressure-induced iso-structural phase transition and metallization in WSe_2 . *Scientific Reports* **7**, 46694 (2017).
303. Pasternak, M. P., Taylor, R. D. & Jeanloz, R. Pressure-induced Mott transition in transition-metal iodides (invited). *Journal of Applied Physics* **70**, 5956–5960 (1991).
304. Grover, S. *et al.* Tuning the mechanical properties of dicyanamide-based molecular perovskites. *CryStEngComm* **25**, 3439–3444 (2023).
305. Fan, X. *et al.* Negative Linear Compressibility of Nickel Dicyanamide. *Chemistry Letters* **48**, 1375–1378 (2019).
306. Dissegna, S. *et al.* Tuning the Mechanical Response of Metal–Organic Frameworks by Defect Engineering. *Journal of the American Chemical Society* **140**, 11581–11584 (2018).
307. Mishra, S. K. *et al.* New insights into the compressibility and high-pressure stability of $\text{Ni}(\text{CN})_2$: A combined study of neutron diffraction, Raman spectroscopy, and inelastic neutron scattering. *Journal of Physics: Condensed Matter* **28**, 045402 (2016).
308. Hodgson, S. A. *et al.* Negative area compressibility in silver(I) tricyanomethanide. *Chemical Communications* **50**, 5264–5266 (2014).
309. Collings, I. E. *et al.* Compositional dependence of anomalous thermal expansion in perovskite-like ABX_3 formates. *Dalton Transactions* **45**, 4169–4178 (2016).
310. Collings, I. E. *et al.* Pressure dependence of spin canting in ammonium metal formate antiferromagnets. *Physical Chemistry Chemical Physics* **20**, 24465–24476 (2018).
311. Kreitlow, J. *et al.* Pressure dependence of $\text{C}_4\text{N}_2\text{H}_4$ -mediated superexchange in $\text{XCl}_2(\text{C}_4\text{N}_2\text{H}_4)_2$ ($\text{X} = \text{Fe}, \text{Co}, \text{Ni}$). *Physical Review B* **72**, 134418 (2005).

312. Vettier, C. & Yelon, W. B. Magnetic properties of FeCl₂ at high pressure. *Physical Review B* **11**, 4700–4710 (1975).
313. Wu, Y. *et al.* Ni(NCS)₂ monolayer: A robust bipolar magnetic semiconductor. *Nanoscale* **13**, 16564–16570 (2021).
314. Manson, J. L. *et al.* Long-Range Magnetic Order in Mn[N(CN)₂]₂(pyz) {pyz = pyrazine}. Susceptibility, Magnetization, Specific Heat, and Neutron Diffraction Measurements and Electronic Structure Calculations. *Journal of the American Chemical Society* **123**, 162–172 (2001).
315. Filik, J. *et al.* Processing two-dimensional X-ray diffraction and small-angle scattering data in *DAWN 2*. *Journal of Applied Crystallography* **50**, 959–966 (2017).
316. Hewat, A. W. D2B, A New High Resolution Neutron Powder Diffractometer at ILL Grenoble. *Materials Science Forum* **9**, 69–80 (1986).
317. Lis, O. *et al.* Structural, Magnetic and Vibrational Properties of Van Der Waals Ferromagnet CrBr₃ at High Pressure. *Materials* **16**, 454 (2023).
318. Zhang, C. *et al.* Pressure-Enhanced Ferromagnetism in Layered CrSiTe₃ Flakes. *Nano Letters* **21**, 7946–7952 (2021).
319. Xu, K. *et al.* Unique 2D–3D Structure Transformations in Trichalcogenide CrSiTe₃ under High Pressure. *The Journal of Physical Chemistry C* **124**, 15600–15606 (2020).
320. Yakovenko, A. A., Chapman, K. W. & Halder, G. J. Pressure-induced structural phase transformation in cobalt(II) dicyanamide. *Acta Crystallographica Section B Structural Science, Crystal Engineering and Materials* **71**, 252–257 (2015).
321. Collings, I. E. *et al.* Structural distortions in the high-pressure polar phases of ammonium metal formates. *CrystEngComm* **18**, 8849–8857 (2016).
322. Pinheiro, C. B. & Abakumov, A. M. Superspace crystallography: A key to the chemistry and properties. *IUCrJ* **2**, 137–154 (2015).
323. Noda, Y., Mori, M. & Yamada, Y. Successive Jahn-Teller Phase Transitions in K₂PbCu(NO₂)₆. *Journal of the Physical Society of Japan* **45**, 954–966 (1978).
324. Bakus Ii, R. C., Atwood, D. A., Parkin, S., Brock, C. P. & Petricek, V. C₆H₄S₂AsCl: Description and interpretation of an incommensurately modulated molecular crystal structure. *Acta Crystallographica Section B Structural Science Crystal Engineering and Materials* **69**, 496–508 (2013).
325. Boča, M., Svoboda, I., Renz, F. & Fuess, H. Poly[methylammonium tris(-formato-*o:o*)cobalt(II)]. *Acta Crystallographica* **C60**, m631–m633 (2004).
326. Mazzuca, L. *et al.* Microscopic Insights on the Multiferroic Perovskite-Like [CH₃NH₃][Co(COOH)₃] Compound. *Chemistry - A European Journal* **24**, 388–399 (2018).
327. Gómez-Aguirre, L. C. *et al.* Magnetic Ordering-Induced Multiferroic Behavior in [CH₃NH₃][Co(HCOO)₃] Metal–Organic Framework. *Journal of the American Chemical Society* **138**, 1122–1125 (2016).
328. Ding, L. *et al.* Lattice dynamics and spin excitations in the metal-organic framework [CH₃NH₃][Co(HCOO)₃]. (2023) doi:10.48550/ARXIV.2307.10746.
329. Lee, D. *et al.* Tailoring structure and magnetic properties of Ni_xCo_{1-x}(N(CN)₂)₂ molecular magnets. *Current Applied Physics* **16**, 1100–1104 (2016).

330. Shanmukaraj, D. & Murugan, R. Synthesis and characterization of $\text{LiNi}_y\text{Co}_{1-y}\text{PO}_4$ ($y = 0-1$) cathode materials for lithium secondary batteries. *Ionics* **10**, 88–92 (2004).
331. Marcos, M. D. *et al.* New lamellar oxophosphorus derivatives of nickel(II): X-ray powder diffraction structure determinations and magnetic studies of $\text{Ni}(\text{HPO}_3) \cdot \text{H}_2\text{O}$, $\text{NiCl}(\text{H}_2\text{PO}_2) \cdot \text{H}_2\text{O}$, and $\text{Ni}_x\text{Co}_{1-x}(\text{HPO}_3) \cdot \text{H}_2\text{O}$ solid solutions. *Inorganic Chemistry* **32**, 5044–5052 (1993).
332. Pato-Doldán, B. *et al.* Atypical Magnetic Behavior in the Incommensurate $(\text{CH}_3\text{NH}_3)[\text{Ni}(\text{HCOO})_3]$ Hybrid Perovskite. *The Journal of Physical Chemistry C* **127**, 3330–3338 (2023).
333. Petříček, V., Eigner, V., Dušek, M. & Čejchan, A. Discontinuous modulation functions and their application for analysis of modulated structures with the computing system JANA2006. *Zeitschrift für Kristallographie - Crystalline Materials* **231**, 301–312 (2016).
334. Ouladdiaf, B. *et al.* CYCLOPS – a reciprocal-space explorer based on CCD neutron detectors. *Journal of Applied Crystallography* **44**, 392–397 (2011).
335. Rodríguez-Carvajal, J., Fuentes-Montero, L. & Cermak, P. The programs of ESMERALDA and their corresponding documentation. (2018).
336. Yang, J. & Mannodi-Kanakkithodi, A. High-throughput computations and machine learning for halide perovskite discovery. *MRS Bulletin* **47**, 940–948 (2022).
337. Greedan, J. E. Magnetic Properties of Perovskite Structure Oxides. in *Complex Oxides: An Introduction* 13–66 (World Scientific, 2019).
338. Spaldin, N. A. & Ramesh, R. Advances in magnetoelectric multiferroics. *Nature Materials* **18**, 203–212 (2019).
339. Knapp, M. C. & Woodward, P. M. A-site cation ordering in $\text{AA}'\text{BB}'\text{O}_6$ perovskites. *Journal of Solid State Chemistry* **179**, 1076–1085 (2006).
340. Wu, Y. *et al.* $[\text{Am}]\text{Mn}(\text{H}_2\text{POO})_3$: A New Family of Hybrid Perovskites Based on the Hypophosphite Ligand. *Journal of the American Chemical Society* **139**, 16999–17002 (2017).
341. Qian, K., Xu, Y., Wang, Z. & Yang, J. Synthesis, crystal structure, and magnetic properties of an azido-bridged Mn(II) complex $[\text{C}_3\text{H}_5\text{NH}_3][\text{Mn}(\text{N}_3)_3]$. *Zeitschrift für Naturforschung B* **72**, 409–413 (2017).
342. Xia, X. *et al.* Oxygen Activity Tuning via FeO_6 Octahedral Tilting in Perovskite Ferrites for Chemical Looping Dry Reforming of Methane. *ACS Catalysis* **12**, 7326–7335 (2022).
343. Leinenweber, K. & Parise, J. High-Pressure Synthesis and Crystal Structure of $\text{CaFeTi}_2\text{O}_6$, a New Perovskite Structure Type. *Journal of Solid State Chemistry* **114**, 277–281 (1995).
344. Stokes, H. T. & Hatch, D. M. *FINDSYM* : Program for identifying the space-group symmetry of a crystal. *Journal of Applied Crystallography* **38**, 237–238 (2005).
345. Stokes, H. T., Hatch, D. M. & Campbell, B. J. *FINDSYM*, *ISOTROPY* Software Suite. (2022).
346. Hollas, D. *et al.* Aqueous Solution Chemistry of Ammonium Cation in the Auger Time Window. *Scientific Reports* **7**, 756 (2017).
347. Steiner, T. The Hydrogen Bond in the Solid State. *Angewandte Chemie International Edition* **41**, 48–76 (2002).
348. Klotz, S., Strässle, Th., Cornelius, A. L., Philippe, J. & Hansen, Th. Magnetic Ordering in Solid Oxygen up to Room Temperature. *Physical Review Letters* **104**, 115501 (2010).

349. Anderson, M., Greenwood, K., Taylor, G. & Poeppelmeier, K. B-cation arrangements in double perovskites. *Progress in Solid State Chemistry* **22**, 197–233 (1993).
350. Pinlac, R. A. F., Stern, C. L. & Poeppelmeier, K. R. New Layered Oxide-Fluoride Perovskites: KNaNbOF_5 and KNaMO_2F_4 ($M = \text{Mo}^{6+}, \text{W}^{6+}$). *Crystals* **1**, 3–14 (2011).
351. Pilania, G. & Uberuaga, B. P. Cation ordering and effect of biaxial strain in double perovskite CsRbCaZnCl_6 . *Journal of Applied Physics* **117**, 114103 (2015).
352. Kennedy, B. J., Howard, C. J., Kubota, Y. & Kato, K. Phase transition behaviour in the A-site deficient perovskite oxide $\text{La}_{1/3}\text{NbO}_3$. *Journal of Solid State Chemistry* **177**, 4552–4556 (2004).
353. Krot, N. N., Bessonov, A. A. & Grigor'ev, M. S. Synthesis and study of Pu(V) formates. *Radiochemistry* **49**, 575–578 (2007).
354. Emerson, A. J., Edwards, A. J., Batten, S. R. & Turner, D. R. A neutron diffraction study of hydrogen bonding in isostructural potassium and ammonium lanthanoidates. *CrystEngComm* **16**, 1625–1631 (2014).
355. An, L. *et al.* Engineering Elastic Properties of Isostructural Molecular Perovskite Ferroelectrics via B-Site Substitution. *Small* **17**, 2006021 (2021).
356. Bedlivy, D. & Mereiter, K. The structures of potassium lead triiodide dihydrate and ammonium lead triiodide dihydrate. *Acta Crystallographica Section B Structural Crystallography and Crystal Chemistry* **36**, 782–785 (1980).
357. Kieslich, G., Sun, S. & Cheetham, A. K. Solid-state principles applied to organic–inorganic perovskites: New tricks for an old dog. *Chem. Sci.* **5**, 4712–4715 (2014).
358. Komaba, S., Hasegawa, T., Dahbi, M. & Kubota, K. Potassium intercalation into graphite to realize high-voltage/high-power potassium-ion batteries and potassium-ion capacitors. *Electrochemistry Communications* **60**, 172–175 (2015).
359. Amat, A. *et al.* Cation-Induced Band-Gap Tuning in Organohalide Perovskites: Interplay of Spin–Orbit Coupling and Octahedra Tilting. *Nano Letters* **14**, 3608–3616 (2014).
360. D'Arrigo, J. S. Screening of membrane surface charges by divalent cations: An atomic representation. *American Journal of Physiology-Cell Physiology* **235**, C109–C117 (1978).
361. Li, W. *et al.* Ferroelasticity in a metal–organic framework perovskite; towards a new class of multiferroics. *Acta Materialia* **61**, 4928–4938 (2013).
362. King, G., Thimmaiah, S., Dwivedi, A. & Woodward, P. M. Synthesis and Characterization of New $\text{AA}'\text{bWO}_6$ Perovskites Exhibiting Simultaneous Ordering of *a*-Site and *b*-Site Cations. *Chemistry of Materials* **19**, 6451–6458 (2007).
363. López, M. L. *et al.* The monoclinic perovskite $\text{La}_2\text{LiSbO}_6$. A rietveld refinement of neutron powder diffraction data. *Materials Research Bulletin* **27**, 647–654 (1992).
364. Lenz, A. & Müller-Buschbaum, Hk. Bi^{5+} Im monoklin verzerrten perowskit $\text{Sr}_2\text{BiNdO}_6$. *Journal of the Less Common Metals* **161**, 141–146 (1990).
365. Hill, J. A. *et al.* Inorganic co-crystal formation and thermal disproportionation in a dicyanometallate 'superperovskite'. *Chemical Communications* **55**, 5439–5442 (2019).
366. Burger, S. *et al.* Designing Geometric Degrees of Freedom in ReO_3 -Type Coordination Polymers. *Advanced Functional Materials* **32**, 2205343 (2022).
367. Bruker. APEX2 version 2.0-22. (2004).

368. Ito, S. *et al.* Structure determination of small molecule compounds by an electron diffractometer for 3D ED/MicroED. *CrystEngComm* **23**, 8622–8630 (2021).
369. Diffraction, R. O. Rigaku Oxford Diffraction CrysAlisPro Software System. (2023).
370. Baltz, V. *et al.* Antiferromagnetic spintronics. *Reviews of Modern Physics* **90**, 015005 (2018).
371. Parkin, S. S. P. Systematic variation of the strength and oscillation period of indirect magnetic exchange coupling through the 3*d*, 4*d*, and 5*d* transition metals. *Physical Review Letters* **67**, 3598–3601 (1991).
372. Magott, M., Dunbar, K. R. & Pinkowicz, D. Correlating magnetic anisotropy with [Mo(CN)₇]⁴⁻ geometry of Mn^{II}–Mo^{III} magnetic frameworks. *Dalton Transactions* **48**, 15493–15500 (2019).
373. Wang, X.-Y., Avendaño, C. & Dunbar, K. R. Molecular magnetic materials based on 4*d* and 5*d* transition metals. *Chemical Society Reviews* **40**, 3213 (2011).

Appendix A

The following pages include the article published from the results in Chapter 3. It reports two previously unpublished thiocyanate post-perovskites as well as, determination of the magnetic structures of post-perovskites using neutron diffraction.

Cite this: *Chem. Sci.*, 2023, 14, 3531

All publication charges for this article have been paid for by the Royal Society of Chemistry

Non-collinear magnetism in the post-perovskite thiocyanate frameworks CsM(NCS)₃†

Madeleine Geers,^{ab} Jie Yie Lee,^{ab} Sanliang Ling,^{bc} Oscar Fabelo,^{bd} Laura Cañadillas-Delgado^{bd} and Matthew J. Cliffe^{ba*}

AMX₃ compounds are structurally diverse, a notable example being the post-perovskite structure which adopts a two-dimensional framework with corner- and edge-sharing octahedra. Few molecular post-perovskites are known and of these, none have reported magnetic structures. Here we report the synthesis, structure and magnetic properties of molecular post-perovskites: CsNi(NCS)₃, a thiocyanate framework, and two new isostructural analogues CsCo(NCS)₃ and CsMn(NCS)₃. Magnetisation measurements show that all three compounds undergo magnetic order. CsNi(NCS)₃ (Curie temperature, $T_C = 8.5(1)$ K) and CsCo(NCS)₃ ($T_C = 6.7(1)$ K) order as weak ferromagnets. On the other hand, CsMn(NCS)₃ orders as an antiferromagnet (Néel temperature, $T_N = 16.8(8)$ K). Neutron diffraction data of CsNi(NCS)₃ and CsMn(NCS)₃, show that both are non-collinear magnets. These results suggest molecular frameworks are fruitful ground for realising the spin textures required for the next generation of information technology.

Received 13th December 2022

Accepted 18th February 2023

DOI: 10.1039/d2sc06861c

rsc.li/chemical-science

1 Introduction

A unifying goal in solid-state science is control over the physical properties of materials, and the tunability of perovskites is perhaps the most striking example. Traditionally these compounds are three-dimensional frameworks with a general chemical formula AMX₃ built from [MX₆] corner-sharing octahedra. Through substitution of the A, M and X ions, materials with remarkable magnetic,¹ electronic conductivity,² photovoltaic³ and non-linear optical properties⁴ have been created.

The perovskite structure is, however, only one of a wide-range of AMX₃ structure-types, with perhaps the most closely related being the post-perovskite structure. In contrast to perovskites, post-perovskites contain [MX₆] octahedra that both edge- and corner-share, resulting in two-dimensional anionic [MX₃] layers, rather than a three dimensional framework. These layers are stacked with interstitial A cations positioned between them. Post-perovskites are amongst the most abundant terrestrial minerals, as the

MgSiO₃ perovskite that makes up much of the Earth's lower mantle undergoes a critical high-pressure and temperature phase transition ($P_C \approx 125$ GPa, $T_C \approx 1250$ K) to the post-perovskite structure-type near the mantle-core boundary.^{5,6} Due to the difficulty of reaching these extreme pressures, post-perovskites which form at more accessible pressures and can be recovered on quenching have proved useful analogues. These include the second- and third-row transition metal oxides AMO₃, A = Na, Ca, and M = Pt, Rh, Ir ($P_{\text{syn}} \approx 5$ GPa);⁷⁻¹⁰ and first-row fluorides NaMF₃, M = Mg, Ni, Co, Fe, Zn.¹¹⁻¹⁵ A handful of post-perovskite compounds can even be obtained at ambient conditions: notably CaIrO₃,¹⁶ the post-actinide chalcogenides AMnSe₃ (A = Th, U)¹⁷ and UFeS₃,¹⁸ and TIPbI₃.¹⁹ As a result of this synthetic challenge, systematic tuning of the properties of post-perovskites is much less well explored than for perovskites.

In particular, there are limits on our current understanding of the magnetic properties of post-perovskites, in part because neutron diffraction studies require large sample sizes. This is despite the fact that post-perovskites, unlike perovskites, tend to have non-collinear magnetic structures.^{12,15,16,20} As a result, both the exploration of fundamental properties of post-perovskites and the potential utility of their non-trivial spin textures for spintronic devices^{21,22} or quantum memory storage²³ remains limited.

In contrast to the relative scarcity of atomic post-perovskites, molecular post-perovskites, where X is a molecular anion, are a growing class of materials.²⁴⁻²⁸ Unlike their atomic analogues, the majority of molecular post-perovskites are stable and synthesisable at ambient pressure. Incorporating molecular components in these frameworks can also allow for novel physical properties,

^aSchool of Chemistry, University Park, Nottingham, NG7 2RD, UK. E-mail: matthew.cliffe@nottingham.ac.uk

^bInstitut Laue Langevin, 71 avenue des Martyrs CS 20156, 38042 Grenoble Cedex 9, France

^cAdvanced Materials Research Group, Faculty of Engineering, University of Nottingham, University Park, Nottingham NG7 2RD, UK

† Electronic supplementary information (ESI) available: Additional experimental details for synthesis, single crystal X-ray and neutron diffraction measurements and analysis, powder neutron diffraction measurements and analysis, magnetic measurements, density functional theory calculations; CIFs and mCIFs. CCDC 2224014, 2224044, 2224061, 2224063, 2224065, 2224087, 2224089 and 2224344. For ESI and crystallographic data in CIF or other electronic format see DOI: <https://doi.org/10.1039/d2sc06861c>



arising from the additional degrees of freedom, including non-linear optics,²⁹ electric polarisation^{30,31} and complex spin textures.³²

Metal dicyanamides, $AM(dca)_3$ $dca = N(CN)_2^-$, are the best established family of molecular post-perovskites.^{33–35} The metal ions are separated by five-atom-bridges and tend to be magnetically isolated, with no conclusive evidence of long-range magnetic ordering.^{24,25,36} To explore collective magnetic behaviour in molecular post-perovskite analogues we therefore focussed on ligands capable of propagating stronger super-exchange interactions.

Thiocyanate (NCS^-) is a promising molecular ligand for creating magnetic coordination frameworks with long-range magnetic ordering, even over extended distances.^{37–42} The thiocyanate also has asymmetric reactivity, unlike both atomic ligands and most common molecular ligands, *e.g.* formate or dca^- .⁴³ Applying the hard-soft acid-base principle,⁴⁴ the nitrogen terminus is less polarisable and so coordinates preferentially to harder first-row transition metals, whereas sulfur has more diffuse orbitals, and preferentially coordinates to softer main group second- and third-row transition metals.³⁸ Homoleptic framework structures are thus comparatively rare, beyond the binary $M(NCS)_2$.^{37,38} Nevertheless, there are two reported $AM(NCS)_3$ homoleptic frameworks with the post-perovskite structure: $RbCd(NCS)_3$ ⁴⁵ and $CsNi(NCS)_3$.²⁶

In this work, we study $CsM(NCS)_3$, $M = Ni, Mn$ and Co . We describe the synthesis of $CsMn(NCS)_3$ and $CsCo(NCS)_3$ and determine their structures, by single crystal X-ray diffraction, to be post-perovskites isomorphous with $CsNi(NCS)_3$. We used bulk magnetometry to show that all three order magnetically. $CsNi(NCS)_3$ ($T_C = 8.5(1)$ K) and $CsCo(NCS)_3$ ($T_C = 6.7(1)$ K) order as weak ferromagnets with significant coercive fields, $CsNi(NCS)_3$ $H_C = 0.331(2)$ T and $CsCo(NCS)_3$ $H_C = 0.052(2)$ T, whereas $CsMn(NCS)_3$ orders as an antiferromagnet $T_N = 16.8(8)$ K. We then report neutron diffraction measurements, with single crystal and powder samples. These found $CsNi(NCS)_3$ to be a canted ferromagnet, $\mathbf{k} = (0, 0, 0)$, and $CsMn(NCS)_3$ to be a non-collinear antiferromagnet which orders with $\mathbf{k} = (0, \frac{1}{2}, \frac{1}{2})$ and four sublattices which all order antiferromagnetically. Additionally, DFT calculations were undertaken (see ESI† for details), which confirm the intralayer interactions are at least an order of magnitude stronger than the interlayer interactions in these compounds.

Our results suggest that magnetic molecular frameworks, and thiocyanates in particular, are a promising ground for exploring the magnetism of otherwise challenging to realise structure-types. The non-collinear structures we have uncovered in these thiocyanate frameworks *via* neutron diffraction suggest that further studies of this family may uncover new routes to complex spin textures.

2 Results

2.1 Synthesis and structure

We synthesised $CsNi(NCS)_3$, $CsMn(NCS)_3$ and $CsCo(NCS)_3$ by salt metathesis of the metal sulfate and caesium sulfate with barium thiocyanate in aqueous solution. $CsNi(NCS)_3$ is stable at

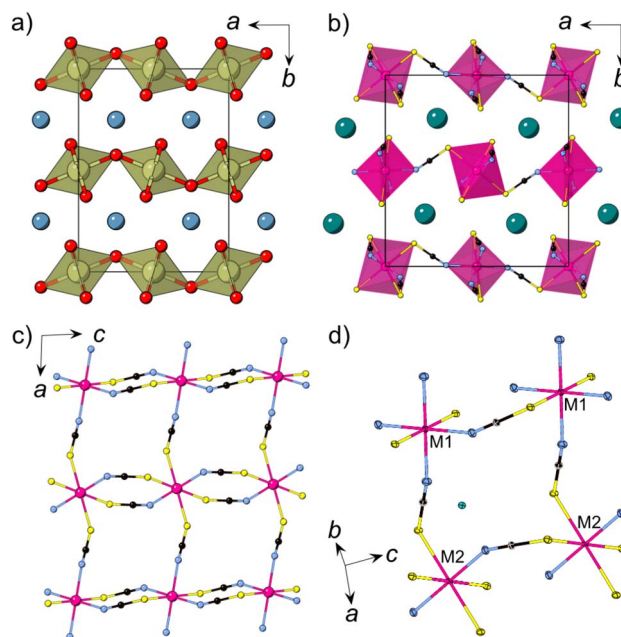


Fig. 1 (a) The structure of $CalrO_3$ with iridium polyhedra connected *via* corner-sharing (a axis) and edge-sharing (c axis) $[IrO_6]$ octahedra, $Ca = blue$, $Ir = brown$, $O = red$. (b) Crystal structure of $CsMn(NCS)_3$ at 120 K obtained from single crystal X-ray diffraction. (c) A single $[Mn(NCS)_3]^-$ layer. (d) Close-up view of the structure highlighting the two chemically independent metal ions (M1, M2). $Cs = green$, $Mn = pink$, $N = blue$, $C = black$, $S = yellow$.

ambient conditions, however $CsMn(NCS)_3$ and $CsCo(NCS)_3$ are sensitive to humidity. Single crystals were obtained through slow evaporation and the structures were determined using single crystal X-ray diffraction to have the monoclinic space group $P2_1/n$, and to crystallise in the post-perovskite structure. We found that, unlike the Ni and Mn analogues, the crystallisation of $CsCo(NCS)_3$ from solution typically occurs in a two step process. Large, deep blue crystals of a second phase, believed to be $Cs_2Co(NCS)_4$, are typically obtained, which recrystallise into small, deep purple single crystals of $CsCo(NCS)_3$ if left undisturbed for several weeks in ambient conditions.

All three compounds are isomorphous and consist of anionic $[M(NCS)_3]$ layers in the ac plane in which the transition metal M^{2+} ions are connected through $\mu_{1,3}NCS$ ligands (Fig. 1c). In between the layers, which are stacked along the b axis, lie the charge balancing caesium counterions. The M^{2+} ions are octahedrally coordinated and there are two crystallographically and chemically distinct metal sites. One transition metal ion (M1, Wyckoff site $2c$) is coordinated by four nitrogen atoms and two sulfur atoms, whilst the second transition metal ion (M2, Wyckoff site $2b$) is bonded to four sulfur and two nitrogen atoms. The metal octahedra corner-share along the a axis and alternate between M1 and M2. Along the c axis, the metal octahedra edge-share, and all the metal sites within an edge-sharing chain are the same.

Moving along the row from manganese to nickel, the average $M-N$ and $M-S$ bond lengths, d_{M-N} and d_{M-S} ,



Table 1 DFT predicted relative energies between the experimental post-perovskite phase ($\text{CsM}(\text{NCS})_3 = \text{pPv}$) and the two known $\text{AM}(\text{NCS})_3$ perovskite structure-types: $\text{CsCd}(\text{NCS})_3 = \text{Cs}[\text{Cd}]$; $(\text{NH}_4)_2\text{-NiCd}(\text{NCS})_6 = \text{NH}_4[\text{NiCd}]$. The perovskite structures were generated by swapping the A site cation for Cs^+ and the B site cation(s) by the appropriate transition metal

M^{2+}	$E(\text{pPv})^a$	$E(\text{Cs}[\text{Cd}])^a$	$E(\text{NH}_4[\text{NiCd}])^a$
Ni	0.0	+90.8	+177.3
Mn	0.0	+84.8	+137.0
Co	0.0	+286.7	+114.5

^a (meV per formula unit).

decrease: $d_{\text{Mn-N}}(13 \text{ K}) = 2.1607(14) \text{ \AA}$, $d_{\text{Co-N}}(120 \text{ K}) = 2.072(3) \text{ \AA}$, $d_{\text{Ni-N}}(15 \text{ K}) = 2.035(5) \text{ \AA}$ and $d_{\text{Mn-S}} = 2.674(3) \text{ \AA}$, $d_{\text{Co-S}} = 2.5652(10) \text{ \AA}$, $d_{\text{Ni-S}} = 2.350(20) \text{ \AA}$. The M–S bond lengths shorten to a greater extent than the M–N bond lengths, likely as a result of the higher polarisability of sulfur. This trend is comparable in other metal thiocyanate frameworks.^{37,46} There are two intralayer M··M distances, between the edge-sharing octahedra ($d_{\text{M1-M1}} = d_{\text{M2-M2}} = c$) and the corner-sharing octahedra ($d_{\text{M1-M2}} = a$). Again, moving from Mn^{2+} to Ni^{2+} , the distances decrease, with $d_{\text{Mn1-Mn1}} = 5.6540(4) \text{ \AA}$ compared to $d_{\text{Co1-Co1}} = 5.57860(11) \text{ \AA}$ and $d_{\text{Ni1-Ni1}} = 5.5409(6) \text{ \AA}$; and $d_{\text{Mn1-Mn2}} = 6.37315(5) \text{ \AA}$, $d_{\text{Co1-Co2}} = 6.30515(5) \text{ \AA}$ and $d_{\text{Ni1-Ni2}} = 6.2631(6) \text{ \AA}$. The interlayer spacing also decreases, with the shortest M··M distances, $d_{\text{M,layer}}$, decreasing from $d_{\text{Mn,layer}} = 7.20052(15) \text{ \AA}$, through $d_{\text{Co,layer}} = 7.18340(10) \text{ \AA}$ to $d_{\text{Ni,layer}} = 7.1050(8) \text{ \AA}$. For the single crystal neutron diffraction measurements of $\text{CsNi}(\text{NCS})_3$, a significantly smaller crystal was used in comparison to the $\text{CsMn}(\text{NCS})_3$, which influences the quality of the reflections, resulting in the larger errors.

In addition to this post-perovskite structure, there are two different perovskite structure-types with composition $\text{AM}(\text{NCS})_3$, $\text{CsCd}(\text{NCS})_3$ ⁴⁵ and $(\text{NH}_4)_2\text{NiCd}(\text{NCS})_6$ (ESI Fig. 7†).⁴⁷ To understand the relative stability of the post-perovskite structure compared to the perovskite-type structures, density functional theory (DFT) calculations were performed. Hypothetical perovskites were generated through atom-swaps, and the geometry optimised relaxation, relative to the experimentally observed post-perovskite structure, was calculated (Table 1). For simplicity, we focused on the spin-ferromagnetic solution of the three different structure-types for this comparison. We found that the post-perovskite structure was more stable than the perovskite structures by around 10 kJ mol^{-1} (0.1 eV per formula unit, approximately $4kT$ at room temperature). This energy is consistent with the observed exclusive formation of the post-perovskite structure, but suggests that more unusual experimental conditions may allow access to the perovskite phases.

2.2 Magnetism

Having synthesised an isostructural series of thiocyanate post-perovskites containing paramagnetic ions, we next sought to understand their magnetic behaviour. We measured the bulk

magnetic susceptibility of each of these compounds, in an applied field of 0.01 T , to determine the magnetic ordering temperature and average interaction strength. We used isothermal magnetisation measurements at 2 K over the range -7 to $+7 \text{ T}$ (-6 to $+6 \text{ T}$ for $\text{M} = \text{Ni}$) to assess the degree of magnetic hysteresis.

The zero-field cooled (ZFC) and field-cooled (FC) susceptibility of $\text{CsNi}(\text{NCS})_3$ diverge below the ordering temperature $T_C = 8.5(1) \text{ K}$ (Fig. 2a). The Curie–Weiss fit of the inverse susceptibility above 180 K gives a value for the Curie–Weiss temperature, θ_{CW} , of $-8.6(8) \text{ K}$. However, this value is particularly sensitive to the fitting temperature range: $\theta_{\text{CW}} = +1.5(4) \text{ K}$ when $100 < T < 300 \text{ K}$, whereas $\theta_{\text{CW}} = -12.7(8) \text{ K}$ for a fit $200 < T < 300 \text{ K}$. This variation is likely due to the presence of significant single-ion anisotropy, typical of Ni^{2+} .^{48,49} The Curie constant, C , is $0.85(2) \text{ emu K mol}^{-1}$, which is lower than the spin only value, $C_{\text{spin only}} = 1 \text{ emu K mol}^{-1}$. The lower than expected Curie constant (ESI Fig. 1†) is likely due to a sample mass error. The isothermal magnetisation of $\text{CsNi}(\text{NCS})_3$ at 2 K shows hysteresis with a coercive field of $H_C = 0.331(2) \text{ T}$ and a remnant magnetisation $M_{\text{rem}} = 0.106(1) \mu_B$ per Ni, implying a canting angle of 6.1° if there are only two distinct spin orientations. Beyond $1.19(1) \text{ T}$, the hysteresis loop closes and there is a magnetic phase transition to a second magnetic phase, reaching a magnetisation of $1.54(1) \mu_B$ per Ni at 6 T .

The magnetic susceptibility of $\text{CsMn}(\text{NCS})_3$ has a cusp at $16.8(8) \text{ K}$ indicating the onset of antiferromagnetic order (Fig. 2b). An increase in susceptibility at low temperature is likely due to a small fraction of a hydrated impurity. Fitting the inverse susceptibility between $100 < T < 300 \text{ K}$ to the Curie–Weiss law gives $\theta_{\text{CW}} = -33.6(2) \text{ K}$, and $C = 3.75(2) \text{ emu K mol}^{-1}$, which is lower than the high-spin spin only expected value of $C_{\text{spin only}} = 4.375 \text{ emu K mol}^{-1}$ for Mn^{2+} . We did not observe any evidence of hysteresis in the isothermal magnetisation data, consistent with antiferromagnetic order. The magnetisation reaches $1.20(6) \mu_B$ per Mn at the largest field measured ($7.00(1) \text{ T}$), well below the spin only saturation magnetisation, $M_{\text{sat.}} = 5 \mu_B$ per Mn, indicative of the presence of significant antiferromagnetic interactions. The ratio of the Curie–Weiss temperature to the ordering temperature is $f = |\theta_{\text{CW}}/T_N| = 2.1$, suggestive of slight frustration or low-dimensionality.

Curie–Weiss fitting of the magnetic susceptibility of $\text{CsCo}(\text{NCS})_3$ between $100 < T < 300 \text{ K}$ suggests predominately antiferromagnetic interactions, $\theta_{\text{CW}} = -19.7(2) \text{ K}$. The large Curie constant, $C = 4.8(2) \text{ emu K mol}^{-1}$, compared to the high-spin spin only value $C_{\text{spin only}} = 1.875 \text{ emu K mol}^{-1}$, indicates that the unquenched orbital moment remains significant in these compounds and the determined θ_{CW} therefore likely also includes the effects of the first order spin–orbit coupling. $d\chi/dT$ shows two sharp minima, suggesting that there are potentially two ordering temperatures for the compound at $6.7(1)$ and $8.4(1) \text{ K}$. The isothermal magnetisation data measured at 2 K show a hysteresis with $H_C = 0.052(2) \text{ T}$ and a remnant magnetisation $M_{\text{rem}} = 0.400(1) \mu_B$ per Co, suggesting a canting angle of 15.3° . The hysteresis disappears at $1.86(1) \text{ T}$, when $M = 0.88(4) \mu_B$ per Co. Above this applied magnetic field, the magnetisation steadily increases, reaching $2.00(7) \mu_B$ per Co at $7.00(1) \text{ T}$,



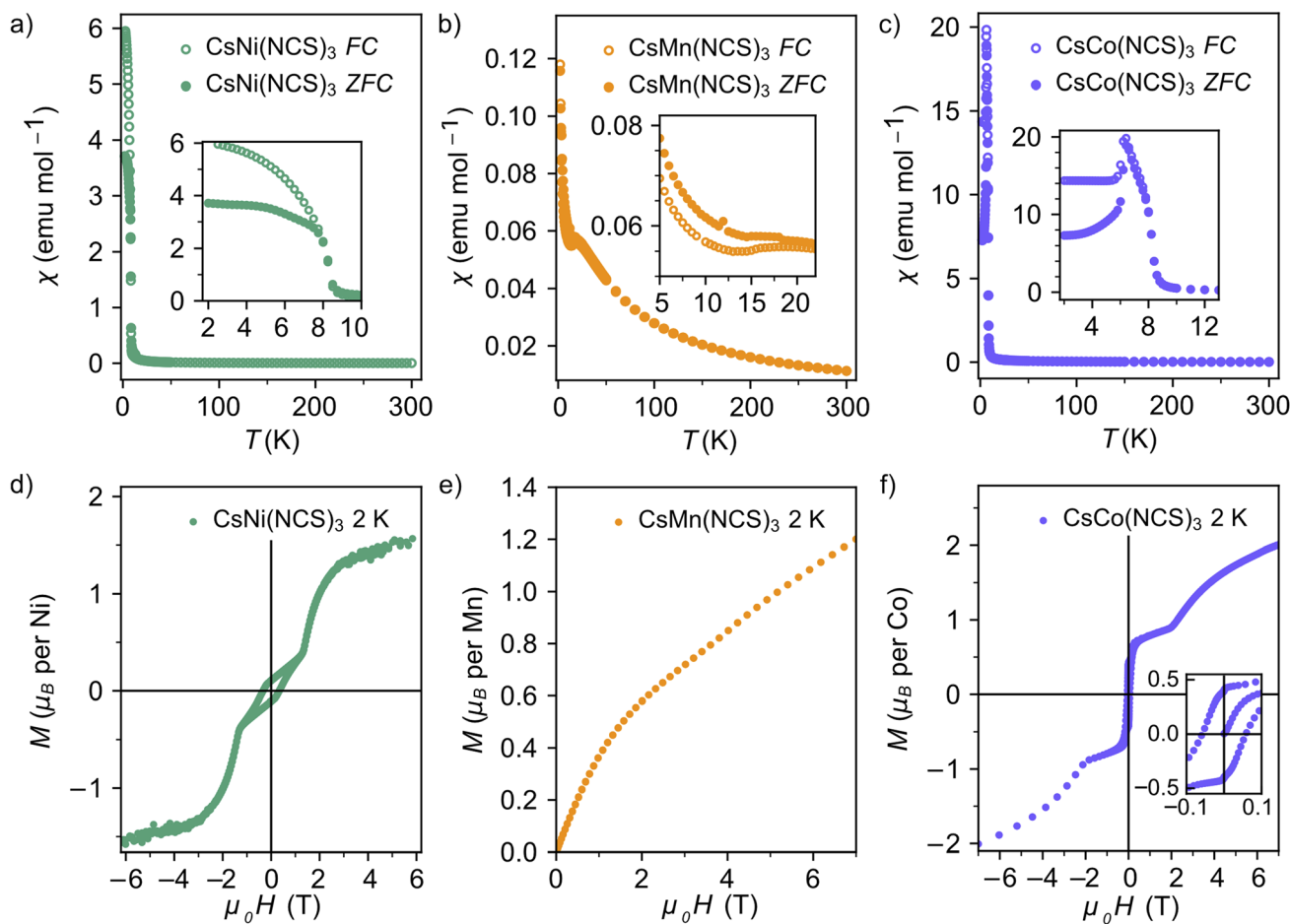


Fig. 2 Magnetic susceptibility data with an applied field of 0.01 T for (a) CsNi(NCS)₃; (b) CsMn(NCS)₃; (c) CsCo(NCS)₃; and isothermal magnetisation measurements at 2 K for (d) CsNi(NCS)₃ (field -6 to +6 T); (e) CsMn(NCS)₃ (field 0 to +7 T); and (f) CsCo(NCS)₃ (field -7 to +7 T).

although the moment remains unsaturated, due to a combination of single-ion anisotropy and antiferromagnetic interactions.

Our bulk magnetic property measurements suggested that both CsNi(NCS)₃ and CsCo(NCS)₃ are weak ferromagnets (canted antiferromagnets), or more generally have uncompensated magnetic moments, with appreciable hystereses and field-induced magnetic phase transitions. Comparatively, the absence of hysteresis and a negative θ_{CW} for CsMn(NCS)₃ suggests it is an antiferromagnet.

2.3 Neutron diffraction

To explore the magnetic properties of these post-perovskites further, we therefore carried out neutron diffraction experiments, both single crystal and powder, to determine their ground state magnetic structures. Scale-up of our initial synthetic routes produced high quality powder and single crystal samples of CsNi(NCS)₃ and CsMn(NCS)₃ suitable for neutron diffraction, however the two-stage synthesis of CsCo(NCS)₃ meant we were unable to obtain either large (mm³) single crystals or gram-scale pure phase microcrystalline powders, precluding neutron studies for this compound.

We carried out single crystal neutron diffraction measurements of CsNi(NCS)₃ (1.8 × 0.9 × 0.3 mm³) using the D19 diffractometer at the Institut Laue Langevin (ILL). A low temperature data collection at 2 K, below the ordering temperature of 8.5 K, allowed us to determine the propagation vector to be $\mathbf{k} = (0, 0, 0)$ by indexing of the magnetic Bragg reflections. We combined these single crystal neutron diffraction (SCND) data with additional powder neutron diffraction (PND) data collected on a polycrystalline sample (1.1 g) using the powder neutron diffractometer D1b (ILL). The magnetic space groups with maximal symmetry which permit magnetic moments to exist on the two Ni²⁺ ions were determined using the Bilbao Crystallographic Server⁵⁰⁻⁵² to be $P2_1'/c'$ and $P2_1/c$ (BNS notation).⁵¹ Both of these models have the same unit cell as the nuclear structure. We then refined models in each space group against the combined PND and SCND data with a multi-pattern refinement and found that only $P2_1/c$ was able to model the additional intensity arising from the magnetic reflections. This refined structure shows weak ferromagnetic order with two unique magnetic sites, corresponding to the two crystallographic Ni²⁺ ions (Ni1 and Ni2) in the nuclear structure. The two moments have a magnitude of 2.01(3) μ_B and were constrained to refine together with a negative correlation. The moments are



directed predominately along the c axis with the canting only present along the b axis. The Ni1 moments (purple arrows Fig. 3) are canted at an angle of 162° along the $-b$ direction, whilst the Ni2 moments (green arrows Fig. 3) are canted at an angle of 105° in the $+b$ direction. The asymmetric canting of the two sublattices results in a net magnetisation of $0.116 \mu_B$ per Ni along the b axis ($+b$ direction). This is equivalent to a single Ni^{2+} canting at an angle of 6.7° , which is in agreement with the magnetometry data. The magnetic moment of Ni1 and Ni2 present a relative tilt of 136° between them.

We found that when subtracting the 2 K PND data from the 10 K data, there are some nuclear peaks which do not directly overlap at the two temperatures. This is particularly evident in the (020) and (200) reflections, which are the most intense in the diffraction patterns (Fig. 3c). On heating from 2 to 10 K, the a axis increases by 0.028%, whereas the b axis decreases in length by 0.019%. In contrast, the c axis remains constant within this temperature range (ESI Fig. 6†).

We were also able to measure a large single crystal of $CsMn(NCS)_3$ ($6.3 \times 2.5 \times 1.1 \text{ mm}^3$) using D19 (ILL). We found in our diffraction data collected at 2 K, below $T_N = 16.8 \text{ K}$, a number of additional Bragg reflections (2938 unique

reflections) not present in our data collected at 20 K, which could not be indexed to the nuclear structure. We were able to index these additional magnetic Bragg reflections with $\mathbf{k} = \left(0, \frac{1}{2}, \frac{1}{2}\right)$. Using the Bilbao Crystallographic Server we determined the possible magnetic space groups for this propagation vector to be $P_5\bar{1}$ and P_51 . We solved the magnetic structures in both magnetic space groups, with the $P_5\bar{1}$ better fitting the experimental data. The model comprises of four unique magnetic sites: Mn1a and Mn1b, which arise from nuclear site Mn1 but are in alternate layers (red and orange arrows Fig. 4c), and Mn2a and Mn2b from nuclear site Mn2 (dark and light blue arrows Fig. 4c). The magnetic unit cell is related to the nuclear cell as follows $a_{\text{mag}} = a_{\text{nuc}}$, $b_{\text{mag}} = 2b_{\text{nuc}}$ and $c_{\text{mag}} = 2c_{\text{nuc}}$. The magnitude of the moments for all Mn sites is $4.63(9) \mu_B$ and were constrained to refine with a single moment value. We found that allowing the moments to refine freely did not significantly improve our fit (constrained refinement, $\chi^2 = 68.5$ compared to free refinement, $\chi^2 = 56.7$), and led to unphysically small moment sizes and unstable moment angles. Constraining the moment angles of Mn1b and Mn2b to be collinear (while allowing Mn1a and Mn2a to be non-

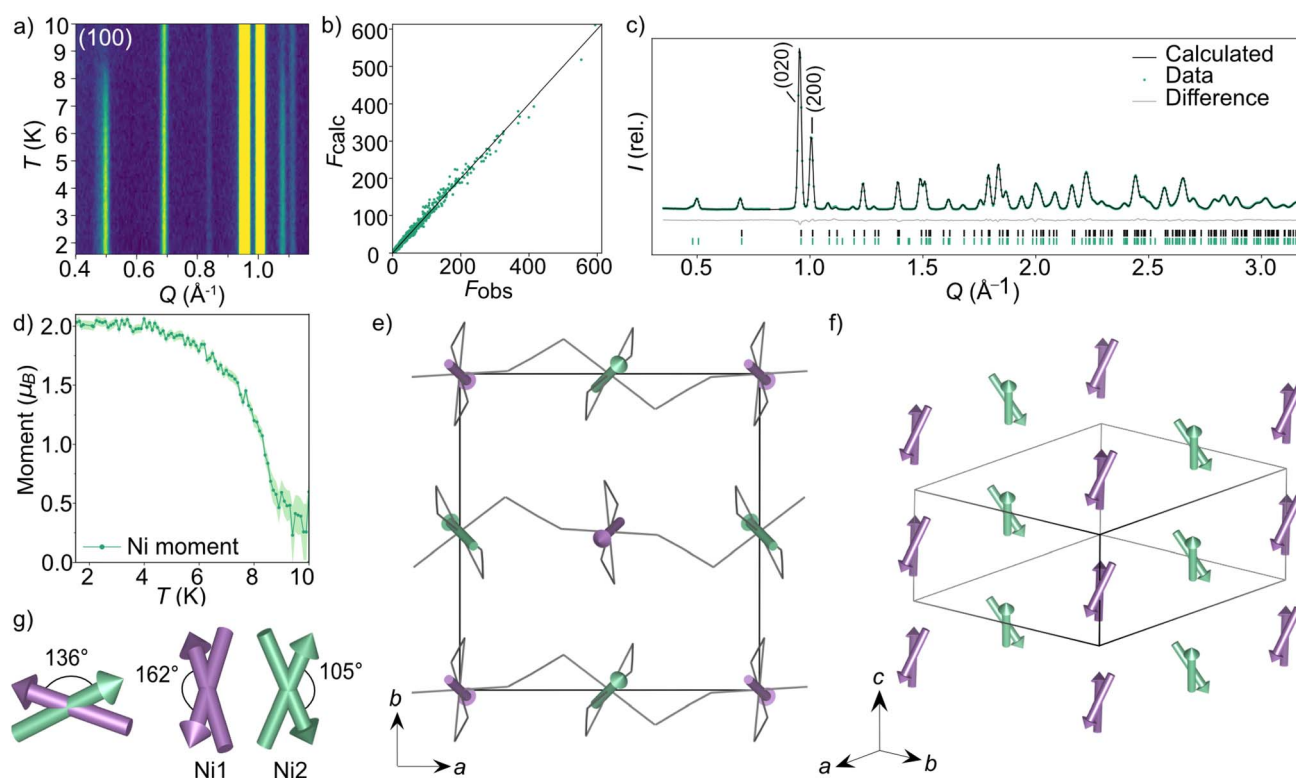


Fig. 3 Neutron diffraction data and the magnetic structure for $CsNi(NCS)_3$. (a) Thermodiffractogram measured between 1.5 and 10 K on the D1b diffractometer (ILL). The most intense magnetic Bragg reflection is indexed as the (100) planes. The F_{obs} against F_{calc} plot obtained from D19 data fit (nuclear and magnetic) collected at 1.8 K (b) and Rietveld fit obtained from D1b data fit at 1.5 K (c) for the multi pattern refinement of the $P2_1/c$ magnetic model describing the magnetic structure of $CsNi(NCS)_3$. (d) The magnetic moment of the Ni^{2+} ions as a function of temperature obtained by Rietveld refinements of the data collected at each temperature point between 1.5 and 10 K. (e) The magnetic structure of $CsNi(NCS)_3$ viewed down the c axis. The two unique magnetic vectors are represented with purple arrows (Ni1) and green arrows (Ni2). The Cs^+ cations have been omitted for clarity and the thiocyanate ligands are represented as a wire frame. (f) The magnetic structure viewed down the [111] direction. (g) Angles describing the non-collinearity of the moments.



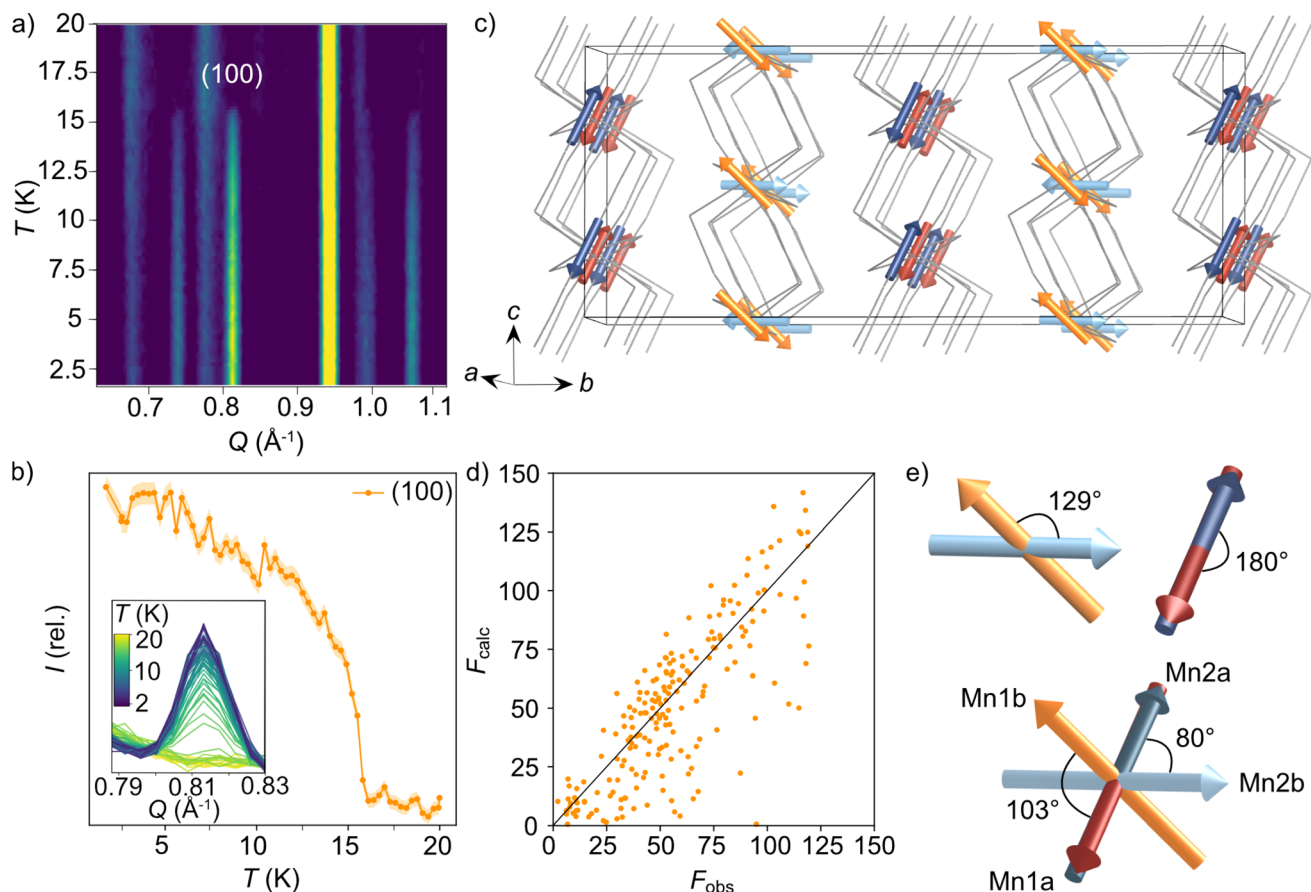


Fig. 4 Neutron diffraction data used to determine the magnetic structure for CsMn(NCS)_3 . (a) Thermodiffractogram measured between 1.5 and 20 K on the D1b diffractometer (ILL). The most intense magnetic Bragg reflection is indexed as the (100) planes. (b) The integrated intensity of the (100) magnetic reflection at 0.81 \AA^{-1} as a function of temperature. (c) The magnetic structure of CsMn(NCS)_3 . The magnetic vectors are depicted with red and orange arrows for Mn1 (red = Mn1a and orange = Mn1b) and blue arrows for Mn2 (dark = Mn2a and light = Mn2b). The Cs^+ cations have been omitted for clarity and the thiocyanate ligands are represented as a wire frame. (d) F_{obs} against F_{calc} for the refinement of the $P2_1$ magnetic model using the magnetic reflections observed at 2 K with the D19 diffractometer (ILL). (e) The angles between the magnetic vectors.

collinear) gave $\chi^2 = 120.3$, whilst constraining all four moments to be collinear gave $\chi^2 = 807.6$. In the determined model, each of the four magnetic sublattices, derived from a unique Mn^{2+} site, order antiferromagnetically as expected from the bulk antiferromagnetic order observed in the magnetisation data. Mn1a and Mn2a moments, are aligned antiparallel within the anionic layer, while Mn1b and Mn2b are at an angle of 103° relative to each other (Fig. 4e). Powder neutron diffraction data were collected on the D1b diffractometer, which clearly shows the additional magnetic Bragg reflections. However, the limited data quality prevented quantitative refinement of these data.

2.4 Density functional theory calculations

Our neutron analysis provided the ground states, but the energetics which yield these states remained opaque. We therefore turned to DFT calculations. In order to correct for the typical delocalisation errors encountered in DFT, a Hubbard U was incorporated.^{38,53} There are four nearest-neighbour interactions (Fig. 5): J_a , through the M1–NCS–M2 corner-sharing bridge; J_{c1} , through the M1–NCS–M1 edge-sharing chain; J_{c2} , through the M2–NCS–M2 edge-sharing chain; and J_b , between

the layers. The magnetic lattice therefore consists of rectangular lattices in which there are two different kinds of chain along one direction, which are then coupled together by J_b . Due to the

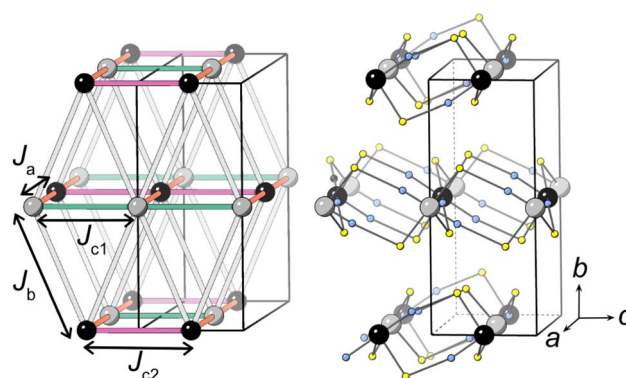


Fig. 5 The four nearest-neighbour magnetic interactions in CsMn(NCS)_3 . M1 and M2 are grey and black respectively and the thiocyanate ligands are represented with sulfur (yellow) and nitrogen (blue) atoms only. Caesium cations and carbon atoms have been removed for clarity.

Table 2 DFT-derived superexchange energy, J_x , as defined in eqn (1) for $\text{CsM}(\text{NCS})_3$, $M = \text{Ni}, \text{Mn}$

M^{2+}	J_a^a	J_b^a	J_{c1}^a	J_{c2}^a
Ni	0.19(4)	-0.02(10)	-0.13(7)	-0.25(7)
Mn	0.78(3)	0.03(6)	2.40(6)	1.79(6)

^a (meV).

offset of the layers, this means that if J_a, J_{c1} and J_{c2} are antiferromagnetic, we would expect this lattice to be frustrated. To calculate each of these interactions we therefore constructed eight $2 \times 1 \times 1$ supercells with distinct ordering patterns (ESI Table 1†), and fitted their DFT+ U energies to the following Hamiltonian:

$$E = \sum_{ij} J_{ij} S_i \cdot S_j + E_0 \quad (1)$$

where J_{ij} denotes the superexchange interaction for the atom pair ij (*i.e.* each interaction is counted once), $|S| = 1$, and E_0 is the energy of a hypothetical non-magnetic state. We found that for $\text{CsNi}(\text{NCS})_3$ and $\text{CsMn}(\text{NCS})_3$ we could obtain self-consistent results, but we were unable to achieve acceptable self-consistency for $\text{CsCo}(\text{NCS})_3$. The residual unquenched orbital moment for the 4T_1 ground state is likely responsible for this and suggests that higher level calculations are likely to be required to appropriately capture the magnetic behaviour of this compound.

Our calculations indicate that all four interactions are antiferromagnetic for $\text{CsMn}(\text{NCS})_3$, with the interactions through the edge-sharing chains (J_{c1} and J_{c2}) stronger than the corner-sharing bridge (J_a) between them (Table 2). The magnitude of the J_b interaction is much smaller than the error and is thus not meaningful. We found that $\text{CsNi}(\text{NCS})_3$ has ferromagnetic interactions within the edge-sharing chains, with the J_{c2} chain notably stronger, and the interactions between chains are antiferromagnetic. As with $\text{CsMn}(\text{NCS})_3$, the J_b interaction is small and zero within error. From these interactions we were able to calculate Curie-Weiss temperatures: for Mn $\theta_{\text{CW,calc.}} = -22.3(5)$ K and for Ni $\theta_{\text{CW,calc.}} = -0.05(65)$ K which are broadly comparable with those found experimentally. The ground states predicted by DFT are largely consistent with those determined experimentally, allowing for the fact that these non-relativistic calculations cannot predict spin-canting.

3 Discussion

The $\text{CsM}(\text{NCS})_3$ compounds all crystallise with the post-perovskite structure. However, unlike most atomic analogues, these thiocyanate compounds adopt the structure at ambient pressure. A common characteristic of atomic post-perovskites is the presence of large octahedral tilt angles in the corresponding perovskite phase, which leaves them more susceptible to undergo the post-perovskite phase transition.¹¹ Thiocyanate perovskites are already very tilted, due to the shape of the frontier bonding orbitals, which could explain the ease for

formation of this structure-type for $\text{CsM}(\text{NCS})_3$.³⁸ Defining the plane as the ac axes, the tilting occurring in these thiocyanate compounds along the edge- and corner-sharing directions can be compared. The corner-sharing octahedra, along the a axis, have smaller deviations away from the ac plane, with angles of $\angle ac\text{-M-S} = 42(1)^\circ$ and $\angle ac\text{-M-N} = 9(1)^\circ$ (ESI Fig. 9†). Along the c axis, the edge-sharing octahedra adopt greater tilting angles as an inherent consequence of having two thiocyanate ligands bridging each pair of metal centres in this direction. The deviation away from the ac plane is $\angle ac\text{-M-S} = 58(1)^\circ$ and $\angle ac\text{-M-N} = 36(1)^\circ$. The incorporation of a molecular ligand permits access to this greater degree of tilting without the need for external pressure. This is evident from our DFT calculations which show that for these $\text{CsM}(\text{NCS})_3$ compounds the post-perovskite structure-type is lower energy than other reported thiocyanate perovskite-type structures (Table 1).

Our magnetometry and neutron diffraction measurements show that the compounds magnetically order between 6 and 16 K, significantly lower than the closest chemical analogues, the binary thiocyanates $\text{M}(\text{NCS})_2$ $M = \text{Mn}, \text{Fe}, \text{Co}, \text{Ni}, \text{Cu}$,^{37,38} which order at $T_N = 29$ K for $\text{Mn}(\text{NCS})_2$, $T_N = 20$ K for $\text{Co}(\text{NCS})_2$ ^{37,42} and $T_N = 54$ K for $\text{Ni}(\text{NCS})_2$.^{37,41} The atomic post-perovskites have a range in ordering temperatures, with the fluorides ordering at similar temperatures to $\text{CsM}(\text{NCS})_3$, for example post-perovskite NaNiF_3 orders at $T_N = 22$ K (compared to $T_C = 156$ K for the perovskite phase).¹² The reported ordering temperatures of the oxide post-perovskites are an order of magnitude larger, for example CaIrO_3 has $T_N = 115$ K,^{8,54,55} likely as the oxides lie closer to the metal-insulator boundary.

One key difference between $\text{CsM}(\text{NCS})_3$ and $\text{M}(\text{NCS})_2$ is that the post-perovskites only have three-atom connections between transition metals ($\mu_{1,3}\text{NCS}$ coordination mode), whereas $\text{M}(\text{NCS})_2$ have both one-atom and three-atom connections ($\mu_{1,3,3}\text{NCS}$). The additional M-S-M superexchange pathway in the binary thiocyanates likely strengthens the magnetic interactions in the binary thiocyanates, although DFT calculations of $\text{Cu}(\text{NCS})_2$ suggest that interactions through the M-S-C-N-M can be as strong or stronger than through M-S-M bridges.³⁸ Our DFT calculations further support this, showing appreciable superexchange through the end-to-end bridging thiocyanates.

In contrast to these compounds, dca⁻ based post-perovskites containing magnetic ions do not appear to order.^{24,25,36} The transition metals in these compounds are separated by six bonds and $d(\text{Mn-NCNCN-Mn}) = 8.9825(4)$ Å ($[\text{Ph}_4\text{P}]\text{Mn}(\text{dca})_3$),²⁴ compared to four bonds and $d(\text{Mn-NCS-Mn}) = 6.37315(5)$ Å ($\text{CsMn}(\text{NCS})_3$). This likely reduces the superexchange further. However, $\text{Cr}[\text{Bi}(\text{SCN})_6]$, with even longer superexchange pathways does order at $T_N = 4.0$ K,³⁹ indicating that orbital overlap and orbital energy matching are also playing a key role in this.

$\text{CsM}(\text{NCS})_3$, $M = \text{Ni}, \text{Mn}, \text{Co}$, all adopt non-collinear magnetic structures. Non-collinearity also appears to be typical in the atomic perovskites. The only previous experimentally reported magnetic structure of a post-perovskite is of CaIrO_3 , which used magnetic resonant X-ray scattering to reveal a canted stripe antiferromagnetic ground state.¹⁶ Octahedral tilting is predicted to be a key parameter in determining the degree of non-collinearity,⁵⁶ so it is expected that the post-



perovskite structures are sensitive to this factor as well. Analysis of our isothermal magnetisation data for CsNi(NCS)₃ (Fig. 2d), assuming that there is only a single magnetic site (*i.e.* only two distinct spin orientations), gives a canting angle of 6°. However our magnetic structure has two magnetic sites (*i.e.* four spin orientations), and so there are in fact three ‘canting angles’, all of which are larger than 6° (9°, 22°, and 38°). The symmetry constraints of the *P*₂₁/*c* magnetic space group means that for each pair of canted moments (*i.e.* a single magnetic site), the components of the magnetic moments along the *a* and *c* axes will be of equal magnitude and so the uncompensated magnetisation lies only along the *b* axis. In CsNi(NCS)₃, the uncompensated moments from each magnetic site have opposite signs: +0.80 μ_B per Ni2 and −0.57 μ_B per Ni1, with a net moment of +0.114 μ_B. Using bulk measurements for materials with complex magnetic structures can therefore lead to underestimates of the degree of non-collinearity.

The magnetic structure of CsMn(NCS)₃, unlike the nickel and cobalt analogues, orders as an antiferromagnet. The neutron data reveal a $\mathbf{k} = \left(0, \frac{1}{2}, \frac{1}{2}\right)$ propagation vector, which leads to four unique sublattices. As a result of the antifercentring translation in the *P*₃₁ magnetic space group, each sublattice, and therefore the overall structure, is antiferromagnetic. There are two distinct kinds of layer within the magnetic structure, ‘A’ and ‘B’. Layer A, containing Mn1a and Mn2a, is antiferromagnetically correlated; but Mn1b and Mn2b in layer B are non-collinear both with respect to each other and also to Mn1a and Mn2a. The complexity of this structure is perhaps surprising, considering the relative simplicity of the nuclear structure and the lack of spin–orbit coupling expected for high spin Mn²⁺. The layers stack so that each consecutive layer is offset by *c*_{nuc}/2, resulting in a triangular relationship between the interlayer moments (Fig. 5). This layered stacking pattern may generate frustration, which could explain the observed non-collinear structure.

4 Conclusion

In this paper, we have reported the synthesis, structure, magnetometry, single crystal and powder neutron diffraction data for three isomorphous post-perovskite thiocyanate frameworks, CsM(NCS)₃ M = Ni, Mn, Co. Our magnetic susceptibility measurements show that all the materials magnetically order, CsNi(NCS)₃ *T*_C = 8.5(1) K, CsMn(NCS)₃ *T*_N = 16.8(8) K and CsCo(NCS)₃ *T*_C = 6.7(1) K. Our neutron diffraction experiments on CsNi(NCS)₃ and CsMn(NCS)₃ revealed both compounds have complex non-collinear ordering.

CsNi(NCS)₃ orders as a weak ferromagnet with two magnetically distinct nickel moments. CsMn(NCS)₃, on the other hand, orders as an antiferromagnet with a magnetic unit cell which is doubled along the nuclear *b* and *c* axes, and has four unique sublattices.

Our neutron diffraction studies have shown that despite the relative simplicity of the chemical structures, these thiocyanate post-perovskites are a rich source of unusual magnetic orderings which cannot be recognised through magnetometry data

alone. Introducing molecular ligands into framework structures may therefore provide a host of unexpected and complex spin textures, motivating both future synthetic and neutron diffraction investigations.

Data availability

Research data and analysis notebooks are available at the Nottingham Research Data Management Repository DOI: <https://doi.org/10.17639/nott.7259>. Raw data sets from ILL experiments can be accessed *via* links provided in references.

Author contributions

M. G. and M. J. C. synthesised the samples; carried out the magnetic measurements and the single crystal X-ray experiments; M. G., L. C. D. and M. J. C. carried out the single crystal X-ray analysis; M. G., J. Y. L., O. F., L. C. D. and M. J. C. carried out the neutron diffraction experiments; M. G., O. F., L. C. D. and M. J. C. carried out the neutron diffraction and magnetic property analysis; S. L. carried out the density functional calculations; M. G., L. C. D. and M. J. C. wrote the paper with contributions from all the authors.

Conflicts of interest

No conflicts of interest to declare.

Acknowledgements

M. G. acknowledges the ILL Graduate School for provision of a studentship. M. J. C. acknowledges the School of Chemistry, University of Nottingham for support from Hobday bequest. We acknowledge the ILL for beamtime under proposal numbers 5-41-1060,⁵⁷ 5-12-344,⁵⁸ 5-31-2767,⁵⁹ 5-31-2816.⁶⁰ Magnetic measurements were carried out in part using the Advanced Materials Characterisation Suite, funded by EPSRC Strategic Equipment Grant EP/M000524/1. S. L. acknowledges the use of the Sulis supercomputer through the HPC Midlands+ Consortium, and the ARCHER2 supercomputer through membership of the UK's HPC Materials Chemistry Consortium, which are funded by EPSRC grant numbers EP/T022108/1 and EP/R029431/1, respectively.

Notes and references

- P. Vishnoi, J. L. Zuo, T. A. Strom, G. Wu, S. D. Wilson, R. Seshadri and A. K. Cheetham, *Angew. Chem., Int. Ed.*, 2020, **59**, 8974–8981.
- A. Jaffe, S. A. Mack, Y. Lin, W. L. Mao, J. B. Neaton and H. I. Karunadasa, *Angew. Chem., Int. Ed.*, 2020, **59**, 4017–4022.
- A. Kojima, K. Teshima, Y. Shirai and T. Miyasaka, *J. Am. Chem. Soc.*, 2009, **131**, 6050–6051.
- J. Xu, X. Li, J. Xiong, C. Yuan, S. Semin, T. Rasing and X. Bu, *Adv. Mater.*, 2020, **32**, 1806736.
- A. R. Oganov and S. Ono, *Nature*, 2004, **430**, 445–448.



- 6 M. Murakami, K. Hirose, K. Kawamura, N. Sata and Y. Ohishi, *Science*, 2004, **304**, 855–858.
- 7 K. Ohgushi, Y. Matsushita, N. Miyajima, Y. Katsuya, M. Tanaka, F. Izumi, H. Gotou, Y. Ueda and T. Yagi, *Phys. Chem. Miner.*, 2008, **35**, 189–195.
- 8 K. Yamaura, Y. Shirako, H. Kojitani, M. Arai, D. P. Young, M. Akaogi, M. Nakashima, T. Katsumata, Y. Inaguma and E. Takayama-Muromachi, *J. Am. Chem. Soc.*, 2009, **131**, 2722–2726.
- 9 F. Rodi and D. Babel, *Z. Anorg. Allg. Chem.*, 1965, **336**, 17–23.
- 10 M. Bremholm, S. Dutton, P. Stephens and R. Cava, *J. Solid State Chem.*, 2011, **184**, 601–607.
- 11 C. D. Martin, W. A. Crichton, H. Liu, V. Prakapenka, J. Chen and J. B. Parise, *Am. Mineral.*, 2006, **91**, 1703–1706.
- 12 Y. Shirako, Y. Shi, A. Aimi, D. Mori, H. Kojitani, K. Yamaura, Y. Inaguma and M. Akaogi, *J. Solid State Chem.*, 2012, **191**, 167–174.
- 13 D. P. Dobson, S. A. Hunt, A. Lindsay-Scott and I. G. Wood, *Phys. Earth Planet. Inter.*, 2011, **189**, 171–175.
- 14 A. Lindsay-Scott, D. Dobson, F. Nestola, M. Alvaro, N. Casati, C. Liebske, K. S. Knight, R. I. Smith and I. G. Wood, *J. Appl. Crystallogr.*, 2014, **47**, 1939–1947.
- 15 F. L. Bernal, K. V. Yusenko, J. Sottmann, C. Drathen, J. Guignard, O. M. Løvvik, W. A. Crichton and S. Margadonna, *Inorg. Chem.*, 2014, **53**, 12205–12214.
- 16 K. Ohgushi, J.-i. Yamaura, H. Ohsumi, K. Sugimoto, S. Takeshita, A. Tokuda, H. Takagi, M. Takata and T.-h. Arima, *Phys. Rev. Lett.*, 2013, **110**, 217212.
- 17 I. Ijjaali, K. Mitchell, F. Q. Huang and J. A. Ibers, *J. Solid State Chem.*, 2004, **177**, 257–261.
- 18 H. Noël and J. Padiou, *Acta Crystallogr., Sect. B: Struct. Crystallogr. Cryst. Chem.*, 1976, **32**, 1593–1595.
- 19 W. Lin, J. He, K. M. McCall, C. C. Stoumpos, Z. Liu, I. Hadar, S. Das, H. Wang, B. Wang, D. Y. Chung, B. W. Wessels and M. G. Kanatzidis, *Adv. Funct. Mater.*, 2021, **31**, 2006635.
- 20 N. A. Bogdanov, V. M. Katukuri, H. Stoll, J. van den Brink and L. Hozoi, *Phys. Rev. B: Condens. Matter Mater. Phys.*, 2012, **85**, 235147.
- 21 F. Jia, S. Hu, S. Xu, H. Gao, G. Zhao, P. Barone, A. Stroppa and W. Ren, *J. Phys. Chem. Lett.*, 2020, **11**, 5177–5183.
- 22 Y. Tokura and N. Kanazawa, *Chem. Rev.*, 2021, **121**, 2857–2897.
- 23 S. Li, Y. Wang, Y. Wang, S. Sanvito and S. Hou, *J. Phys. Chem. C*, 2021, **125**, 6945–6953.
- 24 J. W. Raebiger, J. L. Manson, R. D. Sommer, U. Geiser, A. L. Rheingold and J. S. Miller, *Inorg. Chem.*, 2001, **40**, 2578–2581.
- 25 P. M. van der Werff, S. R. Batten, P. Jensen, B. Moubaraki and K. S. Murray, *Inorg. Chem.*, 2001, **40**, 1718–1722.
- 26 M. Fleck, *Acta Crystallogr., Sect. C: Cryst. Struct. Commun.*, 2004, **60**, i63–i65.
- 27 M. Maćzka, A. Gaćgor, M. Ptak, D. Stefańska and A. Sieradzki, *Phys. Chem. Chem. Phys.*, 2018, **20**, 29951–29958.
- 28 S.-S. Wang, R.-K. Huang, X.-X. Chen, W.-J. Xu, W.-X. Zhang and X.-M. Chen, *Cryst. Growth Des.*, 2019, **19**, 1111–1117.
- 29 H. Triki, B. Nagy, J. Overgaard, F. Jensen and S. Kamoun, *Struct. Chem.*, 2020, **31**, 103–114.
- 30 H. L. Boström, M. S. Senn and A. L. Goodwin, *Nat. Commun.*, 2018, **9**, 1–7.
- 31 J. Y. Lee, S. Ling, S. P. Argent, M. S. Senn, L. Cañadillas-Delgado and M. J. Cliffe, *Chem. Sci.*, 2021, **12**, 3516.
- 32 F. Lou, T. Gu, J. Ji, J. Feng, H. Xiang and A. Stroppa, *npj Comput. Mater.*, 2020, **6**, 114.
- 33 M. Biswas, S. R. Batten, P. Jensen and S. Mitra, *Aust. J. Chem.*, 2006, **59**, 115.
- 34 H.-T. Wang, L. Zhou and X. Wang, *Acta Crystallogr., Sect. C: Struct. Chem.*, 2015, **71**, 717–720.
- 35 S.-S. Wang, X.-X. Chen, B. Huang, R.-K. Huang, W.-X. Zhang and X.-M. Chen, *CCS Chem.*, 2019, **1**, 448–454.
- 36 P. M. van der Werff, S. R. Batten, P. Jensen, B. Moubaraki, K. S. Murray and E. H.-K. Tan, *Polyhedron*, 2001, **20**, 1129–1138.
- 37 E. N. Bassey, J. A. M. Paddison, E. N. Keyzer, J. Lee, P. Manuel, I. da Silva, S. E. Dutton, C. P. Grey and M. J. Cliffe, *Inorg. Chem.*, 2020, **59**, 11627–11639.
- 38 M. J. Cliffe, J. Lee, J. A. M. Paddison, S. Schott, P. Mukherjee, M. W. Gaultois, P. Manuel, H. Sirringhaus, S. E. Dutton and C. P. Grey, *Phys. Rev. B*, 2018, **97**, 144421.
- 39 M. J. Cliffe, O. Fabelo and L. Cañadillas-Delgado, *CrystEngComm*, 2022, **24**, 7250–7254.
- 40 S. Baran, A. Hoser, M. Rams, S. Ostrovsky, T. Neumann, C. Näther and Z. Tomkowicz, *J. Phys. Chem. Solids*, 2019, **130**, 290–297.
- 41 G. C. DeFotis, K. D. Dell, D. J. Krovich and W. W. Brubaker, *J. Appl. Phys.*, 1993, **73**, 5386–5388.
- 42 E. Shurdha, S. H. Lapidus, P. W. Stephens, C. E. Moore, A. L. Rheingold and J. S. Miller, *Inorg. Chem.*, 2012, **51**, 9655–9665.
- 43 M. Boča, I. Svoboda, F. Renz and H. Fuess, *Acta Crystallogr., Sect. C: Cryst. Struct. Commun.*, 2004, **60**, m631–m633.
- 44 R. G. Pearson, *J. Am. Chem. Soc.*, 1963, **85**, 3533–3539.
- 45 G. Thiele and D. Messer, *Z. Anorg. Allg. Chem.*, 1980, **464**, 255–267.
- 46 J. Palion-Gazda, B. Machura, F. Lloret and M. Julve, *Cryst. Growth Des.*, 2015, **15**, 2380–2388.
- 47 K.-P. Xie, W.-J. Xu, C.-T. He, B. Huang, Z.-Y. Du, Y.-J. Su, W.-X. Zhang and X.-M. Chen, *CrystEngComm*, 2016, **18**, 4495–4498.
- 48 S. Liu, B.-W. Wang, Z.-M. Wang and S. Gao, *Dalton Trans.*, 2018, **47**, 11925–11933.
- 49 S. P. M. Curley, R. Scatena, R. C. Williams, P. A. Goddard, P. Macchi, T. J. Hicken, T. Lancaster, F. Xiao, S. J. Blundell, V. Zapf, J. C. Eckert, E. H. Krenkel, J. A. Villa, M. L. Rhodehouse and J. L. Manson, *Phys. Rev. Mater.*, 2021, **5**, 034401.
- 50 M. I. Aroyo, J. M. Perez-Mato, D. Orobengoa, E. Tasci, G. de la Flor and A. Kirov, *Bulg. Chem. Commun.*, 2011, **43**, 183–197.
- 51 S. V. Gallego, E. S. Tasci, G. de la Flor, J. M. Perez-Mato and M. I. Aroyo, *J. Appl. Crystallogr.*, 2012, **45**, 1236–1247.
- 52 J. Perez-Mato, S. Gallego, E. Tasci, L. Elcoro, G. de la Flor and M. Aroyo, *Annu. Rev. Mater. Res.*, 2015, **45**, 217–248.
- 53 Y. Wu, W. Sun, S. Liu, B. Wang, C. Liu, H. Yin and Z. Cheng, *Nanoscale*, 2021, **13**(39), 16564–16570.











- 54 K. Ohgushi, H. Gotou, T. Yagi, Y. Kiuchi, F. Sakai and Y. Ueda, *Phys. Rev. B: Condens. Matter Mater. Phys.*, 2006, **74**, 241104.
- 55 Y. Shirako, H. Satsukawa, H. Kojitani, T. Katsumata, M. Yoshida, Y. Inaguma, K. Hiraki, T. Takahashi, K. Yamaura, E. Takayama-Muromachi and M. Akaogi, *J. Phys.: Conf. Ser.*, 2010, **215**, 012038.
- 56 C. Weingart, N. Spaldin and E. Bousquet, *Phys. Rev. B: Condens. Matter Mater. Phys.*, 2012, **86**, 094413.
- 57 L. Cañadillas-Delgado, M. J. Cliffe, M. Geers and O. Fabelo, ILL experiment 5-41-1060, DOI: [10.5291/ILL-DATA.5-41-1060](https://doi.org/10.5291/ILL-DATA.5-41-1060).
- 58 L. Cañadillas-Delgado, M. J. Cliffe and J. Y. Lee, ILL experiment 5-12-344, DOI: [10.5291/ILL-DATA.5-12-344](https://doi.org/10.5291/ILL-DATA.5-12-344).
- 59 L. Cañadillas-Delgado, M. J. Cliffe, O. Fabelo and M. Geers, ILL experiment 5-31-2767, DOI: [10.5291/ILL-DATA.5-31-2767](https://doi.org/10.5291/ILL-DATA.5-31-2767).
- 60 L. Cañadillas-Delgado, M. J. Cliffe, C. V. Colin, O. Fabelo, M. Geers, V. Nassif and I. Puente Orench, ILL experiment 5-31-2816, DOI: [10.5291/ILL-DATA.5-31-2816](https://doi.org/10.5291/ILL-DATA.5-31-2816).



Appendix B

The following pages include the article published from the results in Chapter 4. It follows the structural and magnetic pressure-activated responses as the layered van der Waals material $\text{Ni}(\text{NCS})_2$ is compressed up to 8.4 kbar.

High-pressure behavior of the magnetic van der Waals molecular framework Ni(NCS)₂

Madeleine Geers ^{1,2} David M. Jarvis,³ Cheng Liu,³ Siddharth S. Saxena,³ Jem Pitcairn,¹ Emily Myatt ¹,
 Sebastian A. Hallweger ⁴, Silva M. Kronawitter ⁴, Gregor Kieslich ⁴, Sanliang Ling ⁵, Andrew B. Cairns,⁶
 Dominik Daisenberger,⁷ Oscar Fabelo ^{2,*} and Matthew J. Cliffe ^{1,†}

¹*School of Chemistry, University Park, University of Nottingham, Nottingham NG7 2RD, United Kingdom*

²*Institut Laue Langevin, 71 avenue des Martyrs CS 20156, 38042 Grenoble Cedex 9, France*

³*Cavendish Laboratory, University of Cambridge, Cambridge CB3 0HE, United Kingdom*

⁴*TUM Natural School of Sciences, Technical University of Munich, D-85748 Garching, Germany*

⁵*Advanced Materials Research Group, Faculty of Engineering, University of Nottingham, University Park, Nottingham NG7 2RD, United Kingdom*

⁶*Department of Materials, Imperial College London, Royal School of Mines, Exhibition Road, London SW7 2AZ, United Kingdom*

⁷*Diamond Light Source, Chilton, Didcot OX11 0DE, United Kingdom*



(Received 7 August 2023; revised 22 September 2023; accepted 28 September 2023; published 31 October 2023)

Two-dimensional materials offer a unique range of magnetic, electronic, and mechanical properties which can be controlled by external stimuli. Pressure is a particularly important stimulus, as it can be achieved readily and can produce large responses, especially in low-dimensional materials. In this paper, we explore the pressure dependence of the structural and magnetic properties of a two-dimensional van der Waals (vdW) molecular framework antiferromagnet with ferromagnetic layers, Ni(NCS)₂, up to 8.4 kbar. Through a combination of x-ray and neutron diffraction analysis, we find that Ni(NCS)₂ is significantly more compressible than comparable vdW metal halides, and its response is anisotropic not only out of the plane, but also within the layers. Using bulk magnetization and neutron diffraction data, we show that the ambient layered antiferromagnetic phase is maintained up to the largest investigated pressure, but with an enhanced Néel temperature, T_N ($\Delta T_N/T_N = +19\%$), and a large pressure sensitivity ($Q = \frac{1}{T_N} \frac{dT_N}{dP} = +2.3\% \text{ kbar}^{-1}$), one of the larger values of magnetic pressure responsiveness for a vdW material. Density functional theory calculations suggest that this is due to increasing three dimensionality. These results provide insights into the pressure response of molecular framework vdW magnets and suggest that the investigation of other molecular framework vdW magnets might uncover contenders for future pressure-switchable devices.

DOI: [10.1103/PhysRevB.108.144439](https://doi.org/10.1103/PhysRevB.108.144439)

I. INTRODUCTION

Magnetic van der Waals (vdW) materials, compounds formed from two-dimensional layers held together through weak dispersion interactions, have been the subject of much recent interest as potential single-layer magnetic materials capable of being embedded in spintronic devices [1]. The weak interactions between layers means pressure can switch the sign of interactions, for example, bilayer CrI₃ undergoes an antiferromagnetic-ferromagnetic transition at 27 kbar [2]. It can also induce large enhancements of magnetic interactions, e.g., the ordering temperature T_c increases by 250 K in FeCl₂ with the application of 420 kbar ($Q = \frac{1}{T_c} \frac{dT_c}{dP} = +2.4\% \text{ kbar}^{-1}$) [3], and in NiI₂, T_c increases by 230 K when compressed to 190 kbar ($Q = +1.6\% \text{ kbar}^{-1}$) [4], as well an

enhancement of the helimagnetic state [5,6]. Pressure can also induce qualitative changes in the electronic structure of vdW magnets [7], such as pressure-induced metal-insulator transitions [8,9]. NiI₂ undergoes a pressure-induced metal-insulator transition at 190 kbar [4], as does the recently reported vdW antiferromagnet FePS₃ at 140 kbar [10]. Pressure can even induce superconductivity in FePSe₃ above 90 kbar [11].

Molecular frameworks, made from metals and molecular ligands, have inherently higher flexibility than nonmolecular materials comprised of only atomic ions. The increased length of the ligands enhances the extent of flexing of the frameworks [12,13]. They therefore can be expected to produce large responses at pressures closer to those realizable in practical devices. For example, the magnetic ordering temperature of the three-dimensional cyanide frameworks, [Mn(4-dmap)]₃[Mn(CN)₆]₂ (4-dmap = 4-dimethylaminopyridine) ($Q = +13\% \text{ kbar}^{-1}$) [14] and [Ru₂(O₂CCH₃)₄]₃[Cr(CN)₆] ($Q = +6.5\% \text{ kbar}^{-1}$) [15], rapidly increase with pressure. Our understanding of the pressure response of the magnetism of vdW molecular framework magnets is rapidly developing [16–18].

Nickel(II) thiocyanate, Ni(NCS)₂, is a binary pseudohalide and the only member of the $M(\text{NCS})_2$ family ($M = \text{Mn, Co, Fe, Ni, Cu}$) thus far reported to have in-layer ferromagnetism

*canadillas-delgado@ill.fr

†matthew.cliffe@nottingham.ac.uk

Published by the American Physical Society under the terms of the [Creative Commons Attribution 4.0 International](https://creativecommons.org/licenses/by/4.0/) license. Further distribution of this work must maintain attribution to the author(s) and the published article's title, journal citation, and DOI.

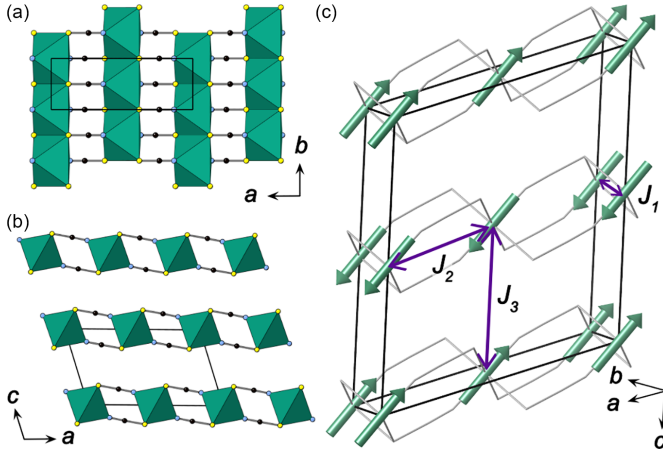


FIG. 1. Structure of $\text{Ni}(\text{NCS})_2$ adapted from Ref. [17]: (a) in-plane structure, (b) layer stacking. Ni = green octahedra, N = blue, C = black, S = yellow. (c) The magnetic structure with the three nearest-neighbor interactions identified. The $\text{Ni}(\text{NCS})_2$ framework is shown as a wire frame for clarity.

[17,19–21] (Néel temperature, $T_N = 54$ K; cf. NiBr_2 $T_N = 52$ K [22]), and is predicted to be a single-layer ferromagnet [23]. It adopts an analogous structure to that of the two-dimensional transition-metal halides MX_2 , comprising NiS_4N_2 octahedra which edge share to form layers in the ab plane (Fig. 1), which stack along the c direction. The rod shape and directionality of the NCS^- lowers the symmetry from the rhombohedral symmetry of NiX_2 to the monoclinic space group $C2/m$ [17]. This relieves the potential frustration and means that no helimagnetic state is found, unlike NiBr_2 and NiI_2 [22].

Here we report the structural and magnetic changes of $\text{Ni}(\text{NCS})_2$ as it is compressed to pressures up to 8.4 kbar. X-ray and neutron powder diffraction experiments have allowed us to follow the evolution of both lattice parameters and the structure under compression. Our combination of magnetometry and low-temperature neutron diffraction measurements show the enhancement of the magnetic ordering temperature with pressure and confirm the magnetic ground state throughout. We carry out density functional theory (DFT) calculations which explain the energetic origins of the observed behavior.

II. METHODS

A. Synthesis

The synthesis of the samples of $\text{Ni}(\text{NCS})_2$ was carried out following the reported synthetic method of Bassey *et al.* [17]. A typical synthesis (quantities as for the neutron sample) is described below.

$\text{NiSO}_4 \cdot 6\text{H}_2\text{O}$ (16.56 g, 63 mmol) was dissolved in deionized H_2O (50 mL), giving a clear green solution. An aqueous solution of $\text{Ba}(\text{SCN})_2 \cdot 3\text{H}_2\text{O}$ (19.37 g, 63 mmol, 120 mL) was added, with the rapid formation of a white precipitate and a green solution. The reaction mixture was stirred at room temperature overnight and the precipitate was removed by centrifugation and filtering under reduced pressure. The

solution was removed *in vacuo*, giving a green-brown microcrystalline powder of $\text{Ni}(\text{NCS})_2$. The compound is stable to humidity in the investigated conditions.

B. Magnetic measurements

Measurements of the magnetic susceptibility were carried out on a pelletized powder sample of $\text{Ni}(\text{NCS})_2$ using a Quantum Design Magnetic Property Measurements System (MPMS) 3 Superconducting Quantum Interference Device (SQUID) magnetometer with moment measurements carried out in direct current (DC) mode. The measured data were collected at pressures of 1.2, 3.8, 5.2, and 8.4 kbar. The zero-field-cooled (ZFC) susceptibility was measured in an applied field of 0.01 T over the temperature range 2 to 300 K. The pressure was applied using a BeCu piston cylinder pressure cell from CamCool Research Ltd., with a Daphne 7373 oil pressure medium. A small piece of Pb was included in the sample space to act as a pressure gauge [24]. As $M(H)$ is linear in this field regime, the small-field approximation for the susceptibility, $\chi(T) \simeq \frac{M}{H}$, where M is the magnetization and H is the magnetic field intensity, was taken to be valid. Isothermal magnetization measurements were carried out on the same sample at 10 K over the field range -7 to $+7$ T for each pressure point.

C. DFT

We have performed density functional theory calculations to probe the structures and energetics of the spin order of $\text{Ni}(\text{NCS})_2$. The spin-polarized DFT + U method (with Grimme's D3 van der Waals correction [25]) was employed in the structural optimizations and energy calculations, using the Vienna Ab initio Simulation Package (VASP) [26]. In our DFT + U calculations, we used a U value of 5.1 eV for the d electrons of Ni^{2+} cations [27,28], and a range of ferromagnetic and antiferromagnetic spin solutions were considered for magnetic Ni^{2+} cations (see Table 2 in the Supplemental Material [29]). We used a plane-wave basis set with a kinetic energy cutoff of 520 eV to expand the wave functions. The Perdew-Burke-Ernzerhof functional [30] in combination with the projector augmented wave method [31,32] was used to solve the Kohn-Sham equations. An energy convergence threshold of 10^{-6} eV was used for electronic energy minimization calculations, and the structural optimizations, including cell parameters and atomic positions, were considered converged if all interatomic forces fell below 0.01 eV/Å. All DFT calculations have been performed in the primitive cell (two formula units per cell) using a k grid with a k -point spacing of around 0.1 \AA^{-1} . To improve the accuracy of the three nearest-neighbor magnetic interactions determined from DFT calculations at different pressures, we additionally performed single-point DFT energy calculations of the various spin configurations at the optimized structures with a higher plane-wave cutoff energy of 800 eV. We note that the relative energy difference between several spin configurations in our DFT calculations can be less than 1 meV/metal (depending on pressure), which is close to the DFT accuracy that we can achieve with our current computational settings.

D. Synchrotron diffraction measurements

X-ray powder diffraction experiments were performed at beamline I15 at the Diamond Light Source, UK, with a wavelength of $\lambda = 0.4246 \text{ \AA}$, applying a custom-made high-pressure powder x-ray diffraction setup suitable for measurements up to 4 kbar [33]. A powder sample of $\text{Ni}(\text{NCS})_2$ was filled into a soft plastic capillary together with silicone oil AP-100 as a nonpenetrating pressure-transmitting medium to maintain hydrostatic conditions. The capillaries were sealed with Araldyte-2014-1. The capillary was loaded into, and in direct contact with, the sample chamber consisting of a metal block filled with water. The water acts as a pressure-transmitting medium, controlled with a hydraulic gauge pump.

Constant wavelength powder x-ray diffraction data were collected at room temperature in the pressure range 0.001 to 4 kbar with a step of 0.2 kbar and an estimated error of ± 0.0030 bar. The data were processed using DAWN [34] with a LaB_6 calibration. Rietveld refinements of the nuclear model were completed using the FULLPROF program [35] and strain analysis carried out using PASCAL [36].

E. Neutron diffraction measurements

1. High-resolution measurements (D2b)

Constant wavelength neutron powder diffraction data were collected on the high-resolution D2b diffractometer [37] at the Institut Laue Langevin (ILL), France. The incident wavelength was $\lambda = 1.59 \text{ \AA}$ and the scattering was measured over an angular range of $10 < 2\theta < 160^\circ$. The sample was loaded in an aluminium holder and placed within an aluminium gas pressure cell with helium used as a pressure-transmitting medium. Diffraction data were collected at room temperature with applied pressures of 1.7, 3.4, 5.1, and 6.7 kbar, with an estimated error of ± 0.5 kbar. Further diffraction data were collected at a pressure of 6.7 kbar at temperatures of 20, 40, and 180 K. The pressure was set at room temperature, then the system was cooled for the low-temperature data. The cell was operated with a gas compressor to regulate the pressure as the temperature was lowered and ensure maintenance of constant pressure. A heater inside the gas capillary ensured the helium was gaseous at low temperatures. NOMAD software [38] from the ILL was used for data collection. Refinements of the nuclear models were completed using the FULLPROF program [35].

2. High-intensity measurements (D1b)

Constant wavelength powder neutron diffraction data were collected on the high-intensity medium resolution D1b diffractometer [39] at the Institut Laue Langevin (ILL), France. The incident wavelength was $\lambda = 2.52 \text{ \AA}$ and the scattering was measured over an angular range of $2 < 2\theta < 128^\circ$. The sample was loaded in an aluminium holder and placed within an aluminium gas pressure cell with helium used as a pressure-transmitting medium. Diffraction data were collected at room temperature with applied pressures of 3, 4.5, and 6.7 kbar, with an estimated error of ± 0.5 kbar. A thermal diffractogram was collected at 3 kbar, heated with a programmed ramp of 0.05 K min^{-1} between 34 and 65 K.

A second thermal diffractogram was collected at 4.5 kbar, heated with a programmed ramp of 0.07 K min^{-1} between 44 and 60 K. At a pressure of 6.7 kbar, data were collected at a constant temperature of 20 K. The pressure was set at room temperature, then the system was cooled for the low-temperature data. The cell was operated with a gas compressor to regulate the pressure as the temperature was lowered and ensure maintenance of constant pressure. A heater inside the gas capillary ensured the helium was gaseous at low temperatures. NOMAD software [38] from the ILL was used for data collection. Refinements of the nuclear and magnetic model were completed using the FULLPROF program [35].

III. RESULTS

The structural and magnetic changes that $\text{Ni}(\text{NCS})_2$ undergo with temperature at ambient pressure have previously been determined by Bassey *et al.* [17]. The compound crystallizes in the monoclinic $C2/m$ space group as two-dimensional layers stacked along the c axis. It has an ambient magnetic ordering temperature, T_N^0 , of 54 K, below which it magnetically orders as an antiferromagnet. The moments correlate ferromagnetically within the ab plane and antiferromagnetically between adjacent planes, ordering with a propagation vector of $\mathbf{k} = (0, 0, \frac{1}{2})$ in the magnetic space group C_c2/c . The moments are oriented along the N-Ni-N bond direction and are restricted to the ac plane by symmetry. The three nearest-neighbor interactions are J_1 through Ni-S-Ni (b direction), J_2 along Ni-NCS-Ni (a direction), and J_3 occurs between the metals on adjacent layers [c direction; Fig. 1(c)].

A. Nuclear structure under pressure

Ambient temperature diffraction measurements were carried out on a powder sample of $\text{Ni}(\text{NCS})_2$ using x rays (I15, Diamond, UK) between 0.001 and 4.0 kbar (in 0.2 kbar steps) and with neutrons (D2b, ILL, France) at 1.7, 3.4, 5.1, and 6.7 kbar. The variation in lattice parameters was determined by performing Rietveld refinements for both the x-ray and neutron data (Fig. 2). The atom positions and anisotropic displacement parameters were fixed to that of the structure at ambient pressure [17]. Throughout the refinements, the lattice parameters were refined freely, along with background and peak shape parameters. From these analyses, we found no evidence of a phase transition, with $\text{Ni}(\text{NCS})_2$ retaining its monoclinic symmetry throughout the pressure regime. From refinements of the x-ray data, the volume is reduced from $225.18(6) \text{ \AA}^3$ at 0.001 kbar to $220.65(6) \text{ \AA}^3$ at 4.0 kbar. Fitting the x-ray data to a third-order Birch-Murnaghan equation of state [40] gives a bulk modulus $B_0 = 170(2)$ kbar and $B' = 15(1)$. Comparable trends are observed for the compressibilities and reduction in axes observed for the neutron data up to 6.7 kbar as well [$B_0 = 156(6)$ kbar and $B' = 22(3)$; Fig. 3].

Both data sets, x ray and neutron, show that as $\text{Ni}(\text{NCS})_2$ is compressed, all unit cell axes decrease in length, while the β angle remains broadly constant (Fig. 3). To assess the degree of anisotropy, the strains along the principal axes were calculated (Table I) using the PASCAL program [36]. The principal axes X_1 , X_2 , and X_3 lie in the following directions: $X_1 \approx a$, along the Ni-NCS-Ni pathway; $X_2 = b$, along the Ni-S-Ni

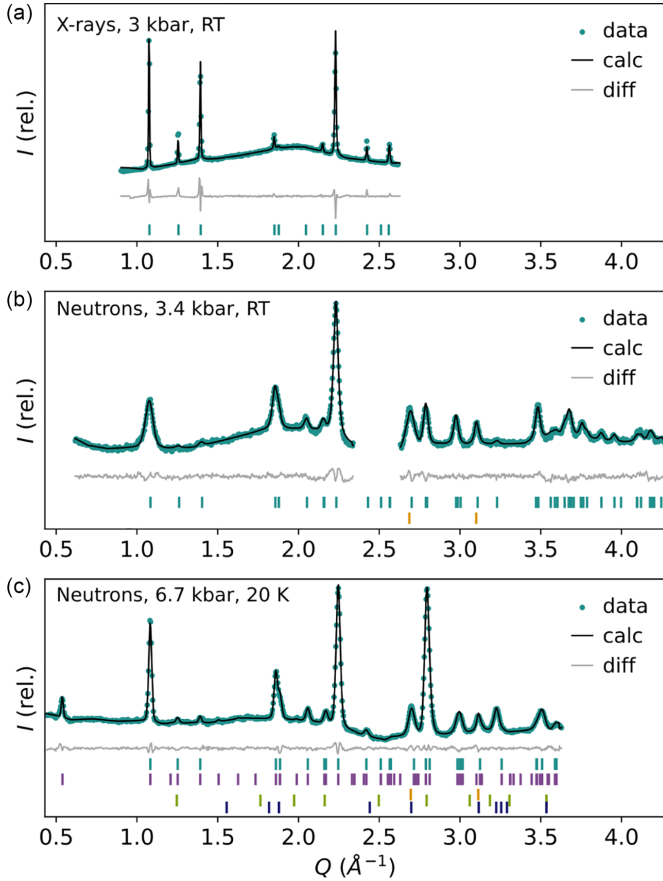


FIG. 2. Rietveld refinements of diffraction data. (a) Synchrotron x-ray data (I15, Diamond) measured at 3 kbar and at ambient temperature, (b) neutron data (D2b, ILL) measured at 3.4 kbar and at ambient temperature, (c) neutron data (D1b, ILL) measured at 6.7 kbar and at 20 K. Le Bail fits were made to account for reflections arising from the aluminium, oxygen, and nitrogen. The tick marks show the position of structural reflections (turquoise), magnetic reflections (purple), the aluminium sample holder (orange), oxygen (light-green) and nitrogen (dark-blue) phases.

bonds; $X_3 \approx c$, between the layers. The pressure dependence of the principal axes shows that the compressibilities, $K_i = -1/\varepsilon_i \frac{d\varepsilon_i}{dP}$, derived from fitting an empirical equation of state [$\varepsilon_i(P) = \varepsilon_0 + \lambda(P - P_C)^\nu$], are very anisotropic. $K_3 = 32.5(3) \text{ TPa}^{-1}$ is more than double $K_2 = 13.5(1) \text{ TPa}^{-1}$, and $K_1 = 3.8(4) \text{ TPa}^{-1}$ is an order of magnitude smaller.

TABLE I. Compressibilities (K) for the principle axes of $\text{Ni}(\text{NCS})_2$ calculated from synchrotron x-ray data (I15, Diamond) at 4 kbar and from neutron data (D2b, ILL) at 6.7 kbar. The definition of the principal axes (X_i) is given relative to the unit cell (a, b, c) for the structure at 4 kbar.

Axes	$K \text{ (TPa}^{-1}\text{)}$			a	b	c
	X-rays	Neutrons				
X_1	3.8(4)	3(2)		0.990	0.0	0.141
X_2	13.5(1)	13.9(8)		0.0	1.0	0.0
X_3	32.5(2)	26.9(6)		0.124	0.0	0.992
V	50.0(5)	48(1)				

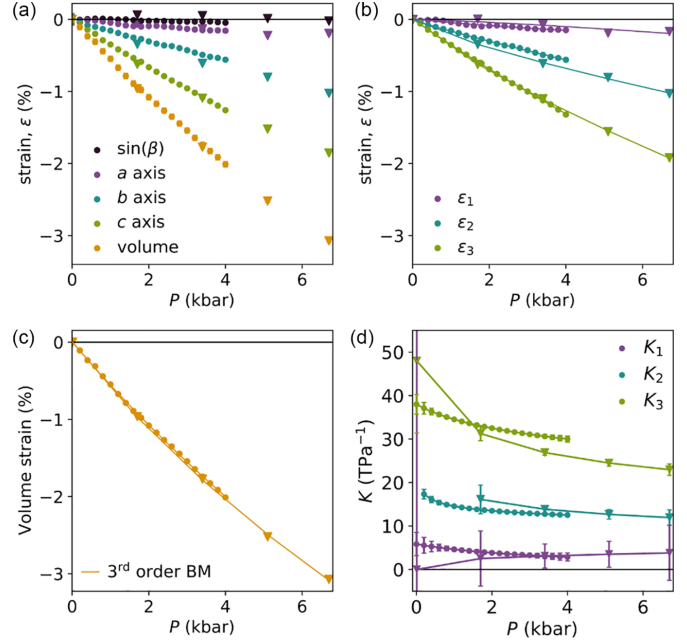


FIG. 3. Crystallographic parameter variations determined from Rietveld refinements at ambient temperature using x rays (circles, measured with I15, Diamond, 0.001 to 4 kbar) and neutrons (triangles, measured with D2b, ILL, 0.001 to 6.7 kbar). (a) Normalized change of the unit cell parameters. (b) Strain (ε_i) along the principal axes (X_i) with lines showing the linear compressibilities. (c) The volume dependence with pressure, fitted with the third-order Birch-Murnaghan (BM) equation of state with $B_0 = 170(2) \text{ kbar}$ and $B' = 15(1)$ at 4 kbar for x rays and $B_0 = 156(6) \text{ kbar}$ and $B' = 22(3)$ at 6.7 kbar for neutrons. (d) The compressibility (K) along the principal axes as a function of pressure. Standard errors are shown with vertical lines.

To explore the changes in the structure over a broader pressure range, DFT calculations were performed at nominal pressures of 0, 5, 10, 20, 50, and 100 kbar. These calculations, as they were carried out at 0 K, were in the experimentally derived layered antiferromagnetic ground state. The fitted bulk modulus using the third-order Birch-Murnaghan equation of state is $255.7(2) \text{ kbar}$, with $B' = 6.42(9)$. The compressibilities at 10 kbar are $K_3 = 18.1(5) \text{ TPa}^{-1}$, $K_2 = 10.1(4) \text{ TPa}^{-1}$, and $K_1 = 3.0(2) \text{ TPa}^{-1}$, broadly consistent with the measured compressibilities. On increasing the pressure to 100 kbar, we find, as expected, a significant stiffening: $K_3 = 5.1(5) \text{ TPa}^{-1}$, $K_2 = 5.5(8) \text{ TPa}^{-1}$, and $K_1 = 1.9(5) \text{ TPa}^{-1}$.

B. Variable-temperature high pressure

We also sought to investigate the effect of high pressure on the thermal expansion of this material by measuring variable-temperature neutron diffraction patterns ($T = 20, 40, 180, \text{ and } 298 \text{ K}$) at our maximum pressure of 6.7 kbar. We find normal volumetric thermal expansion, with a coefficient of thermal expansion $\alpha_V = 1/V \frac{dV}{dT} = 42(3) \text{ MK}^{-1}$. At 6.7 kbar, the thermal expansion is anisotropic with linear thermal expansivities along the principal strain directions of $\alpha_1 = 1/\varepsilon_1 \frac{d\varepsilon_1}{dT} = 26(1) \text{ MK}^{-1}$, $\alpha_2 = 14(2) \text{ MK}^{-1}$, and $\alpha_3 = 1.12(5) \text{ MK}^{-1}$ [broadly in the same directions as the compressibilities; Fig. 4(a)]. There are also significant

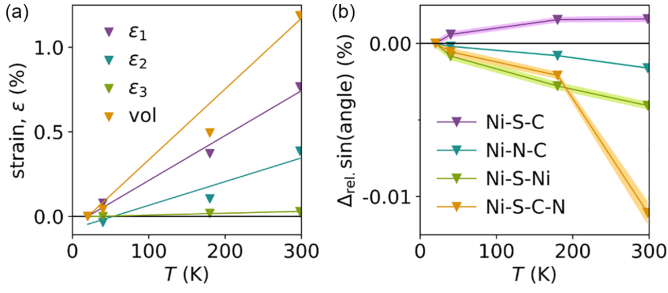


FIG. 4. Selected data from Rietveld refinements at 6.7 kbar measured at 20, 40, 180, and 298 K using the D2b diffractometer (ILL). (a) Relative change in the principle axes and volume, (b) relative change in $\sin(\text{angle})$ of Ni-ligand bonds and the dihedral angle Ni-S-C-N. The shaded regions show the calculated errors.

structural changes: with $\angle\text{Ni-S-Ni}$ (along X_2) expanding significantly on cooling, $\Delta\sin(\text{Ni-S-Ni}) = -0.0041(2)\%$, whereas $\angle\text{Ni-N-C}$ and $\angle\text{Ni-S-C}$ (predominantly along X_1) change much less, $\Delta\sin(\text{Ni-N-C}) = -0.00160(6)\%$ and $\Delta\sin(\text{Ni-S-C}) = +0.0016(2)\%$. The torsion angle between Ni-S-C-N decreases by $\Delta\sin(\text{Ni-N-C}) = -0.0111(7)\%$ [Fig. 4(b)].

At this highest pressure of 6.7 kbar, additional peaks emerged in the neutron datasets at high Q at temperatures below approximately 55 K, which is well into the magnetic ordered phase. These likely arise from a combination of oxygen and/or nitrogen phases crystallizing due to the presence of air in the pressure cell, and we accounted for them using additional Le Bail phases [41,42]. We found no anomalies in the magnetometry data corresponding to this transition, further supporting our assumption that this is not sample related.

C. Magnetometry

To assess how the bulk magnetic properties of the material vary with pressure, we carried out zero-field-cooled susceptibility measurements at 1.2(1), 3.8(1), 5.2(1), and 8.4(1) kbar on a pelletized polycrystalline sample. At each pressure, the magnetic susceptibility increases on cooling until a broad maximum is reached at the ordering temperature [Fig. 5(a)]. The ordering temperature shifts to higher values as the sample is compressed and is accompanied by a decrease in the maximum susceptibility. At the highest measured pressure, 8.4(1) kbar, $\text{Ni}(\text{NCS})_2$ orders at $T_N = 64.6(4)$ K, which is a +19% increase from ambient pressure, giving $Q = +2.3\% \text{ kbar}^{-1}$ [Fig. 5(b)].

We also carried out isothermal measurements at the same pressure points at 10 K between -7 and $+7$ T [Fig. 5(c)], which did not show saturation in this field regime, as expected for a bulk antiferromagnet. We found that the maximum magnetization that was measured increased up to 3.8(1) kbar, before decreasing at higher pressures.

D. Magnetic structure

Our bulk magnetic measurements showed a significant enhancement in magnetic ordering temperature; however, to understand the detailed evolution of the magnetic structure, we carried out neutron diffraction measurements on a powder sample (1.2 g) using the high-flux D1b diffractometer at

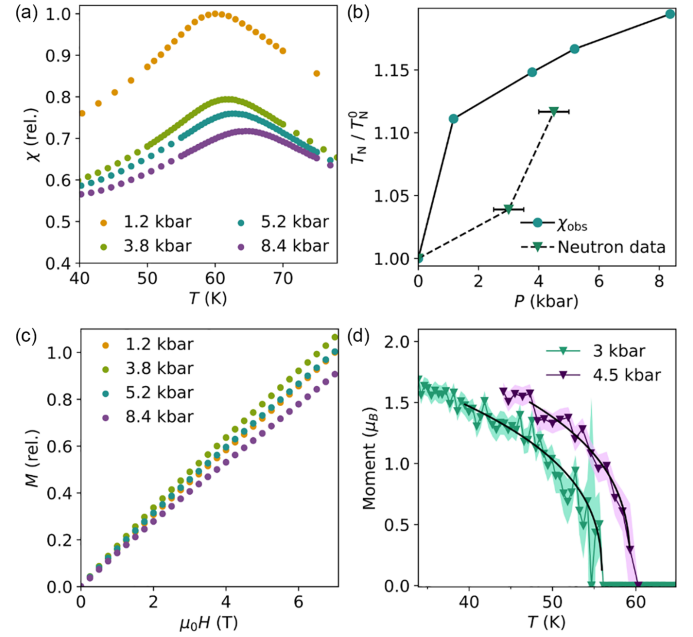


FIG. 5. (a) Magnetic susceptibility measured at 1.2(1), 3.8(1), 5.2(1), and 8.4(1) kbar; the relative susceptibility has been normalized to the maximum susceptibility at 1.2 kbar. (b) Relative change in T_N as a function of pressure derived from susceptibility (circles) and neutron diffraction data (triangles). Error bars related to pressure determination are shown for the neutron data; the error bars are contained within the symbols for the magnetometry data. The ordering temperatures were normalized to the ambient pressure ordering temperature, $T_N^0 = 54$ K. (c) Isothermal magnetization measurements carried out at 10 K plotted between 0 and +7 T, showing the relative magnetization normalized to the maximum magnetization at 1.2 kbar. The magnetic moment determined from Rietveld refinement of the neutron diffraction data (D1b, ILL) at 3 and 4.5 kbar, fitted by a power law, given by Eq. (1) (black line). The shaded regions show the calculated errors of the magnitude of the moment.

the ILL. Neutron diffraction data were collected below the ordering temperatures at 3, 4.5, and 6.7 kbar at the lowest temperatures for each pressure ($P = 3$ kbar, $T = 34$ K; $P = 4.5$ kbar, $T = 44$ K; $P = 6.7$ kbar, $T = 20$ K). In these low-temperature data sets, we observed the appearance of an additional Bragg reflection at 0.54 \AA^{-1} at all pressures [Fig. 2(c)] and no other additional reflections, which allowed us to confirm that the propagation vector is $\mathbf{k} = (0, 0, \frac{1}{2})$, identical to that of the ambient pressure material. This propagation vector corresponds to a doubling along the c axis, and we found that of the two maximal magnetic space groups, only the ambient pressure structure C_2/c was able to reproduce the observed intensity with a reasonable moment size.

We then carried out Rietveld refinements on these datasets in which the magnitude of the nickel moment was fixed to $1.75 \mu_B$, in accordance with the reported size of the moment at 2 K at ambient pressure [17], due to the paucity of magnetic Bragg peaks. This then allowed for the angle to be refined as the only free magnetic parameter. At all three pressures, the angle of the moment remains broadly unchanged from the ambient structure model, that is, the moment is oriented along the N-Ni-N bond within the ac plane. As the moment direction does not change up to 6.7 kbar or on warming at

ambient pressure [17], for the following magnetic refinements, therefore, we fixed the moment direction to point along the N-Ni-N bonds. This allowed us to refine the size of the magnetic moment as the only free magnetic parameter in the last cycles of the refinement.

Having established that the magnetic ground state remained unchanged, we next looked to understand the nature of the ordering transition. We collected variable temperature data at 3 kbar ($T = 34\text{--}65$ K) and 4.5 kbar ($T = 44\text{--}60$ K). At 3 kbar, the magnetic moment was refined to $1.68(7)\mu_B$ for the lowest-temperature point ($T = 34$ K) and the ordering temperature is found at $T_N = 56.1(5)$ K. At 4.5 kbar, the refined moment is $1.58(7)\mu_B$ ($T = 44$ K) and decreases with temperature to $0\mu_B$ at $T_N = 58.0(5)$ K. We were able to fit the refined magnetic moments to a power law in the vicinity of the transition,

$$M = A(T_N - T)^\beta, \quad (1)$$

where A is a proportionality constant, T_N is the ordering temperature, and β is a critical exponent [Fig. 5(d)]. For the fits, the errors for A , T_N , and β are calculated from the square root of the covariance matrix from the errors of the refined magnetic moment. At 3 kbar, the fitted values were $\beta = 0.36(6)$ and $T_N = 55.9(7)$ K. At 4.5 kbar, the fitted values were $\beta = 0.33(5)$ and $T_N = 59.3(3)$ K. The values of β are in between 0.326 and 0.367, which is expected for a three-dimensional Ising and Heisenberg antiferromagnet [43].

To gain a deeper understanding of the exchange interactions responsible for the magnetic behavior, we carried out DFT calculations on a variety of spin states as a function of pressure. Geometry optimizations, including both atomic positions and cell parameters, were carried out to probe the magnetic ground state at the same pressures as previously explored (0, 5, 10, 20, 50, and 100 kbar), for six high-symmetry configurations (Table 3 of the Supplemental Material [29]), and the resultant energies and enthalpies were calculated using the Hamiltonian $E = \sum_{ij} J_{ij} S_i S_j + E_0$.

We fitted these DFT-derived energies to a Heisenberg collinear spin Hamiltonian to extract three interactions: J_1 along the Ni-S-Ni direction, J_2 along the Ni-S-C-N-Ni direction, and J_3 corresponding the interactions between layers. At ambient pressure, J_1 is large and ferromagnetic, $-43(8)$ K, J_2 is weaker and also ferromagnetic, $-4(4)$ K, and J_3 is zero within error, consistent with the expected ground state (Fig. 6). The large values of the error suggest that the Heisenberg Hamiltonian that we employed is perhaps not appropriate, either due to large single-ion effects or higher-order interactions (e.g., biquadratic interactions). It is likely that up to 50 kbar, the reported ambient antiferromagnetic structure is the most stable configuration. However, we did not find a strong trend in the predicted J values with pressure beyond the error of the calculations since the relative energy differences between selected spin configurations here are less than 1 meV/metal, meaning we are close to the limits of accuracy for these DFT calculations.

IV. DISCUSSION

From our diffraction data, we have calculated the bulk modulus of $\text{Ni}(\text{NCS})_2$ to be $B_0 = 170(2)$ kbar, which shows that $\text{Ni}(\text{NCS})_2$ is one of the softer van der Waals compounds,

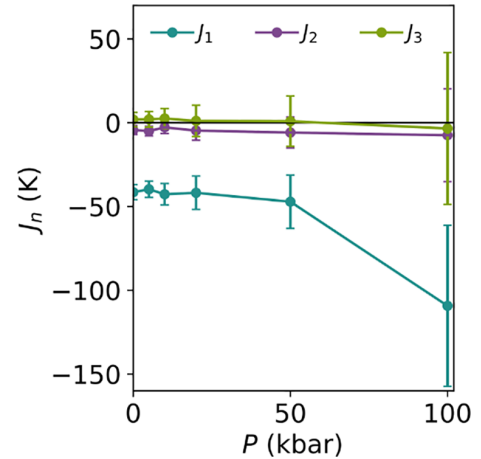


FIG. 6. Calculated enthalpies of the three nearest-neighbor interactions obtained from DFT calculations at ambient, 5, 10, 20, 50, and 100 kbar, where $J > 0$ describes antiferromagnetic interactions and $J < 0$ describes ferromagnetic interactions. The calculated uncertainties associated with fitting to the Heisenberg Hamiltonian are shown with vertical lines.

e.g., for CrBr_3 , $B_0 = 230$ kbar [44], and for FePSe_3 , $B_0 = 828$ kbar [11]. High-pressure structural phase transitions are common in layered compounds [10,45,46]; however, our DFT calculations do not provide any evidence of a structural phase transition up to 100 kbar. *Ab initio* structure searches and larger supercell calculations, together with higher-pressure calculations, would allow further exploration of the potential for new $\text{Ni}(\text{NCS})_2$ phases. These calculations also suggest that any metallization transition occurs significantly above 100 kbar, compared to NiI_2 , $P_c = 190$ kbar [47]; FeCl_2 , $P_c = 450$ kbar [8]; and FePS_3 , $P_c \approx 140$ kbar [10].

We can also compare $\text{Ni}(\text{NCS})_2$ with other pseudobinary molecular frameworks. Since changing the metal cation species can influence the flexibility of the structure, we focus here on Ni^{2+} frameworks [48]. The three-dimensional $\text{Ni}(\text{dca})_2$ [$\text{dca} = \text{N}(\text{CN})_2$] has a larger bulk modulus, $B_0 = 360$ kbar [49], than $\text{Ni}(\text{NCS})_2$. As the ligand length increases, it would be expected that the structure becomes more flexible [50]; however, as $\text{Ni}(\text{dca})_2$ is three-dimensionally connected, the resultant bulk modulus is larger than that of layered $\text{Ni}(\text{NCS})_2$. The volumetric compressibility provides only a partial picture, as both compounds are anisotropic. The compressibility of $\text{Ni}(\text{dca})_2$ along the b and c axes is similar to that of $\text{Ni}(\text{NCS})_2$ along the X_2 and X_3 ($b = 11.1 \text{ TPa}^{-1}$ and $c = 24.1 \text{ TPa}^{-1}$), but $\text{Ni}(\text{dca})_2$ shows negative linear compressibility (NLC) in the third (a) direction. The materials have similar ligand arrangements along the a axis, where the nickel ions are bridged by two ligands coordinated in an end-to-end arrangement. In both materials, the hinge ligand-metal-ligand bond angles ω ($\omega = \angle \text{N-Ni-S}$ and $\angle \text{N-Ni-N}$; Fig. 7) decrease: $[\Delta \cos(\frac{\omega}{2})]/P = 0.09\% \text{ kbar}^{-1}$ (NCS), compared to $[\Delta \cos(\frac{\omega}{2})]/P = 0.16\% \text{ kbar}^{-1}$ (dca). In $\text{Ni}(\text{NCS})_2$, the softer Ni-L bonds mean that there is still contraction in the bond lengths (Ni-N = $-0.12\% \text{ kbar}^{-1}$ and Ni-S = $-0.18\% \text{ kbar}^{-1}$). This competition between the two components is likely the cause of the apparent stiffness of the a axis. In contrast, the square-planar $\text{Ni}(\text{CN})_2$ is significantly

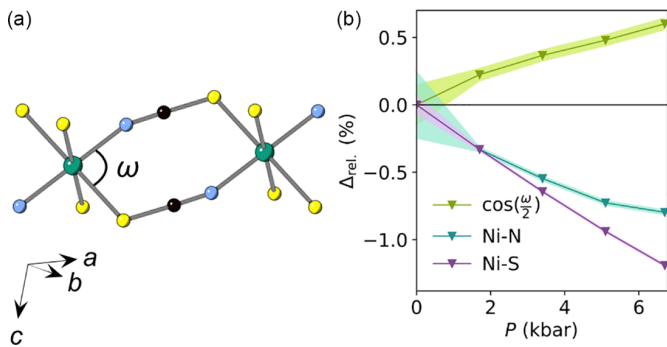


FIG. 7. (a) Nickel ions connected through two NCS ligands, showing the “hinge” angle, ω . Ni = green, N = blue, C = black, S = yellow. (b) Relative change in the bond lengths Ni-N and Ni-S, and the relative change in $\cos(\frac{\omega}{2})$ with pressure. The ambient pressure values were obtained from Ref. [20]. The shaded regions show the errors.

stiffer, $B_0 = 1050$ kbar, perhaps due to the planarity of the structure and linearity of Ni-CN-Ni bonds [51].

Our high-pressure variable-temperature data show that despite being a layered structure, Ni(NCS)₂ has near zero thermal expansion along the X_3 direction. In comparison, there is positive thermal expansion along the X_1 and X_2 directions (Fig. 4). Calculating the thermal expansion coefficients from the published ambient pressure data [17] gives values of $\alpha_1 = 26(2) \text{ MK}^{-1}$, $\alpha_2 = 2.1(9) \text{ MK}^{-1}$, and $\alpha_3 = -5.9(9) \text{ MK}^{-1}$. Here, the principal axes are defined as $X_1 = 0.47a + 0.88c$, $X_2 = b$, and $X_3 = -0.56a + 0.83c$ at 100 K. This is rotated slightly in comparison to the high-pressure data (definitions are approximately equal to the directions given in Table I). X_3 exhibits negative thermal expansion, which is uncommon; however, it can be observed in other anisotropic molecular framework compounds [52,53]. These values are comparable to those seen at 6.7 kbar, but the within-layer expansion has decreased. This behavior is not uncommon in layered molecular frameworks and likely reflects the stiffening of the transverse out-of-plane vibrations [52]. Since the ambient pressure structure was measured between 1 and 100 K, and our high-pressure data were measured between 20 and 298 K, direct comparison of coefficients should be done cautiously. Future investigations would be needed for detailed quantitative comparisons.

The most significant change observed on compressing Ni(NCS)₂ is the marked increase in magnetic ordering temperature, $Q = +2.3\% \text{ kbar}^{-1}$. This increase is large compared to other nickel molecular frameworks, such as Ni(dca)₂ ($Q = +0.4\% \text{ kbar}^{-1}$) [54], NH₄Ni(HCOO)₃ ($Q = +0.2\% \text{ kbar}^{-1}$) [55], and NiCl₂(pym)₂, pym = pyrimidine ($Q = +1.3\% \text{ kbar}^{-1}$) [56]. For additional examples, see Refs. [3,4,8,10,11,49,54–65] summarized in the Supplemental Material [29], Fig. 4 and Table 5. The increase of ordering temperatures in these compounds results from both changes in exchange interactions, including the increase in strength of interactions and reduction of frustrating interactions, and the single-ion anisotropy. Our DFT calculations suggest that this compound is not magnetically frustrated, and so the general anticipated enhancement of exchange will be largely reinforcing. The significant uncertainties in the DFT-derived

superexchange parameters suggest that higher-level calculations, incorporating single-ion anisotropy and higher-order exchange interactions, might be necessary for a complete understanding of the underlying magnetic Hamiltonian. The interlayer J_3 pathway, through Ni-S···S-Ni, significantly decreases in distance and is likely the limiting factor in the ordering temperature.

This shift towards a three-dimensional exchange network can be seen in the critical exponent of the temperature dependence of the staggered magnetic moment. A power-law fit [Eq. (1)] of the Rietveld-refined magnetic moment as a function of temperature at 3 and 4.5 kbar [Fig. 5(d)], gave critical exponents of $\beta = 0.36(6)$ and $0.33(5)$, comparable to the three-dimensional Heisenberg results ($\beta = 0.367$), whereas fitting to the published ambient pressure data [17] gave $\beta = 0.25(4)$ and $T_N = 60.3(6)$ K. The high-pressure value is consistent with those of three-dimensional molecular framework magnets, e.g., Mn(dca)₂(pyz) (pyz=pyrazine), where $\beta = 0.38$ [66], whereas the ambient pressure exponent is closer to that of other vdW magnets, e.g., NiCl₂, $\beta = 0.27$ [67]; and FeCl₂, $\beta = 0.29$ [68]. Unfortunately, comparatively large errors (relative to the small energy differences between selected spin configurations) in our DFT-derived superexchange parameters do not allow us to further buttress this picture (Fig. 6). More direct exploration of the changes in the exchange parameters, whether through spectroscopy or other bulk measurements, would be valuable to explore this two-dimensional to three-dimensional crossover.

We find no evidence of any spin rotation with pressure in Ni(NCS)₂ up to 6.7 kbar. This is consistent with the behavior of other vdW metal halides, including NiI₂, CoI₂ [47], and FeCl₂ [58]. This is perhaps due to strong easy-axis single-ion anisotropy in this material [23,69].

V. CONCLUSION

We have investigated the effects of pressure on the structure and magnetism of the van der Waals framework Ni(NCS)₂. X-ray and neutron powder diffraction data reveal strongly anisotropic strain, with the interlayer direction being an order of magnitude more compressible than the a direction. Low-temperature neutron diffraction measurements combined with susceptibility data show there is a significant increase in the magnetic ordering temperature with pressure driven by the reduction of interlayer separation. This work has explored the use of a thiocyanate framework as a source of flexibility to enhance the changes in the magnetic properties of a van der Waals material. It suggests that further molecular framework magnets hold potential to show marked responses to compression. Following this work, it would also be worthwhile to explore the monolayer limits of Ni(NCS)₂ under pressure to observe if more drastic changes to the magnetic structure can be obtained for a few-layer molecular framework.

The raw data sets are available at Refs. [70,71].

ACKNOWLEDGMENTS

M.G. acknowledges the Institut Laue Langevin (ILL, France) Graduate School for provision of a studentship. M.J.C. acknowledges the School of Chemistry,

University of Nottingham for support from Hobday bequest. We acknowledge the ILL for beam time under Proposal No. 5-24-660. S.L. acknowledges the use of the Sulis supercomputer through the HPC Midlands+ Consortium, and the ARCHER2 supercomputer through membership of the UK's HPC Materials Chemistry Consortium, which are funded by EPSRC Grants No. EP/T022108/1 and No. EP/R029431/1, respectively. The MPMS measurements were carried out using the Advanced Materials Characterisation Suite in the Maxwell Centre, University of Cambridge, funded by EPSRC Strategic Equipment Grant No. EP1M000524/1.

We acknowledge Diamond Light Source (UK) for beam time on beamline I15 under Proposal No. CY30815-2.

M.G. and M.J.C. synthesized the samples. M.J.C., D.M.J., C.L., and S.S.S. carried out the magnetometry measurements and analysis. A.B.C., M.G., O.F., L.C.D., and M.J.C. carried out the neutron diffraction experiment and analysis. S.L. carried out the density functional theory calculations. J.P., E.M., S.A.H., S.M.K., G.K., and D.D. carried out the x-ray diffraction measurements. M.J.C., M.G., and L.C.D. performed the analysis of the x-ray diffraction data. M.G., L.C.D., and M.J.C. wrote the paper with contributions from all authors.

-
- [1] D. L. Cortie, G. L. Causer, K. C. Rule, H. Fritzsche, W. Kreuzpaintner, and F. Klose, Two-dimensional magnets: Forgotten history and recent progress towards spintronic applications. *Advanced functional materials*, *Adv. Funct. Mater.* **30**, 1901414 (2020).
- [2] T. Song, Z. Fei, M. Yankowitz, Z. Lin, Q. Jiang, K. Hwangbo, Q. Zhang, B. Sun, T. Taniguchi, K. Watanabe, M. A. McGuire, D. Graf, T. Cao, J.-H. Chu, D. H. Cobden, C. R. Dean, D. Xiao, and X. Xu, Switching 2D magnetic states via pressure tuning of layer stacking, *Nat. Mater.* **18**, 1298 (2019).
- [3] W. M. Xu and M. P. Pasternak, Magnetism in FeCl₂ at high pressures, in *Mössbauer Spectroscopy*, edited by P. Gülich, B. W. Fitzsimmons, R. Rüffer, and H. Spiering (Springer, Dordrecht, 2003), pp. 175–181.
- [4] M. P. Pasternak, R. D. Taylor, A. Chen, C. Meade, L. M. Falicov, A. Giesekus, R. Jeanloz, and P. Y. Yu, Pressure-induced metallization and the collapse of the magnetic state in the antiferromagnetic insulator NiI₂, *Phys. Rev. Lett.* **65**, 790 (1990).
- [5] J. Kapteghian, D. Amoroso, C. A. Occhialini, L. G. P. Martins, Q. Song, J. S. Smith, J. J. Sanchez, J. Kong, R. Comin, P. Barone, B. Dupé, M. J. Verstraete, and A. S. Botana, Effects of pressure on the electronic and magnetic properties of bulk NiI₂, [arXiv:2306.04729](https://arxiv.org/abs/2306.04729).
- [6] C. A. Occhialini, L. G. P. Martins, Q. Song, J. S. Smith, J. Kapteghian, D. Amoroso, J. J. Sanchez, P. Barone, B. Dupé, M. J. Verstraete, J. Kong, A. S. Botana, and R. Comin, Signatures of pressure-enhanced helimagnetic order in van der Waals multiferroic NiI₂, [arXiv:2306.11720](https://arxiv.org/abs/2306.11720).
- [7] G. K. Rozenberg, W. Xu, and M. P. Pasternak, The Mott insulators at extreme conditions; structural consequences of pressure-induced electronic transitions, *Z. Kristallogr. Crystal. Mater.* **229**, 210 (2014).
- [8] G. K. Rozenberg, M. P. Pasternak, P. Gorodetsky, W. M. Xu, L. S. Dubrovinsky, T. Le Bihan, and R. D. Taylor, Pressure-induced structural, electronic, and magnetic phase transitions in FeCl₂ studied by x-ray diffraction and resistivity measurements, *Phys. Rev. B* **79**, 214105 (2009).
- [9] M. P. Pasternak, W. M. Xu, G. K. Rozenberg, R. D. Taylor, G. R. Hearne, and E. Sterer, Pressure-induced magnetic and electronic transitions in the layered Mott insulator FeI₂, *Phys. Rev. B* **65**, 035106 (2001).
- [10] M. J. Coak, D. M. Jarvis, H. Hamidov, A. R. Wildes, J. A. M. Paddison, C. Liu, C. R. S. Haines, N. T. Dang, S. E. Kichanov, B. N. Savenko, S. Lee, M. Kratochvílová, S. Klotz, T. C. Hansen, D. P. Kozlenko, J.-G. Park, and S. S. Saxena, Emergent magnetic phases in pressure-tuned van der Waals antiferromagnet FePS₃, *Phys. Rev. X* **11**, 011024 (2021).
- [11] Y. Wang, J. Ying, Z. Zhou, J. Sun, T. Wen, Y. Zhou, N. Li, Q. Zhang, F. Han, Y. Xiao, P. Chow, W. Yang, V. V. Struzhkin, Y. Zhao, and H.-k. Mao, Emergent superconductivity in an iron-based honeycomb lattice initiated by pressure-driven spin-crossover, *Nat. Commun.* **9**, 1914 (2018).
- [12] P. Serra-Crespo, A. Dikhtarenko, E. Stavitski, J. Juan-Alcañiz, F. Kapteijn, F.-X. Coudert, and J. Gascon, Experimental evidence of negative linear compressibility in the MIL-53 metal-organic framework family, *CrystEngComm* **17**, 276 (2015).
- [13] H. Wu, T. Yildirim, and W. Zhou, Exceptional mechanical stability of highly porous zirconium metal-organic framework UiO-66 and its important implications, *J. Phys. Chem. Lett.* **4**, 925 (2013).
- [14] W. Kaneko, M. Mito, S. Kitagawa, and M. Ohba, Interpenetrated three-dimensional Mn^{II}M^{III} ferrimagnets, [Mn(4-dmap)₄]₃[M(CN)₆]₂·10 H₂O (M=Cr, Mn): Structures, magnetic properties, and pressure-responsive magnetic modulation, *Chem. Europ. J.* **14**, 3481 (2008).
- [15] W. Shum, J.-H. Her, P. Stephens, Y. Lee, and J. Miller, Observation of the pressure dependent reversible enhancement of T_c and loss of the anomalous constricted hysteresis for [Ru₂(O₂CMe)₄]₃[Cr(CN)₆], *Adv. Mater.* **19**, 2910 (2007).
- [16] J. López-Cabrelles, S. Mañas-Valero, I. J. Vitorica-Yrezabal, P. J. Bereciartua, J. A. Rodríguez-Velamazán, J. C. Waerenborgh, B. J. C. Vieira, D. Davidovikj, P. G. Steeneken, H. S. J. Van Der Zant, G. Mínguez Espallargas, and E. Coronado, Isoreticular two-dimensional magnetic coordination polymers prepared through pre-synthetic ligand functionalization, *Nat. Chem.* **10**, 1001 (2018).
- [17] E. N. Basseý, J. A. M. Paddison, E. N. Keyzer, J. Lee, P. Manuel, I. da Silva, S. E. Dutton, C. P. Grey, and M. J. Cliffe, Strengthening the magnetic interactions in pseudobinary first-row transition metal thiocyanates, M(NCS)₂, *Inorg. Chem.* **59**, 11627 (2020).
- [18] P. Perlepe, I. Oyarzabal, A. Mailman, M. Yquel, M. Platonov, I. Dovgaliuk, M. Rouzières, P. Négrier, D. Mondieig, E. A. Sutura, M. A. Dourges, S. Bonhommeau, R. A. Musgrave, K. S. Pedersen, D. Chernyshov, F. Wilhelm, A. Rogalev, C. Mathonière, and R. Clérac, Metal-organic magnets with large coercivity and ordering temperatures up to 242°C, *Science* **370**, 587 (2020).

- [19] E. Shurdha, S. H. Lapidus, P. W. Stephens, C. E. Moore, A. L. Rheingold, and J. S. Miller, Extended network thiocyanate- and tetracyanoethanide-based first-row transition metal complexes, *Inorg. Chem.* **51**, 9655 (2012).
- [20] E. Dubler, A. Reller, and H. R. Oswald, Intermediates in thermal decomposition of nickel(II) complexes: The crystal structures of $\text{Ni}(\text{SCN})_2(\text{NH}_3)_2$ and $\text{Ni}(\text{SCN})_2$, *Z. Kristallogr.* **161**, 265 (1982).
- [21] M. J. Cliffe, J. Lee, J. A. M. Paddison, S. Schott, P. Mukherjee, M. W. Gaultois, P. Manuel, H. Siringhaus, S. E. Dutton, and C. P. Grey, Low-dimensional quantum magnetism in $\text{Cu}(\text{NCS})_2$: A molecular framework material, *Phys. Rev. B* **97**, 144421 (2018).
- [22] A. Adam, D. Billerey, C. Terrier, R. Mainard, L. Regnault, J. Rossat-Mignod, and P. Mériel, Neutron diffraction study of the commensurate and incommensurate magnetic structures of NiBr_2 , *Solid State Commun.* **35**, 1 (1980).
- [23] Y. Wu, W. Sun, S. Liu, B. Wang, C. Liu, H. Yin, and Z. Cheng, $\text{Ni}(\text{NCS})_2$ monolayer: a robust bipolar magnetic semiconductor, *Nanoscale* **13**, 16564 (2021).
- [24] A. Eiling and J. S. Schilling, Pressure and temperature dependence of electrical resistivity of Pb and Sn from 1-300K and 0-10 GPa-use as continuous resistive pressure monitor accurate over wide temperature range; superconductivity under pressure in Pb, Sn and In, *J. Phys. F* **11**, 623 (1981).
- [25] S. Grimme, J. Antony, S. Ehrlich, and H. Krieg, A consistent and accurate ab initio parametrization of density functional dispersion correction (DFT-D) for the 94 elements H-Pu, *J. Chem. Phys.* **132**, 154104 (2010).
- [26] G. Kresse and J. Furthmüller, Efficient iterative schemes for ab initio total-energy calculations using a plane-wave basis set, *Phys. Rev. B* **54**, 11169 (1996).
- [27] W. E. Pickett, S. C. Erwin, and E. C. Ethridge, Reformulation of the LDA + U method for a local-orbital basis, *Phys. Rev. B* **58**, 1201 (1998).
- [28] F. Zhou, M. Cococcioni, C. A. Marianetti, D. Morgan, and G. Ceder, First-principles prediction of redox potentials in transition-metal compounds with LDA + U, *Phys. Rev. B* **70**, 235121 (2004).
- [29] See Supplemental Material at <http://link.aps.org/supplemental/10.1103/PhysRevB.108.144439> for density functional theory spin configurations and results, and unit cell parameters for X-ray and neutron refinements.
- [30] J. P. Perdew, K. Burke, and M. Ernzerhof, Generalized Gradient Approximation Made Simple, *Phys. Rev. Lett.* **77**, 3865 (1996).
- [31] P. E. Blöchl, Projector augmented-wave method, *Phys. Rev. B* **50**, 17953 (1994).
- [32] D. Hobbs, G. Kresse, and J. Hafner, Fully unconstrained non-collinear magnetism within the projector augmented wave method, *Phys. Rev. B* **62**, 11556 (2000).
- [33] N. J. Brooks, B. L. L. E. Gauthé, N. J. Terrill, S. E. Rogers, R. H. Templer, O. Ces, and J. M. Seddon, Automated high pressure cell for pressure jump x-ray diffraction, *Rev. Sci. Instrum.* **81**, 064103 (2010).
- [34] J. Filik, A. W. Ashton, P. C. Y. Chang, P. A. Chater, S. J. Day, M. Drakopoulos, M. W. Gerring, M. L. Hart, O. V. Magdysyuk, S. Michalik, A. Smith, C. C. Tang, N. J. Terrill, M. T. Wharmby, and H. Wilhelm, Processing two-dimensional X-ray diffraction and small-angle scattering data in DAWN 2, *J. Appl. Crystallogr.* **50**, 959 (2017).
- [35] J. Rodríguez-Carvajal, Recent advances in magnetic structure determination by neutron powder diffraction, *Physica B: Condens. Matter* **192**, 55 (1993).
- [36] M. J. Cliffe and A. L. Goodwin, PASCAL: a principal axis strain calculator for thermal expansion and compressibility determination, *J. Appl. Crystallogr.* **45**, 1321 (2012).
- [37] A. Hewat, A New High Resolution Neutron Powder Diffractometer at Ill Grenoble, *Mater. Sci. Forum* **9**, 69 (1986).
- [38] P. Mutti, F. Cecillon, A. Elaazzouzi, Y. Le Goc, J. Locatelli, H. Ortiz, and J. Ratel, Nomad more than a simple sequencer (unpublished).
- [39] I. P. Orench, J. F. Clergeau, S. Martínez, M. Olmos, O. Fabelo, and J. Campo, The new powder diffractometer D1B of the Institut Laue Langevin, *J. Phys.: Conf. Ser.* **549**, 012003 (2014).
- [40] F. Birch, Finite elastic strain of cubic crystals, *Phys. Rev.* **71**, 809 (1947).
- [41] L. Tassini, F. Gorelli, and L. Ulivi, High temperature structures and orientational disorder in compressed solid nitrogen, *J. Chem. Phys.* **122**, 074701 (2005).
- [42] F. A. Gorelli, M. Santoro, L. Ulivi, and M. Hanfland, Crystal structure of solid oxygen at high pressure and low temperature, *Phys. Rev. B* **65**, 172106 (2002).
- [43] S. Blundell, *Magnetism in Condensed Matter*, Oxford Master Series in Condensed Matter Physics (Oxford University Press, Oxford, 2001).
- [44] A. S. Ahmad, Y. Liang, M. Dong, X. Zhou, L. Fang, Y. Xia, J. Dai, X. Yan, X. Yu, J. Dai, G.-j. Zhang, W. Zhang, Y. Zhao, and S. Wang, Pressure-driven switching of magnetism in layered CrCl_3 , *Nanoscale* **12**, 22935 (2020).
- [45] C. S. R. Haines, M. J. Coak, A. R. Wildes, G. I. Lampronti, C. Liu, P. Nahai-Williamson, H. Hamidov, D. Daisenberger, and S. S. Saxena, Pressure-induced electronic and structural phase evolution in the van der Waals compound FePS_3 , *Phys. Rev. Lett.* **121**, 266801 (2018).
- [46] X. Wang, X. Chen, Y. Zhou, C. Park, C. An, Y. Zhou, R. Zhang, C. Gu, W. Yang, and Z. Yang, Pressure-induced iso-structural phase transition and metallization in WSe_2 , *Sci. Rep.* **7**, 46694 (2017).
- [47] M. P. Pasternak, R. D. Taylor, and R. Jeanloz, Pressure-induced Mott transition in transition-metal iodides (invited), *J. Appl. Phys.* **70**, 5956 (1991).
- [48] S. Grover, S. Burger, K. T. Butler, K. Hemmer, P. Vervoorts, G. Kieslich, and R. Grau-Crespo, Tuning the mechanical properties of dicyanamide-based molecular perovskites, *CrystEngComm* **25**, 3439 (2023).
- [49] X. Fan, T. Yan, Q. Wang, J. Zheng, Z. Ma, and Z. Xue, Negative linear compressibility of nickel dicyanamide, *Chem. Lett.* **48**, 1375 (2019).
- [50] S. Dissegna, P. Vervoorts, C. L. Hobday, T. Düren, D. Daisenberger, A. J. Smith, R. A. Fischer, and G. Kieslich, Tuning the mechanical response of metal-organic frameworks by defect engineering, *J. Am. Chem. Soc.* **140**, 11581 (2018).
- [51] S. K. Mishra, R. Mittal, M. Zbiri, R. Rao, P. Goel, S. J. Hibble, A. M. Chippindale, T. Hansen, H. Schober, and S. L. Chaplot, New insights into the compressibility and high-pressure stability of $\text{Ni}(\text{CN})_2$: A combined study of neutron diffraction, Raman spectroscopy, and inelastic neutron scattering, *J. Phys.: Condens. Matter* **28**, 045402 (2016).
- [52] S. A. Hodgson, J. Adamson, S. J. Hunt, M. J. Cliffe, A. B. Cairns, A. L. Thompson, M. G. Tucker, N. P. Funnell, and

- A. L. Goodwin, Negative area compressibility in silver(I) tricyanomethanide, *Chem. Commun.* **50**, 5264 (2014).
- [53] I. E. Collings, J. A. Hill, A. B. Cairns, R. I. Cooper, A. L. Thompson, J. E. Parker, C. C. Tang, and A. L. Goodwin, Compositional dependence of anomalous thermal expansion in perovskite-like ABX_3 formates, *Dalton Trans.* **45**, 4169 (2016).
- [54] C. J. Nuttall, T. Takenobu, Y. Iwasa, and M. Kurmoo, Pressure dependence of the magnetization of $M^{II}(N(CN)_2)_2$: Mechanism for the long range magnetic ordering, *Mol. Cryst. Liq. Cryst. Sci. Technol., Sect. A* **343**, 227 (2000).
- [55] I. E. Collings, R. S. Manna, A. A. Tsirlin, M. Bykov, E. Bykova, M. Hanfland, P. Gegenwart, S. van Smaalen, L. Dubrovinsky, and N. Dubrovinskaia, Pressure dependence of spin canting in ammonium metal formate antiferromagnets, *Phys. Chem. Chem. Phys.* **20**, 24465 (2018).
- [56] J. Kreitlow, D. Menzel, A. U. B. Wolter, J. Schoenes, S. Süllow, R. Feyerherm, and K. Doll, Pressure dependence of $C_4N_2H_4$ -mediated superexchange in $XCl_2(C_4N_2H_4)_2$ ($X = Fe, Co, Ni$), *Phys. Rev. B* **72**, 134418 (2005).
- [57] O. Lis, D. Kozlenko, S. Kichanov, E. Lukin, I. Zel, and B. Savenko, Structural, magnetic and vibrational properties of van der Waals ferromagnet $CrBr_3$ at high pressure, *Materials* **16**, 454 (2023).
- [58] C. Vettier and W. B. Yelon, Magnetic properties of $FeCl_2$ at high pressure, *Phys. Rev. B* **11**, 4700 (1975).
- [59] C. Zhang, Y. Gu, L. Wang, L.-L. Huang, Y. Fu, C. Liu, S. Wang, H. Su, J.-W. Mei, X. Zou, and J.-F. Dai, Pressure-enhanced ferromagnetism in layered $CrSiTe_3$ flakes, *Nano Lett.* **21**, 7946 (2021).
- [60] K. Xu, Z. Yu, W. Xia, M. Xu, X. Mai, L. Wang, Y. Guo, X. Miao, and M. Xu, Unique 2D–3D structure transformations in trichalcogenide $CrSiTe_3$ under high pressure, *J. Phys. Chem. C* **124**, 15600 (2020).
- [61] A. A. Yakovenko, K. W. Chapman, and G. J. Halder, Pressure-induced structural phase transformation in cobalt(II) dicyanamide, *Acta Crystallogr. Sect. B Structur. Sci. Crystal Engineer. Mater.* **71**, 252 (2015).
- [62] I. E. Collings, M. Bykov, E. Bykova, M. G. Tucker, S. Petitgirard, M. Hanfland, K. Glazyrin, S. Van Smaalen, A. L. Goodwin, L. Dubrovinsky, and N. Dubrovinskaia, Structural distortions in the high-pressure polar phases of ammonium metal formates, *CrystEngComm* **18**, 8849 (2016).
- [63] A. Clune, N. Harms, K. R. O’Neal, K. Hughey, K. A. Smith, D. Obeysekera, J. Haddock, N. S. Dalal, J. Yang, Z. Liu, and J. L. Musfeldt, Developing the pressure-temperature-magnetic field phase diagram of multiferroic $[(CH_3)_2NH_2]Mn(HCOO)_3$, *Inorg. Chem.* **59**, 10083 (2020).
- [64] I. E. Collings, M. Bykov, E. Bykova, M. Hanfland, S. Van Smaalen, L. Dubrovinsky, and N. Dubrovinskaia, Disorder-order transitions in the perovskite metal-organic frameworks $[(CH_3)_2NH_2][M(HCOO)_3]$ at high pressure, *CrystEngComm* **20**, 3512 (2018).
- [65] A. Wolter, H.-H. Klauss, F. Litterst, T. Burghardt, A. Eichler, R. Feyerherm, and S. Süllow, A pressure study of the antiferromagnetic phase of $FePM_2Cl_2$ (PM =pyrimidine), *Polyhedron* **22**, 2139 (2003).
- [66] J. L. Manson, Q.-z. Huang, J. W. Lynn, H.-J. Koo, M.-H. Whangbo, R. Bateman, T. Otsuka, N. Wada, D. N. Argyriou, and J. S. Miller, Long-range magnetic order in $Mn[N(CN)_2]_2(py_z)$ (py_z = pyrazine). Susceptibility, magnetization, specific heat, and neutron diffraction measurements and electronic structure calculations, *J. Am. Chem. Soc.* **123**, 162 (2001).
- [67] P. A. Lindgard, R. J. Birgeneau, H. J. Guggenheim, and J. Als-Nielsen, Spin-wave dispersion and sublattice magnetization in $NiCl_2$, *J. Phys. C* **8**, 1059 (1975).
- [68] W. B. Yelon and R. J. Birgeneau, Magnetic properties of $FeCl_2$ in zero Field. II. Long-range order, *Phys. Rev. B* **5**, 2615 (1972).
- [69] G. C. DeFotis, K. D. Dell, D. J. Krovich, and W. W. Brubaker, Antiferromagnetism of $Ni(SCN)_2$, *J. Appl. Phys.* **73**, 5386 (1993).
- [70] See <https://doi.ill.fr/10.5291/ILL-DATA.5-24-660> for the raw data sets.
- [71] See <http://doi.org/10.17639/nott.7336> for all raw data sets.